Organic and Printed Electronics for Biological Microfluidic Applications

Lakshmi Jagannathan

Electrical Engineering and Computer Sciences
University of California at Berkeley

Technical Report No. UCB/EECS-2012-84
http://www.eecs.berkeley.edu/Pubs/TechRpts/2012/EECS-2012-84.html

May 10, 2012

Organic and Printed Electronics for Biological Microfluidic Applications

By

Lakshmi Jagannathan

A dissertation submitted in partial satisfaction of the

requirements for the degree of

Doctor of Philosophy

in

Engineering - Electrical Engineering and Computer Sciences

in the

Graduate Division

of the

University of California, Berkeley

Committee in charge:

Professor Vivek Subramanian, Chair
Professor Sayeef Salahuddin
Professor Ronald Gronsky

Spring 2012

Abstract

Organic and Printed Electronics for Biological Microfluidic Applications

by

Lakshmi Jagannathan

Doctor of Philosophy in Engineering - Electrical Engineering and Computer Sciences

University of California, Berkeley

Professor Vivek Subramanian, Chair

Advances in research and technology are happening now more than ever in the biotechnology industry. Efficient methods for biological processes and better detection and treatment methods are constantly being sought by researchers. Collaboration among different fields of science and technology has brought us one step closer towards achieving this goal in this work. One such technology that has the capability of providing efficient methods and processes for biology is printed electronics. Printed electronics is an attractive paradigm for realization of biological microfluidic systems. The large area of these systems makes printing valuable from a cost perspective. Furthermore, since printing allows for easy integration of disparate materials on the same substrate through spatially-specific deposition, printed electronics is particularly useful for integration of diverse biological microfluidic functionality on the same substrate.

While there have been instances of printed transistors and passive components, there have been no demonstrations to date of the critical components required for biological microfluidic applications or lab on a chip (LOC) devices. In this work, for the first time, we present all-printed gold heaters, gold resistive temperature detectors, and electrostatically actuated PDMS microfluidic valves designed for biological microfluidic applications. In addition, work on DNA sensors using printable organic (pentacene) thin film transistors (OTFTs) is also presented for use in LOC devices.

Many biological applications require precise control and stability of temperature, which is demonstrated here through the integration of printed heaters and printed RTDs into a microchip bioprocessor system capable of polymerase chain reaction (PCR). Flow rate measurements and dynamic characteristics of printed PDMS valves are also presented to demonstrate the effectiveness of these devices. With the 440μm wide and 16μm deep microfluidic channels used in this project, the valve with the thinnest PDMS membrane (55μm) closed the channel completely (i.e. flow rate = 0) at a pull-in voltage of 250V. This valve closed and opened in approximately 1.5 and 5.5 seconds, respectively. Pentacene surface has also been optimized to arrive at the best sensitivity for DNA immobilization and hybridization, bringing us a step closer in realizing printed OTFT DNA sensors for 'tag-free' electrical detection. To summarize the sensor results, thinner films, higher substrate temperature, and higher input current during pentacene evaporation ensured that DNA immobilized in the channel part of the transistor and therefore provided for highest sensitivity of pentacene film to DNA.

This work has thus successfully revealed the potential of printed electronics in real-world biological applications and has also paved the way for exciting future research areas for this technology.

Acknowledgements

I dedicate this dissertation to my family, friends, colleagues, and advisor. I've realized that doing a PhD cannot be an individual journey; my PhD would not have been possible without each one of them.

I'm very fortunate to have an incredible support system. I'm blessed to have the most loving and supportive family. I thank my parents for inspiring me to be a better person everyday. Their unconditional love, encouragement, and support have made me who I am and helped me get my PhD. I really could not have done it without them. I thank my husband, Srinath, for being most loving and supportive. His patience with my unpredictable research schedule everyday, his encouraging words when I was discouraged with all things research related, and most importantly his love and support for me always has helped me tremendously in completing this journey. In addition, I want to also thank him for patiently proofreading my PhD thesis for me! My heartfelt thanks to his incredible and loving family as well for supporting and encouraging me in this journey. I would also like to thank my sister, my brother-in-law, and my 2-year old nephew, Keshav, for their love, inspiration, and constant encouragement. Keshav helped me get through a lot of dull moments in my PhD with his smile, love, and mischief ☺. I also want to express my heartfelt thanks to my aunts, uncles, and my cousins in San Jose for their incredible love and support always. They were truly a home away from home, and it was comforting and wonderful to have them close by.

A big inspiration for me during my PhD was my advisor, Dr. Vivek Subramanian. Vivek is a great role model for all of us. When I came into grad school, I remember him saying that his goal is to make me (and all of his students) a leader and not a follower. His pursuit of making us thorough in every aspect of research and relevant subject areas has really made me strive towards perfection in what I do. His high expectations have made me a more confident person and a meticulous researcher. He has the perfect amount of involvement where he lets us be creative and lead our own projects and at the same time steers us in the right direction when we most need it. I thank him for being a great advisor and helping me grow as a student, researcher and as a person!

I am fortunate to also have an incredible group of friends. My friends in my youth group gave me the strength and encouragement I needed on this challenging PhD journey! My youth group advisor, Karen Flagg, had the perfect and most encouraging words to say when I most needed her. My friends and roommate at Berkeley shaped my wonderful Berkeley experience. All my friends were really there for me when I needed them the most. I really thank them for everything they have done for me and making this journey possible.

I also had the wonderful opportunity to work with many inspiring students, colleagues, and professors at Berkeley. I want to thank Professor Ronald Gronsky for inspiring discussions on my research project and for giving me important inputs on my dissertation. I want to thank Professor Sayeef Salahuddin for taking the time to read my dissertation and giving me valuable inputs as well. I also want to thank Professor Ali Javey for reading and providing suggestions on my Master's thesis. I want to thank Samantha Cronier from Professor Richard Mathies' group for collaborating with me in making the biological demonstrations possible and giving me valuable inputs in making the projects work well. I want to also thank Professor Richard Mathies and his group for allowing me to use their lab at all times and giving me important insights to understand and analyze my results. I want to thank Professor Wilbur Lam, now at Emory University, for working with me on a project on early detection of cancer earlier in my PhD career. It inspired to continue working on projects that used electrical engineering and

printed electronics for biology. I want to thank Dr. Qintao Zhang, a graduate from our group, for being a mentor on my project when I started graduate school. I would like to thank my entire research group (EECS Organics Electronics Group), for always being there for me when I needed them! I was truly humbled and honored to work everyday with such a hard working and intelligent group of people. They really made my Berkeley experience meaningful and fun! I want to also thank three undergrads who helped me with my project over the summers, Dwight Williams, Daniel Forchheimer, and Walter Li. Their insights and hard work contributed towards my project.

I also owe my thanks to a lot of other people at Berkeley. Ruth Gjerde, Pat Hernan, and Sheila Humphreys were there for me from the very beginning of graduate school. Gwen Lindsey and Charlotte Jones have also helped me numerous times during my PhD. I could not have done it without the help of the nanolab staff, who attended to my concerns in the lab as soon as possible. In particular, I would like to thank Danny Pestal, Joe Donnelly, and Al Briggs for helping me!

I would like to thank my undergraduate alma mater, Southern Methodist University (SMU), for helping me explore and develop a passion for engineering, math, and biology. I would like to thank Professor Richard Williams in SMU for his constant encouragement and confidence in me! In addition, I would like to thank Texas Instruments for allowing me to do many internships with them and inspiring me to do graduate school and research in semiconductor devices. Last but not least, I want to thank Semiconductor Research Corporation (SRC) and Intel for providing me with a fellowship to support me through all my years in graduate school!

Again, I'm indebted to all of these people for directly and indirectly helping me with my PhD. My heartfelt gratitude and appreciation goes to each one of them, without whom my PhD would not have been possible. Thank you!

Table of Contents

1. Introduction

Advances in research and technology are happening now more than ever in the biotechnology industry. Efficient methods for biological processes and better detection and treatment methods are constantly being sought by researchers. Collaboration among different fields of science and technology has brought us one step closer towards achieving this goal in this dissertation.

One such technology that has the capability of providing efficient methods and processes for biology is printed electronics. Printed electronics refers to electronics that are based on materials that can be deposited onto a surface using printing techniques. It represents a major paradigm shift from conventional fabrication of electrical and electronic components (ex: silicon chips) by enabling the production of lightweight, flexible, and thin film electronic devices on inexpensive materials such as paper, plastic or similar flexible substrates. Specifically, for biological applications, the ability of printed electronics to efficiently form thin film structures using additive processing plays an important role in increasing the overall efficiency in fabrication and functioning of biological systems. Additive processing, which refers to the ability of creating a structure by laying down successive layers of materials, allows for deposition of materials where needed and saves cost in material consumption as compared to conventional processing methods. In Table 1, conventional processing techniques used for the fabrication of electronic devices and structures in silicon and biology are compared with processing techniques possible with printed electronics.

Conventional Processing	Processing using Printed Electronics
Subtractive processing (photolithography and wet/dry etching for layer definitions)	Additive processing (printing) for layer definitions
Controlled (e.g. a vacuum environment)	Ambient temperature and pressure conditions
Typically requires a high thermal budget during processing	Requires a low thermal budget allowing for use of flexible and plastic substrates

Table 1. Comparison between conventional processing and processing using printed electronics.

Conventional fabrication of electronic components involves multiple steps that require high temperatures and a controlled environment. In addition, photolithography and masks are required to enable the fabrication of desired patterns on a substrate [1]. Many steps are involved in the lithography process including the making of masks and etching/removal (and therefore waste) of materials. In contrast, printed electronics is cost-effective (since material is only deposited in the required areas) especially for large-area applications [2] and can be performed with fewer steps at lower temperatures suitable for flexible, plastic substrates. In addition, vacuum conditions are not required for printed electronics, thereby eliminating the need for auxiliary equipment that may be needed otherwise.

To implement printed electronics, a variety of techniques have been used in industry and research, including screen printing, offset printing, gravure, flexography, inkjet printing and extrusion printing. Among the various printing techniques, gravure (continuous roll-to-roll printing), inkjet, and extrusion printing are the most attractive systems to realize printed electronics due to their relatively high printing resolution. The principle behind each of these printing methods is illustrated in Figure 1.

To begin with, in gravure printing (Figure 1a), the print layout is engraved on a plate cylinder. The engraving depressions in this plate cylinder carry the ink from the ink tray. The excess ink is stripped off by means of a doctor blade. The impression cylinder presses the substrate against the plate cylinder and the ink therefore transfers onto the substrates, creating the desired images [3]. Numerous research efforts are being made to achieve single micron features with this technology. One of the biggest advantages of gravure is that since it is capable of continuous roll-to-roll printing, it yields faster throughput and is especially suitable for high volume productions.

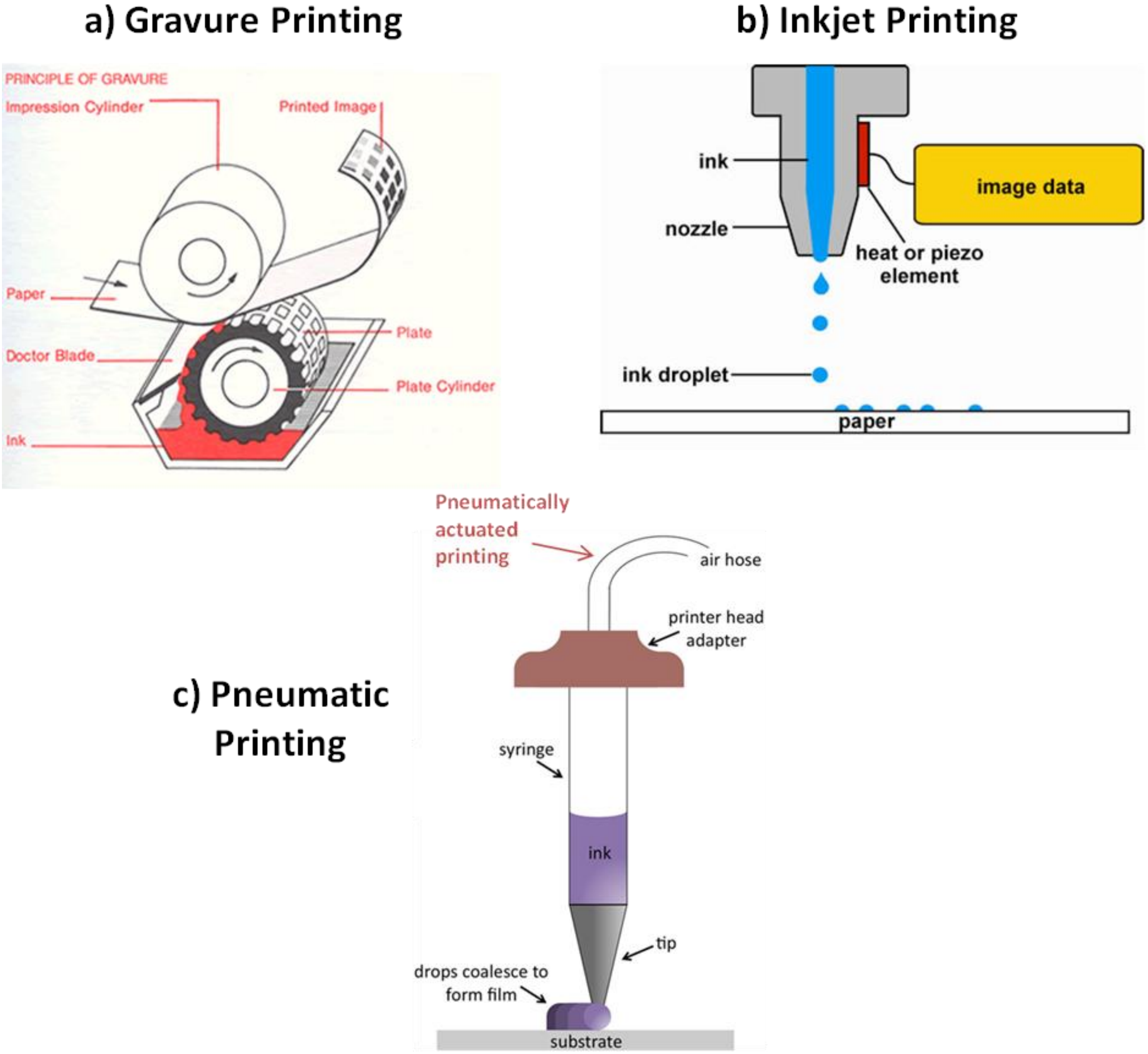

Figure 1. The principle behind a) gravure [3], b) inkjet [4], and c) pneumatic [5] printing methods.

Inkjet printing (Figure 1b), and particularly drop-on-demand inkjet printing technology used in this thesis, only ejects drops of ink as required. Using either piezoelectric or thermal actuation methods, the ink is forced out of the cartridge and nozzle in response to digital signals created by the input image data[4]. The ink is thereby deposited on the substrate to create the desired pattern. Inkjet printing allows for printing of fine features (~20μm wide and <1μm thick lines) and is capable of utilizing ink with viscosities between 5-20cPs.

Finally, pneumatic printing (Figure 1c), also known as extrusion and dispenser printing, uses 'direct write dispenser printing' technology for printing of materials [5]. The pneumatic printing system is composed of a syringe and needle connected to a pneumatic controller and is mounted on an *x–y–z* stage. To pattern a material using the dispenser printer, ink is loaded into a syringe, extruded through a hollow needle of predetermined dimensions and 'written' onto a substrate via a succession of drops. The drop size is determined by the needle's dimensions, ink rheology and applied pressure. The resulting printed film morphology depends on the dimensions of the extruded drops as well as the traversing distance, speed and time between shots. In contrast to the former two printing methods, pneumatic printing allows for a variety of substrates including printed circuit boards (PCB), glass, and silicon wafers, and a wide range of viscosities for printable inks. In this thesis, inkjet printing and pneumatic printing will be used to implement devices for biological applications, and therefore these printing techniques will be discussed in more detail in the following chapters.

The three printing techniques discussed thus far faciliate the use of printed electronics in numerous applications, as listed in Figure 2. OLED displays and photovoltaics are major emerging markets in this field. The sensors market, although small, has tremendous potential, as demonstrated in this work.

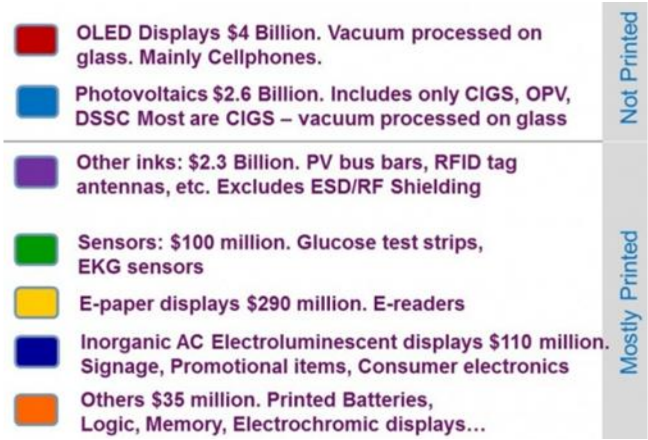

🟥 OLED Displays $4 Billion. Vacuum processed on glass. Mainly Cellphones.

🟦 Photovoltaics $2.6 Billion. Includes only CIGS, OPV, DSSC Most are CIGS – vacuum processed on glass

Not Printed

🟪 Other inks: $2.3 Billion. PV bus bars, RFID tag antennas, etc. Excludes ESD/RF Shielding

🟩 Sensors: $100 million. Glucose test strips, EKG sensors

🟨 E-paper displays $290 million. E-readers

🟦 Inorganic AC Electroluminescent displays $110 million. Signage, Promotional items, Consumer electronics

🟧 Others $35 million. Printed Batteries, Logic, Memory, Electrochromic displays...

Mostly Printed

Figure 2. Printed and potentially printed electronics market size by component type in 2012 (*IDTechEx*, 2012).

The promising potential of printed electronics in biological applicationsis demonstrated in this thesis by incorporating printed devices and structures in integrated biological microfluidic systems, also known as lab-on-a-chip (LOC) systems. LOC systems reduce biological and chemical laboratories to a microscale system, hand-held size or smaller. They are typically in the form of a hand held 4-inch chip composed of multiples layers of glass and/or PDMS (polydimethylsiloxane). LOC devices have the advantage of low fluid volume consumption, faster processes and higher throughput.

Low volume requirements are beneficial since biological analysts are limited by the amount of sample they can obtain from a patient to perform all the necessary analyses. An example of this limitation is obtaining a sample from a crime scene for forensics analysis, where the amount of sample available is usually very small. Obtaining a blood sample from a newborn is another example where analysts have a limitation on the amount of blood that they can draw. Many such situations justify the need for low volume requirements. Moreover, narrow channels in the microfluidic chip allow for faster process through capillary electrophoresis (CE) [6]. Multiple lanes (microfluidic channels or etched trenches in the subtrate) on the chip allow for simulatenous processes to occur, allowing for higher throughput. LOC devices are also more automated and robust, and reduce manual sample handling to minimize the risk of sample mix-up and contamination.

A top view and a cross-section view of a typical microfluidic lab on a chip system are shown in Figure 3. This 4-inch (in diameter) LOC system requires at least 2 substrate layers to form microfluidic channels (paths through which biological fluids are transported to different areas of the chip) and usually multiple layers to accommodate all the components necessary for the functioning of the LOC system (shown in Figure 3b). This will be explained in more detail in Chapters 3 and 4.

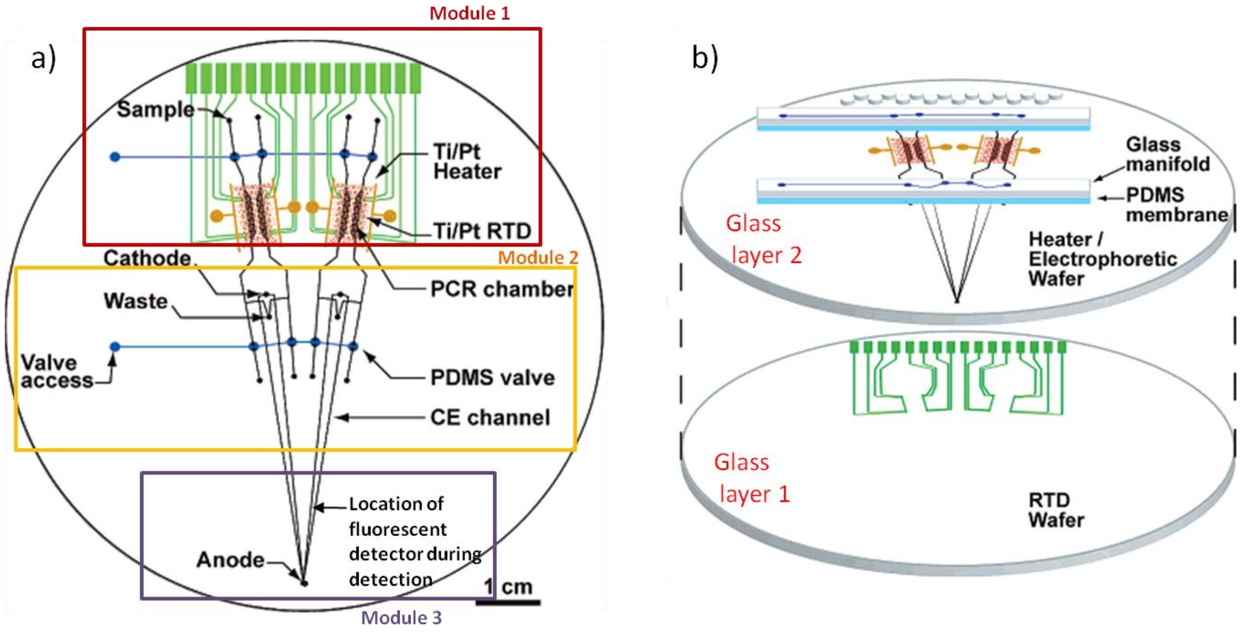

Top View: microfluidic chip that is 4-inch in diameter and separated into 3 different modules

Cross-section: multiple layers required to form channels and accommodate all necessary components

Figure 3. a) Top View and b) Cross-section of a typical biological microfluidic system [7, 8].

The main modules of an example LOC device, as labeled in Figure 3a, include: 1) biological reactions, 2) electrophoretic separation and capture, and 3) detection. Biological reactions almost always include the polymerase chain reaction (PCR) process (described in detail in Chapters 3 and 4). Medical research and clinical medicine are benefiting from PCR mainly in two areas: detection of infectious disease organisms, and detection of variations and mutations in genes, especially human genes. Because PCR can amplify unimaginably tiny amounts of DNA (deoxyribonucleic acid), even that from just one cell or a gene with just one base pair mismatch (mutation), physicians and researchers can examine a single sperm, or track down the source of a mysterious infection. In other words, PCR allows for precise and accurate detection of diseases by amplifying the amount of starting DNA to increase the sensitivity and accuracy of the analysis. It is thus able to aid in early detection of an infection or a disease such as cancer by highlighting the seemingly insignificant changes in genetic material that occur in the early stages of disease development. Its selective capability works on extremely complicated mixtures, seeking out, identifying, and duplicating a particular bit of genetic material from blood, hair, or tissue specimens, to assist in disease analysis.

To summarize, PCR is a powerful process that amplifies the amount of starting DNA to enable precise and accurate analyses of diseases. It involves a thermal cycling process that is able to produce 68 billion copies of a single DNA in 35 thermal cycles. *The thermal cycling process requires heaters and resistive temperature detectors (RTDs).* The PCR chamber, the heaters, and RTDs are all labeled in module 1 of Figure 3a. Heaters perform the thermal cycling while the RTDs are in close contact with the PCR reactor to monitor the temperature of the reactor at any given time. RTDs are required since biological samples are very sensitive to changes in temperature. A cross-section of a typical heater and RTD structure is shown in Figure 4. *The heaters and RTDs are currently lithographically defined, requiring multiple processing steps that affect the entire chip during the definition of each of these devices.*

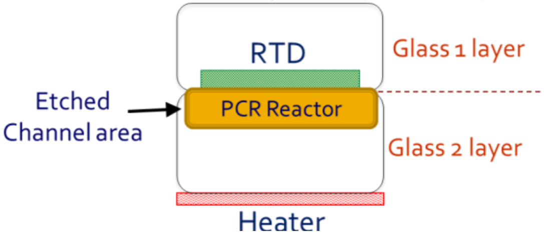

Figure 4. Cross-section of a typical RTD and heater structure used for PCR thermal cycling in LOC devices.

The second module of an LOC device (Figure 3a) is the electrophoretic separation and capture module. The process flow for this module is illustrated in Figure 5. The amplified product from the PCR needs to be purified, and the species of interest from this product needs to be captured. Therefore, a capture gel is formed inside the channel and contains a protein or a DNA sequence that has an affinity to the species of interest. Once the species of interest is captured (STEP A), it is electrophoretically driven through the fluorescent detector to obtain the results (STEP B). *For this step, microfluidic valves (indicated as PDMS valve in Figure 3a) are required to control the flow of fluid in the different parts of the channel.*

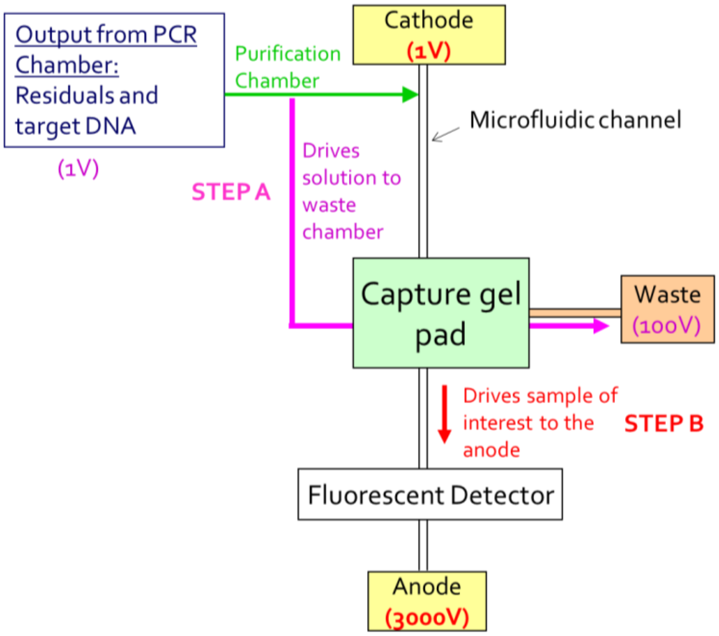

Figure 5. Process flow of the electrophoretic separation and capture step.

The final module of an LOC device is detection. The location of the fluorescent detector relative to the microfluidic chip is indicated in Figure 3a. The existing state of the art DNA microarray technology uses detection of fluorescent-tagged DNA for applications such as genome sequencing and genetic mutation detection, to name a few. This microarray process is summarized in Figure 6. A DNA microarray represents an orderly arrangement of samples where matching of known and unknown DNA samples is done based on DNA base pairing rules. Microarray technology is capable of simultaneously and therefore efficiently analyzing hundreds to thousands of genes (a specific set of DNA sequence) in a single square inch glass substrate [9]. For example, microarrays can be used to compare genes in two different cell types or tissue samples, such as in healthy and diseased tissue. A standard process in discriminating DNA between healthy and diseased samples using microarray technology is discussed next. A DNA sequence, referred to as the probe, is first immobilized on a given substrate. The probe is usually a complement (or has an affinity towards) a healthy DNA sequence. A patient’s DNA is then extracted and denatured, where the double stranded DNA (dsDNA) sequence is melted to split into two single stranded DNA (ssDNA) sequences. One of these ssDNA sequences (complement to the probe) is labeled with a fluorescent molecule, and is referred to as the target sequence. The target sequence is then hybridized (allowed to bind) with the probe sequence. Successful hybridization is indicated by a fluorescent signal in a given sample and verified using a fluorescent detector. If the hybridization occurred, in simple terms, the patient is free of diseases since their DNA (target) has hybridized to the healthy DNA (probe). If a fluorescent signal cannot be found, then the hybridization did not occur, and the patient’s DNA (probe) is considered abnormal (indicating a possible genetic disease). This microarray technology involves a meticulous and long process that requires fluorescently labeled DNA and fluorescent detectors. In addition, since the microarray technology uses conventional hybridization techniques [10], it requires about 12-18 hours for the probe and target sequences to completely hybridize.

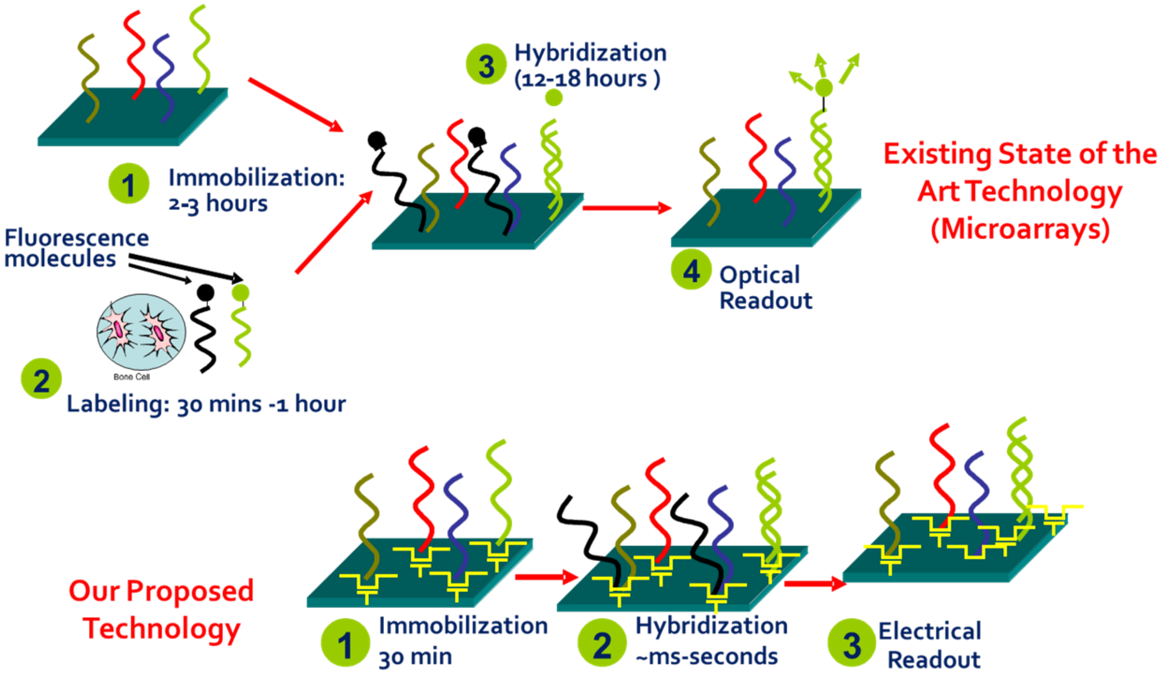

Figure 6. Protocol comparison between fluorescent technology and DNA sensor technology [11].

Our proposed sensor technology (also illustrated in Figure 6) uses pentacene organic thin film transistors (OTFTs). This system has several potential advantages compared to the current optical detection technology, the first being *higher sensitivity*. As many previous researchers have already shown, electrical detection is more sensitive than optical detection since the latter is limited by the resolution of the fluorescent detection technology. The second advantage is that it is a *label-free method*, as it does not require the use of fluorescent molecules or a laser detector. Also, the pentacene TFT sensor is *disposable*, *portable*, and *ultra-low cost* since OTFTs can be printed on relatively inexpensive plastic substrates. Finally, the electrical detection system has the potential of being an *overall faster* process. Pulse-enhanced hybridization, a method of accelerating hybridization of DNA on chip, has been demonstrated previously [11] and plays an important role in realizing a faster system. The OTFT detection method will be discussed in more detail in Chapter 2.

Each of the three modules discussed thus far requires components and devices that can potentially and very efficiently be printed. A more detailed top view and cross section of an LOC system, highlighting the components required in the discussed modules, is shown in Figure 7.

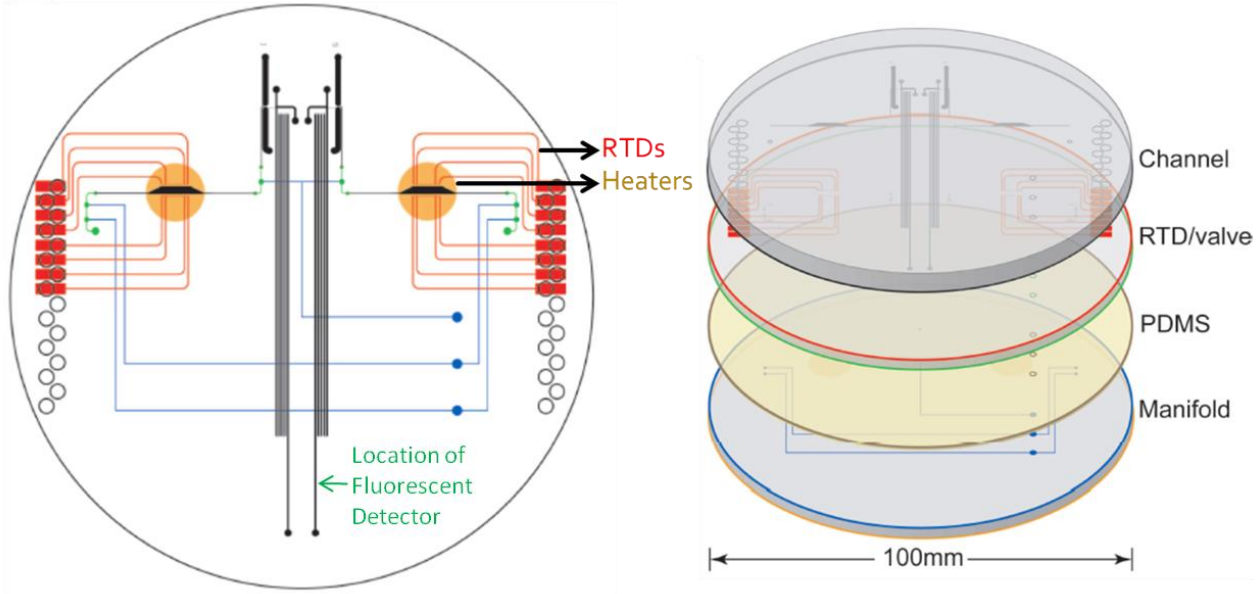

Figure 7. Top view (left) and cross-section (right) of a typical lab on a chip device showing the different thin film components and layers needed to form the chip [12].

To begin with, in the first module, PCR requires thin film components such as heaters and resistive temperatures in different layers of the chip. These components can be efficiently printed saving time and cost in fabrication as compared to the conventional process (discussed in Table 1) currently used to define the structures. Moreover, valves are useful in controlling the flow of fluids during electrophoretic separation and capture of the biologic species of interest. The fabrication of some of the current valve structures requires multiple substrate layers to form the valves. This is shown in the cross-section (right) of Figure 7. Although the channel and RTD/valve wafers are the only substrates really required to form the microfluidic chip, the PDMS and manifold layers are additionally needed just to form valves. Again, the number of layers and fabrication steps required to make valves can be dramatically reduced using printed electronics. Finally, the fluorescent detection system described earlier can be replaced by a simpler and faster process using printable DNA sensors.

Printed electronics is therefore an attractive paradigm for realization of biological microfluidic systems. The large area of typical biological microfluidic systems makes printing attractive from a cost perspective. Additive processing in printed electronics also saves time and cost in fabrication. Furthermore, since printing allows for easy integration of disparate materials on the same substrate through spatially-specific deposition, printed electronics is particularly attractive for integration of diverse biological microfluidic functionality (as required by LOC devices) on the same substrate.

To demonstrate the use of printed electronics in biological microfluidic systems, the first part of this dissertation (Chapter 2) presents work on DNA sensors using printable pentacene (organic) thin film transistors (OTFT) [11], [13]. Pentacene TFTs, our proposed sensor technology, are useful for biosensors because of the advantages they provide over current state of the art fluorescent detection/DNA microarray technology.

Chapters 3 and 4 will present inkjet printed heaters and RTDs, integration of these devices in a biological LOC system, and the demonstration of PCR using these printed devices. Finally, Chapter 5 delves into the printing and characterization of all-printed electrostatically actuated PDMS valves designed for biological applications. Chapter 6 concludes the dissertation and addresses the future directions of this project.

To summarize, the goal of this dissertation is to demonstrate the capability of printed electronics to make important aspects of biological microfluidic systems more efficient and effective. Having thus introduced and motivated the dissertation in this chapter, we begin to address the different modules of the biological microfluidic system beginning with printable DNA sensors in the following chapter (chapter 2).

Sources

[1] "Photolithography," *Georgia Tech Research Labs,* [Online]. Available: http://www.ece.gatech.edu/research/labs /vc/theory/photolith.html. [Accessed: 18-Apr-2012].

[2] V. Subramanian, J. B. Chang, A. de la FuenteVornbrock, D. C. Huang, L. Jagannathan, F. Liao, B. Mattis, S. Molesa, D. R. Redinger, D. Soltman, S. K. Volkman, and Q. Zhang, "Printed electronics for low-cost electronic systems: Technology status and application development," in *Solid-State Circuits Conference, 2008. ESSCIRC 2008. 34th European,* 2008, pp. 17 –24.

[3] "Flexographic Printing | Gravure Printing." [Online]. Available: http://www.prismpak.com/Printing-Options-s/103.htm. [Accessed: 18-Apr-2012].

[4] "DP3: Digital Print Preservation Portal | Inkjet." [Online]. Available: http://www.dp3project.org/technologies/digital-printing/inkjet. [Accessed: 18-Apr-2012].

[5] C. C. Ho, J. W. Evans, and P. K. Wright, "Direct write dispenser printing of a zinc microbattery with an ionic liquid gel electrolyte," *Journal of Micromechanics and Microengineering*, vol. 20, no. 10, p. 104009, Oct. 2010.

[6] J. A. Luckey and L. M. Smith, “Optimization of electric field strength for DNA sequencing in capillary gel electrophoresis,” *Anal. Chem.*, vol. 65, no. 20, pp. 2841–2850, 1993.

[7] N. M. Toriello, E. S. Douglas, N. Thaitrong, S. C. Hsiao, M. B. Francis, C. R. Bertozzi, and R. A. Mathies, “Integrated microfluidic bioprocessor for single-cell gene expression analysis,” *Proceedings of the National Academy of Sciences*, vol. 105, no. 51, pp. 20173 – 20178, Dec. 2008.

[8] P. Liu, S. A. Greenspoon, S. H. Yeung, J. R. Scherer, and R. A. Mathies, “Integrated sample cleanup and microchip capillary array electrophoresis for high-performance forensic STR profiling,” *Methods Mol. Biol.*, vol. 830, pp. 351–365, 2012.

[9] “DNA Microarray Technology.” *National Human Genome Research Institute.* [Online]. Available: http://www.genome.gov/10000533. [Accessed: 26-Apr-2012].

[10] H. Koltai and C. Weingarten-Baror, “Specificity of DNA Microarray Hybridization: Characterization, Effectors and Approaches for Data Correction,” *Nucl. Acids Res.*, vol. 36, no. 7, pp. 2395–2405, Apr. 2008.

[11] Q. Zhang, “OTFT-Based DNA Detection System,” *Ph.D. dissertation*, University of California-Berkeley, 2007.

[12] R. G. Blazej, P. Kumaresan, and R. A. Mathies, “Microfabricated bioprocessor for Integrated nanoliter-scale Sanger DNA sequencing,” *Proceedings of the National Academy of Sciences*, vol. 103, no. 19, pp. 7240 –7245, May 2006.

[13] S. E. Molesa, “Ultra-Low-Cost Printed Electronics,” Ph.D. dissertation, University of California-Berkeley, 2006.

2. DNA Detection Using Organic Thin Film Transistors

2.1. Introduction and Motivation

The vision of achieving a personalized system of disease detection and treatment is the motivation for this chapter. Electrical means of sensing and detection have the ability to enable this vision. Previous work by Dr. Qintao Zhang has shown the potential of organic (pentacene) thin film transistors (OTFT) for DNA detection by showing different electrical performance shifts in response to single and double stranded DNA [1]. Single stranded DNA (ssDNA) contains exposed base pairs or nucleotides (adenine, guanine, thiamine, and cytosine) on its structure and therefore immobilizes on pentacene surface through physical adsorptive immobilization (explained later in this chapter). In double stranded DNA (dsDNA), the base pairs are enclosed within the structure, preventing the immobilization of this DNA on pentacene. Therefore, in Zhang et al.'s work [14], ssDNA causes a shift in the electrical characteristics of the pentacene transistor while dsDNA does not affect the transistor. The net-effect of ssDNA immobilization on pentacene is an electron withdrawing behavior. Pentacene TFTs are p-type accumulation devices. Therefore, after DNA immobilizes on the pentacene transistor channel surface, the hole current of the TFT increases. Consequently, the threshold voltage (V_t) becomes more positive (i.e. shifts to the right). By monitoring shifts in electrical characteristics, different DNA structures can be analyzed, eventually leading to the possibility of detecting genetic mutations (base pair mismatch) and diseases.

To achieve the ultimate goal of detecting genetic diseases using OTFTs, the sensor needs to be able to detect at the level of single nucleotide polymorphisms (SNP) [2]. In order to enable this level of detection, this chapter delves into two aspects of using OTFTs for genetic disease detection, namely the investigation of physical origins of the observed electrical shifts, and the characterization of the pentacene surface to allow optimization of the same for DNA immobilization and sensor sensitivity.

DNA detection is important to detect mutations that cause genetic disorders. A genetic disorder is a disease that is caused by an abnormality in an individual's DNA. Abnormalities can range from a small mutation in a single gene (made up of DNA sequences) to the addition or subtraction of an entire chromosome or set of chromosomes. In addition, DNA detection is also required in many other applications such as DNA sequencing (for forensics).

The current DNA detection system, the DNA microarray technology [3, 4], involves a tedious process as described in chapter 1. Since DNA is currently detected using optical means, this process requires fluorescent-tagged DNA and laser detectors. The accuracy is limited by the resolution of optical detection systems. In addition, this process is also time-consuming because of limitations posed by conventional immobilization and hybridization techniques [5]. Using OTFTs for DNA detection provides a solution to these barriers. Specifically, OTFTs detect DNA electrically, eliminating the need for auxiliary optical tools and increasing the accuracy of the detection system. Using pulse enhanced hybridization techniques [1], OTFTs provide for a faster detection system. Many other advantages of the proposed sensor system are discussed later in the chapter. Using OTFTs for DNA detection thus paves the path for an ideal DNA detection system

An ideal detection system, as depicted in Figure 8, would consist of an ultra low-cost, disposable DNA detection chip, which can be analyzed with a handheld device (e.g. PDA), using a quick and easy testing protocol. Moreover, the results/feedback from the chip would be available within a few hours.

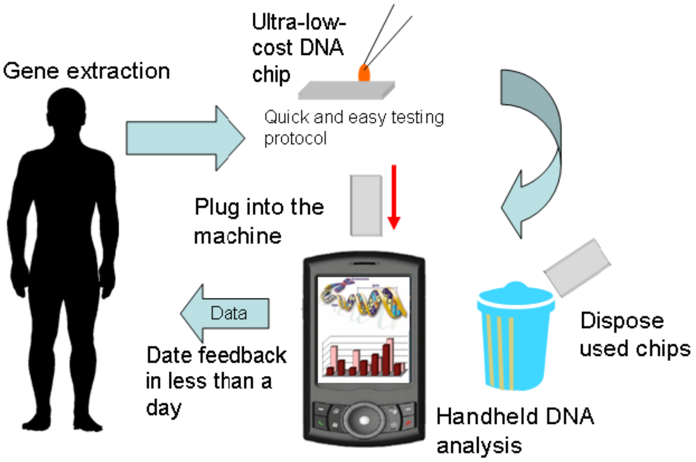

Figure 8. An Ideal DNA Detection System.
(Image: Courtesy of Dr.Qintao Zhang, Graduate from EECS Organics Electronics Group, UC Berkeley)

Use of organic transistors facilitates the possibility of an ultra low-cost, disposable DNA chip through printed electronics. Fully printed organic transistors have been demonstrated, including appropriately formulated organic and nanomaterial inks [6]. All of these materials have plastic substrate compatible activation temperatures (<200°C).

Printed electronics using organic semiconductors have many advantages over typical silicon processes [6]. The processing steps for printed electronics have a low thermal budget, allowing for a variety of low-cost and flexible substrates. Printed electronics also allows for additive processing, which facilitates selective deposition of materials, reducing the overall consumption of the same. Figure 9 depicts a typical process flow for printed OTFTs. In this process, the source, drain, and gate electrodes are printed using gold nanoparticle based inks. Nanoparticle inks require low temperature anneals to form conductive films, enabling the use of flexible substrates. The dielectric and semiconductor layers are usually printed using organic (solution processable) or nanoparticle based inks.

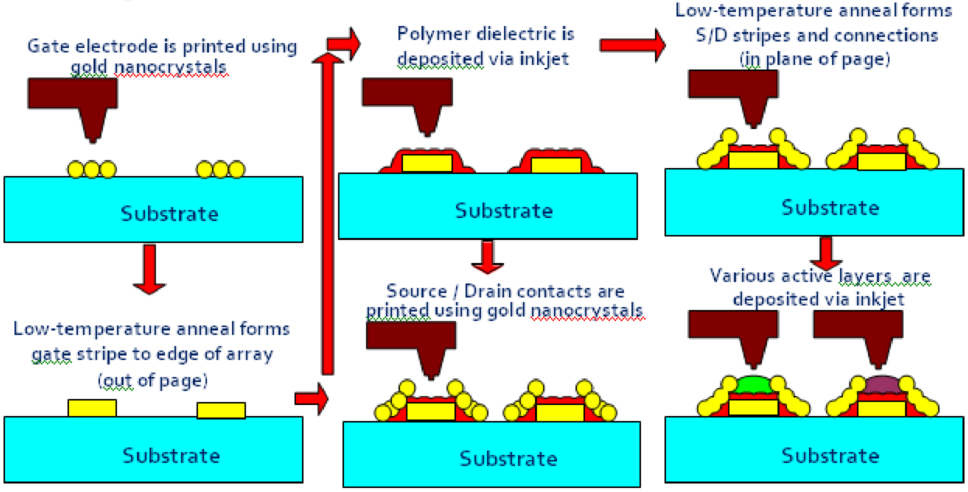

Figure 9. Process flow for formation of printed FETs.
(Image: Courtesy of Dr. Vivek Subramanian, UC Berkeley)

Among organic semiconductors, pentacane is known to have the highest performance in thin film phase. This renders it an optimal choice for use in an OTFT sensor. A thin film structure is needed to maximize sensitivity of biological analytes to the pentacene surface. In other words, the thin film structure facilitates the immobilization of analytes in the channel part of the active layer, increasing overall sensitivity of the sensor. This is highlighted in the results section of this chapter.

In addition, the morphology of the pentacene surface is critical to the immobilization of the DNA and the sensitivity of the sensor, as explained later. By evaporating pentacene instead of printing it, the surface structure can be controlled very precisely. For the purposes of the work covered in this chapter, the control of this surface was very important for optimization. Therefore, evaporated pentacene transistors were used. Translating from evaporated to printed transistors has previously been mastered [6] and can be implemented in the future.

2.2. Pentacene Organic Thin Film Transistors for Biosensing

The pentacene TFT bottom gated structure used for the DNA sensor in this work is shown in Figure 10 below. The bottom gated structure allows for the channel layer to be exposed. This, in turn, allows for easy and non-destructive inclusion of analytes, biological molecules/proteins, etc., as the final step. Having an open active layer is also important to be able to perform measurements that determine the sensitivity of the OTFT sensor. The thickness of the pentacene layer can be varied as necessary, but for the purposes of this project, it ranges from 10-30nm, a range known to have the desired thin film like characteristics [6, 7] . The steps required for the fabrication of the OTFT and the immobilization of DNA will be detailed in section 2.5.

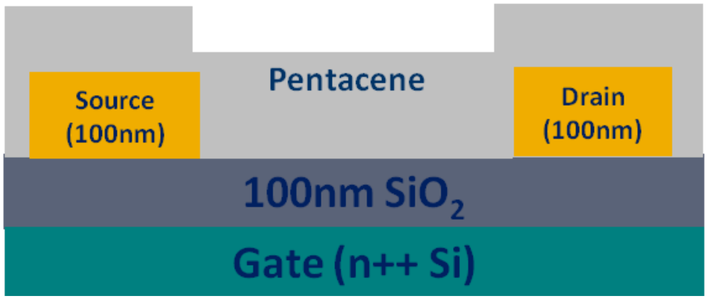

Figure 10. Pentacene TFT Structure.

Pentacene TFTs are useful for biosensors because of the advantages they provide over current state of the art fluorescent detection technology. The current DNA microarray technology involves a meticulous process as described in chapter 1. Specifically, since DNA (mutation and sequencing) detection is performed using optical means, this process requires fluorescent-tagged DNA and laser detectors. In addition, since the microarray technology uses conventional hybridization techniques [5], it requires about 12-18 hours for the DNA sequences to completely hybridize, making the process time consuming.

With the pentacene TFT sensor, the DNA detection can be performed electrically. Instead of using fluorescent laser technology to correlate the extracted fluorescent signals with genetic mutations for example, the sensor will detect the mutations by analyzing conductance and threshold voltage shifts. The OTFT sensor technology has several advantages compared to the current optical detection technology:

1) *Higher Sensitivity:* As many previous researchers have already shown, electrical detection is known to be more sensitive than optical detection [9], especially since optical methods are limited by the resolution of the fluorescent detector. If electrical detection is more

sensitive, needless to say, the diseases can be detected earlier (important for early cancer detection, for example) and much more accurately. Also, the limiting factor in many disease detection systems is the amount of reagent (ex: blood sample) available. By having a more sensitive system, the amount of reagent required for the desired analysis can be reduced.

2) *Label free method:* The DNA used with the proposed OTFT sensor technology does not need to be tagged with fluorescent molecules. This also eliminates the need for a fluorescent laser detection system, thus rendering the process much simpler.

3) *Disposable/Portable/Ultra-low cost:* The elimination of a fluorescent laser detection system makes the OTFT sensor inexpensive and easily accessible. Also, OTFTs can be printed on plastic substrates, further reducing the overall cost of the system. For easy integration into the biological microfluidic chip, a disposable and portable sensor is necessary. The current DNA microarray process requires fluorescent-labeling of DNA before immobilization and the use of an auxiliary fluorescent detector to subsequently perform the detection, inhibiting accessibility and portability. Therefore, it is difficult to make a portable DNA sensor unless it is done with an electrical, label-free method.

4) *Faster Process:* The method of hybridization, which takes 12-24 hours, poses a bottleneck for the current DNA microarray technology process. Amongst other steps that could potentially save time in the proposed OTFT sensor technology, the possibility of pulse-enhanced hybridization [1]can reduce the hybridization time to milliseconds, making the proposed electrical detection process much faster.

Having thus motivated and introduced this chapter, the next few sections will discuss the OTFT DNA sensor system further.

2.3. OTFT DNA Sensor Operation

Previously, it has been shown that pentacene can be used to detect DNA [1]. Detailed discussion on DNA immobilization, DNA Doping, and DNA Interaction with pentacene films are discussed in a previous report [10].

Pentacene TFTs are p-type accumulation devices (negative gate voltage and negative current). After DNA immobilization on the channel surface, the hole current of the TFT increases. Consequently, the threshold voltage (V_t) becomes more positive (i.e. shifts to the right). The results from one of the experiments, shown in Figure 11, illustrate the sensor characteristics observed after DNA interaction with pentacene. The DNA used in all of the experiments in this chapter, is a 125-base pair custom designed single strand DNA sequence, synthesized by Biosynthesis, Inc.

I_{on} Ratio is defined as:

$$\mathbf{I_{on}\ Ratio} = \frac{I_{dsat} AfterDNA\_immobilization}{I_{dsat} BeforeDNA\_immobilization}$$

where I_{dsat}, also referred to as the on current, is the drain current of the transistor in saturation mode. In addition, I_{on} ratio is also referred to as I_{dsat} ratio in this chapter. The bigger the I_{on} ratio, the higher the sensitivity of the sensor.

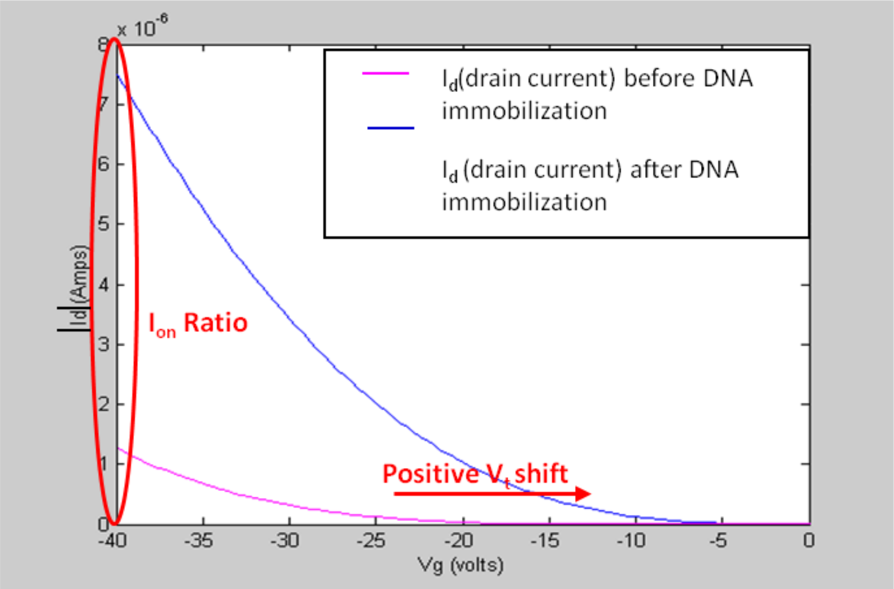

Figure 11. Current-voltage characteristics from an experiment show a positive V_t shift and a higher hole current after DNA immobilization.

The interaction between DNA and pentacene contributed to the results seen in Figure 11 and can be explained using two different mechanisms. One is the direct doping of DNA on pentacene. The net-effect of DNA on pentacene surface is electron withdrawing, therefore increasing the hole current of the transistor. Although DNA is known to be negatively charged because of the phosphate groups on its backbone, the possible interaction of the aromatic structures in DNA base pairs (such as adenine) and the inherent aromaticity of the 5 benzene ring pentacene structure results in a net electron withdrawing behavior. The result of this electron withdrawing interaction is explained further, and supported using Kelvin Probe Microscopy technique in previous reports [10,1, 11].

Another explanation for this interaction is that DNA fills traps on the pentacene surface improving the overall performance of the transistor, resulting in the shift seen in Figure 11. Using SCLC (Space Charge Limited Current) measurement technique, Zhang et al. are able to support this hypothesis [11]. Further details on the trap filling mechanisms of DNA can be found in Dr. Zhang's thesis, *OTFT Based DNA Detection System* [1].

2.4. Investigation of Physical Origins of Electrical Transduction Behavior

An important step in making a viable DNA sensor is to show that what is being detected is the DNA, and to eliminate any other noise that might affect the sensitivity. One way to do this is to directly correlate the amount of DNA on the surface with the electrical shift that is seen after DNA immobilization. A few methods were used to obtain this data, namely atomic force microscopy (AFM), fluorescent microscopy (FM), and time-of-flight secondary ion mass spectroscopy (TOF-SIMS). AFM has been used by Dr. Zhang to study this behavior previously [1]. Fluorescent microscopy has also been used for detection of this behavior with initial promising results shared in a previous report [10]. FM measurements have shown great potential for use in directly correlating the amount of DNA immobilized on the surface with the shift observed in the transistor performance characteristics.

TOF-SIMS is a surface analytical technique that focuses a pulsed beam of primary ions onto a sample surface, producing secondary ions in a sputtering process. Analyzing these secondary ions provides information about the molecular and elemental species present on the surface. TOF-SIMS is known to be one of the most sensitive surface analytical techniques, with a detection limit of 10^7-10^{10}atoms/cm^{2}sub-monolayer and a depth resolution of 2-3nm. It provides specific molecular information on thin (sub-monolayer) organic films/contaminants with an excellent detection limit (ppm) for most elements. It is a non-destructive process tailored to work with soft substrates such as pentacene [12]. Since TOF-SIMS technique is extremely sensitive and reliable, it was used to analyze the immobilization of DNA on pentacene surface. The following section presents results from TOF-SIMS analysis of pentacene samples with and without DNA.

2.4.1 Time-of-Flight Secondary Ion Mass Spectroscopy (TOF-SIMS)

The definition and technical capabilities of TOF-SIMS as well as experimental protocols used for the following TOF-SIMS analysis is discussed in detail in a previous report [10]. Experimental results are discussed below.

2.4.1.1 Summary of Experimental Results

The TOF-SIMS analysis was performed in the Evans Analytical Group labs in Sunnyvale, CA. The TOF-SIMS analysis was performed to get a visual proof of DNA on surface and assess the possibility of correlating these results with the electrical measurements.

More specifically, the purpose of this analysis was to determine the relative levels of DNA on three samples: *Sample #1- Control:* Pentacene substrate with no buffer or DNA but which has gone through the same experimental protocol (fabrication and storage) as samples 2 and 3; *Sample #2- Buffer:* Pentacene substrate with just pure buffer and no DNA. The buffer is saline-sodium citrate solution; Sample *#3-DNA in buffer:* DNA was pipetted on the channel of the transistor. Note that all 3 samples were taken from the same substrate and went through the same cleaning, evaporation, and storage procedures.

In each case the analytical area was 80µm × 80µm. This allowed data to be acquired only from the channel, eliminating signal from the surrounding gold lines of the transistor structure. The relative levels of DNA were assessed by monitoring the levels of sodium (Na) for buffer and phosphate (PO_x) ions for DNA. Phosphate ions are a signature of DNA since they are the main compounds in the backbone of the DNA structure.

Summary of Results:

The highest levels of PO_x and Na were observed on sample #3. These species were observed at significantly lower levels on sample #2. No PO_x was observed on sample #1 which had the lowest levels of Na.

Other species observed from all samples included the pentacene substrate ($C_{22}H_{14}$), and the incorrectly labeled Polydimethylsiloxane(PDMS), which is a signal observed because of the hexamethyldisilazane (HMDS) layer in the dielectric/pentacene interface.

Discussion of Results:

The results are obtained as mass spectra, which are displayed as the number of secondary ions detected (Y-axis) versus the mass-to-charge (m/z) ratio of the ions (X-axis). Mass Spectra results can be found in the appendix shared in a previous report [10].

The results are also presented as tables of normalized intensities. These tables can be used to compare the relative levels of a given species between samples; however, they cannot be used to extract the exact amount of DNA in a given sample. This is because different species have different secondary ion yields in TOF-SIMS analysis, sometimes skewing the data depending on the substrate or the amount of one material over the other in a given sample. Because of this limitation, a combination of fluorescent microscopy and TOF-SIMS analysis can be used in the future to provide a reliable way of quantitatively correlating the amount of DNA immobilized on the surface to electrical shifts observed.

Table 2 and Table 3 show the mean of three measurements performed for each of the samples and the corresponding standard deviations.

		1, control		**2, buffer**		**3, (DNA + buffer)**	
m/z	formula	*mean*	*σ*	*mean*	*σ*	*Mean*	*σ*
Elements							
23	Na	16.1	6.0	569	146	4790	580
28	Si	3670	180	3610	160	587	38
Pentacene							
278	$C_{22}H_{14}$	105	11	40.4	7.7	55.0	6.2
PDMS							
73	C_3H_9Si	408	31	317	42	95.9	12.0
147	$C_5H_{15}Si_2O$	16.5	5.6	73.1	13.0	15.6	1.7

Table 2. Normalized positive ions of interest
(normalized relative to total ion counts ×10000)

		1, control		**2, buffer**		**3, DNA + buffer)**	
m/z	formula	*mean*	*σ*	*mean*	*σ*	*mean*	*σ*
47	PO	Nd	-	0.337	0.018	0.551	0.150
63	PO_2	Nd	-	0.295	0.022	2.91	0.81
79	PO_3	Nd	-	nd	-	2.45	0.73

"nd" indicates species not detected on that sample

Table 3. Normalized negative ions of interest
(normalized relative to total ion counts ×10000)

Table 2 presents the normalized intensities of the positive ions of interest. Elemental species observed from all three samples included Na and Si. The levels of Na varied significantly among the samples with the highest levels observed from sample #3 and the lowest levels on Sample #1. The highest levels are expected from sample #3 because the DNA was in buffer solution during immobilization, and the Na ions in the buffer solution attach themselves to the

DNA to maintain stability. Sample #1 has Na ions because of contaminants from the environment. Comparable levels of Si were observed on samples #1 and #2 while lower levels were found on #3. The lower levels in sample #3 indicate that the Si levels are ‘shadowed’ by the strong signal exhibited by the Na in this sample. This can also be observed in the mass spectra included in the appendix shared in a previous report [10].

Table 3 presents the normalized intensities of the negative ions of interest. The focus was on the PO_x ions to determine the presence of DNA on the surface and the relative amounts of DNA on the different samples. Phosphate ions (PO_x) were observed in negative polarity only on samples #2, and #3. The levels of PO_x on sample #3 were significantly higher than those observed from sample #2. The PO_3^- ion in particular was observed only on sample #3.

TOF-SIMS analysis has shown the presence of phosphate groups, particular PO_2 and PO_3 (from DNA) and sodium (from buffer solution) in highest concentrations in sample #3, the sample with DNA immobilized in the channel. The control sample (sample #1) shows small traces of sodium and the buffer sample (sample #2) shows small traces of PO possibly due to environment contribution and/or contamination. **Since Sample #3 has shown significantly higher amounts of the PO_x species, the immobilization of DNA in this sample has been confirmed.**

To correlate the TOF-SIMS results to electrical measurements, Figure 12 shows the measured I_{dsat} ratios of the control sample (sample1), sample with buffer (sample2) and sample with DNA (sample3). The results show that only the sample with the immobilized DNA (sample3) has an I_{dsat} ratio greater than 1. This is also the sample with the highest amount of **PO_x** species or DNA as shown by the TOF-SIMS analysis. This correlation verifies the selective sensitivity of the sensor to DNA and the physical origin of the electrical transduction behavior seen in the OTFT sensor.

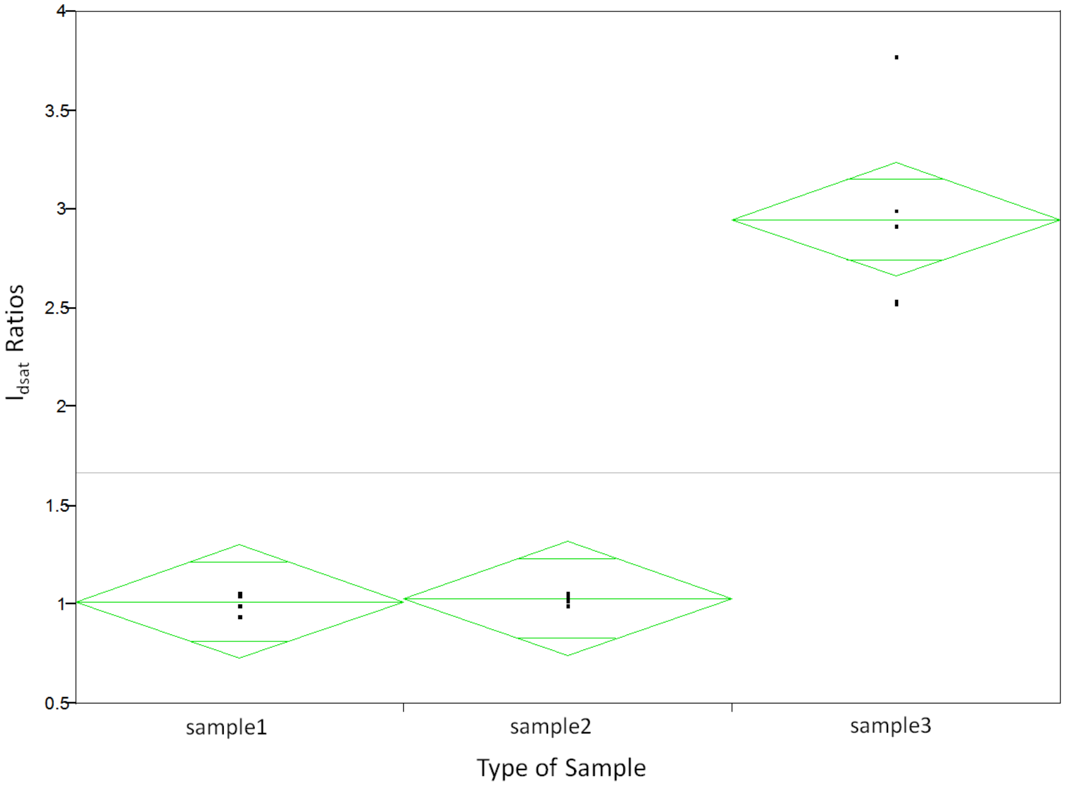

Figure 12. The results above correlate the TOF-SIMS results with the electrical measurements (I_{dsat} ratios).

To summarize, this section has presented TOF-SIMS analysis of control, buffer, and DNA samples of the OTFT sensor. As expected, the sample with the DNA resulted in the highest amount of PO_x species, confirming the immobilization of DNA in this sample. Moreover, by correlating the TOF-SIMS results to I_{dsat} ratios, the selective sensitivity of the OFTF sensor to DNA has been highlighted, emphasizing the effectiveness of the proposed sensor.

To further enhance the sensitivity of the OTFT sensor, the next section presents ways of optimizing the pentacene surface for effective DNA immobilization and sensor sensitivity.

2.5. Optimization of DNA Immobilization and Sensor Sensitivity

In addition to having high selectivity in detecting the species of interest (shared in the previous section), a DNA sensor also needs to be highly sensitive. The sensitivity is quantified by the I_{dsat} ratio factor defined in section 2.3. The following section presents information on maximizing this sensitivity factor by optimizing the pentacene surface on which the DNA is immobilized.

Physical absorptive immobilization, the mechanism through which DNA immobilizes on pentacene[10,1], highlights the importance of the topology of the pentacene film surface for immobilization of DNA and the sensitivity of the sensor. DNA is known to segregate to topological features on pentacene surface. We are able to exploit the control of pentacene evaporation conditions to tune pentacene film morphology to maximize sensitivity. In this section, DNA detection using optimized films is demonstrated.

The optimization experiment is split into two parts. Section 2.5.1 presents a set of experiments that characterize pentacene and vary its morphology by changing input parameters. Section 2.5.2 presents the integration of DNA into the experiments, thereby arriving at the best surface and evaporation conditions for highest sensor sensitivity.

2.5.1. Pentacene Characterization Experiment

In this section, the pentacene surface is systematically characterized to tailor the surface for effective DNA immobilization. Physical absorptive immobilization, a method through which DNA immobilizes on pentacene surface, occurs through the interaction of the hydrophobic pentacene surface with the DNA in buffer (‘salt water’) solution. DNA is diluted in saline-sodium citrate (SSC) buffer solution. The 20x solution of buffer consists of 3M sodium chloride and 300 mM trisodium citrate. The buffer solution is further diluted in water, as it is usually done in practice, to give a 2x concentration solution.

The hydrophobic interaction immobilization (interactions between DNA molecules and crevices on hydrophobic substrate surface) is a very common method in the early stage of DNA microarray development and has been studied very well [13]. Using this method, we can explain the pentacene film interaction with DNA. When the DNA in buffer solution is pipetted onto the pentacene surface, the DNA segregates to hydrophobic ‘holes’ on the surface. During this process, the salt water, in which DNA is diluted, gets pushed out, ‘physically’ immobilizing the DNA in the crevices of the pentacene surface.

Roughness and grain boundaries of pentacene form the crevices necessary for DNA immobilization on this surface. Being able to understand how input variables (during evaporation) affect these morphological output parameters is therefore important. To study the morphology of pentacene, output parameters such as mean roughness, grain size, and coverage area were analyzed. Evaporation rate was also studied as an output since rate of growth of pentacene affects its grain size [14], an important parameter in determining morphology. Finally, since saturation current plays an important role in quantifying the sensitivity of the sensor, it was also extracted as an output parameter. The purpose of measuring each of these outputs is discussed further in the results section of this chapter.

The variables that can be controlled during pentacene evaporation compose the set of input parameters used for the pentacene characterization experiment. These input parameters include thickness of pentacene (controlled by the duration of the evaporation), substrate temperature (during evaporation), and input current. The input current changes the temperature of the crucible holding the pentacene that is to be evaporated, thereby affecting the rate of evaporation. The interaction among these input parameters causes changes in pentacene morphological and electrical characteristics and is therefore analyzed in this section. The input and output parameters are summarized in Table 4.

Input Variables	**Output Characteristics**
Thickness of Pentacene film Input Current Substrate Temperature	I_{dsat} (Saturation Current) Mean Roughness Grain Size Evaporation Rate Coverage Area

Table 4. Input and Outputs for Pentacene Characterization Experiment.

2.5.1.1. Fabrication of OTFT Sensor

The first step in characterizing the pentacene is to fabricate the OTFT. The OTFT structure used here is a bottom gated TFT structure. This structure has advantages over the top gated structure for use as a sensor. The bottom gated structure allows for the active channel layer to be deposited last and for it to be exposed. This structure therefore facilitates easy and non-destructive inclusion of analytes, biological molecules/proteins, etc., as the final step. Having the channel layer on top also enables electrical measurements before and after the inclusion of the biological analytes in order to determine the sensitivity of the OTFT sensor. The experimental procedure for fabricating the bottom gated pentacene TFT structure is discussed below:

STEP1: Formation of Gate and Dielectric

Since pentacene is a p-type semiconductor and operates in accumulate mode, an N++ silicon substrate is required as a gate material. Other substrate materials such as glass (coupled with a conductive gate material) can be considered in the future if optical properties of glass are needed for the biological application of interest. In addition, for realization of a fully-printed process, plastic substrates and nanoparticle-based printed gate electrodes may be used.

The dielectric layer is formed next. The roughness and morphology of the dielectric has a distinct influence on the formation (morphology and structural properties) of the pentacene layer. Since controlling the morphology and electrical characteristics of pentacene using the previously mentioned input variables is the main goal of this experiment, minimizing the effects of the dielectric layer on pentacene formation is important. Silicon nitride and thermally grown oxide have both been shown to be good dielectric materials for pentacene. In particular, thermally grown oxide has been shown to facilitate highly ordered pentacene films independent of the deposition conditions [8]. Therefore, to form the dielectric layer, the silicon substrate is thermally oxidized to form a 100nm SiO_2 dielectric layer. The cross section of the TFT structure at the end of step1 is shown in Figure 13.

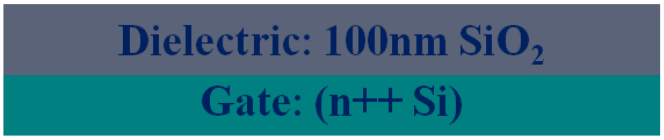

Figure 13. The cross section of the TFT structure at the end of step1.

<u>STEP2:</u> Source and Drain Contacts

The source and drain contacts were defined using conventional fabrication methods of photolithography, evaporation, and lift-off. Since photolithography and etching steps require the use of photoresist and organic etchants, these process steps are not compatible with pentacene. Therefore, source and drain contacts are defined before the deposition of the semiconductor (pentacene) layer.

The most commonly used source and drain contact material for pentacene TFTs is Au (gold) because the work function of Au, $\varphi = 5.1$ eV [15] matches very well with the ionization energy of pentacene, $\chi = 4.9$ eV [16]. Therefore, gold was lithographically defined here to form source and drain contacts.

The substrate from step 1 is first cleaned in piranha solution (Sulfuric acid and Hydrogen Peroxide Mixture) to remove organic and atmospheric contaminants. Next, the surface energy of the SiO_2 surface is adjusted for the deposition of photoresist. Since SiO_2 is hydrophilic, and the subsequent photoresist layer needed for photolithography is hydrophobic, HMDS (hexadimethyldisilazane) is first deposited on the SiO_2 layer. HMDS is generally used in silicon fabrication to optimize the interface between hydrophobic and hydrophilic surfaces.

Next, the source and drain contacts are defined using photolithography. 100nm of gold is thermally evaporated under vacuum. A lift-off process concludes the definition of the source and drain contacts. The lift-off is performed with an initial soak of the substrate in acetone for 45 minutes. To clean the surface even further, the substrate is sonicated in acetone for 45 minutes followed by 45 minutes of sonication in isopropyl alcohol (IPA). The final 1.5 hours of sonication and cleaning in acetone and IPA is performed to enhance sensor sensitivity. Since the pentacene layer will be deposited next on this cleaned surface, this cleaning step is important in establishing the interface between the dielectric and the semiconductor. Moreover, this clean is also important for the sensor because DNA immobilizes and interacts very close to this interface to cause the shift in the transistor characteristics.

The cross-section of the TFT structure after the definition of the source and drain contacts is shown in Figure 14.

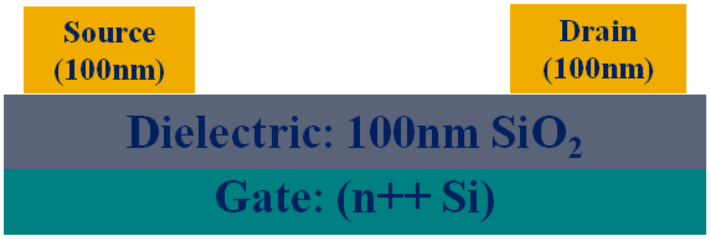

Figure 14. The TFT structure after the definition of source and drain contacts.

STEP3: **Semiconductor Layer**

As explained earlier in this chapter, pentacene was chosen as the semiconductor material because in thin film phase, pentacene exhibits superior transistor performance. Again, a thin film structure is preferred because of better coupling and sensitivity of the pentacene sensor to the biological analytes.

Before the pentacene layer is evaporated, the surface needs to be treated again in order to create an appropriate surface energy and enable good adhesion of pentacene. To bridge the interface between the hydrophilic SiO_2 layer and the hydrophobic pentacene layer, HMDS is again deposited on the cleaned surface from Step 2. The pentacene film is then deposited using a thermal evaporation system. The pentacene evaporation is performed under vacuum with a chamber pressure of ~2.2 x10^{-7} Torr.

Multiple experiments were conducted to study the effect of the input parameters on the outputs. The evaporation conditions for each of these experiments were set by varying the input parameters in Table 4 and will be discussed in the following section using a design of experiments (DOE) methodology. The cross-section of the final OTFT structure after evaporation of pentacene is shown in Figure 15.

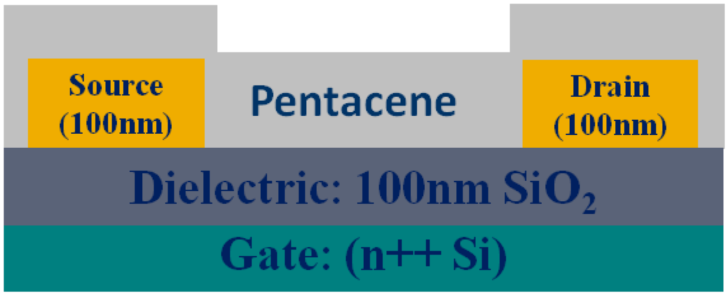

Figure 15. Final cross section of the pentacene bottom gated TFT structure.

2.5.1.2. Experimental Setup: Response Surface Design of Experiments (DOE)

Since the goal of this pentacene characterization experiment is to relate the input and output parameters, the experiment needed to be tailored to ultimately result in providing these relationships. To perform this comprehensive analysis, a multifactorial design of experiments (DOE) was used. In particular, a surface response DOE was used because of the importance of gaining a thorough understanding of the output characteristics for optimizing DNA immobilization.

The DOE set-up was configured using JMP [17], a statistical design and analysis software package. The DOE platform in JMP is an environment for describing the factors, responses and other specifications, thus creating a designed experiment. JMP allows the design of different types of DOE frameworks including screening designs and response surface designs. The former is to get an overall definition of the dependencies while the latter is gain an in-depth understanding of the relationships between input and output parameters. Detailed discussion on the type of DOE used for this experiment is available in a previous report [10].

Using a surface response design and more specifically, a uniform precision CCD set up[10], [28], the DOE shown in Table 5 was followed. A set of 17 evaporation conditions were designed for the experiment.

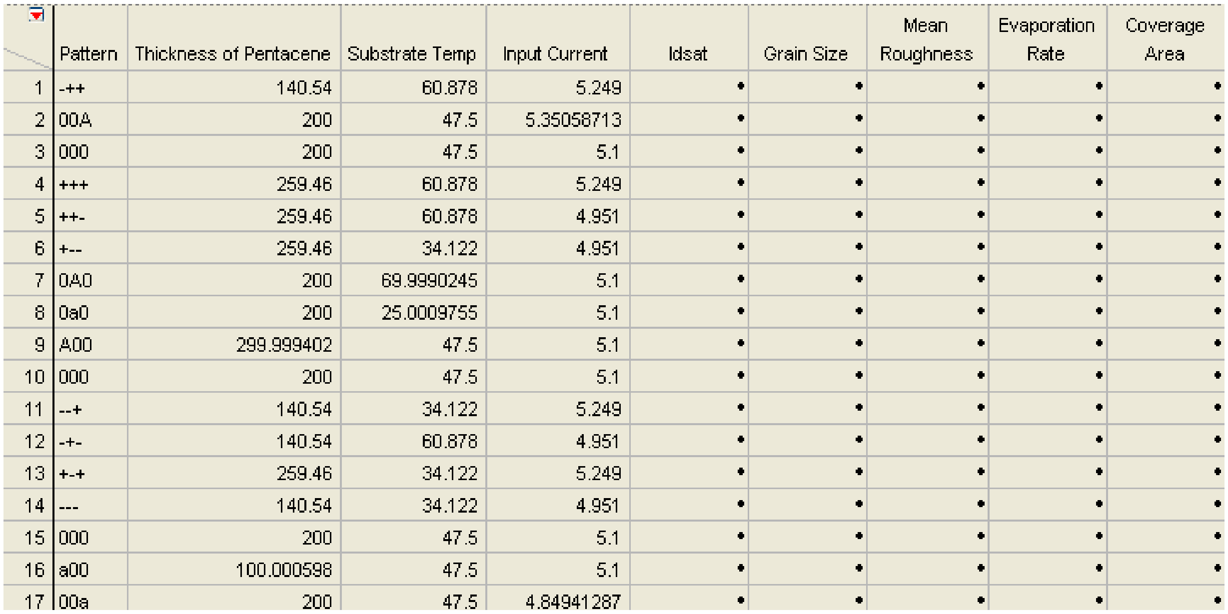

	Pattern	Thickness of Pentacene	Substrate Temp	Input Current	Idsat	Grain Size	Mean Roughness	Evaporation Rate	Coverage Area
1	-++	140.54	60.878	5.249	•	•	•	•	•
2	00A	200	47.5	5.35058713	•	•	•	•	•
3	000	200	47.5	5.1	•	•	•	•	•
4	+++	259.46	60.878	5.249	•	•	•	•	•
5	++-	259.46	60.878	4.951	•	•	•	•	•
6	+--	259.46	34.122	4.951	•	•	•	•	•
7	0A0	200	69.9990245	5.1	•	•	•	•	•
8	0a0	200	25.0009755	5.1	•	•	•	•	•
9	A00	299.999402	47.5	5.1	•	•	•	•	•
10	000	200	47.5	5.1	•	•	•	•	•
11	--+	140.54	34.122	5.249	•	•	•	•	•
12	-+-	140.54	60.878	4.951	•	•	•	•	•
13	+-+	259.46	34.122	5.249	•	•	•	•	•
14	---	140.54	34.122	4.951	•	•	•	•	•
15	000	200	47.5	5.1	•	•	•	•	•
16	a00	100.000598	47.5	5.1	•	•	•	•	•
17	00a	200	47.5	4.84941287	•	•	•	•	•

Table 5.JMP Surface Response DOE for Pentacene Characterization Experiment.

The input variables are shown in columns 3, 4, and 5. The output characteristics are in columns 6-10. For the DNA immobilization part of this experiment, 2 or 3 more output columns will be added, namely I_{dsat} ratio, Threshold Voltage (V_t) shift, and mobility shift.

The range of values chosen for each of the input parameters will now be discussed. The thickness of the pentacene layer was varied from 10-30nm, a range known to have the desired thin film like characteristics [7, 8], which is necessary for an effective sensor. This can be explained using Figure 19, which presents results from an x-ray diffraction analysis. To summarize, each pentacene monolayer is about 2-3nm. The thicker the pentacene layer, the higher the number of monolayers required to form the desired layer. After a certain thickness (~40nm), the pentacene layer becomes highly disordered and starts exhibiting bulk-like characteristics as shown in Figure 19. Since a disordered pentacene layer is not ideal for use as a sensor, the pentacene thickness range was chosen to be between 10 and 30nm.

The effect of substrate temperature on pentacene growth has been studied previously [8]. This previous study showed that when the substrate temperature was increased beyond 90°C, it inhibited the growth of pentacene on the substrate. In other words, the sticking coefficient, a parameter that quantifies the affinity and adhesion of the pentacene to the SiO_2 surface, is very low at high temperatures (such as 90°C) such that none of the pentacene actually sticks to the surface [8]. The values for substrate temperature were therefore finalized to be between 25°C (room temperature) and 70°C.

The input current parameter was initially studied using a screening experiment to understand its relationship on evaporation rate. As a result, in this multifactorial experiment, the input current range was chosen to ensure that a wide range of evaporation rates was observed in order to perform a comprehensive study of its effects on pentacene formation.

Thus, the pentacene characterization experiment has now been set up, and the choice of input and output parameters has been discussed. The following section presents results from the characterization experiment (DOE in Table 5).

2.5.1.3. Results

In this section, the morphological and electrical results of pentacene are analyzed as a function of input variables. In addition to measuring the output parameters, the variation (standard deviation) in the measured outputs was also monitored. The variation in each of these experiments has a direct correlation with the ordering and uniformity of the pentacene formation. A higher variation (bigger standard deviation) in an experiment is likely a result of lack of uniformity (in grain orientation, morphology, etc.) of the pentacene surface, which eventually leads to an unreliable DNA sensor. This non-uniformity can result from the chosen evaporation input parameters or inconsistencies with the fabrication protocol. In these cases, the experiment was repeated to isolate the cause of the non-uniformity and the variation was reduced if possible.

To measure the five output parameters and the variation within each experiment, the output parameters were measured such that the entire substrate was sampled. Specifically, nine points were collected from the substrate, as illustrated in Figure 16.

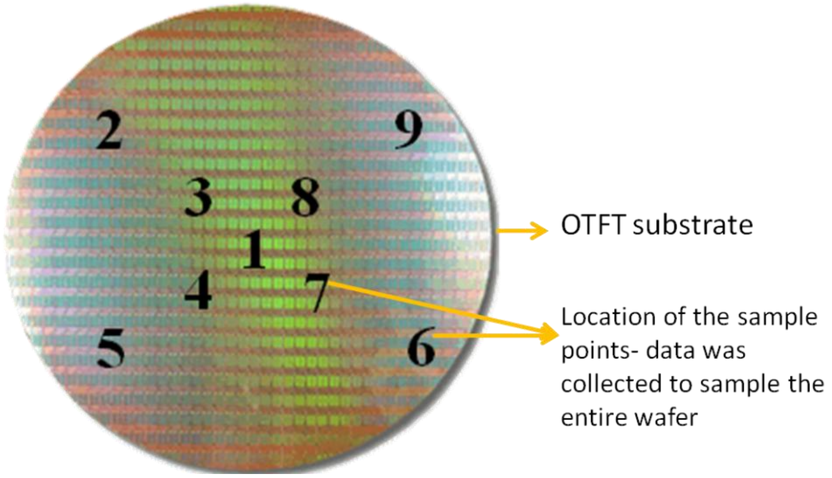

Figure 16. Schematic of measurements performed on the substrate to sample the entire wafer; this helps in monitoring variation within each experiment.

The relationships between the input and output parameters were graphed using JMP. The results shown in the following sections use JMP's Prediction Profiler or profiler plot, a type of plot that statistically validates and graphs the relationship between input and outputs. The profiler displays prediction traces for each *X* variable. A *prediction trace* is the predicted response as one variable is changed while the others are held at a constant value. JMP is able to is able to derive a prediction profiler by using leverage plots [10, 17], extracted by relating input and output parameters.

The profiler plot is powerful because it is not merely a graph that verifies the relationship between X and Y variables. It also statistically validates the relationship and incorporates this statistical data into the slopes of the traces and error bars shown in the profiler plots. An example of a profiler plot is shown in Figure 17.

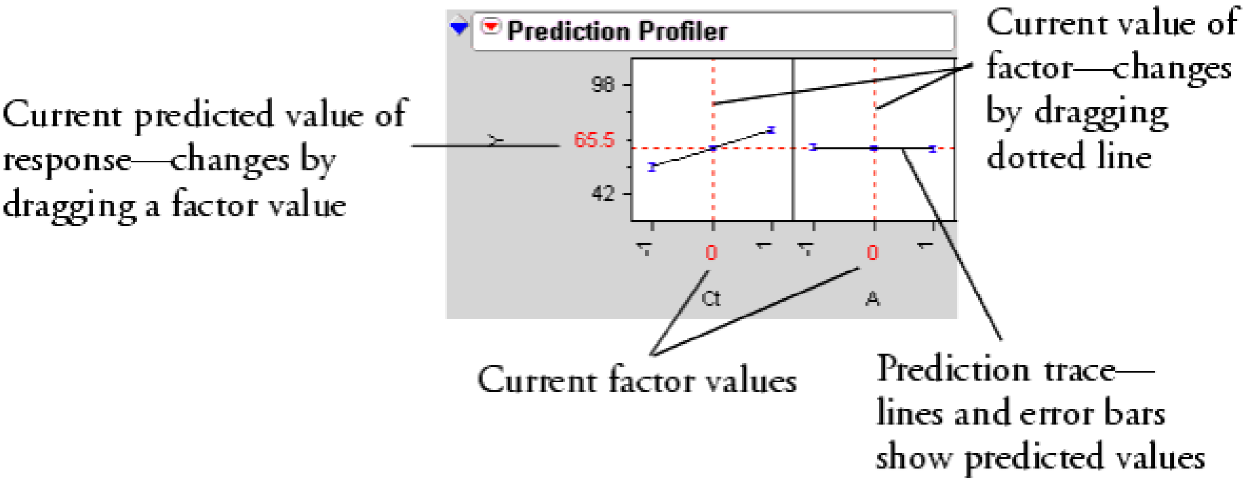

Figure 17. Example of an Prediction Profiler plot in JMP [17].

The low and high values are shown on the *x*-axis for each input factor. The vertical dotted line for each *X* variable shows its *current value* or *current setting*. The horizontal dotted line shows the *current predicted value* of each *Y* variable for the current values of the *X* variables. The lines and markers within the plots show how the predicted value changes when the current value of an individual *X* variable is changed. The 95% confidence interval for the predicted values is shown by *error bars* above and below each marker [17].

When interpreting a prediction profiler, the importance of a factor can be assessed to some extent by the steepness of the prediction trace. If there are interaction effects among the input parameters to cause a change in outputs or cross-product effects in the model, the prediction traces can shift their slope and curvature as the current values of the X factors are changed. If there are no interaction effects, the traces only change in height, not slope or shape. These interaction effects are summarized using the interaction plots in JMP. More information on profiler plots and interaction plots can be found in the JMP manual [17].

Using the prediction profiler, the measured results from the five output parameters, namely I_{dsat}, mean roughness, grain size, evaporation rate, and coverage area, are graphed and discussed in the following section.

A) Output 1: Saturation Current (I_{dsat})

To begin with, saturation current is an important output parameter since it is used to quantify the sensitivity of the OTFT sensor by comparing the saturation current values before (this section) and after (section 2.5) the inclusion of biological analytes. In addition, the saturation current also provides information on the quality of the pentacene film. A highly ordered and uniform film will have better electrical performance than a disordered pentacene film. This information eventually becomes important to determine the quality of the OTFT sensor.

Therefore, saturation current (I_{dsat}) and other transistor performance characteristics were measured using the Agilent HP4156 probe station purged in nitrogen. The measurements were done under nitrogen, as is usually the practice when measuring pentacene transistors since pentacene is oxygen and moisture sensitive.

Using profiler plots, Figure 18 shows the effect that the three input parameters (Input Current, Thickness of Pentacene, and Substrate Temperature) have on saturation current (I_{dsat}).

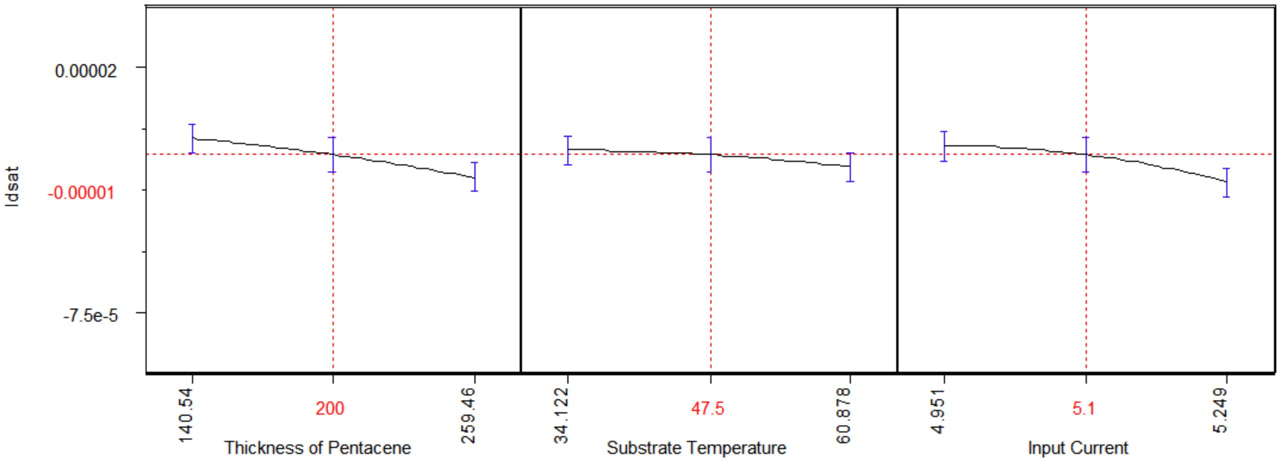

Figure 18. Relationship between the input parameters (substrate temperature (°C), input current (Amps), thickness of pentacene (Å)), and I_{dsat} or saturation current (Amps).

As mentioned earlier, the pentacene TFT device is a p-type accumulation device; the Y-axis in Figure 18 is negative current representing hole current. Figure 18 shows that as the thickness of the pentacene increases, the hole current (magnitude) also increases. This result can be justified using a schematic of the known growth modes of pentacene shown in Figure 19. The stacking of the pentacene and surface coverage causes the observed increase in electrical characteristics. Figure 19 shows the schematic diagram of pentacene on SiO_2 over a range of pentacene thicknesses; its effect on the electrical characteristics is explained below.

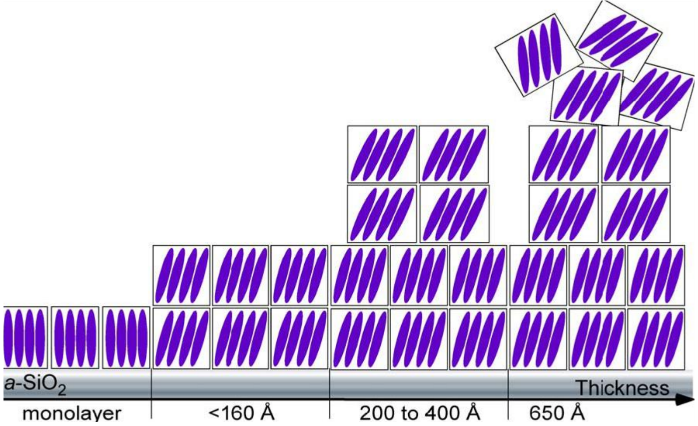

Figure 19. Schematic diagram depicting the phases and grain orientation in various pentacene film thicknesses [7].

The schematic diagram shown above is based on GIXD (grazing incidence X-ray diffraction) characterization done by Dr. Sandra Fritz [7]. The schematic diagram shows that after about 400Å, pentacene starts exhibiting ‘bulk-like’ characteristics. 200-400 Å represents the transition. The increase in current in this experiment is mainly due to stacking of monolayers and uniform coverage till about 200 Å or so. In this experiment, thicknesses were varied from 100-300 Å. Throughout this range, the uniform coverage and stacking helps increase the mobility and conductivity.

The results in Figure 18 also show that as the substrate temperature increases, the saturation current increases. As the substrate temperature increases, the grain size increases due to thermodynamic factors such as sticking coefficient and diffusion of the pentacene grains during evaporation. As many groups have shown, as grain size increases, the mobility increases. Since electrical conductivity is limited by charge transfer across grain boundaries, the formation of larger crystallites lead to enhanced conductivity [18]. Thus, an increase in mobility leads to an increase in current as seen in this experiment.

Increase in input current increases the overall saturation current as well. Although higher input current usually leads to smaller grain size (explained later in this chapter), and therefore relatively lower saturation currents, the uniform stacking facilitated by high input current dominates and contributes towards the observed increase in output saturation current. The higher the input current, the faster the evaporation and therefore less time for the pentacene crystals to diffuse and grow. This in turn contributes to uniform stacking, enhancing transport between grains and increasing overall output saturation current.

In addition, Figure 20 shows the wide range of electrical characteristics obtained by varying evaporation conditions. The saturation current varied from about ~2μA in the lowest performing sample to ~60μA on the highest performing sample. The order of magnitude difference in I_{dsat} seen here by varying the evaporation conditions highlights the importance of tuning and optimizing the input parameters to obtain a reliable, repeatable, and robust sensor.

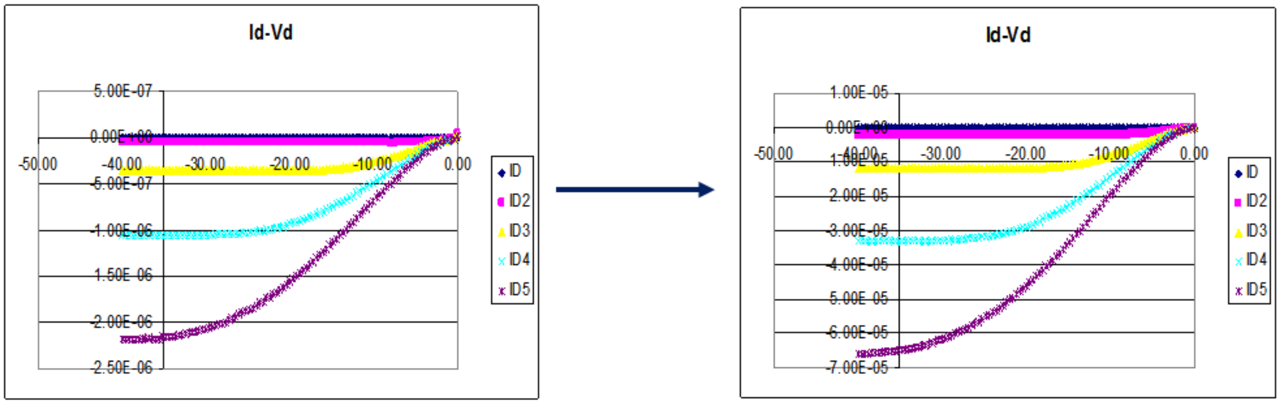

Figure 20.I_d- V_d characteristics from 2 different experiments with the lowest (left) and highest (right) performing samples.

To summarize the results for output 1, the three input factors affect I_{dsat} in the following way. Increase in thickness of pentacene causes an increase in the hole current because of the increase in film stacking and coverage explained using the GIXD characterization results. The increase in substrate temperature leads to bigger grain sizes, which consequently results in enhanced conductivity. Finally, an input current increase also enhances the performance because of more uniform stacking of pentacene layers.

The roughness of the pentacene film is discussed next as a function of the input parameters.

B) Output 2: Mean Roughness of Pentacene Film

The roughness of the pentacene film determines the morphology of the pentacene. As discussed earlier, the roughness creates crevices in the film, which is important for physical adsorptive immobilization of DNA on pentacene surface. In other words, roughness is an important output parameter to optimize for effective DNA immobilization and sensor sensitivity.

The relationship between the input factors and mean roughness has been extracted and is shown in the form of profiler plots in Figure 21. In all experiments, mean roughness was measured using Atomic Force Microscopy (AFM).

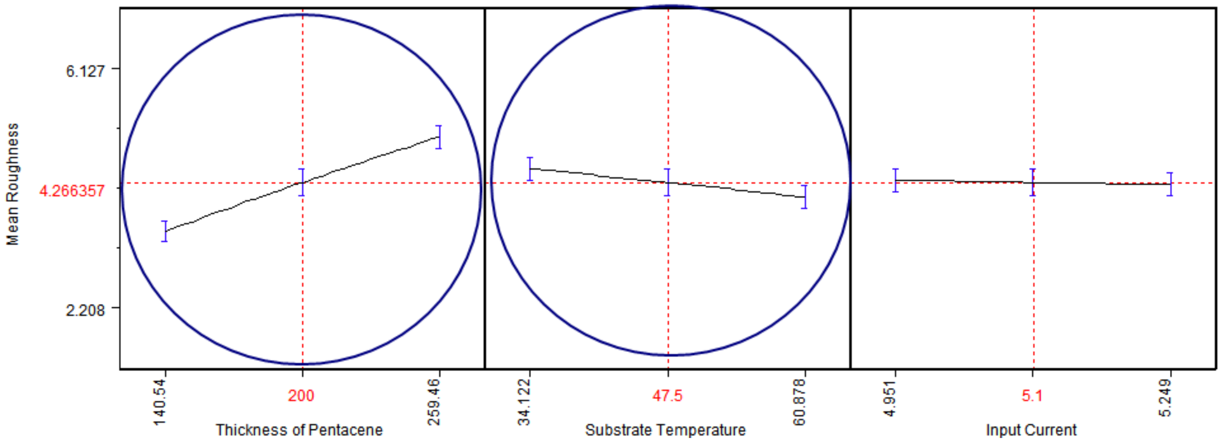

Figure 21. Relationship between the input parameters (substrate temperature (°C), input current (A), thickness of pentacene (Å)) and mean roughness (nm).

As the thickness of pentacene increases, the film roughness increases because the higher the number of monolayers, the rougher the film usually tends to be. This is further confirmed when looking at the schematic diagram in Figure 19. As the thickness of the pentacene film increases, the stacking becomes misaligned, especially after about 160Å or so. Despite the increase in roughness, the current has still gone up with thicker films possibly because other factors that affect the current, such as better transport within a monolayer, dominated.

As the substrate temperature increases, the roughness decreases. When evaporation of pentacene is done at higher substrate temperatures, the formation of the pentacene crystals on the surface is more ordered, thereby reducing the overall roughness. The effect of substrate temperature on the ordering of thin films of pentacene has been analyzed previously [19].

The input current does not affect the mean roughness according to Figure 21. At a pentacene thickness of 200Å and a substrate temperature of 47.5^{o}C (X values in Figure 21), the input current does not affect the mean roughness. At other values of thicknesses and substrate temperatures though, it does have an effect, as shown in Figure 22. In this case, the thickness of pentacene was set at 140.54Å and substrate temperature was set at 60.878^{o}C. The effect seen in Figure 22 is likely a result of the substrate temperature input factor dominating over the input current. Therefore, depending on what thickness and substrate temperature turns out to be ideal for DNA immobilization and overall sensitivity, the input current will have to be tuned accordingly.

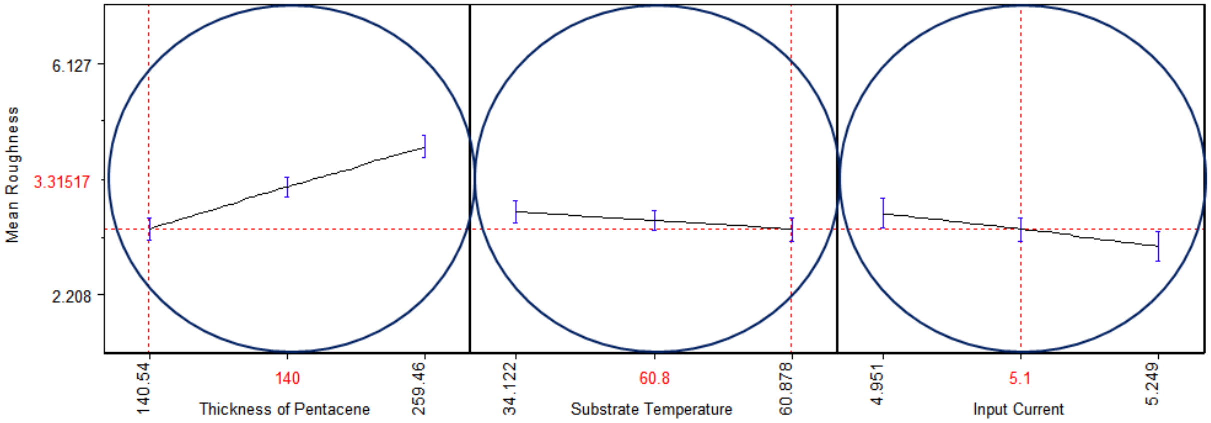

Figure 22. By changing the chosen X values of 2 of the input parameters, this profiler plot shows that input current also changes roughness.

As previously discussed, the topological features on the pentacene film are critical for DNA immobilization and sensor sensitivity. By performing AFM analysis on these samples, surface roughness data on the samples were extracted. Figure 23 shows AFM images of samples from 2 different experiments, representing surfaces with the lowest (2.208nm) and highest (6.127nm) mean roughness. The wide range (given the 10-30nm thicknesses of the pentacene layers) of the surface roughness data further emphasizes the need and importance of controlling the input parameters to get optimum morphological conditions for highest DNA sensitivity.

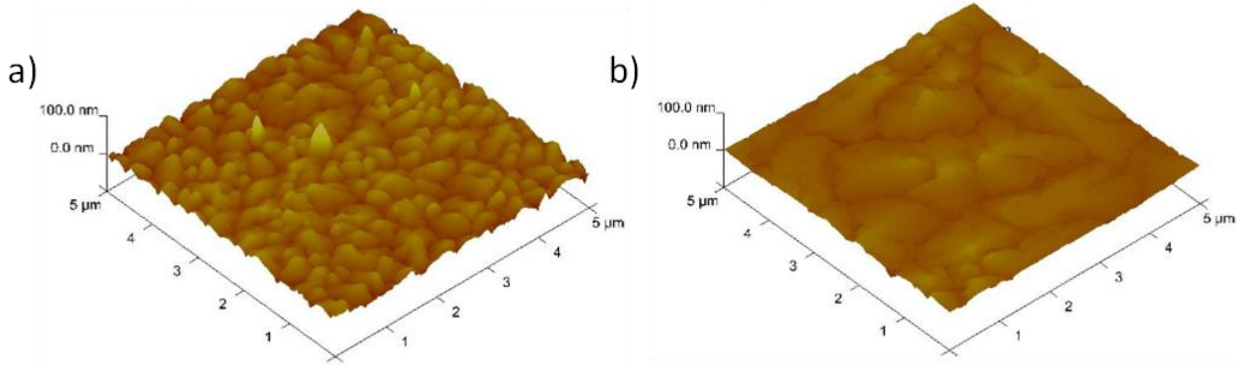

Figure 23. AFM images of samples from 2 different experiments with the lowest (a) and highest (b) surface roughness parameters. The lowest extracted roughness value was 2.208nm while the highest was 6.127nm.

The results for output 2 can be summarized in the following way. Increase in thickness of pentacene contributes to a rougher film because the stacking of the pentacene layers becomes disordered in thicker films. The increase in substrate temperature facilitates uniform formation of pentacene films leading to smoother films. Finally, the input current affects the roughness of the film only at certain substrate temperatures and thicknesses of pentacene. The interaction effects of this input parameter needs to be studied further and tuned appropriately when optimizing for DNA immobilization.

The importance of tuning the third output parameter, the grain size in the pentacene film, is discussed in the following section.

C) Output 3: Pentacene Grain Size

Grain boundaries are important topological features where DNA can immobilize. Grain size determines the number of grain boundaries on the surface, which in turn establishes the amount of crevices and features available for DNA to immobilize. Therefore, grain size was measured here as a function of the input parameters in order to eventually optimize this parameter for effective DNA immobilization.

Atomic Force Microscopy (AFM) was used to measure grain size. After extracting AFM images from tapping mode scans, the grain size was measured by boxing the area around an average-size grain in a particular scan. Keeping the systematic variation in consideration, this measurement technique is valid to make a general comparison across the different experiments. The profiler plots in Figure 24 illustrate the effect of input parameters on grain size.

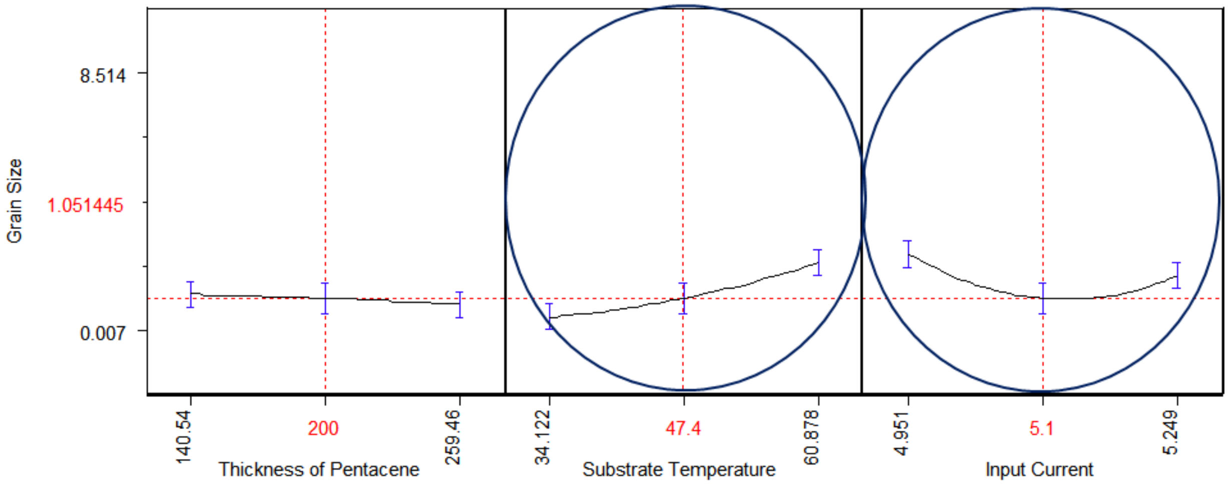

Figure 24. Relationship between the input parameters and grain size.

To begin with, the thickness of pentacene, as expected, does not affect the grain size, at least over the range of thicknesses studied. This is because the initial nucleation sites of the film established in the first few monolayers determine the morphology and grain size of the final layer. Therefore, the final thickness of the pentacene is irrelevant to grain size formation [8].

Figure 24 also shows that as substrate temperature increases, the grain size increases (which in turn leads to better electrical performance due to enhanced transport characteristics). During evaporation, a high substrate temperature facilitates diffusion. The enhanced diffusion allows more grain growth relative to nucleation of new small grains. In other words, with a higher substrate temperature, the sticking coefficient (defined earlier in this chapter) is lower, inhibiting nucleation, and surface diffusion is higher, favoring growth. The growth mechanism of pentacene is such that the grain grows until it is stopped by the formation and presence of another grain on the surface. Therefore, if sticking coefficient is low, the nucleation of new grains is less likely and therefore having bigger sized grains is more likely. This explains the relationship seen in Figure 24, where higher substrate temperatures lead to bigger grain sizes.

The input current shows a non-linear relationship with grain size in Figure 24. The expected relationship here would be that as input current decreases, the grain size would increase linearly because of the way the grains are formed. As described in the previous paragraph, when the pentacene crystals hit the substrate as they are being evaporated, they grow till they hit another crystal around them. With a lower evaporation rate, crystals have time and space to grow bigger on the surface. This linear relationship is not seen because of two possible reasons. First, the interaction effects between input parameters, as seen in the interaction plot in a previous report [10], could be contributing towards this result. The other reason could be the way the grain size was measured. Since the grain size measurement was taken using an average sized grain from each sample's AFM result, this could have contributed toward an error with the results. A more precise way of measuring the grain size needs to be implemented to get more accurate data and a clearer relationship between input current and grain size.

Again, since grain size and grain boundaries are an important part of sensitivity of the sensor, grain sizes ranging from 8.514 μm^2 down to 0.314 μm^2, as illustrated in Figure 25, emphasize the importance of tuning the morphology to suit the necessary conditions for DNA interaction.

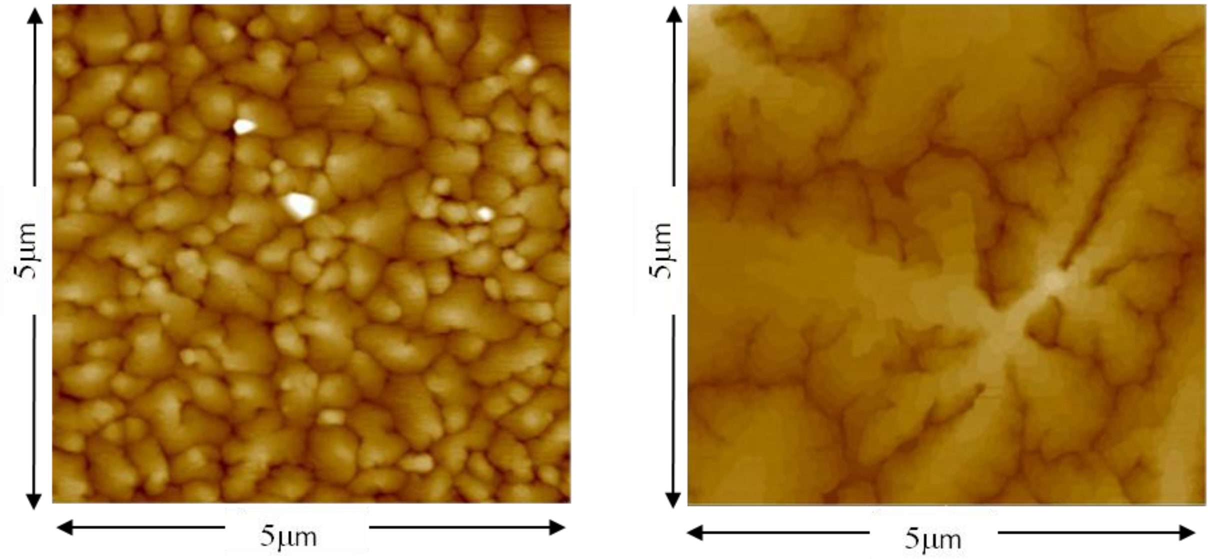

Figure 25. AFM images of samples from 2 different experiments consisting of the smallest grain size (left) of 0.314 μm^2 and the biggest grain size (right) of 8.514 μm^2.

To summarize the results presented in this subsection, substrate temperature and input current have an effect on grain size in pentacene film. Higher substrate temperatures lead to larger grains due to enhanced surface diffusion at these high temperatures. Also, lower input currents lead to formation of large grains because at low evaporation rates, the mechanism of pentacene grain growth facilitates growth of bigger grains.

Finally, the results of the last two output parameters, evaporation rate and coverage area, are presented below.

D) Outputs 4 and 5: Evaporation Rate and Coverage Area

Evaporation rate and coverage area play an important role in determining morphology of pentacene. Evaporation rate, as discussed in the previous subsection, determines the grain size of pentacene because of the growth mechanism of pentacene crystals. Since the grain size determines the grain boundaries in the film, and since grain boundaries play an important role in the immobilization of DNA, evaporation rate is an important parameter to analyze and optimize for effective DNA immobilization.

Evaporation rate was calculated using the data from a quartz crystal monitor within the pentacene evaporator. The quartz crystal oscillates at a resonance frequency that is dependent on the thickness and mass of the film deposited onto it. As a material gets deposited onto a quartz crystal monitor, the crystal monitor's mass increases, and its oscillation frequency thereby decreases. The oscillation frequency change is directly related to the thickness of the film deposited on the crystal. The quartz crystal monitor therefore needs to be placed very close the substrate to yield accurate results.

Coverage area determines the quality of pentacene film. For example, looking at Figure 27, the AFM of the sample with the lowest coverage area shows that the SiO_2 layer is exposed throughout the sampled area. The lack of pentacene in these areas worsens electrical performance and reduces areas available for DNA immobilization. Therefore, coverage area is also an important output parameter to measure and optimize.

The coverage area was calculated from the images scanned using AFM. Using a contrast tool in an image editing software, the pentacene grains were isolated from the SiO_2 layer underneath, and coverage area of the pentacene on the surface was thereby calculated.

According to the relationships seen in Figure 26, evaporation rate is affected only by the input current, and the coverage area does not show any strong relationships with the input factors. The higher the input current, the higher the temperature is of the crucible holding the pentacene for evaporation. This in turn will cause a higher evaporation rate. The evaporation rate ranged from 0.838Å /min to 18.391Å /min depending on the value of the input current. As expected, the evaporation rate is independent of the other two input parameters.

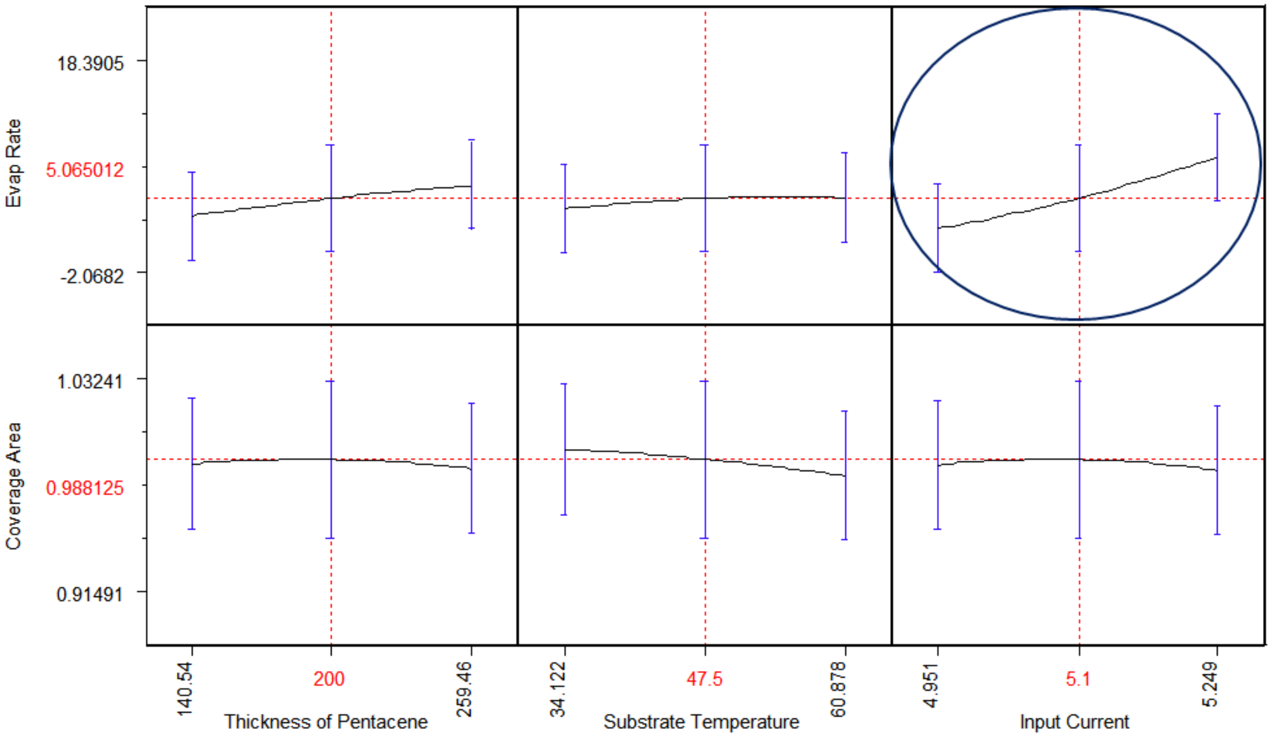

Figure 26. Relationship between the input parameters and evaporation rate and coverage area.

Although clear trends were not obtained to understand the factors that affect coverage area, Figure 27 shows the lowest and highest coverage area from samples of 2 different experiments. Since coverage area of pentacene on SiO_2 surface determines the electrical performance of the OTFTs and the quality of the OTFT sensor, the different surfaces that resulted (Figure 27) highlight the importance of finding better ways of characterizing the factors that affect coverage area. The left image with the lowest coverage area exposes a lot of the dielectric surface. The stacking of the image on the right is better, and coverage area is much higher since the dielectric surface is completely covered by the pentacene crystals.

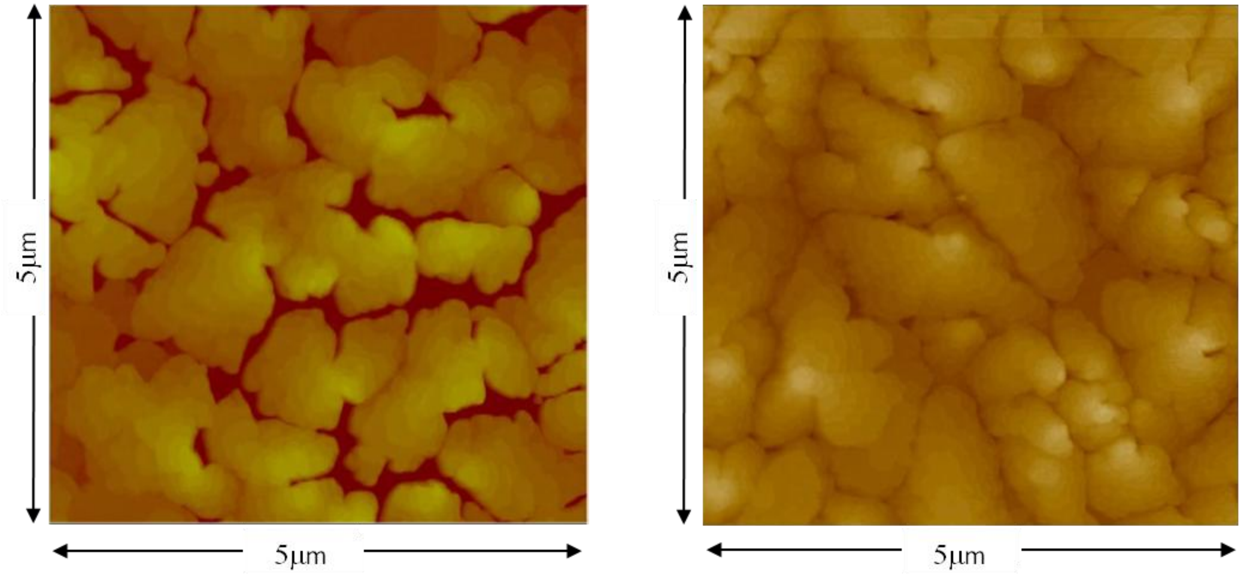

Figure 27. AFM Images of samples from 2 different experiments that resulted in the lowest (left) and highest (right) coverage area. The yellow area in the images represents the pentacene crystals, and the dark red area is the SiO_2 (dielectric) surface.

To summarize, in this subsection, evaporation rate and coverage area were both analyzed. Input current was the only parameter that affected evaporation rate. No clear trends were observed to understand the factors that affect coverage area. Future work will focus on studying coverage area to better understand the factors that determine the coverage of pentacene on the SiO_2 surface.

Subsections A-D presented thus far in section 2.5.1 have highlighted the importance of the different input parameters and their effect on the morphological and electrical characteristics of pentacene TFTs. The following section takes this analysis a step further and integrates the DNA immobilization experiment into the data obtained so far, to arrive at the optimum input conditions for highest sensitivity.

2.5.2. Optimization of DNA Immobilization and Sensor Sensitivity

In the previous section, the morphological and electrical characteristics of pentacene was thoroughly analyzed and understood as a function of the input parameters. This initial analysis is crucial in order to understand the type of pentacene surface that will provide the highest sensitivity for DNA. Since the sensitivity of the sensor surface will be related to the input parameters in this section, the results and analysis in the previous section helps in understanding the optimum surface in terms of morphology (grain size, roughness, etc.) and electrical performance (I_{dsat}). The data collected from both sections 2.5.1 and this section will also help verify and explain the mechanism of DNA doping and DNA immobilization on the pentacene surface.

To summarize, the purpose of this section is to determine pentacene evaporation conditions that facilitate optimum DNA immobilization and highest sensitivity. This section first presents the experimental protocol followed to immobilize DNA on the pentacene surface and to perform measurements to calculate the sensitivity (quantified by I_{dsat} ratios) of each of the OTFT sensors from Table 5. Subsection 2.5.2.2 then presents the results that relate I_{dsat} ratios to the three input parameters, ultimately arriving at the optimum surface for highest sensor sensitivity of DNA.

2.5.2.1 Experimental Protocol

To begin with, the experimental protocol that was followed for DNA immobilization and sensitivity measurements is listed and discussed below. For each of the experiments from the DOE in Table 5, the following steps are followed:

1) Electrical characteristics of the OTFT are first measured using a probe station purged under N_2. In order to maintain stability of the OTFT during electrical measurements, the N_2 purge is required since pentacene is oxygen and moisture sensitive. The measurements were made such that the entire wafer was sampled as shown in Figure 16. The transistor performance characteristics measured here is before the inclusion of DNA on the surface. It is therefore used eventually as a factor in calculating the I_{dsat} ratio.

2) The pentacene surface has been characterized thoroughly and is now ready for the inclusion of DNA. The DNA used for immobilization is a 125 base-pair custom synthesized single stranded DNA sequence synthesized by BioSynthesis, Inc. The DNA is first dissolved in 2X concentration of saline-sodium citrate (SSC) buffer to yield a DNA concentration of 0.5μg/μL. 1.5μLof this DNA is then pipetted on channels of the pre-measured transistors (~9-12 transistors in each experiment). The channels of the transistors in all of the experiments were110μmlong and 1mm wide.

3) The substrate is then left under atmosphere (in air) for DNA to immobilize on the channels. In solution, the DNA is mobile and travels until it immobilizes in the morphological features of the pentacene. The immobilization process is considered complete when the buffer solution on the surface is completely dry. This takes about 30 minutes.

4) The substrate and channels are then washed with nuclease free DI water for about 1-2 minutes. This step removes excess buffer solution from the channels along with excess DNA that did not immobilize. The substrate is then gently dried with nitrogen to remove moisture.

5) Next, the substrate is stored in nitrogen overnight to neutralize any changes in the pentacene surface caused by the use of buffer solution and DI water in the previous steps. This storage condition was finalized based on control experiments performed using different storage protocols on similar substrates. Since pentacene is moisture sensitive, control experiments had to be performed to make sure that the effects of buffer solution and water on the pentacene transistors do not confound the electrical shifts caused by DNA immobilization. More experiments need to be performed in the future to optimize storage time and conditions.

6) The pentacene transistors now have the DNA immobilized in its channels. In order to measure the shifts caused by the DNA on the surface, electrical characteristics of the OTFT are measured again using the same probe station setup as step 1. These measurements also play an important role in the calculation of the I_{dsat} ratio.

7) Using electrical measurements performed in step 1 and step 6 above, the sensitivity of pentacene surface in each of the experiments is calculated using the I_{dsat} ratio defined in section 2.3.

The experimental protocol for DNA immobilization and sensitivity measurements has thus been described above. The results from the calculations performed in step 7 is related to the input parameters and shared in the following section.

2.5.2.2 Results: Optimization of DNA Immobilization and Sensor Sensitivity

Understanding the factors that affect the sensitivity of a sensor surface is crucial in being able to obtain an effective and reliable DNA sensor. Although immobilized DNA was previously shown to cause electrical shifts on the pentacene surface [1], the magnitude of this electrical shift was not optimized or maximized to obtain the most effective sensor. Since the sensitivity (i.e. magnitude of electrical shift) is a vital characteristic of a good sensor, the purpose of this subsection is to arrive at the highest sensitivity possible by optimizing the pentacene surface.

The pentacene surface has been thoroughly studied and related to the evaporation conditions or input parameters in section 2.5.1. This section presents the results from integrating the DNA on the pentacene surface and understanding the electrical shifts caused by the same. These shifts characterize the sensitivity of the OTFT sensor and are quantified by the I_{dsat} ratio.

To review, the I_{dsat} ratio is defined as:

$$\mathbf{I_{dsat}\ Ratio} = \frac{I_{dsat} AfterDNA\_immobilization}{I_{dsat} BeforeDNA\_immobilization}$$

where I_{dsat} is the drain current of the transistor in saturation mode. Similar to results presented in section 2.5.1, profiler plots are used in Figure 28 to illustrate the relationship between the input parameters varied during pentacene evaporation and the calculated I_{dsat} ratios.

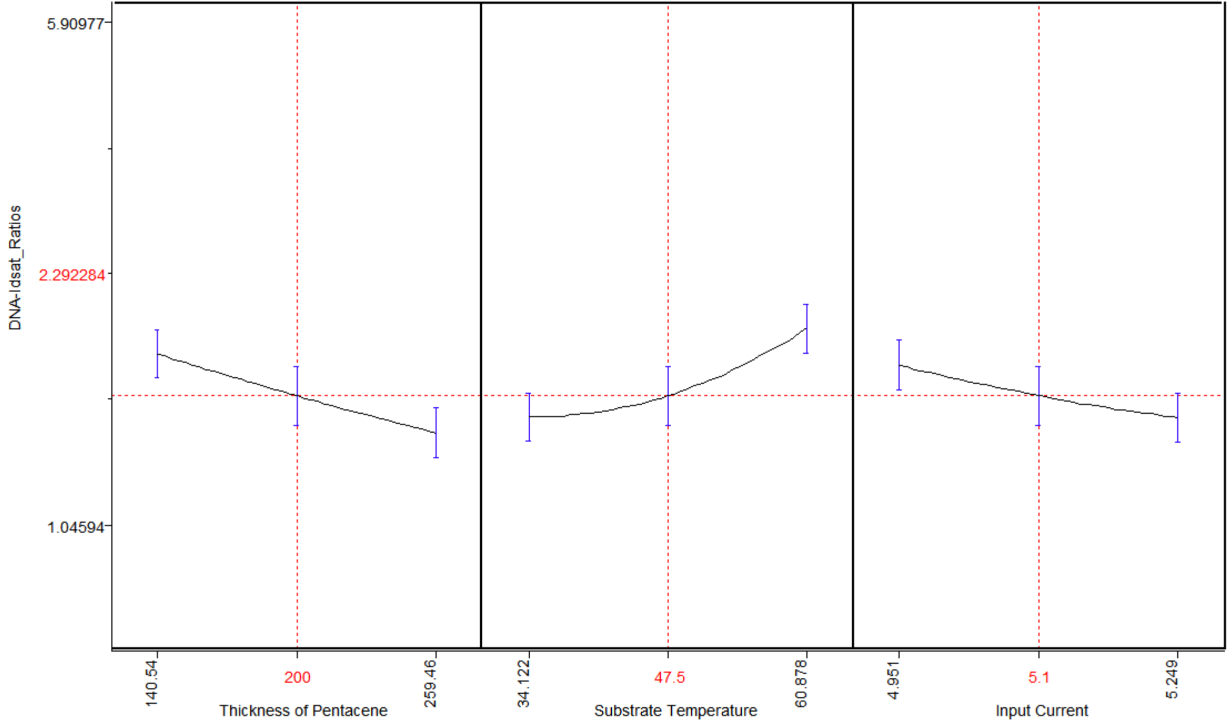

Figure 28. Relationship between input parameters and I_{dsat} ratios.

The input parameters have already been related to the morphological and electrical characteristics in the previous section. In this section, the input parameters are related to sensor sensitivity. To begin with, as the thickness of pentacene increases, the I_{dsat} ratio or sensitivity of the sensor goes down. To review, the OTFT used for the sensor is of a bottom gated structure and the channel is formed in the first few monolayers (monolayer = 15Å) of the pentacene film. Thinner films allow the DNA to be immobilized in the channel part of the film and affect the performance more, causing the higher shift in transistor performance characteristics. This is illustrated in Figure 29, where the DNA immobilization in thinner films is in contact with the channel part of the transistor.

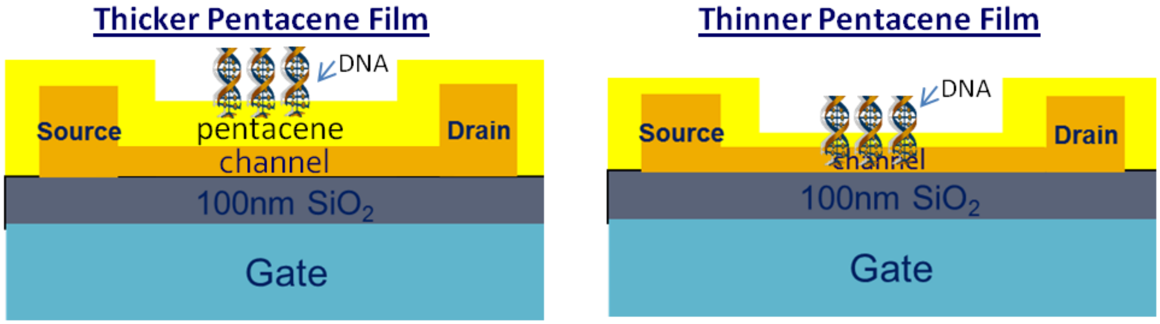

Figure 29.DNA immobilization in thinner films is more effective because immobilization occurs in channel part of the film causing a higher shift in electrical characteristics.

Although thicker pentacene likely immobilizes more DNA because of higher surface roughness, the sensitivity will not be high because not all of the DNA will be immobilized in the channel part of the pentacene film to actually cause an effect on the transistor characteristics. Therefore, thinner films are ideal for an effective DNA sensor.

Next, as substrate temperature increases and input current decreases, sensitivity increases. Higher substrate temperatures and lower input currents (lower deposition rate) lead to formation of bigger grains in the pentacene film. At thin film phases, the pentacene film growth produces a terrace like structure on SiO_2 substrates [20]. This can also be seen in the AFMs in Figure 25 and Figure 27. Because of the terrace formation, the bigger the grain size, the more exposure there is to the first few monolayers of the film. In other words, bigger grains allow for a wider area of exposure of the first few monolayers of the film where the channel forms. With smaller sized grains on the pentacene film, the terrace structure does not allow the channel part of the film to be as widely exposed. Therefore, the bigger the grain size, the more area (in the channel part of the film) the DNA has to immobilize. Therefore, with lower input current and higher substrate temperature, bigger grains are grown, allowing the DNA to more effectively immobilize and affect the channel part of the film, thereby causing the highest electrical shift and giving the highest sensitivity. This agrees very well with the data seen in Figure 28 as the I_{dsat} ratio is higher for lower input currents and higher substrate temperatures.

To summarize the results seen in Figure 28, thinner pentacene films, higher substrate temperature, and lower input current, led to the highest sensitivity. *The sensitivity values ranged from 1.0456 up to 5.909.* The sensor with the highest sensitivity or the most effective DNA immobilization changed the transistor characteristics by a factor of 6, thereby highlighting the potential of pentacene OTFTs to function as effective DNA sensors.

We have thus studied the impact of evaporation parameters on pentacene morphology, and tuned/ analyzed morphology to maximize the sensitivity of the OTFT platform. Results emphasize that the sensitivity of the OTFT DNA sensor can be maximized by optimizing the morphology of the pentacene film to expose as much of channel part of the film as possible for DNA immobilization.

2.6. Conclusion and Future Work

By finding reliable methods to relate the electrical transduction behavior to physical origins, and by optimizing the pentacene film surface for highest DNA sensitivity, we have come one step closer to achieving the goal of making a viable DNA sensor using pentacene TFTs. To begin with, in this chapter, results from TOF-SIMS analysis along with corresponding electrical results have confirmed the immobilization of DNA on pentacene surface. These results have revealed the high selectivity of the sensor to detecting DNA and have confirmed the physical origin of the observed electrical transduction behavior.

The morphological and electrical characteristics of pentacene transistors were then studied as a function of pentacene evaporation conditions (input parameters). Next, the DNA was immobilized on the pentacene surface, and the electrical shifts (quantified by I_{dsat} ratios) were analyzed as a function of the input parameters. A combination of both of these experiments allowed for the optimization of pentacene surface (in terms of morphology) for highest DNA sensitivity and effective DNA immobilization. *To summarize the results, thinner films, higher substrate temperature, and higher input current allowed for DNA to immobilize in the channel part of the OTFTs and therefore resulted in the highest sensitivity of pentacene film to DNA.*

To improve the sensor system even further, the experiments and results from this chapter point to several interesting directions for future work. In section 2.5.2, the experimental protocol used for the DNA optimization experiment was discussed. In this protocol, storage of samples in nitrogen was required to neutralize effects of buffer solution and DI water. In order to optimize the time and atmosphere of storage, more work can be done to understand the effects of nitrogen on buffer solution, DI water and the pentacene surface. Also, to make the DNA immobilization more stable and predictable, future work can focus on chemically modifying the pentacene surface to covalently bind to the DNA. This way, the orientation of the DNA is clear, and future experiments with hybridization will be more controllable. Since the goal is to be able to ultimately use the OTFT DNA sensor for genetic disease detection, more work on hybridization detection and particularly on single point mutation ('single nucleotide polymorphism') needs to be performed to arrive at a more versatile sensor.

2.7. Sources

[1] Q. Zhang, "OTFT-Based DNA Detection System," Ph.D. dissertation, University of California-Berkeley, 2007.

[2] "What are single nucleotide polymorphisms (SNPs)?"*Genetics Home Reference.*[Online]. Available: http://ghr.nlm.nih.gov/handbook/genomicresearch/snp. [Accessed: 07-Jan-2012].

[3] "Genome.gov | DNA Microchip Technology Fact Sheet," *National Human Genome Research Institute.*[Online]. Available: http://www.genome.gov/10000205. [Accessed: 07-Jan-2012].

[4] M. J. Heller, "DNA microarray technology: devices, systems, and applications," *Annual*

Review of Biomedical Engineering, vol. 4, pp. 129-153, 2002.

[5] H. Koltai and C. Weingarten-Baror, “Specificity of DNA Microarray Hybridization: Characterization, Effectors and Approaches for Data Correction,” *Nucl. Acids Res.*, vol. 36, no. 7, pp. 2395–2405, Apr. 2008.

[6] S. E. Molesa, “Ultra-Low-Cost Printed Electronics,” Ph.D. dissertation, University of California-Berkeley, 2006.

[7] S. E. Fritz Vos, “Structure and Transport in Organic Semiconductor Thin Films,” Ph.D. dissertation, University of Minnesota, USA, May 2006.

[8] D. Knipp, R. A. Street, A. Völkel, and J. Ho, “Pentacene thin film transistors on inorganic dielectrics: Morphology, structural properties, and electronic transport,” *Journal of Applied Physics*, vol. 93, no. 1, pp. 347-355, Jan. 2003.

[9] M. Gabig-Ciminska, “Developing nucleic acid-based electrical detection systems,” *Microbial Cell Factories*, vol. 5, p. 9, Mar. 2006.

[10] L. Jagannathan, “DNA Detection Using Organic Thin Film Transistors: Physical Origins of Electrical Transduction Behavior and Optimization of Sensitivity,” Master’s Thesis, University of California-Berkeley, 2008.

[11] Q. Zhang, L. Jagannathan, and V. Subramanian, “Label-free low-cost disposable DNA hybridization detection systems using organic TFTs,” *Biosensors & Bioelectronics*, vol. 25, no. 5, pp. 972-977, Jan. 2010.

[12] Evans Analytical Group, “Time-of-Flight Secondary Ion Mass Spectrometry (TOF-SIMS),”*Analytical Techniques.* [Online]. Available: http://www.cea.com/techniques/analytical_techniques/tof_sims.php. [Accessed: December 2, 2008].

[13] D. Gillespie, “A quantitative assay for DNA-RNA hybrids with DNA immobilized on a membrane,” *Journal of molecular biology,* vol. 12, pp.829, 1965.

[14] M. Shtein, J. Mapel, J. B. Benziger, and S. R. Forrest, “Effects of film morphology and gate dielectric surface preparation on the electrical characteristics of organic-vapor-phase-deposited pentacene thin-film transistors,” *Applied Physics Letters*, vol. 81, no. 2, pp. 268 – 270, Jul. 2002.

[15] D. R. Lide, *CRC Handbook of Chemistry and Physics: A Ready-reference Book of Chemical and Physical Data*. CRC Press, 2004.

[16] E. A. Silinsh and V. Capek, *Organic Molecular Crystals: Interaction, Localization, and Transport Phenomena*, 1st ed. American Institute of Physics, 1997.

[17] JMP Statistical Discovery Software, *JMP 5.0.1a Software Manual*, 1989.

[18] A. J. Salih et al., “Improved thin films of pentacene via pulsed laser deposition at elevated substrate temperatures,” *Applied Physics Letters*, vol. 69, no. 15, pp. 2231-2233, Oct. 1996.

[19] T. Minakata, H. Imai, and M. Ozaki, “Electrical properties of highly ordered and amorphous thin films of pentacene doped with iodine,” *Journal of Applied Physics*, vol. 72, no. 9, pp. 4178-4182, Nov. 1992.

[20] I. P. M. Bouchoms, W. A. Schoonveld, J. Vrijmoeth, and T. M. Klapwijk**,** “Morphology identification of the thin film phases of vacuum evaporated pentacene on SiO_2 substrates,” *Synthetic Metals*, Vol. 104, Issue 3, pp.175-178, July 1999.

[21] J.W. Chang, H. Kim, J.K. Kim, B. K. Ju, J. Jang, and Y.H. Lee, “Structure and Morphology of Vacuum-Evaporated Pentacene as a Function of the Substrate Temperature,” *Journal of the Korean Physical Society,* Vol. 42, pp. S647-S651, February 2003.

[22] Arizona State University, “Single Molecule Spectroscopy,” *Arizona State University.*[Online]. Available: http://www.public.asu.edu/~laserweb/woodbury/smf.html. [Accessed: December 11, 2008].

[23] G. Horowitz and M .E. Hajlaoui, “Mobility in polycrystalline oligothiophene field-effect transistors dependent on grain size,” *Advanced Materials,* vol.12, no.14, pp. 1046-1050, 2000.

[24] D.Knipp, D.K. Murti, B. Krusor,R. Apte, L. Jiang, J.P. Lu, B.S. Ong, and R. Street, “Photoconductivity of Pentacene Thin Film Transistors,” *Materials Research Society Symposium Proceedings,* Vol. 665, pp. 207-212, 2002.

[25] K. Puntambekar, “Characterization of Structural and Electrostatic Complexity in Pentacene Thin Films By Scanning Probe Microscopy,” Ph.D. dissertation, University of Minnesota, USA, October 2005.

[26] K.O Lee and T.T. Gan, “Space-Charge-Limited Currents in Evaporated Films of Pentacene,” *Physics Stat. Solutions, vol. 43, p. 565, 1977.*

3. Inkjet Printed Gold Heaters and Resistance Temperature Detectors(RTDs)

3.1 Introduction and Motivation

While there have been demonstrations of many printed devices such as transistors [1] and RFID structures [2], there have been no demonstrations to date of printing the critical reactor components required for biological microfluidic applications; in particular, virtually all integrated biological reactors require integrated heaters and resistance temperature detectors (RTDs). Resistive heaters, in particular, are used innumerous applications such as microfluidics [3, 4], fiber optics [5]and electronics/substrate heating. In this chapter, for the first time, we demonstrate inkjet printed resistive heaters and resistive temperature detectors specifically designed for biological microfluidic applications.

Many biological applications (Polymerase Chain Reaction (PCR), Sanger sequencing, RT-PCR and other enzymatic reactions, for example) require precise control and stability of temperature, which is demonstrated through integration into a microchip bioprocessor system capable of PCR.PCR will be discussed in detail in Chapter 4. To give context to the printed devices in this chapter, PCR will be briefly introduced here.

PCR is a scientific technique in molecular biology to amplify a single or a few copies of a piece of DNA to generate thousands to millions of copies of the same. The bottleneck in many biological processes is the amount of sample that can be obtained from a patient. To be able to perform all the necessary tests, the amount obtained from a patient is usually not sufficient. This is an example of when PCR becomes useful since it multiplies the amount of DNA from the sample to provide enough for all the analyses.

The PCR method relies on thermal cycling, consisting of cycles of repeated heating and cooling of the PCR mixture made up of DNA, primers, and enzymes. To achieve PCR, it is necessary to provide heaters and temperature detectors to allow for accurate thermal cycling. In collaboration with Professor Richard Mathies' group in University of California, Berkeley, the inkjet printed heaters and RTDs in this chapter are integrated into a microchip bioprocessor system, very similar to the one shown in Figure 30 and used to demonstrate PCR. This figure has been explained in detail in Chapter 1.

The components of this chip that are of interest to this chapter and chapter 4 are shown in the zoomed in version on the right of Figure 30. This is module 1 of the microfluidic system as explained in Chapter 1. In this module, the important components are the PCR chamber, the Ti/Pt heater, and the Ti/Pt RTD. The PCR chamber is directly under the heater and is formed by channels or trenches etched out in glass. The PCR chambers typically have a capacity of 200-250nL and hold the sample during thermal cycling. The heaters (in red) in this figure are made of platinum and have a titanium layer underneath to enable adhesion to glass. Since platinum is an inert metal, it is ideal for use in heaters. The RTDs are shown in green and are also made of platinum with a titanium adhesion layer. Platinum is the most common material for RTDs because of its wide temperature range, accuracy, and stability. The RTDs and heaters are explained in more detail shortly.

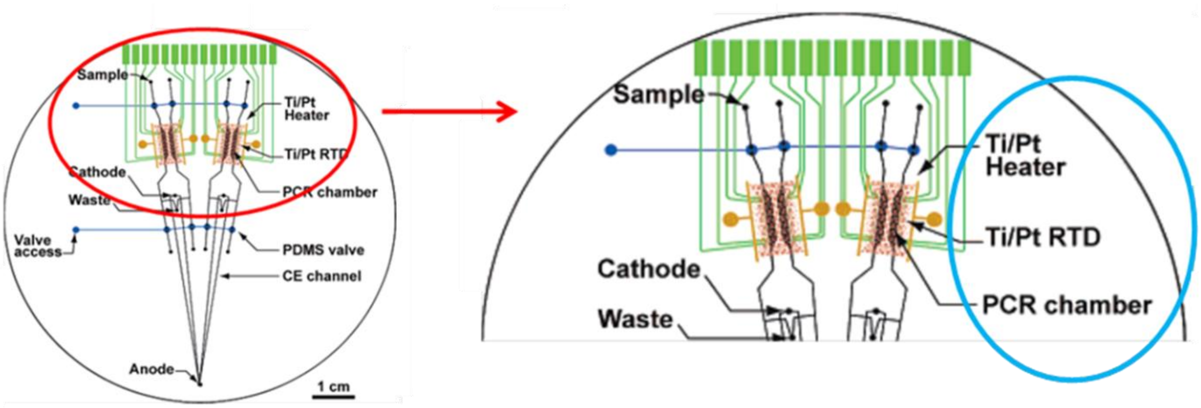

Figure 30. Schematic of a typical microchip bioprocessor system (left) and the section of the chip that is of interest to this chapter (right) [4].

The top view of the bioprocessor chip is seen in Figure 30. The cross section is shown in Figure 31. The basic configuration of a bioprocessor chip contains at least 2 layers of substrates in order to form microfluidic channels. The functioning and efficiency of an LOC system relies on the channels (or trenches that are etched out in the substrate), in which all reactions and processes occur. In other words, a fast (through capillary electrophoresis) and efficient (low volume consumption and no evaporation during thermal cycling) microfluidic system is possible because of the narrow channels that are etched in the substrate. To form the channels, one layer of the substrate contains etched trenches while the other substrate 'closes' the channels to form a leak-free bioprocessor chip capable of electrophoresis. The two substrate layers (shown in Figure 31 as glass layers) are therefore thermally bonded to form channels in the chip before use in a biological microfluidic system. The other devices on this chip (heaters and RTDs) will be explained next.

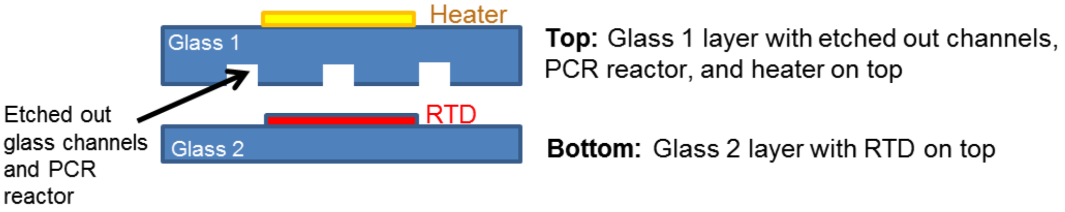

Figure 31. Cross-sectional view of the bioprocessor chip.

An RTD is a temperature sensor that is based on the principle of metal resistance increasing with temperature. In this project, RTDs are used to monitor the temperatures during thermal cycling (done with heaters), a process required for PCR. The temperature must be tightly controlled because the PCR efficiency drops dramatically if the temperature is inaccurate even by a few degrees. For this reason, RTDs are placed as close to the PCR reactor as possible (usually 0.25 – 1 mm away), as seen in the magnified view in Figure 30.

The RTDs (in green) are placed very close to the PCR chamber (in black). In previous work by researchers in Professor Mathies' group, the RTD wafer (glass 2 in Figure 31) was formed using the following process steps. A 0.55-mm-thick borofloat glass wafer is first piranha cleaned. This substrate is then sputter coated with 200 Å of Ti followed by 2000 Å of Pt. Patterns are then lithographically defined and etched using hot aqua regia (3:1 HCl/HNO_3 at 90 °C).

The heaters are photolithographically defined using a similar process. In addition to the process described above, gold leads (good conductor) are patterned on top of the defined Ti/Pt heater pattern using gold plating solution. Lithography and ionmilling are then used to etch the Ti/Pt, resulting in200μm wide Ti/Pt resistive heaters with500μm wide gold leads[4].

The RTD and heater fabrication process described above is typical among most microchip bioprocessor systems capable of PCR. Printed electronics in an effective and efficient system for producing thin film structures needed for biological applications and eliminates the need for the numerous steps described to fabricate the heaters and RTDs. Since printed electronics uses additive processing, the use of masks, photolithography, sputtering, and aquaregia and ionmill etching are all eliminated. Moreover, since the microfluidic chip is constantly evolving for higher throughput and sensitivity, printed electronics allows for flexibility of changing heater and RTD patterns and their placement as and when needed.

This section has thus presented the motivation for using printed electronics for definition of heaters and RTDs for biological microfluidic applications. To implement this, heaters and RTDs will be optimized, printed, and characterized in this chapter. Since the goal is to demonstrate the feasibility of the printed devices by integration into the bioprocessor chip from Mathies group, the dimensions of the RTD and heater will be matched to their chip.

The following section begins with an introduction to inkjet printing, a technique used to print heaters and RTDs in this chapter.

3.2 Inkjet Printing

3.2.1 Ink Jet Printing Process

The inkjet printing process is a computer to print technology in which the desired image is created on the computer and transferred directly to the printer and its imaging unit. The ink is jetted from nozzles to create the desired patterns, which means that no image carrier is needed. The imaging unit is the ink jet system itself, which transfers the ink to the substrate via nozzles, mostly directly or in some applications indirectly depending on the technology used.

Ink Jet printing technology can be split up into two variants, namely continuous ink jet and drop of demand ink jet. The functioning principle of the continuous ink jet system can be summarized using Figure 32.

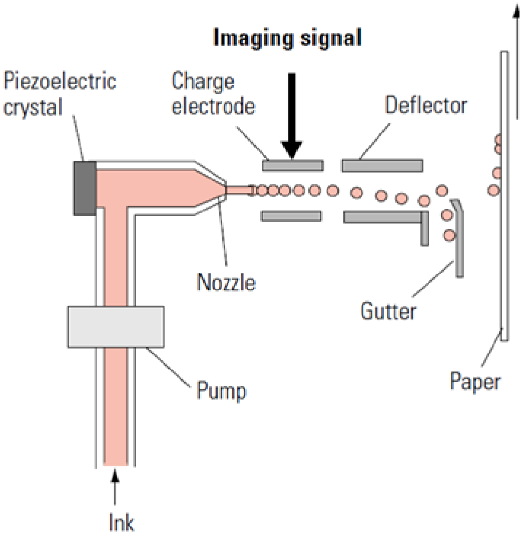

Figure 32. Functioning Principle of Continuous Ink Jet System[6].

In a continuous ink jet system, a high frequency stream of drops (of 1MHz or more) is created as shown in the image above. The pressurized liquid is pressed out of the nozzle. The high frequency excitation via a piezo-oscillator results in the constriction of the stream due to fluid dynamics-related effects and the separation of individual drops from the stream.

The individual drops are electrically charged by an electrode in accordance with the input print image just before separation from the jet. The charged drops are deflected in a subsequent electrical field (plate capacitor, *deflector*) and fed to a collecting device. The uncharged drops reach the substrate (shown as paper in Figure 32) [6].

With drop on demand technology, a drop is only generated if the print image requires it. The drop on demand technology is split up into 3 different systems: thermal ink jet system, piezo ink jet system, and electrostatic ink jet system.

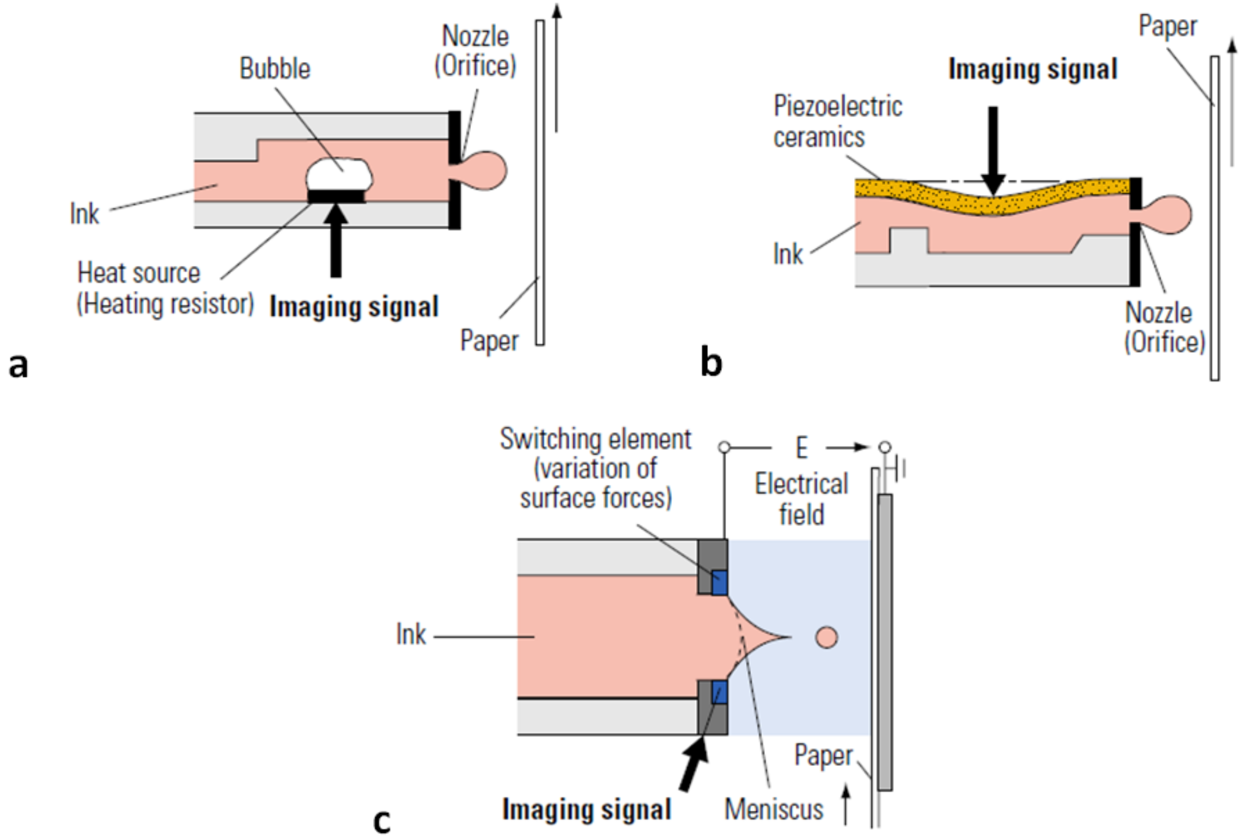

Figure 33. Functioning Principle of Drop on Demand Technology: a) Thermal Ink Jet System , b) Piezo Ink Jet System, and c) Electrostatic Ink Jet System**[6]**.

As shown in Figure 33a, in a thermal ink jet process, the liquid ink is heated up until it vaporizes, thereby creating a vapor bubble inside the ink carrier. The pressure exerted by the vapor bubble squeezes a certain quantity of ink through the nozzle, thereby landing a pattern on the substrate.

In piezo ink jet systems (Figure 33b), the drop is generated as a result of a change of volume within the ink chamber due to mechanical displacements caused by piezoelectric effect. The displacement in the ink channel causes the ejection of an ink drop.

And finally, in an electrostatic ink jet system (Figure 33c), an electric field is generated between the ink jet writing system and the substrate. Ink drops are generated by sending image-dependent control impulses to the nozzles. These impulses cause a drop to be released and routed through the electric field onto the substrate [6].

The Dimatix Fujifilm ink jet printer used to print the heaters and RTDs in this chapter utilizes the drop on demand piezo jet printing system. The Dimatix printer is discussed in more detail in the following section.

3.2.2 Dimatix Inkjet Printer

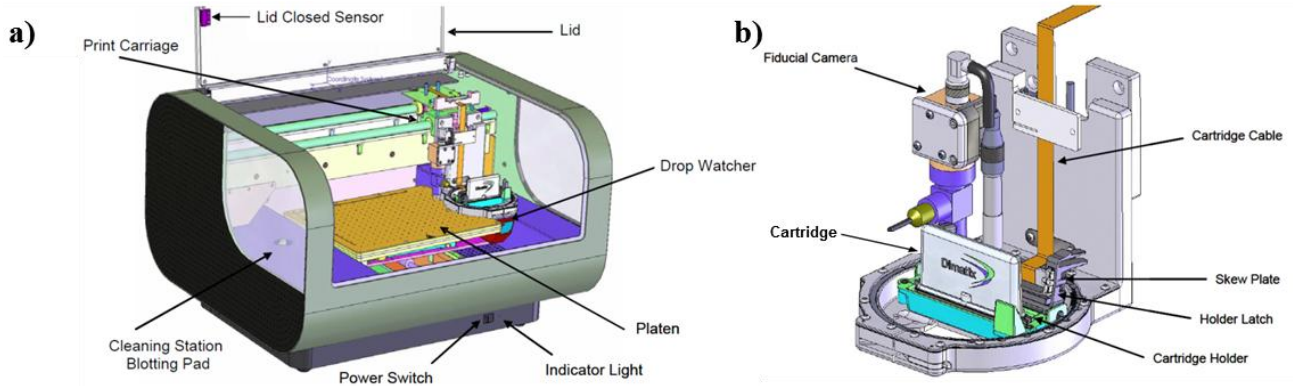

Figure 34. Image of the a) Dimatix DMP-2800 Series Printer and b) The print cartridge and holder**[7]**.

The Dimatix DMP-2800 series printer (shown in Figure 34a) is a commercial research inkjet printer that allows the deposition of fluidic materials on an 8x11 inch or A4 *platen*/chuck (indicated in Figure 34a), utilizing a disposable piezoinkjet print cartridge (indicated in Figure 34b). This printer can create and define patterns over an area of about 200 x 300 mm and handle substrates up to 25 mm thick. The temperature of the vacuum platen, which secures the substrate in place, can be adjusted to heat to 60°C.

Additionally, a waveform editor and a drop-watch camera system allows manipulation of the electronic pulses to the piezo jetting device for optimization of the drop characteristics as it is ejected from the nozzle. A fiducial camera allows for good alignment of the substrate on the platen. There is a built-in cleaning station with a program editor that includes an automatic capping mechanism. This system thereby enables easy printing of structures and samples for process verification and prototype creation.

The print cartridge is available in 2 nozzle sizes. The 10pL drop volume nozzles provide for slightly wider lines, but it is easier to unclog the nozzles during prints, especially after storage. The 1pL drop volume nozzles provide for finer lines, but it is harder to unclog and manage the cartridge and the ink, especially after multiple prints. *For this project, 10pL drop volume nozzles were used throughout.*

The input pattern file to the printer can be in the inbuilt pattern editor software format or a bitmap or gerber format. The heaters and RTD pattern in this project were drawn using outside software and sent to the printer in a .bmp format. *Each pixel in the drawing represents a dot or a drop on the substrate.* The dimensions of the pattern are adjusted accordingly. More information about the different features of the Dimatix printer can be found in the Dimatix Fujifilm Printer Manual [7].

In order to achieve optimum performance with the Dimatix, some physical characteristics of the ink are defined. The viscosity of the ink needs to be 10-12 centipoise (cP) at jetting temperature, the surface tension of the ink is recommended to be between 28-33 dynes at jetting temperature, and boiling point of the ink is to be higher than 100^{o}C.

In addition to optimal ink properties, three other parameters within the Dimatix printer contribute towards a good print, namely drop spacing, print height and drop velocity. The definition and optimization of these parameters are presented in the following section, which begins by discussing the ink and substrate used for printing heaters and RTDs.

3.3 Optimizing Print of Gold Lines on Glass

3.3.1 Materials: Substrate and Ink

Since the heaters and RTDs in this project are being designed for use in biological applications, the ink material and substrate used for printing need to be compatible for this application. To begin with, new research reveals many new substrates emerging for biological microfluidics. For instance, DeSimone et al, in collaboration with Quake et al, has developed a class of silicones called photocurable perfluoropolyethers (PFPEs) [8]. PFPEs are fluoropolymers that are liquids at room temperature and can be easily photocured into microfabricated devices. PFPE exhibits low modulus, high gas permeability, low toxicity, and most importantly, high chemical resistance to acids, bases, and organic solvents. Chong Ahn at the University of Cincinnati has developed several microfluidic devices with a thermoplastic polymer called cyclicolefin copolymer (COC) [9], used for its low porosity, hydrophobicity, and ability to go through physiochemical property changes. Many others follow this list of new materials including thermoset polyester (TPE) [10], and hybrid materials [11, 12, 13]. But the two most popular substrates continue to be glass and PDMS.

Both glass and PDMS have their advantages and disadvantages. For example, using PDMS molds to make microfluidic channels is much easier than making channels in glass using photolithography and hydrofluoric acid. Other benefits of PDMS include its elastic properties (to make valves for example) and its ease of availability and disposability. But in many experts' opinions, glass is better because it does not possess the disadvantages of PDMS, many of which are crucial to biological processes. Some of these disadvantages include absorption of (and therefore swelling due to) organic solvents and small molecules, innate hydrophobicity (making osmotic and electrophoretic flow of fluids more difficult), translucent properties (not as transparent as glass), innate fluorescence, and high porosity. The transparency and innate fluorescence poses a problem during laser detection and final characterization steps. The porosity becomes a problem during thermal cycling processes and electrophoretic applications since it leads to evaporation of reagents. To utilize the advantages of both PDMS and glass, Mathies et al. use a hybrid of glass and PDMS in their microfluidic chips [3, 4].

For the purposes of this project, glass substrates best served the application, especially in terms of porosity and transparency. The glass substrates used for printing of heaters and RTDs are borofloat glass wafers from Precision Glass and Optics (PG&O), which are 0.5mm in thickness and 100mm in diameter [14].

In arriving at the best conductive ink material for heaters and RTDs, two conditions had to be met. The material had to be an inert metal that was nonreactive to solutions used in biological applications. In addition, because it will be used for thermal applications, the material could not oxidize at high temperatures. Two metals that fit this profile were gold and platinum. Gold was picked because gold nanoparticle ink has been previously studied in our group on silicon and plastic substrates.

Metal nanoparticles allow for printable metal inks because nanoparticles are able to solubilize in a solvent, converting the metal into a ‘liquid’ or ink form. Nanoparticles are usually encapsulated by ligands or dispersants that adhere to the nanoparticles. These ligands are soluble in solvents that hold the nanoparticles together in ink form. When annealed at a certain temperature, the solvent and the ligands evaporate, the nanoparticles fuse together, and essentially, a metal thin film is left behind. The metal in this form has thin-film like characteristics with high conductivity. The process described above is illustrated in Figure 35.

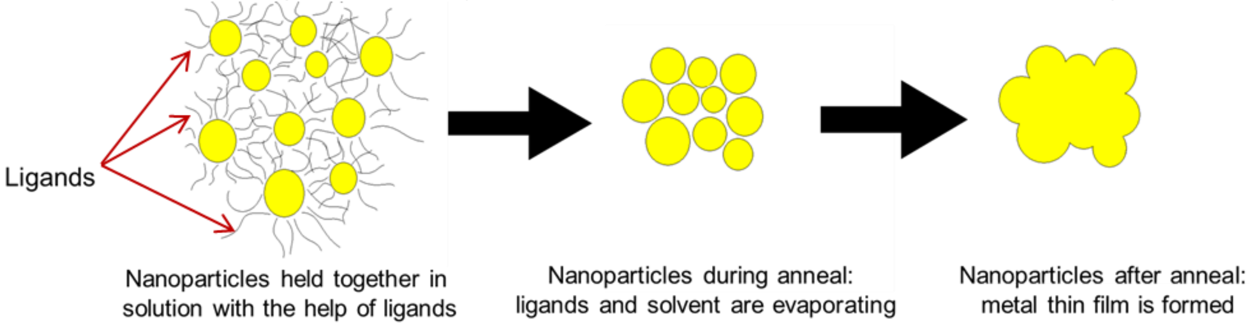

Nanoparticles held together in solution with the help of ligands

Nanoparticles during anneal: ligands and solvent are evaporating

Nanoparticles after anneal: metal thin film is formed

Figure 35. The process of printable metal nanoparticle inks transforming into a metal thin film.

Moreover, small particle size (nm) significantly reduces the melting temperature of nanoparticles from the bulk melting point, allowing for low processing temperatures for sintering nanoparticles into conducting films[15].

The conductive ink used for this project is a gold nanopaste called NPG-J, made by Harimatec, Inc. NPG-J is a nanoparticle based ink that is composed of 2-6nm sized nanoparticles, has a viscosity of 5-10cPs, cures/anneals at 230-250^{o}C for 1 hour, and has specific resistivity of 7μOhm-cm after annealing.

The substrate and ink for this project have thus been finalized. Optimization of the substrate surface and print parameters are discussed in the following sections.

3.3.2 Optimizing Substrate Surface

Before printing patterns such as heaters and RTDs, the first step is to be able to print controllable drops/dots and continuous and smooth lines on a given substrate. A combination of optimizing the substrate treatment conditions and the print parameters helps achieve this goal.

Printing an ink on a substrate requires optimization because the cleanliness of the surface contributes to pinning of the ink, and the surface energy of the substrate determines the contact angle that the ink forms with the substrate. Both of these parameters are critical in arriving at good pattern formation. Therefore, various cleaning treatments were investigated on the borofloat glass substrate to arrive at the optimum surface energy and cleanliness; the treatments and the consequent results are shown in Figure 36. Each of these treatments is known to result in different combinations of surface pinning and surface energy; the goal is to arrive at an ideal combination for the borofloat glass substrate and the NPG-J gold ink.

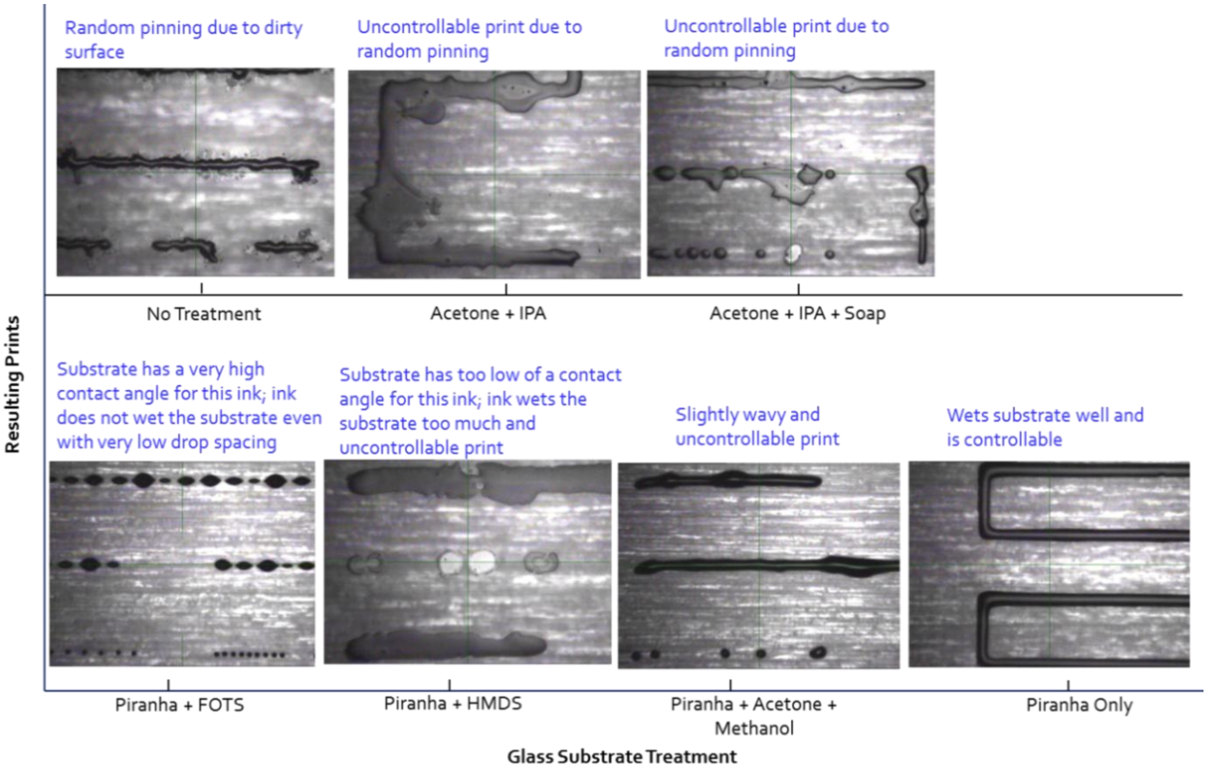

Figure 36. Printing Results after different substrate treatments and cleans.

As seen in Figure 36, when the gold ink (NPG-J) is printed on the substrate without any treatment, random pinning and 'webbing' occurs right around the patterns because the surface contains organic and atmospheric contaminants that have not been removed. The ink spreads and pins at random spots around the pattern. The Acetone+IPA and the Acetone+IPA+Soap cleans have removed the organic contaminants. Since the webbing pattern from the 'no treatment' case has disappeared, this indicates a cleaner surface. The random pinning and spreading still seen here indicate that the appropriate surface energy has not yet been achieved for the ink. Acetone, IPA, and water-based soap are all known to make the surface more hydrophilic (decrease contact angle for water-based solvents/inks), and the gold ink (not water-based) does not form good prints with the surface energy created by these cleans.

FOTS (fluoroctatrichlorosilane) and HMDS (hexamethyldisilazane) treatments are known to make a surface more hydrophobic (increase contact angle for water based inks/solvents).Glass, as is, has a contact angle of about 20-30^{o} with water. A typical HMDS recipe yields a contact angle of 65-75 ^{o}, while a typical FOTS recipe results in a contact angle of 110 ^{o} for water on $SiO_2$and glass (amorphous SiO_2) substrates[16]. Piranha solution ($H_2SO_4 + H_2O_2$) is used to make glass surface more hydrophilic by hydroxylating the surface, thus increasing the number of silanol groups. The Piranha+FOTS clean provides a surface that forms too high of a contact angle for the gold ink. Therefore, even with very low drop spacing, a line could not be formed. The contact angle formed by the gold ink on the Piranha + HMDS treated surface is too low because the ink spreads too much on the surface. The Piranha + Acetone + Methanol clean helps the ink form a good contact angle on the surface, but there is still some random pinning because the surface is not clean enough yet.

Finally, the piranha clean leaves a surface energy that is appropriate for the gold ink. Continuous, smooth lines are formed as seen in Figure 36.

Since the ink is commercially bought, the ink wetting properties are slightly different between batches. Depending on the batch of ink, sometimes an additional 10 minutes of UV-Ozone (UVO) treatment [17, 18] is required after the piranha clean to get a good print.

Having thus optimized the substrate treatment conditions for a good print, the next step is to optimize the print parameters that were mentioned earlier.

3.3.3 Optimizing Print Parameters

Three important print parameters that contribute towards a good, stable print are drop spacing, drop velocity, and print height. The following optimization experiment was done on piranha treated borofloat glass substrate using gold NPG-J ink and was printed at room temperature.

Drop spacing is defined as the center to center distance from one drop to the next. The actual value for this drop spacing is defined and optimized based on the ink, the pattern, and the substrate properties. The drop spacing in the following experiment was varied from 25μm - 40μm. The resulting prints on the borofloat glass substrate are shown in Figure 37.

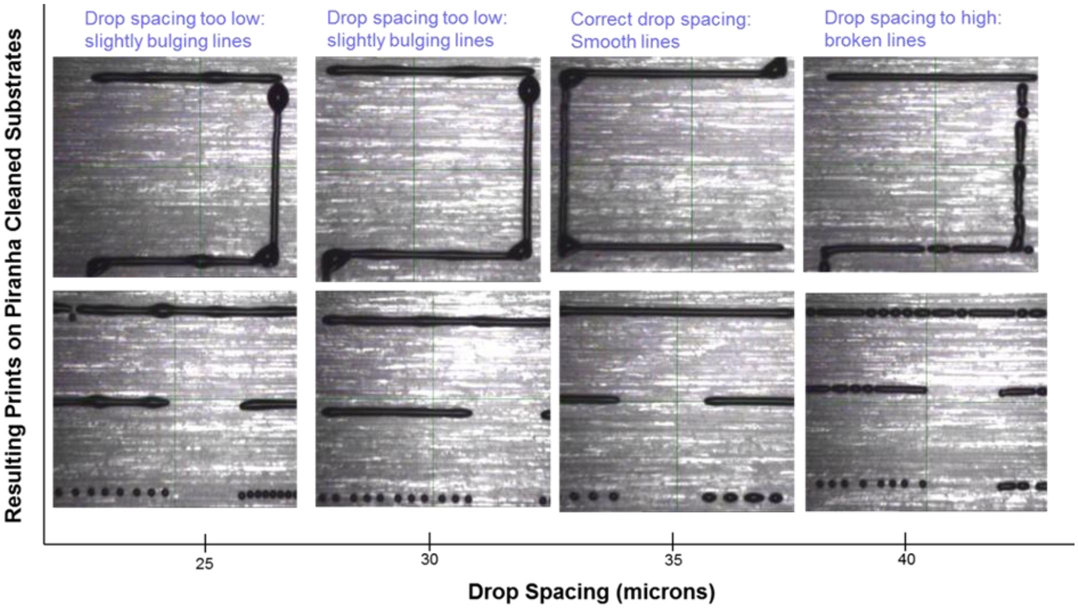

Figure 37. Drop Spacing (print parameter 1) varied and optimized to achieve smooth lines.

The stability of ink jet printed lines and inkjet printed line morphologies have been studied previously by Duineveld[19] and Soltman et al [20], explaining the bulging lines, individual drops, and stable lines seen in Figure 37. To summarize, if the drop spacing is too high (40μm spacing or higher in this case), the drops are printed too far apart to interact to form a smooth line. Therefore, they stay and dry as individual drops (or broken lines in this case). Printing the drops too close together (30μm spacing or lower in these prints) causes bulges in the printed lines. When drops are printed too close together, excess fluid and volume result in a given printed area. This additional volume exceeds a drop's equilibrium contact angle, and regions of outflow in the lines create rounded bulges in the printed line. Finally, the narrowest, smooth, straight lines are printed when the equilibrium contact angle is reached for each drop and they are printed close enough to interact with each other. *This occurs for NPG-J gold ink and glass substrate at 35 μm drop spacing.* Duineveld[19] and Soltman et al [20] explain the discussed printed line behavior further using mathematical and analytical models in their publications.

To characterize and quantify drop spacing further, line edge roughness (LER) measurements and resistance values were recorded. LER results in Figure 38 quantify the prints in Figure 37.

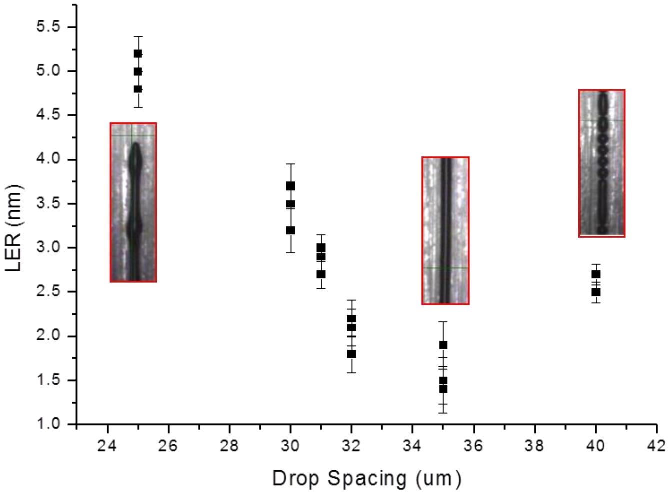

Figure 38. Line Edge Roughness measurements of gold inkjet prints with different drop spacing.

LER was calculated using SuMMIT LER (a software program for determining line quality from captured images) to detect the edges of each line in their entirety to calculate how 'smooth' or 'rough' the line is. The higher the LER value, the 'rougher' and more non-ideal the line is. As seen above, the LER is high at lower drop spacing due to the bulges. As the ideal drop spacing is reached, the LER is at its lowest valve. At the other end of the spectrum, individual drops created by higher drop spacing increase the LER again. LER is therefore a good metric of the stability of a printed line. The goal is to optimize the drop spacing and other parameters to achieve lowest LER.

To electrically characterize the lines as a function of drop spacing, resistance measurements were collected. The measurements and the best fit line are shown in Figure 39.

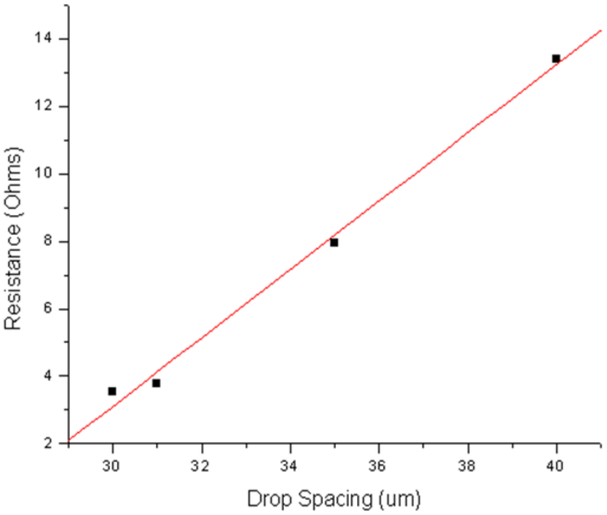

Figure 39. Resistance measurements of inkjet printed gold lines as a function of drop spacing.

The resistance measurements for this print parameter were done using four-point probe structures. Moreover, the resistance measurements were performed after printing the NPG-J gold ink on the borofloat glass substrate, and annealing it for 1 hour at 250 ^{o}C.

To explain Figure 39, lower drop spacing (< 35µm drop spacing) leads to more ink volume (metal film when annealed) in a given area. The line is especially wider in certain places because of bulges. This lowers the overall resistance as seen in Figure 39. As the line gets smooth and narrow at 35µm spacing, the resistance slightly increases. With too high of a drop spacing (40µm or higher), the broken lines contribute towards an even higher resistance. At a certain drop spacing where the lines become discreet individual drops, the resistance will go towards infinity since there will be no current flowing through the line.

Drop velocity is defined as the velocity/speed at which the ink travels to the substrate during printing. This is calculated using the drop watcher camera nozzle image, an example of which is shown in Figure 40. The formula used to calculate drop velocity is:

$$\textbf{Drop Velocity (m/s)} = \frac{\textbf{[Distance between the nozzle and the `end of the drop']}(\mu m)}{\textbf{[strobe delay]}(\mu s)}$$

Each of the components in this equation is labeled and defined in Figure 40. The stability of a drop landing on the substrate is dependent on a well-tuned drop velocity for a given ink, substrate, and pattern.

For the NPG-J gold ink and borofloat glass substrate used in this project, *the prints and the LER measurements performed (shown in Figure 41) helped conclude that a drop velocity between 8 and 9 m/s gave the best print.* The LER was at its lowest value, and when printed along with the optimized drop velocity and print height, the lines were smooth and stable.

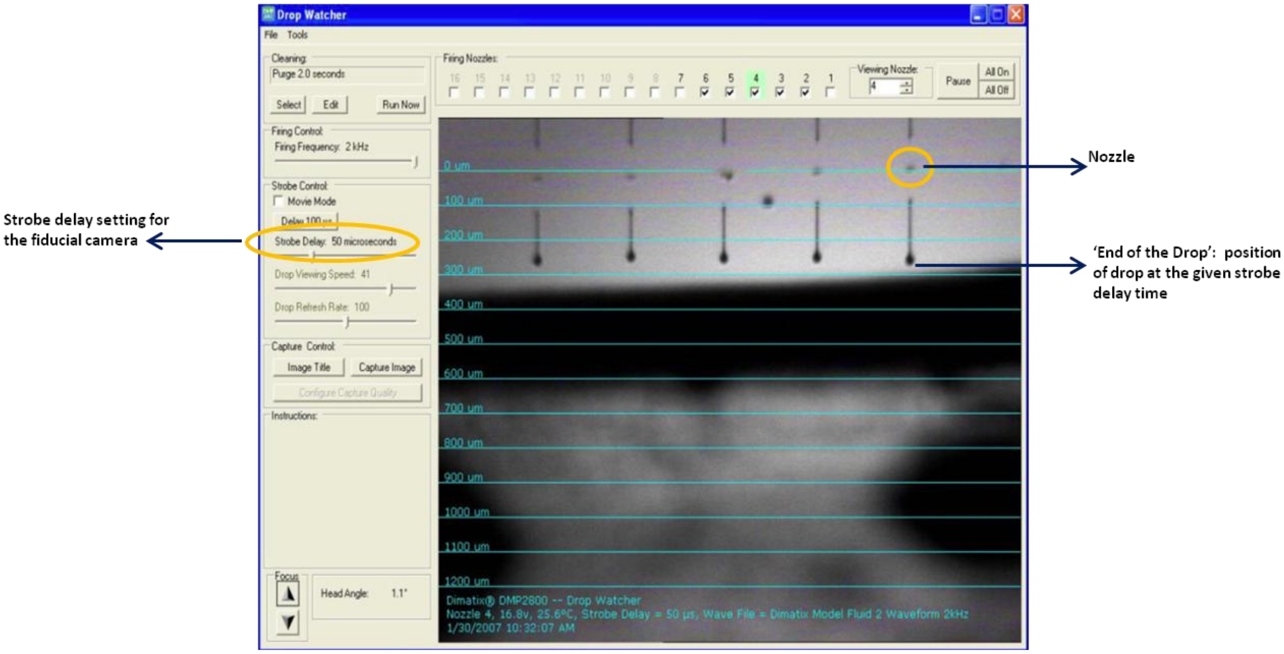

Purge 2.0 seconds

Firing Frequency: 2 kHz

Strobe Delay: 50 microseconds

Drop Viewing Speed: 41

Drop Refresh Rate: 100

Head Angle: 1.1°

Viewing Nozzle: 4

Dimatix® DMP2800 -- Drop Watcher
Nozzle 4, 16.8v, 25.6°C, Strobe Delay = 50 µs, Wave File = Dimatix Model Fluid 2 Waveform 2kHz
1/30/2007 10:32:07 AM

Strobe delay setting for the fiducial camera

Nozzle

'End of the Drop': position of drop at the given strobe delay time

Figure 40. Drop Watcher image serves to show how drop velocity is calculated [2]

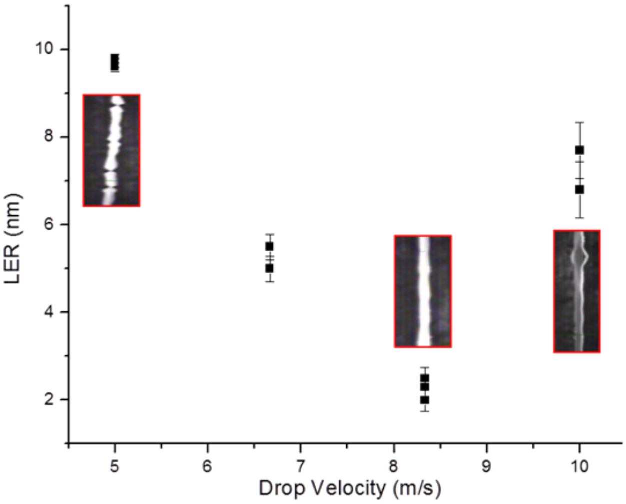

Figure 41. LER Measurements of gold inkjet printed lines performed to obtain optimum drop velocity.

The last print parameter of interest is print height. Print height sets the distance of the printhead above the substrate during printing. It can be adjusted from .250 mm to 1.50 mm. The substrate thickness and cartridge print height needs to be set accurately. If the cartridge is too close to the substrate, it can hit/drag the substrate and/or drag patterns during printing. An example of this occurrence from prints in this project is shown in Figure 42. Alternatively, the farther the distance from the cartridge to the substrate, the less accurate the landing of the drop becomes in terms of the position of landing. This can be explained in terms of the angular spread of ejection. Angular spread of ejection determines the area on the substrate where a drop has the highest probability of landing. Ideally, this area would be as small as possible so that the desired print pattern is maintained. As the distance from the cartridge to the substrate increases, the angular spread of ejection also increases, thereby increasing the area around the desired spot where a drop could land. This increases the probability of inaccurate prints. The print height was set at its maximum in Figure 43, showing that sometimes inaccurate landing of drops occur because of the wrong print height setting.

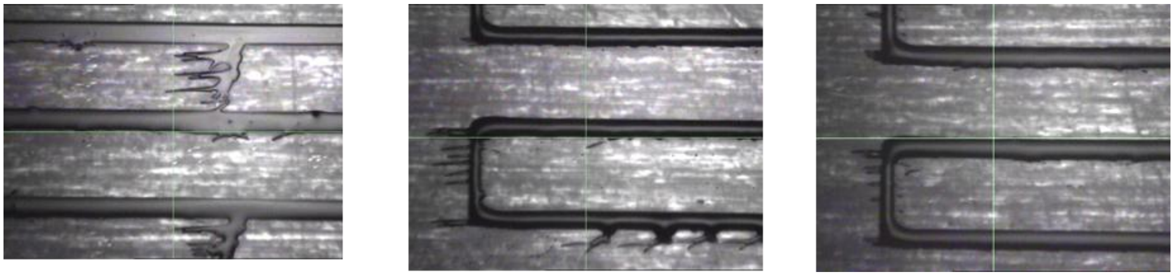

Figure 42. Dragged prints caused as a result of low print height.

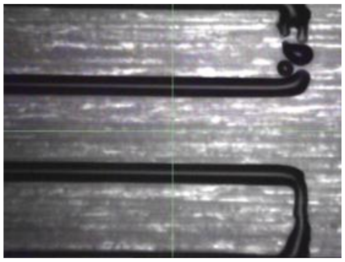

Figure 43. Inaccurate landing of drops in a pattern due to increased print height.

As with the other two print parameters, print height also needs to be tuned every time a new substrate, pattern, and/or ink are used. The rule of thumb is to have the print height as low as possible without creating the dragged patterns and yet getting the most accurate prints possible. *The optimum print height for the substrate and ink in this project is between 0.95 and 1mm.*

In addition, vertical and horizontal profile measurements of the printed gold lines on borofloat glass were conducted using the Tensor Alpha Step 200 Profilometer. The features measured were printed using 1 pixel wide lines. The Dimatix inkjet printer's raster pattern is only in the +/- X direction. In other words if a vertical line needs to be printed, the printer would raster in the +/- X direction as many times as needed to make the vertical line of desired length. The height and width profile of the printed gold lines in the direction of the rastering (+/- X direction) and perpendicular to the direction of rastering is shown in Figure 44 and Figure 45, respectively.

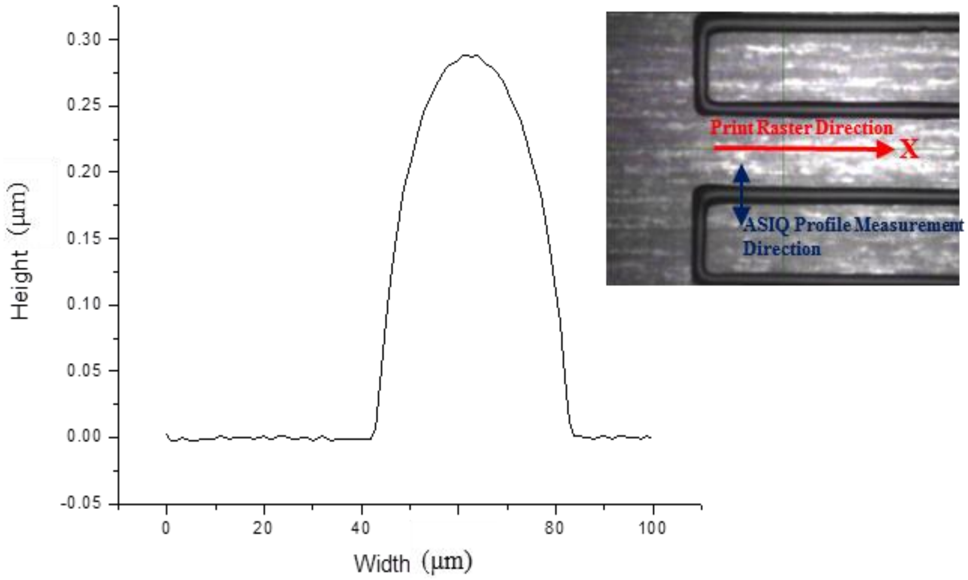

Figure 44. Height and Width profiles of gold lines printed in the direction of rastering.

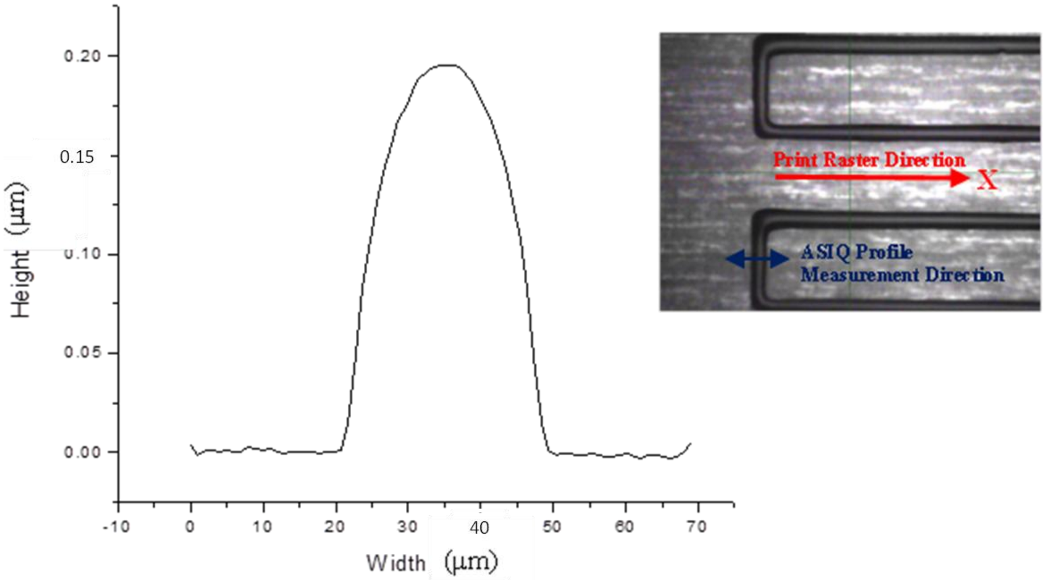

Figure 45. Height and Width profile of gold lines printed perpendicular to the direction of rastering.

The gold line that is printed in the printer rastering direction (Figure 44) has a higher width and taller feature than that printed perpendicular to the rastering direction (Figure 45). The expected profile for Figure 45 is a lower width and a taller feature. Since the direction of the print is perpendicular to the line, when each drop in a vertical line is printed, the drop dries a little before the next drop is printed and before the interaction between the two drops happens. During this time, each drop dewets a little before the next drop is printed, thereby creating a narrower and taller line. In Figure 45, although the width is smaller, the feature is shorter because of the particular print pattern that was measured, which was a serpentine (snake shaped) pattern. The corners of the serpentine pattern pull in some of the ink from the vertical line. A combination of equilibrium contact angle and surface energy minimization creates this effect [21]. This will be discussed further in the next few sections.

Moreover, in most inkjet prints that use low viscosity inks, a coffee ring pattern [20] is visible. With one pixel wide line patterns, sometimes, the coffee ring effect is not seen with the Harima gold ink, likely due to the solvent formulation used in the ink.

In this section, important factors have been defined and optimized. To summarize, a good stable print can be made with piranha cleaned (with ~10 minutes of UVO as needed) borofloat glass substrates, ink drop spacing of 35μm, print speed of 8-9m/s, and a print height between 0.95 and 1mm. The next step is to determine the optimum pattern for the heaters and RTDs. The dimensions and pattern for the RTD have been pre-determined by the position of the PCR chamber in Mathies group's bioprocessor chip. The 4-point probe structure used for the RTDs will be explained later in this chapter. While the heater dimensions correlate with the size of the PCR chamber on the microfluidic chip, the pattern has not yet been finalized. Therefore, the following section optimizes the heater pattern using simulation based design.

3.4 Design of Heaters

Designing an optimum heater pattern is important for biological applications since precise control of heating is required during PCR. In particular, the optimum heater pattern for biological microfluidic applications will have the lowest temperature gradient in order to achieve uniform heating. Since PCR efficiency drops with the slightest change in temperature, uniform heating ensures that the temperature is uniform across all parts of the PCR chamber. In addition, the ideal heater pattern would also have the highest temperature differential (and power output) given the lowest input voltage. Finally, keeping the design simple ensures the printability of the pattern with minimum print inconsistencies.

In order to arrive at a design that meets all the criteria, simulation-based design was utilized. Simulation-based design (SBD) is an efficient way of testing various designs simultaneously to meet the desired criteria. Since SBD uses first-principle-based simulations of underlying multiphysics phenomena in the heater designs, it is accurate and deterministic. In other words, once a simulated design is finalized and implemented, the experimental results can be expected to be very similar to the simulated results if not identical. In addition, SBD also saves time and cost since it is an efficient way of comprehensively studying numerous designs. Especially when combined with a prior knowledge of heater designs from literature sources, SBD can be a powerful method to arrive at an optimum heater design.

Therefore, in this section, the heater pattern is designed using COMSOL, a simulation tool that is based on finite element method calculations.

3.4.1 Introduction to COMSOL

COMSOL Multiphysics is an interactive environment for modeling and solving scientific and engineering problems based on partial differential equations (PDEs) and multiphysics models. COMSOL allows the user to define physical quantities such as material properties, and relevant equations are automatically extracted. A set of PDEs are then internally compiled to represent and solve the model generated from a given problem.

When solving models, COMSOL uses the proven *finite element method (FEM)*. The software runs the finite element analysis together with adaptive meshing and error control using a variety of numerical solvers. A more detailed description of this mathematical and numerical foundation can be found in the *COMSOL Multiphysics User's Guide* [22] and in the *COMSOL Multiphysics Modeling Guide*[23].

COMSOL includes built-in modules for many real-world applications. The COMSOL version used for this project contains the following modules: AC/DC, Acoustics, Chemical Engineering, Earth Science, Heat Transfer, MEMS, RF and Structural Mechanics. For the simulation of heaters, COMSOL uses AC/DC, Heat Transfer, and Structure Mechanics modules. These modules and their corresponding sub-modules (known as modes) will be explained below.

1) <u>AC/DC Module: Conductive Media DC</u>

The AC/DC Module provides for simulation of AC/DC electromagnetics in 2D and 3D. With this module, static, quasi-static, transient, and time-harmonic simulations can be run in an easy-to-use graphical user interface. Material properties of inhomogeneous and fully anisotropic materials, media with gains or losses, and complex-valued material properties can be entered as inputs into the module. In addition to the standard COMSOL postprocessing features, the AC/DC Module supports direct computation of lumped parameters such as capacitances and inductances as well as electromagnetic forces and torques. Using as a basis, a set of fundamental equations, namely Maxwell's equations, current continuity equation, and appropriate boundary conditions for voltage and other important parameters, COMSOL creates a set of PDEs for a given problem and arrives at a solution.

In particular, the conductive media DC mode uses Ohm's law along with the fundamental equations already discussed and allows for definition of voltage, current, and/or resistance for 3D, 2D in-plane, and 2D axisymmetric models. For the simulation of microfluidic heaters, this module helps define the input voltage for the heaters and allows the user to view profiles of electric field, current density, and resistive heating trends in a heater pattern as a function of input parameters.

2) <u>Heat Transfer Module: General Heat Transfer</u>

Heat transfer is defined as the movement of energy due to a temperature difference. It is characterized by the following three mechanisms: conduction, convective heat transfer, and radiation. Conduction is heat transfer by diffusion in a stationary medium due to a temperature gradient. The medium can be a solid or a fluid. Convective heat transfer is when heat is transported by a fluid motion. Radiation is heat transfer via electromagnetic waves between two surfaces [23].

The Heat Transfer Module supports all fundamental mechanisms of heat transfer, including *conductive*, *convective*, and *radiative* heat transfer. Among the different modes available within this module [22, 23], the general heat transfer mode used for the simulation of the heaters uses the fundamental equations from the three mechanisms of heat transfer to simulate the model. Since the heaters are intended for biological applications, uniform heating is critical to conduct a stable biological reaction. This module allows for understanding of trends of temperature, temperature gradients, heat flux, and thermal conductivity of the microfluidic heater to help with optimization of the pattern.

3) The Structural Mechanics Module: Solid Stress-Strain & Shell

The Structural Mechanics Module solves problems in structural mechanics and solid mechanics. This module analyzes stress-strain relationships for 2D and 3D geometries. The shell and solid stress and strain modes in particular track stress, strain, traction, rotation, and displacements in all directions of the models.

Although more critical to the simulation of valves (explained further in Chapter 5), the use of this module for the heaters is to track any deformation, cracking, or delamination that might occur as a result of heating. For the desired biological application, a range of 25-100°C is sufficient, and the deformation that the simulation predicts for this range is not significant or problematic.

COMSOL uses the discussed modules in arriving at an optimum pattern for the heaters. The simulations results will be presented in the following section.

3.4.2 Finalizing Heater Pattern Design

The optimum heater pattern for the desired biological microfluidic application will have the highest temperature differential (and power output) given the lowest input voltage, and also have the lowest temperature gradient in order to achieve uniform heating. Also, keeping the design simple ensures the printability of the pattern with minimum print inconsistencies. Different designs were considered and simulated, some from literature [4, 24, 25, 26], and some that were created keeping in mind the optimum criteria of simple design, low voltage requirement, high temperature differential, and a low temperature gradient. The choices were narrowed down using simulations and calculations, and the designs and the COMSOL simulation results of the three final patterns are discussed in this section.

COMSOL Simulation of the Final Patterns

The schematics of the three final patterns are shown in Figure 46.

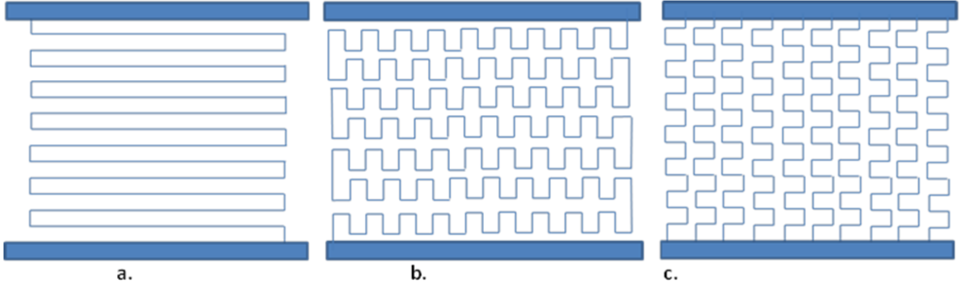

Figure 46. Schematics of final designs: **a.** Design 1: 'Long Snake', **b.** Design 2: 'Snakes within Long Snake', **c.** Design 3: 'Multiple Vertically Parallel Snakes.'

To narrow it down further to the optimum design, COMSOL simulations were analyzed to understand the voltage requirements and temperature gradients.

To set up the problem, the substrate was specified as silica glass; COMSOL's inbuilt library has all the material properties needed for this substrate to perform a valid simulation. These material properties were verified to match those of the borofloat glass wafers from PG&O. A glass substrate thickness of 0.5mm was also specified in the simulation.

The heater device dimensions of ~13.5mm by 9mm were also maintained in the simulation. The above mentioned heater dimensions ensures the coverage of the entire biological polymerase chain reaction (PCR) reactor for which the heater will be used. The heater pattern itself was drawn according to scale. From Figure 44 and Figure 45, the dimension of a single pixel line was measured to be about 40μm wide and ~0.5 μm thick. These parameters were entered as inputs into the simulation. Moreover, material, thermal, and physical properties of gold were entered into the COMSOL simulation for all parts of the heater pattern. The horizontal and vertical spacing in the serpentine patterns and other parts of the heater were optimized and will be discussed in the next section. The spacing parameter was also specified to match the experimentally measured spacing between the serpentine patterns.

The dimensions and parameters discussed above are illustrated in Figure 47, using a screen shot of the 'draw mode' in COMSOL with one of the heater patterns.

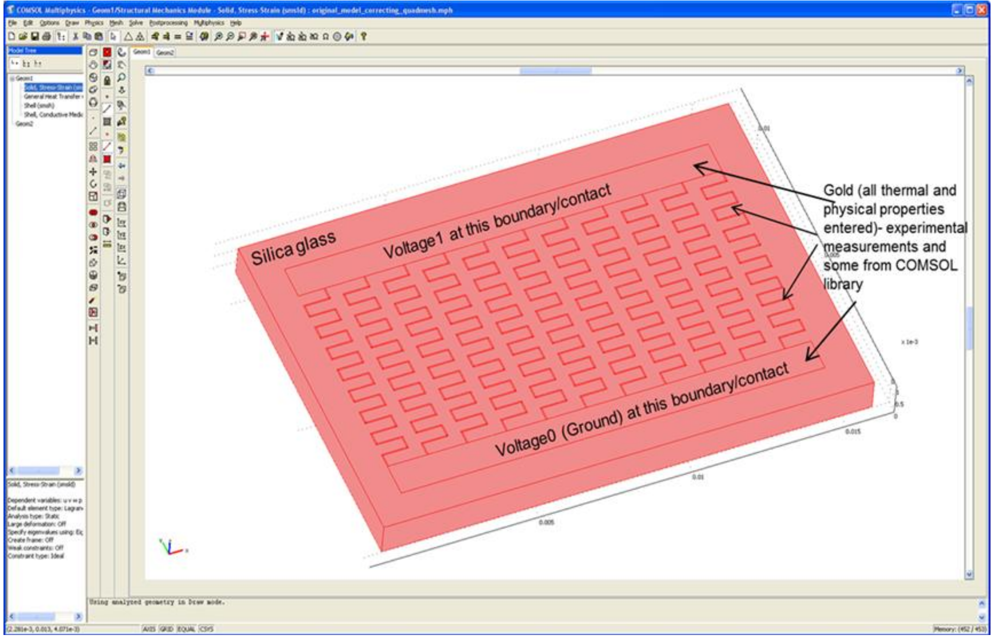

```
Using analyzed geometry in Draw mode.
```

Figure 47. Setup of the heater model in COMSOL.

The heater pattern was defined with current continuity conditions at the boundaries and subdomain, and the voltage was specified at the contacts. The silica glass was defined as an electrical insulator with relevant thermal parameters. Using adaptive meshing, error control, PDEs, heater pattern and parameters, and voltage inputs at the contacts/boundaries, COMSOL solves the model. Temperature and temperature gradients are studied as outputs in order to arrive at an optimum heater pattern.

A temperature gradient is a change in temperature as a function of distance and is expressed in units of degrees per unit length (Kelvin/meter). It helps quantify heating uniformity across a heater pattern. The simulation results of the optimized version of each of the three final patterns are shown in the next three figures. Optimizing each of the patterns means that the spacing between and within the serpentine structures in each of the designs is minimized for lowest temperature gradient (discussed in section 3.4.3). In all simulations, 2 pixel wide lines (80μm line width) were used. The next three pages (Figure 48, Figure 49, and Figure 50) present the simulation results of the three final designs. In particular, the temperature and the temperature gradient profiles show the uniformity of heating in all three designs.

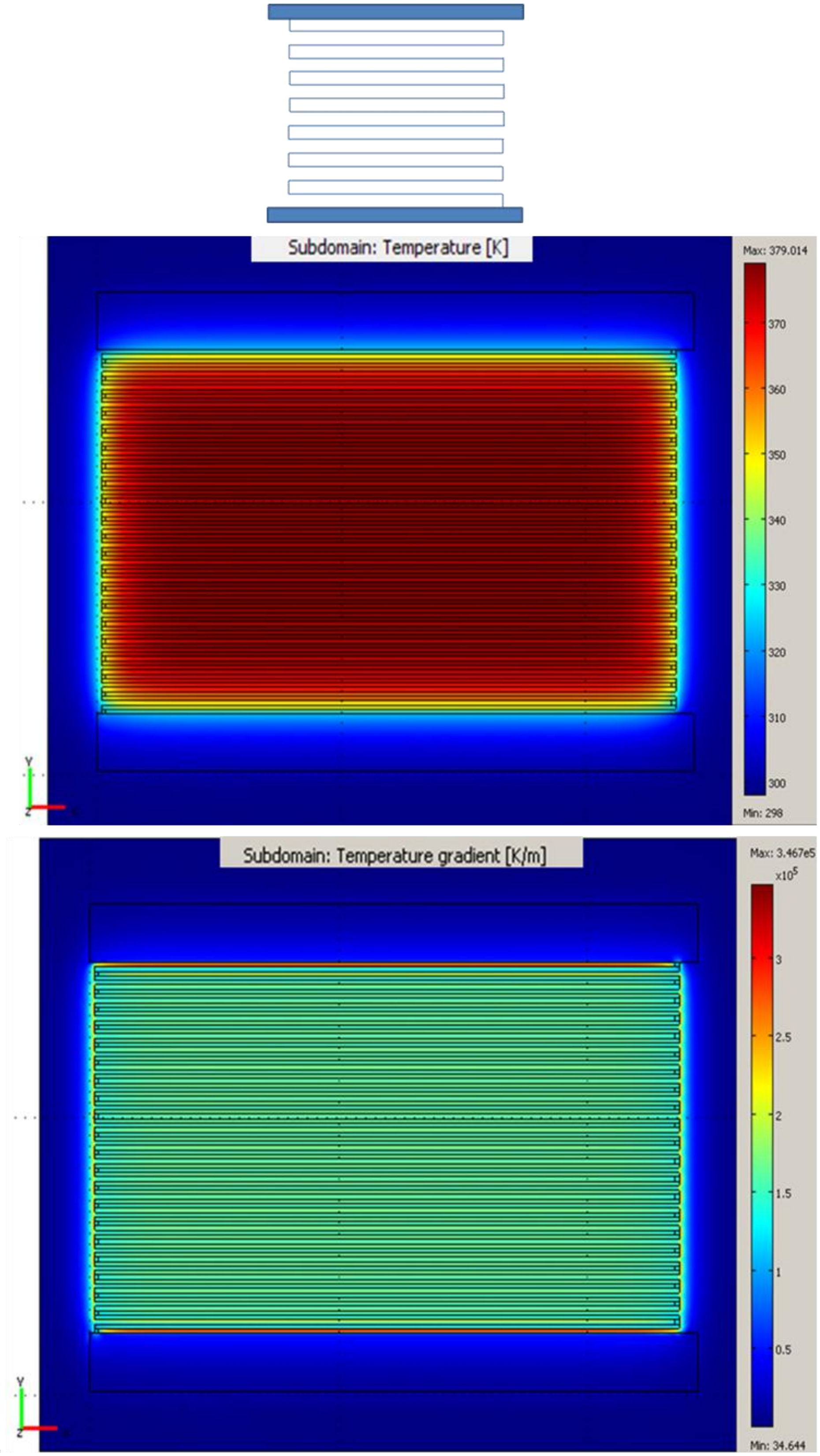

Figure 48. Temperature and Temperature Gradient Profiles obtained from COMSOL Simulation for Design 1.

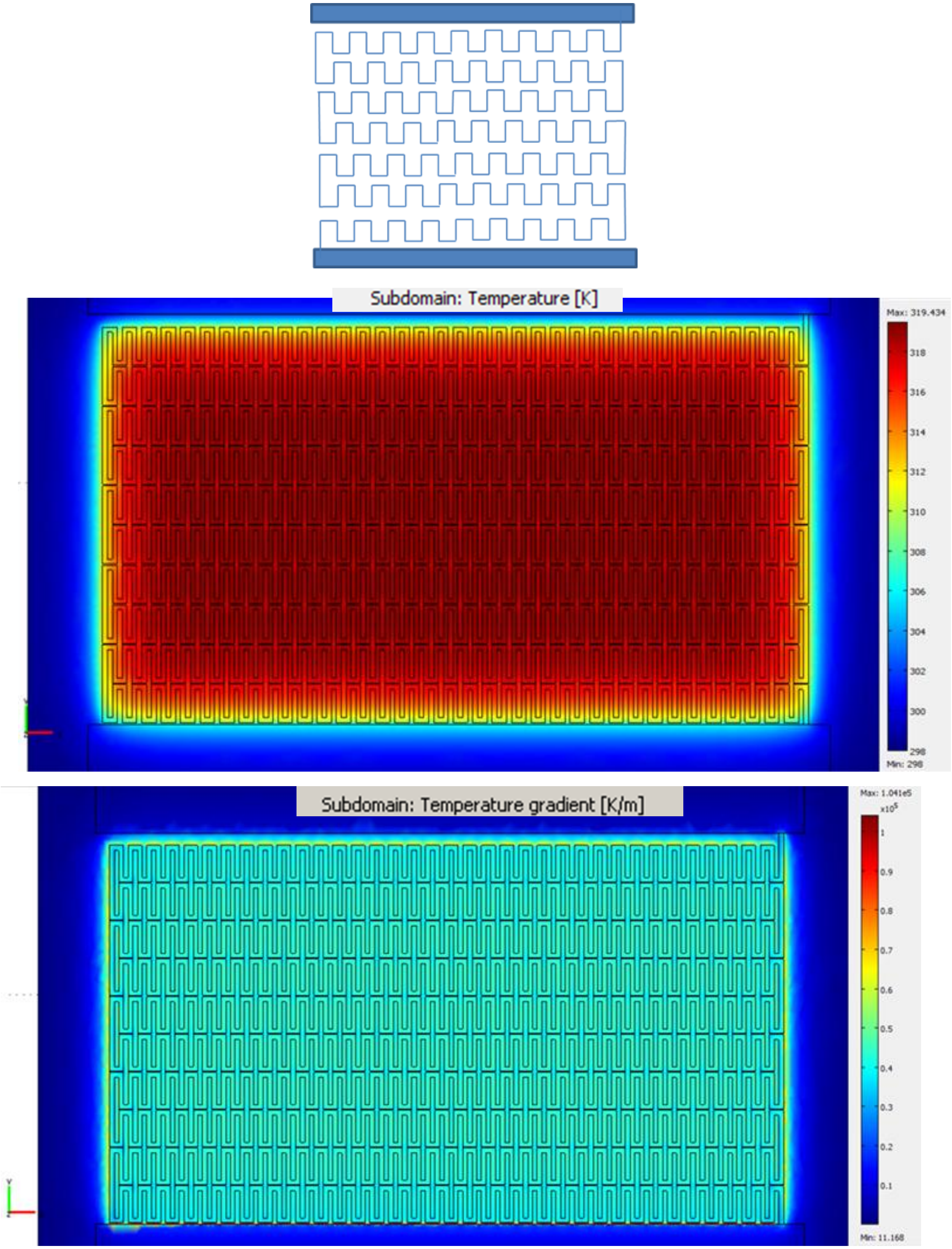

Figure 49. Temperature and Temperature Gradient Profiles obtained from COMSOL Simulation for Design 2.

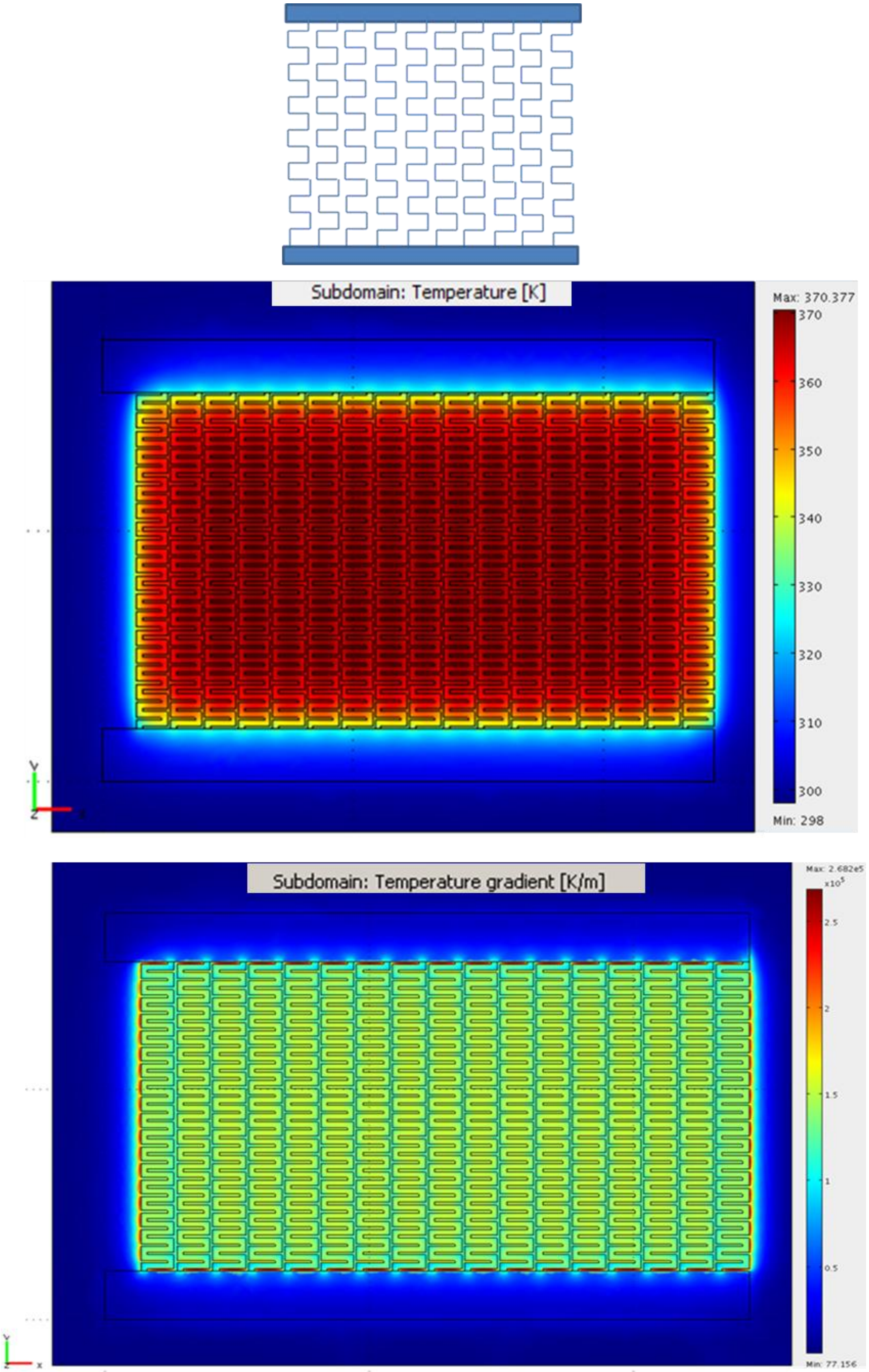

Figure 50. Temperature and Temperature Gradient Profiles obtained from COMSOL Simulation for Design 3.

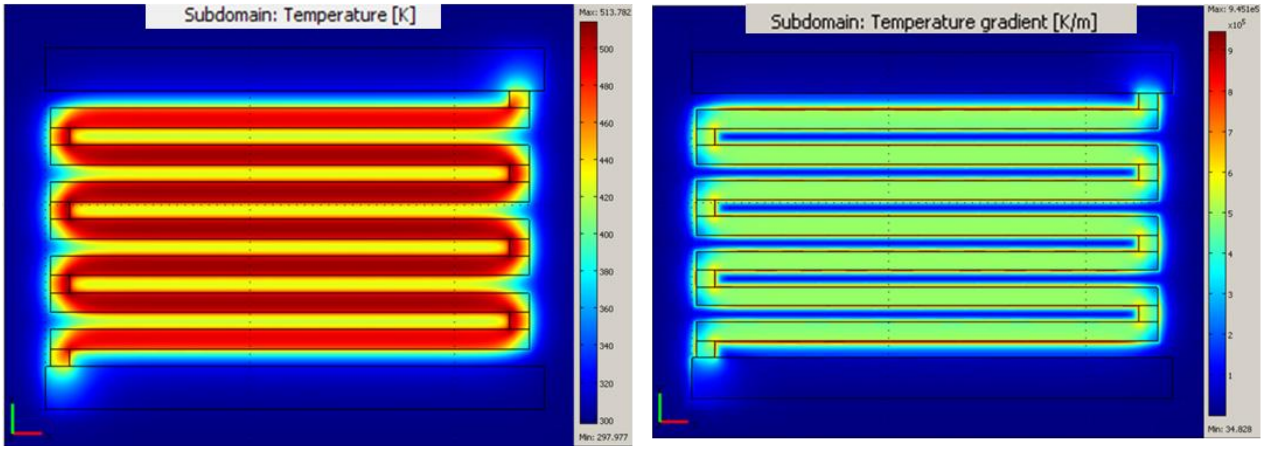

Figure 51. An example of a relatively non-uniform heating device with a large temperature gradient.

The temperature gradient profiles of all three designs exhibit uniform heating. To give a perspective, a non-uniform heating device would have a temperature gradient profile as shown in Figure 51, where the temperature varies almost 80^{o}C within the given pattern.

The *temperature gradient range* metric used in the rest of this chapter is defined as the difference in temperature gradient as calculated from just the heater pattern section of a simulated pattern. The top, bottom, right and left edges of the pattern that connect to the glass are ignored since they do not represent the temperature gradient of the actual heater. The *temperature gradient range* term is explained using the temperature gradient profile from Figure 51, as an example.

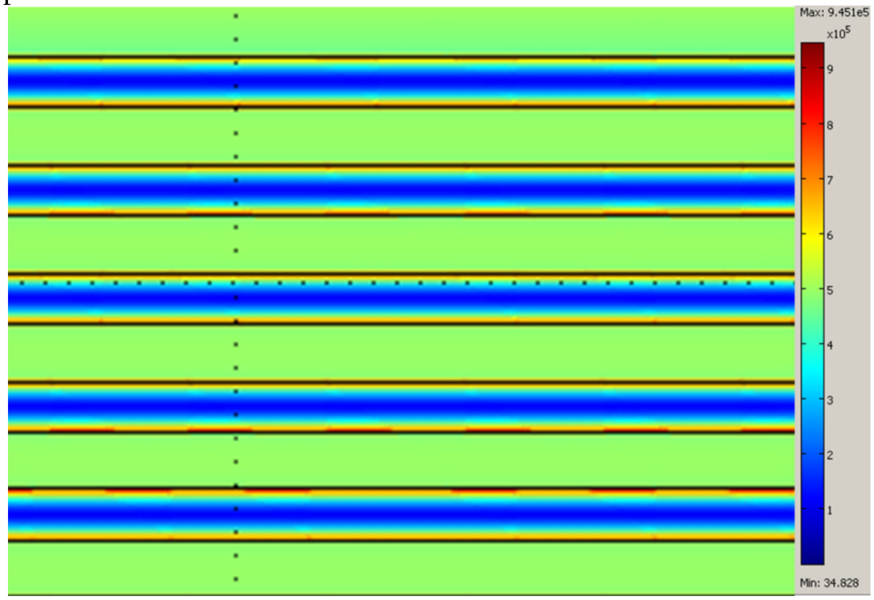

Figure 52. Zoomed-in version of temperature gradient profile of the heater section (minus the edges) from Figure 51.

After zooming in to the center section of the heater temperature gradient profile (as shown in Figure 52), the *temperature gradient range* metric is calculated by subtracting the lowest and highest temperature gradient in this zoomed in area. The dark blue in between the serpentine pattern above would be ~1*10^5 K/m while the orange-red color at the edges of the serpentine pattern would be ~8*10^5 K/m. The temperature gradient range would therefore be 7*10^5

K/m. This metric is effective in comparing and normalizing the temperature gradients of simulated patterns. The lower the value of this metric, the more uniform the heating will be.

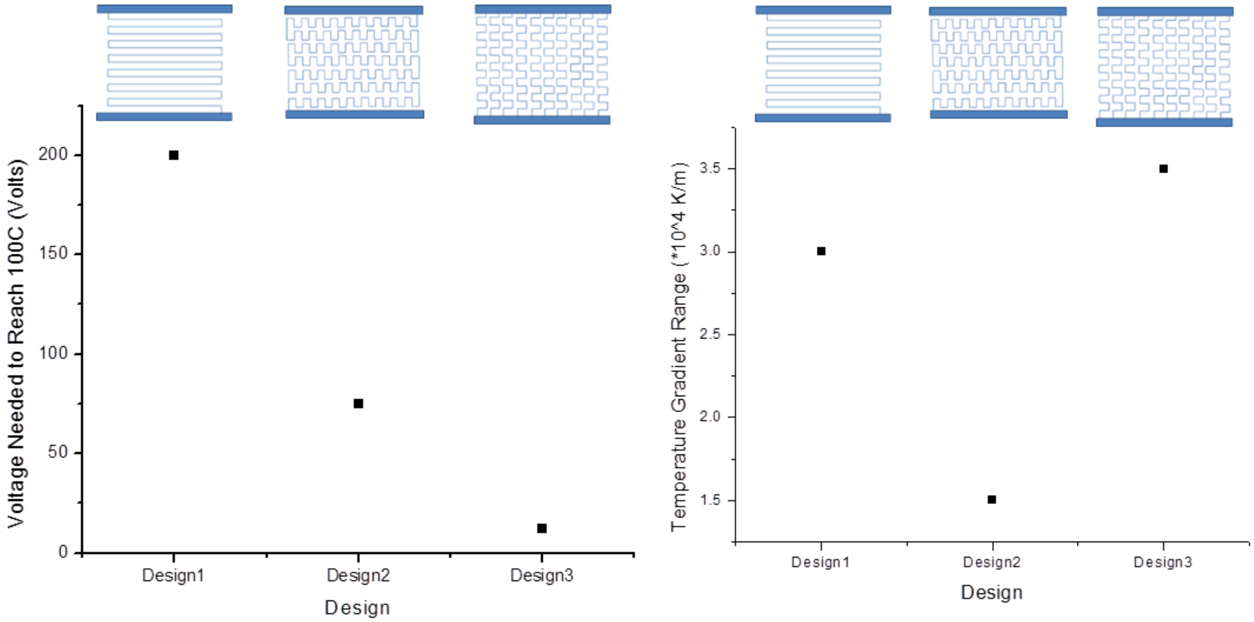

Figure 53. Summary of data collected from simulation results of the three final designs.

Figure 53 summarizes the results seen in Figure 48, Figure 49, and Figure 50. These results show that the temperature gradient range in all three designs is low, although Design 2 exhibits the lowest value. The biological application in this project requires temperatures as high as 95 °C. Therefore, the voltage required to reach this temperature was also analyzed. Design 1 requires 200V to reach 100 °C, Design 2 requires 75V to reach 100 °C, and Design 3 requires only 12V to reach 100°C.

Therefore, although all three designs exhibit low temperature gradients and uniform heating, and are relatively simple and printable with minimum inconsistencies, Design 3 has been chosen because it is able to provide a high temperature differential (0-100 °C) with a low input voltage (of 12V). Before printing, Design 3 is optimized further using COMSOL. These results and trends will be shared next.

3.4.3 Optimization of Chosen Heater Pattern Using COMSOL

To understand and optimize the heater pattern (design 3) further, line widths and spacing parameters within the pattern are varied to understand temperature gradient trends. These parameters are illustrated in Figure 54.

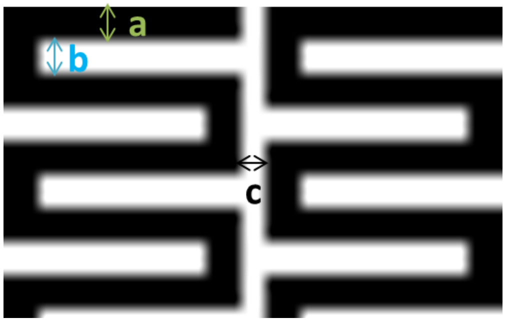

Figure 54. Parameters (a, b, and c) varied to understand and optimized design 3 further.

The three parameters, as indicated in Figure 54, are: ***a)*** *the thickness of the lines (1 pixel wide, 2 pixel wide and 3 pixel wide lines),* ***b)*** *vertical spacing within the serpentine pattern, and* ***c)****horizontal spacing between each of the serpentine lines.*

The absolute temperature reached given a certain voltage is not expected to change significantly among these variations; the expected change is the temperature gradient profiles provided by COMSOL simulations. The results of these simulations are graphed and compared in Figure 55, Figure 56, and Figure 57.

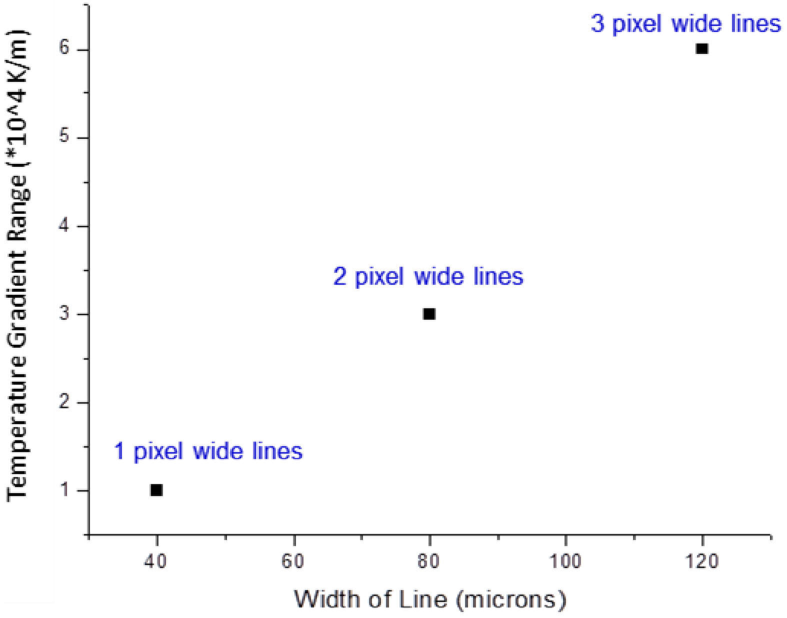

Figure 55. Temperature Gradient range as a function of the width of line('a' in Figure 54).

To begin with, when obtaining the results in Figure 55, the horizontal spacing between the serpentine lines ('c' in Figure 54) and the vertical spacing within the serpentine pattern ('b' in Figure 54) were kept constant at 40µm, and the input voltage to the heater was maintained at 12V. With wider lines, the resistance is smaller and the power output is larger. Given a constant voltage, the temperature is therefore higher for a bigger line width. With wider lines, the drop in temperature from the conductive gold lines to the glass spacing between and within the serpentine pattern is going to be higher as well, leading to a higher temperature gradient. The ideal width of a printed line for the heater pattern will be discussed further in section 3.5 using experimental results.

Next, Figure 56 and Figure 57 present the temperature gradient range results as a function of vertical spacing (‘b’ in Figure 54) and horizontal spacing (‘c’ in Figure 54), respectively.

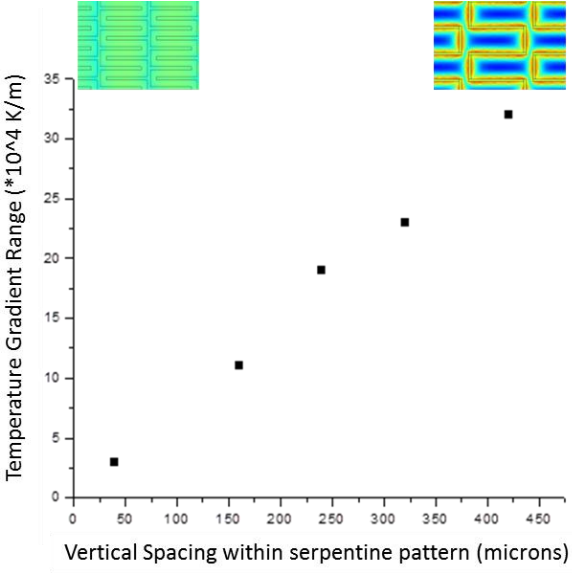

Figure 56. Temperature gradient range as a function of vertical spacing ('b' in Figure 54**)**.

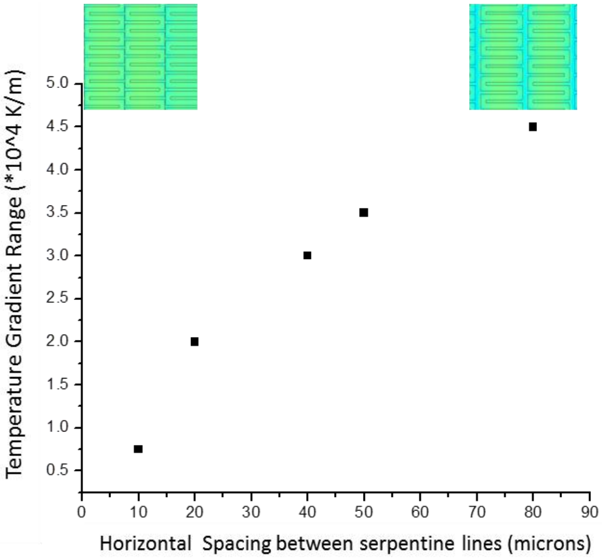

Figure 57. Temperature gradient range as a function of horizontal spacing ('c' in Figure 54).

In Figure 56 and Figure 57, as the spacing (vertical and horizontal, respectively) increases, the temperature gradient also increases. When spacing within the gold heater pattern increases, the glass surface is more exposed. Glass has lower thermal conductivity (2 orders of magnitude lower) than gold and therefore causes a temperature drop in the spaces within the pattern. Thus, the higher the spacing in a pattern, the higher the overall temperature gradient will be.

In this section, simulation based design has allowed for the optimization of the heater pattern by incorporating important trends in temperature and temperature gradients. The optimized pattern will be implemented through printing in the following section.

3.5 Print, Optimization, and Characterization of Heaters and RTDs

3.5.1 Print and Optimization of Heater and RTDs

The printing of heater and RTD prints in this section are done with NPG-J gold nanoparticle ink on PG&O's borofloat glass substrates.

The dimensions of the heater and RTD structures were determined by the biological microfluidic chip, as discussed in section 3.1. The RTD dimensions evolved slightly depending on the placement of the PCR reactor on the particular chip that was to be tested. The RTD pattern is that of a four point probe structure. The four point probe method is an electrical impedance measuring technique that uses separate pairs of current-carrying and voltage-sensing electrodes to make more accurate measurements than traditional two-terminal sensing. The key advantage of four-terminal sensing is that the separation of current and voltage electrodes eliminates the impedance contribution of the wiring and contact resistances. The functioning principle of the RTD depends on the accuracy of this resistance measurement. The resistance of the RTD is first calibrated as a function of temperature. This data is then used to measure temperature of a surface using the RTD. Resistance is linearly related to the temperature as $R(T) = R_0[1 + \alpha(T - T_0)]$ where R_0 is the resistance at temperature T_0, R(T) is the resistance at the temperature of interest T, and α is the temperature coefficient of resistance. Therefore, since the accuracy of the resistance values is important to the RTDs, the four point probe structure was used.

The final image files of RTD and heater patterns that were entered into the Dimatix inkjet printer are shown in Figure 58 and Figure 59.

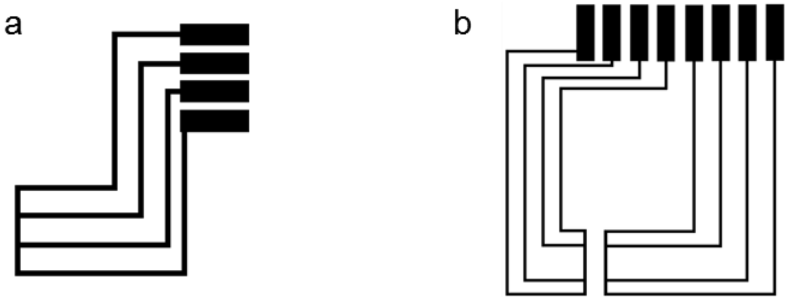

Figure 58. Final RTD patterns used for printing of RTDs on microfluidic chip: a) 1 RTD structure (~2.25 X 2.45cm) b) 2-RTDs structure (~2.45 X 2.65cm).

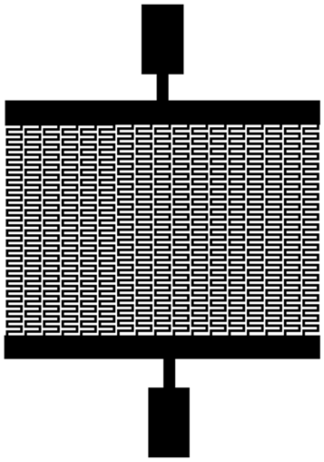

Figure 59. Final heater pattern (~13.5 X 19mm including leads) used for printing of heaters on microfluidic chip.

In printing these structures, an interesting print phenomenon was encountered. The sharp corners in the serpentine patterns in the heater structure and the corner turns in the RTD structure both led to formation of bulges in the prints. Both patterns were printed with 1 pixel wide lines. The bulges seen in both RTD and heater structures are shown in Figure 60.

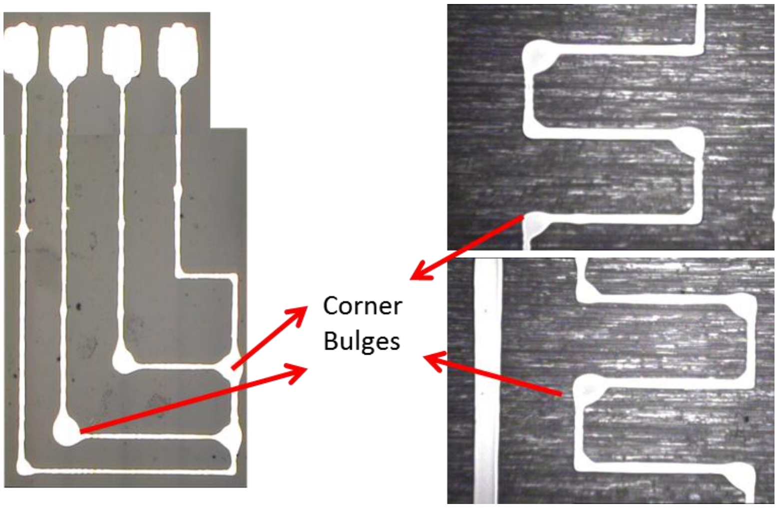

Figure 60. Concave corner bulges seen in ink jet printed gold RTD (left) and heater (right) patterns.

The bulges seen in Figure 60 are especially a concern for the heaters because bulges cause hot spots during heating. This leads to a high temperature gradient in those areas alone, preventing the uniform heating required for biological applications.

As a result of the observed behavior, Dr. Dan Soltman attempted to understand the concave corner bulges using numerical and analytical models. Dr. Soltman's detailed explanation for this behavior can be found in his PhD dissertation [21]. A summary of his discussion is presented below to explain the formation of corner bulges.

Soltman models this behavior using a cross ('plus sign') structure. This model can be extrapolated to elbow and T-junction patterns seen in the RTD and heater structures. In general, concave corners formed by the meeting of high aspect ratio features are unstable and are known to drain their constituent lines to form a large bulge at the intersection.

Volume of ink, V_{tot}, is conserved in the line-bulge system. In his model, Soltman assumes that the contact line of the bulge and line are pinned. He also assumes that 'n' lines have a normalized width (w_l), and that the system volume begins entirely in the lines. Then, volume is permitted to exchange between the bulge and lines so the system may lower its total interfacial energy. In this arrangement, the line contact angle, θ_l, decreases as the spherical cap (bulge) grows with contact angle, θ_{eq}, and increasing wetting radius. *Minimizing total surface/interfacial energy is the main reason for the bulges and line to exchange fluid (i.e. reason for bulges to form).* Examining the change in this total surface energy as a bulge grows helps understand the reasons behind a system's tendency to form a bulge. *His models also indicate that bulging behavior can be mitigated by ensuring that the line effective contact angle* (θ_{l0}) *is sufficiently lower than* θ_{eq} *at the moment of junction creation.*

An additional trend seen with the bulge formation is shown in Figure 61. As the vertical spacing increases, the size of the bulges decreases. At the same time, as the vertical spacing increases, the number of bulges per every symmetric turn increases. In other words, the serpentine pattern with the lowest spacing (left-most column of Figure 61) has one *big* bulge for every symmetric ‘S’ pattern, while the serpentine pattern with the largest vertical spacing (right-most column of Figure 61) has almost negligible sized bulges but on all 8 corners of the symmetric ‘S’ pattern; the latter is preferred as the size of the bulges has been reduced. Although the reasoning behind this trend is yet to be studied, based on the modeling that has been done by Dr. Soltman, it can be extrapolated that increase in vertical spacing within the serpentine pattern enables the minimization of interfacial energy, thereby reducing the formation (and size) of bulges. Based on COMSOL results from the previous section, increased vertical spacing leads to higher temperature gradients. Therefore, another solution has to be found to eliminate the formation of bulges.

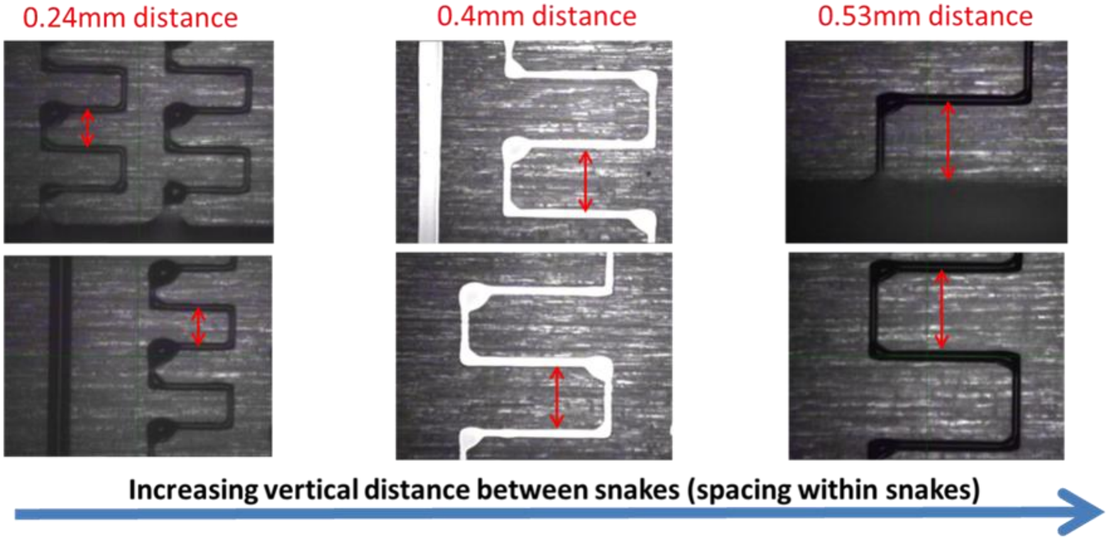

Figure 61. Size of the bulges increases and the number of bulges for each symmetric ‘S’ pattern in a serpentine structure decreases as vertical distance within the serpentine pattern decreases.

As mentioned earlier, the heater and RTD structures have been printed so far with 1 pixel wide lines. By increasing the width of the lines in each of the structures, ideal ‘bulge-free’ structures are achieved for both the heaters and RTDs. The micrographs of parts of the new ‘bulge-free’ RTD and heater structures are shown in Figure 62 and Figure 63, respectively.

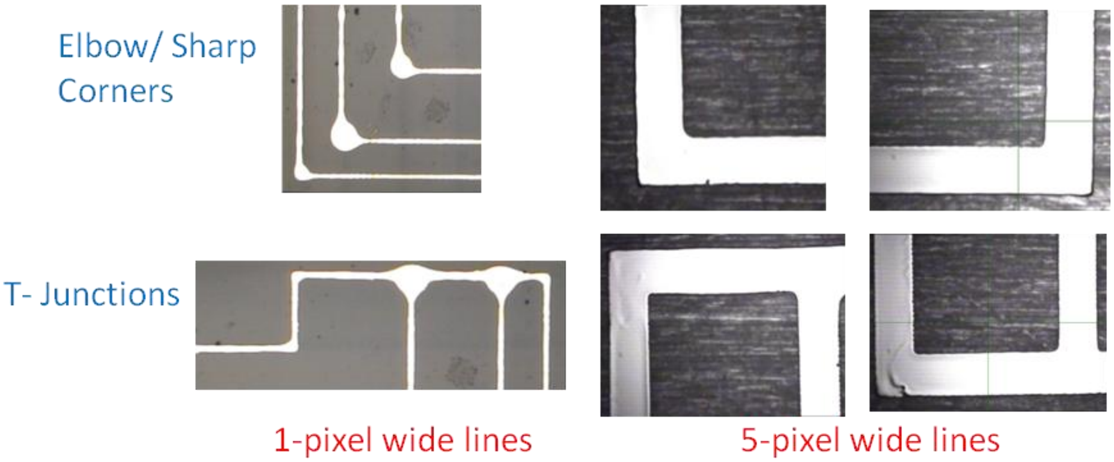

Figure 62. Parts of the RTD structure printed with 1 pixel wide and 5 pixel wide lines; the latter has produced 'bulge-free' corners and T-junctions in the RTD pattern.

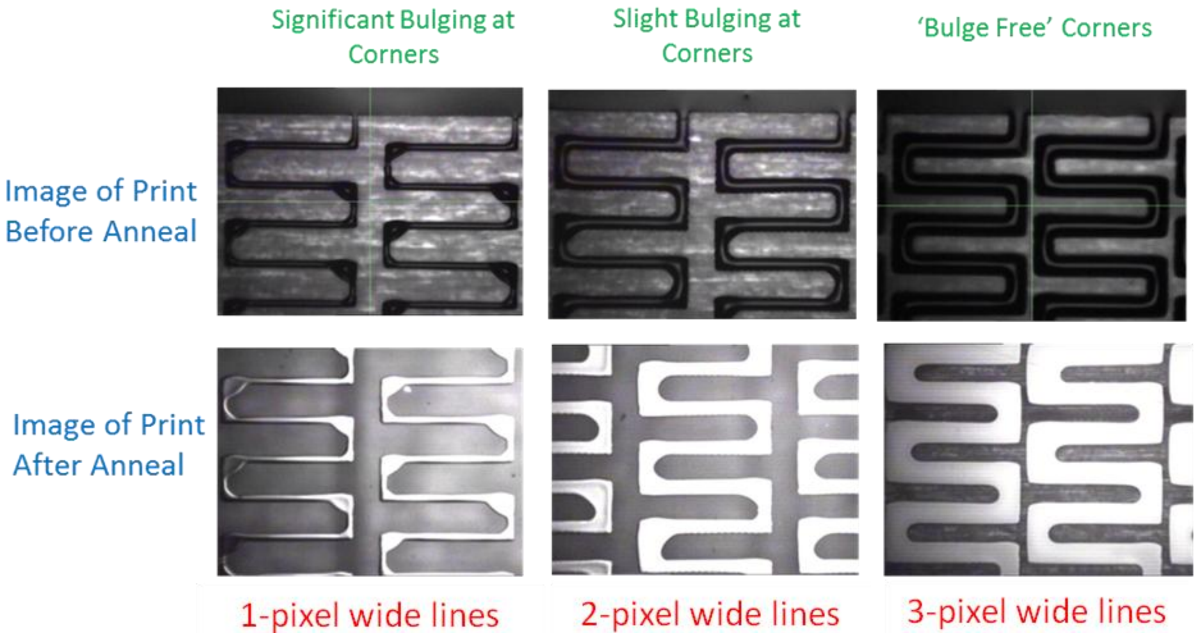

Figure 63. Image of heater prints with 1, 2, and 3-pixel wide lines; bulging completely disappears with 3 pixel wide lines.

To review, 1-pixel wide lines with the optimized 35µm print drop spacing results in ~40µm wide lines after printing and annealing. As seen above, 5-pixel wide lines provide for bulge free corners and T-junctions in RTDs, and 3-pixel wide lines result in bulge free serpentine patterns in heaters.

Dr. Soltman uses the results in Figure 62 and Figure 63 to support his explanation for the mitigation of the bulges [21]. In short, contact angle of printed two-dimensional features decrease with increasing line (pixel) count. The single pixel lines have a contact angle of θ_{eq}, and grow significant bulges as predicted analytically and numerically by his work. However, the multiple pixel-wide lines have contact angle sufficiently lower that θ_{l0} (effective contact angle of the line) and falls in the no-bulge region, as seen in his plots modeled using *Surface Evolver* (an interactive program for the modeling of liquid surfaces shaped by various forces and constraints). The exact value for the # of pixels (or line width) needed depends on the type of pattern that needs to be printed.

To summarize, bulge size always decreases as θ_{l0} decreases below θ_{eq}. Moreover, the size of the bulge can vary depending on the length of the feeding lines. Finally, as the prints in Figure 62 and Figure 63 have also shown, increasing the width of the line (# of pixels) can help mitigate the bulge formation in convex corner prints. The causes behind these trends are yet to be studied and understood.

Increasing line width also resulted in the ability to print perfect rectangles and squares for contact pads in RTDs and heaters. Figure 64 shows a micrograph of the contact pads section of the printed RTD structure. With 1 pixel wide lines, the rectangular contact pads are not quite rectangular. They dewet and tend to pull in to form circular structures instead (a behavior also modeled by Dr. Soltman in his work [21]). The contact pad pulls in fluid from the connecting line, a behavior known as 'wicking'. If the pads pull in too much volume in order to get to a lower interfacial energy, they sometimes separate from the lines, leading to non-conductive RTDs. Increase the width of the lines has helped eliminate this problem.

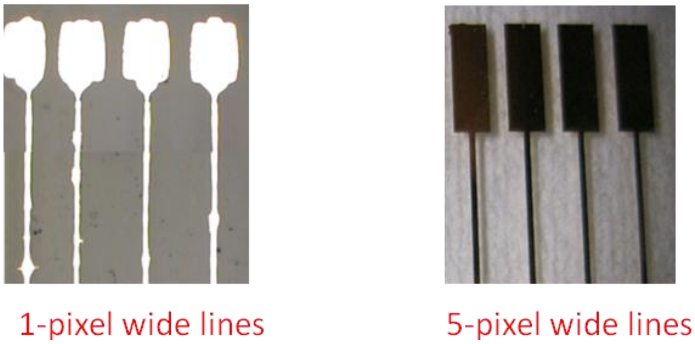

Figure 64. The contact pads of gold inkjet printed RTD structure is also perfected with multiple-pixel wide lines.

As mentioned in section 3.4, although the ideal heater print will have serpentine patterns placed as close as possible horizontally and vertically, as shown in Figure 65a, experimentally, this is not always possible because unavoidable print inconsistencies occur when patterns are too close to each other, an example of which is shown in Figure 65b. Therefore, the print patterns have to be spaced taking these inconsistencies into consideration.

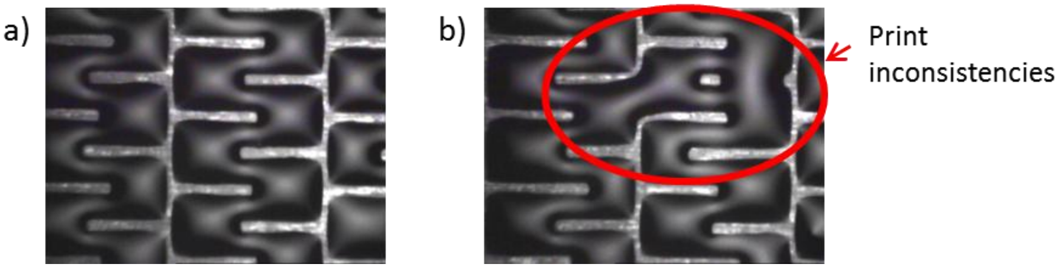

Figure 65. a) Closest spaced heater pattern demonstrated with printing; b) because of unavoidable print inconsistencies that occur, this print with very close spacing is not experimentally feasible.

Incorporating everything that has been discussed so far in this chapter regarding heater and RTD print optimization, the final optimized inkjet printed gold RTD and heater structures on biocompatible borofloat glass substrates are shown in Figure 66 and Figure 67, respectively.

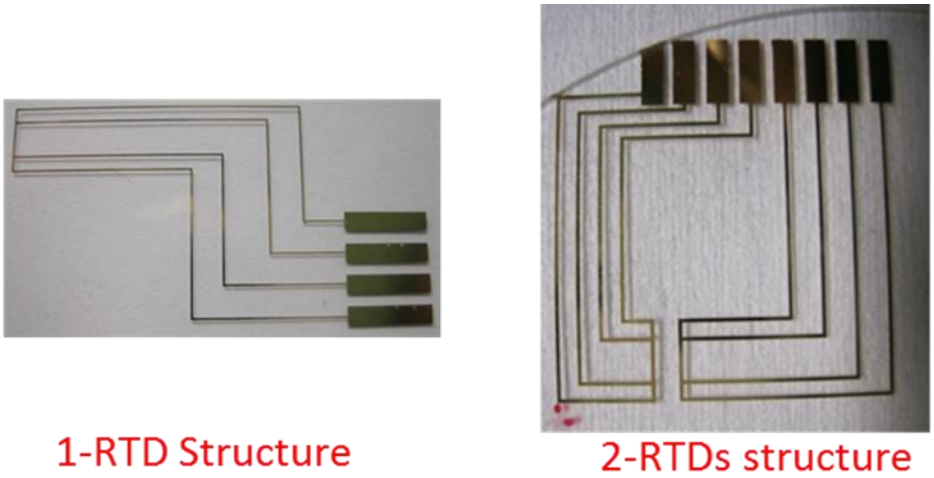

Figure 66. Final optimized gold RTDs inkjet printed on biocompatible borofloat glass substrates.

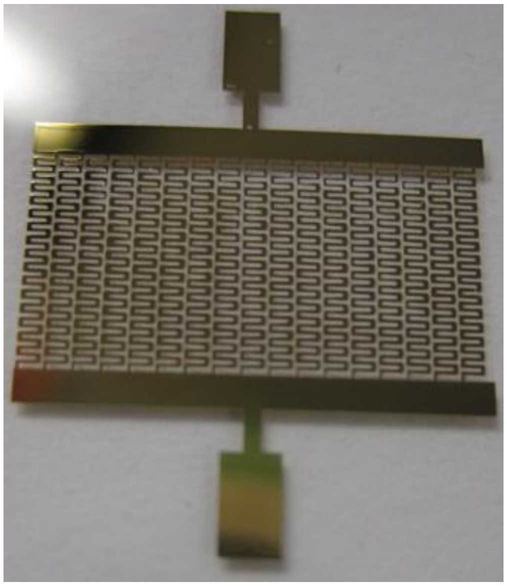

Figure 67. Final optimized gold heater inkjet printed on biocompatible borofloat glass substrates.

The final dimensions of the complete 1-RTD structure in Figure 66 are ~3 X 2cm, the complete 2-RTDs structure in Figure 66 are ~2.45 X 2.65cm, and the heater (with leads) in Figure 67 are ~13.5 X 19mm.

Going back to Figure 54 with COMSOL simulations, and relating it to the printed structures, the *final optimized values* for the three important parameters in the heater pattern, namely **a)** the thickness of the lines (line width), **b)**vertical spacing within the serpentine pattern, and **c)** horizontal spacing between serpentine lines, are all indicated in Figure 68. The values for ‘b’ and ‘c’ were minimized as much as experimentally possible in order to minimize the overall temperature gradient in the full heater structure.

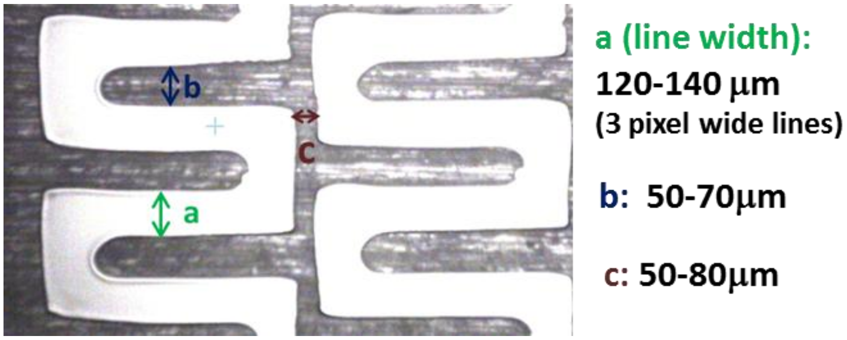

Figure 68. Final values for three important parameters of the printed heater.

Now that the final heater and RTD structures have been optimized and printed, they are electrically and thermally characterized in the following section.

3.5.2 Characterization of RTDs

The RTDs were characterized as a 4-point probe structure using Cascade Probe Station [27] with a temperature controllable chuck. The chuck was heated from 30-200^{o}C, and for each of these temperatures, the resistance was calculated using 4-point probe set-up measurement. The resistance-temperature relationship for the RTD prints is shown in Figure 69.

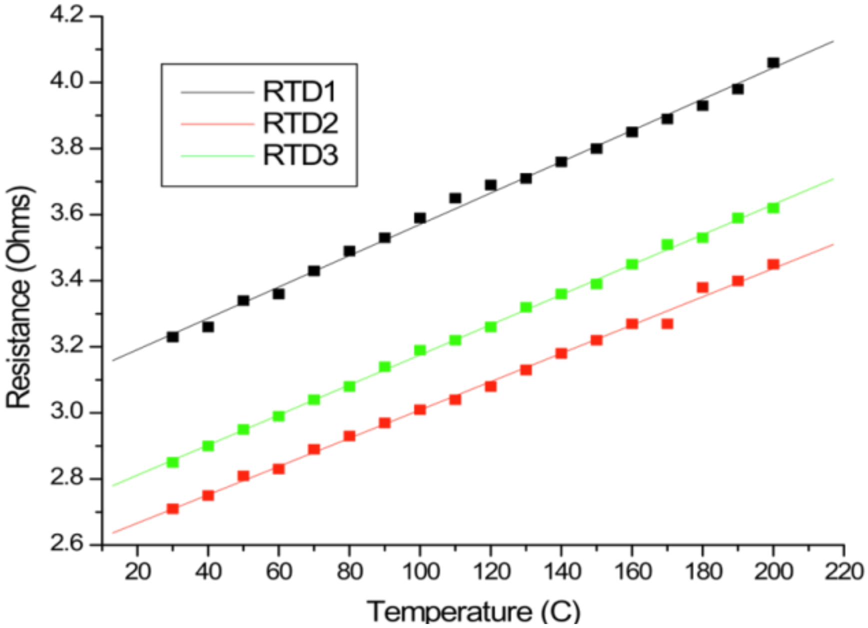

Figure 69. Resistance-temperature relationship of gold inkjet printed RTDs.

The expected linear relationship between resistance and temperature is seen with the printed gold RTDs. To review, resistance is linearly related to the temperature as $R(T) = R_0[1 + \alpha(T - T_0)]$ where R_0 is the resistance at temperature T_0, R(T) is the resistance at the temperature of interest T, and α is the temperature coefficient of resistance. The reported αof pure gold is 0.003715 at 20°C. The printed gold RTDs have an average α value between ~0.002 and 0.0035, which is comparable to the reported value. ***In addition, the average sheet resistivity calculated from the printed gold RTDs (0.5cm wide and 1cm long) is 3.9x10^{-5} Ohms-cm.***

3.5.3 Characterization of Heaters

To measure the heating behavior of the inkjet printed gold heaters, a thermocouple was carefully placed in close contact with the substrate with printed heaters. Three different heaters on different substrates treated under the same optimized conditions were measured to obtain the data. Moreover, the three heaters had the same dimensions and spacing parameters (‘a’, ‘b’ and ‘c’ in Figure 54) so as to keep all parameters constant. The substrate was thermally isolated to prevent heat loss to surrounding structures. A voltage was applied to the heaters using an external power supply, the current was recorded using Rucker & Kolls Probe Station, and the temperature was recorded using a thermocouple. This setup is illustrated in Figure 70.

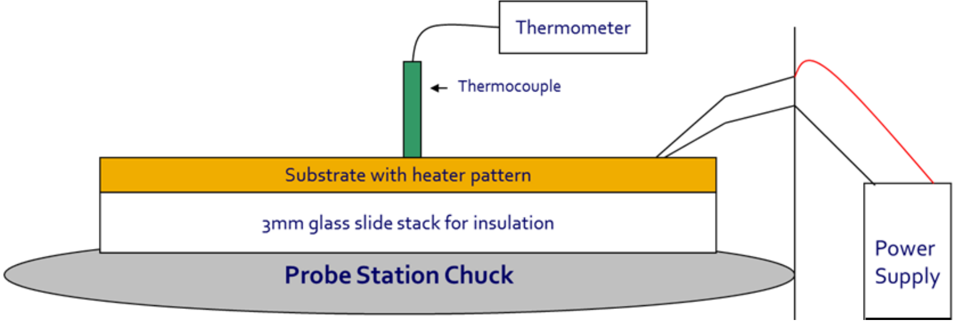

Figure 70. Measurement set-up used to characterize printed heaters.

The current-voltage characteristics of three different printed gold heaters on different substrates are shown in Figure 71. As expected, the relationship is linear with an average resistance of 33 ohms for the printed heater configuration.

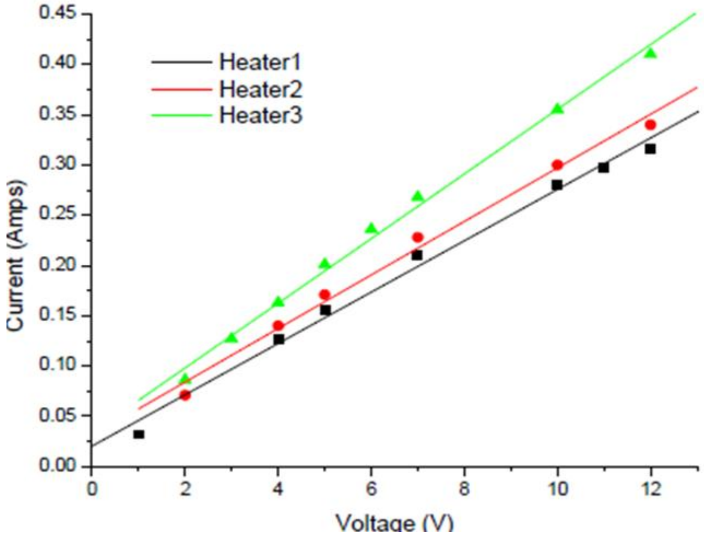

Figure 71. Current-Voltage characteristics of three different heaters devices on different substrates.

Figure 72 shows the relationship between temperature and voltage of the three heaters. For the heaters measured, at an applied voltage of 12V, temperatures of >100°C were achieved, thus covering the full temperature range necessary for PCR. Although biological applications do not typically require temperatures higher than 100°C, the heaters have successfully reached temperatures of 250-270°C at 25V showing potential for use in other applications as well. The quadratic relationship seen between temperature and voltage in Figure 72 correlates well with $P=V^2/R$ relationship since power represents and is proportional to the heat output, which is recorded here as temperature.

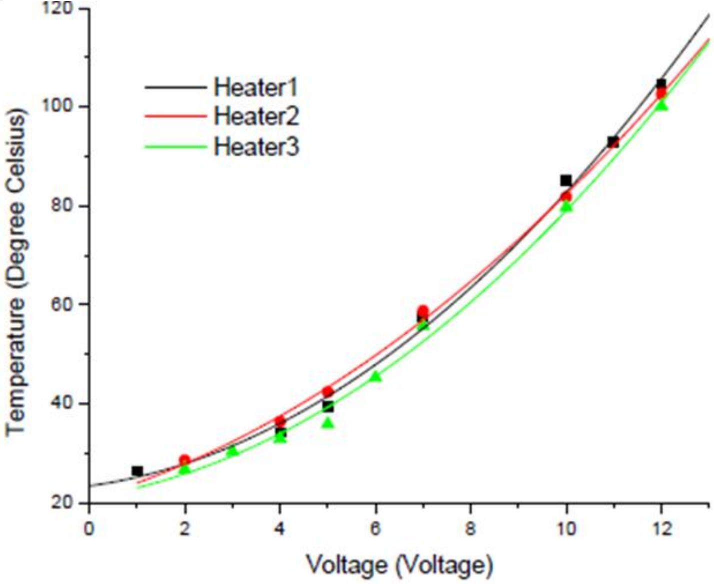

Figure 72. Relationship between temperature and applied voltage for the three different heaters.

The heaters can also be used as resistive temperature detectors (RTDs) by monitoring the resistance of the elements themselves. Figure 73 depicts the linear relationship between temperature and resistance of the heaters. The heaters measured here have anα of 0.003314, comparable to the reported value of α of pure gold at 0.003715.

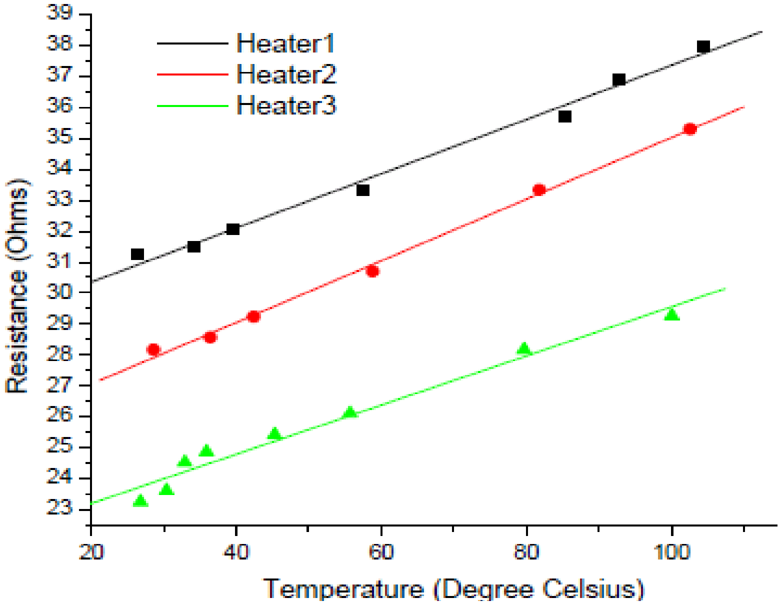

Figure 73. Resistance of the 3 heaters as a function of a range of temperatures; the linear relationship shows that the heater can also be used as an RTD.

The following experiment further characterizes the heater and helps in understanding the factors that affect rate of heating. The measurement setup used in this experiment is depicted in Figure 74. The heater was printed on one side of the substrate while the RTD was printed on the other side right behind the heater. The RTD was first calibrated and then used to measure the temperature of the heater during characterization.

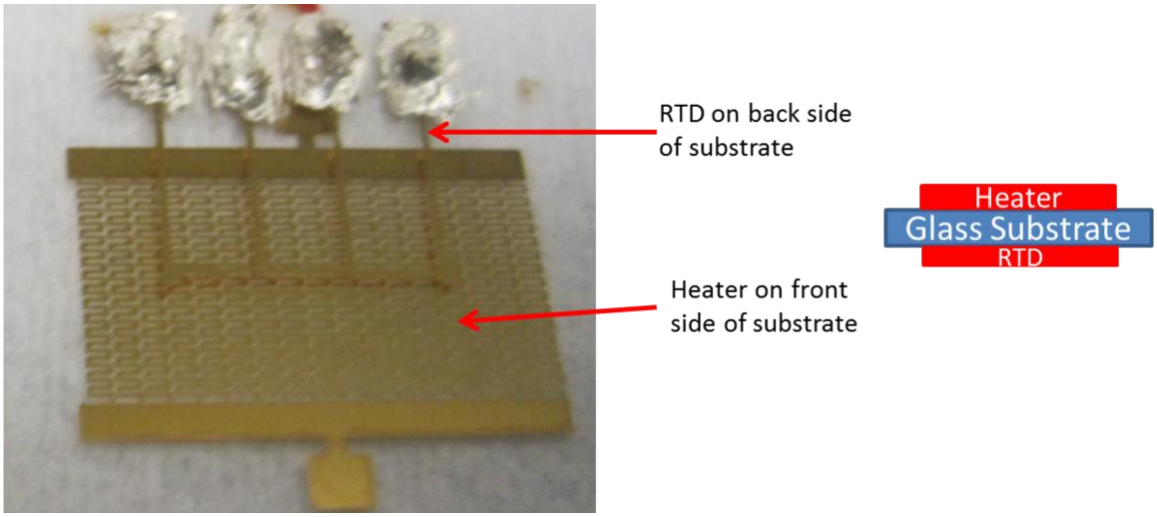

Figure 74. Setup used to measure rate of heating, coverage area, and heater resistance in the following experiment.

Line widths and spacing parameters within the pattern are varied for the following experiment. These parameters have been illustrated previously in Figure 54. Parameters ‘a’, ‘b', and ‘c’ (Figure 54) are used to understand the factors that affect resistance, coverage area, and rate of heating. *The rate of heating is important for PCR based applications because depending on the type of primer (short pieces of single-stranded DNA that are complementary to the target sequence) used in the PCR reaction, different heating rates are required*. Having this data for different heater configurations is useful for printing the appropriate heater pattern for the desired PCR application. The resistance and coverage area of the heaters are important factors in determining the rate of heating.

The **rate of heating** results in Figure 75, Figure 76, and Figure 77 are measured using the PCR/thermal cycling setup in Mathies Lab in UC Berkeley. RTDs are contacted by using electrical pins, and 1 mA is passed through the outer leads. The voltage drop across the inner leads as a function of temperature is measured in real-time by using a signal conditioner (5B31-01; Analog Devices) and a data acquisition board(National Instruments). The output drives a proportional integral derivative (PID) controller that regulates the necessary voltage for heating to a certain temperature and pressurized air for active cooling as necessary [4]. The rate of heating was measured using the measurement configuration in Figure 74. This setup emulates the microchip bioprocessor system.

Coverage area in this experiment is defined as the amount of gold in a given area of the heater pattern (Total surface area – Glass surface area). Coverage area was calculated using a contrast tool in GIMP, an imaging software. **Resistance** of the heaters was calculated by inputting a constant voltage of 5V to each heater pattern and recording the resulting current.

Throughout this experiment, the total heater area and dimensions (~13.5mm wide by 19.5mm long including leads) were kept constant while the input parameters were changed. To begin with, line width was varied from 1 pixel wide lines (~40μm) to 3 pixel wide lines (~120μm), while keeping the other two parameters, ‘b’ and ‘c’ in Figure 54, constant. The results from the variation of this parameter are shown in Figure 75. Micrographs of part of the heater pattern printed with the different line widths are shown at the top of Figure 75.

As line width increases, the resistance of each serpentine pattern decreases, and therefore the total heater resistance also decreases. Although parameters ‘b’ and ‘c’ are kept constant as inputs, as line width increases, the coverage area increases because the lines in the heater pattern slightly spreads after print and anneal, effectively reducing ‘b’ and ‘c’. Therefore the 2nd graph in Figure 75 shows increasing coverage area with increasing line width, which is also apparent in the micrographs at the top of the figure. Finally, with lower resistance and higher coverage area, the joule heating is higher and therefore the rate of heating increases. With the line widths (40 to 120μm) tested in this experiment, the rate of heating varied from 0.3 to 3^{o}C/s.

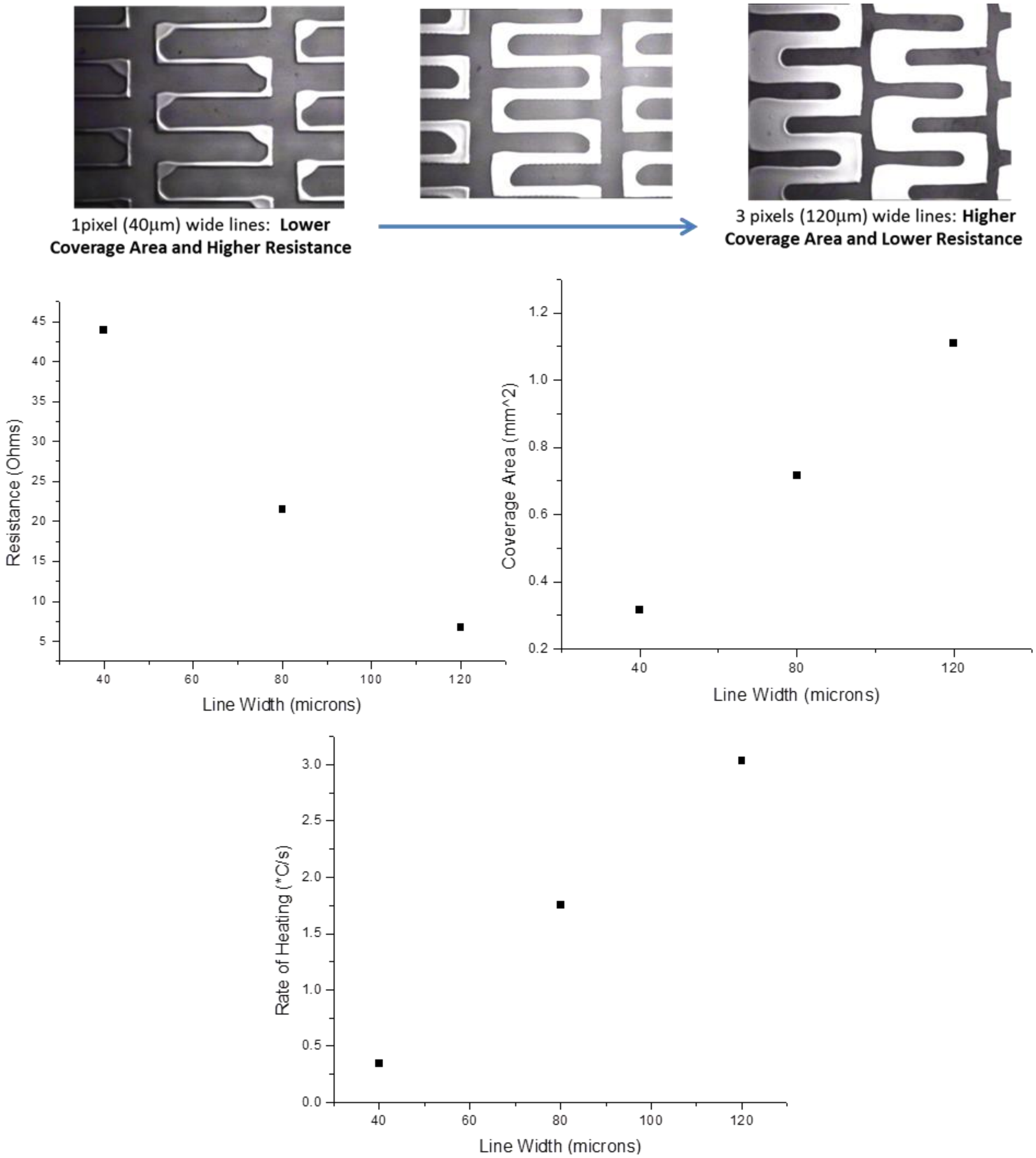

Figure 75. Resistance, Coverage Area, and Rate of Heating as a function of line width (parameter ‘a’ in Figure 54).

Figure 76 shows the trends of resistance, coverage area, and rate of heating a function of vertical spacing within the serpentine pattern (‘c’ in Figure 54); parameters ‘a’ and ‘b’ are kept constant. As the vertical spacing increases and the total heater pattern length is kept constant, each individual serpentine pattern is now shorter and less resistive, decreasing the overall heater resistance. As the vertical spacing increases, the coverage area decreases because there is less gold and more glass in any given section of the heater, also apparent in the micrographs at the top of Figure 76. Since the rate of heating increased with more vertical spacing, it can be concluded that resistance is a more dominant factor than coverage area in this case. Therefore, as resistance goes down, the rate of joule heating goes up, also increasing rate of heating.

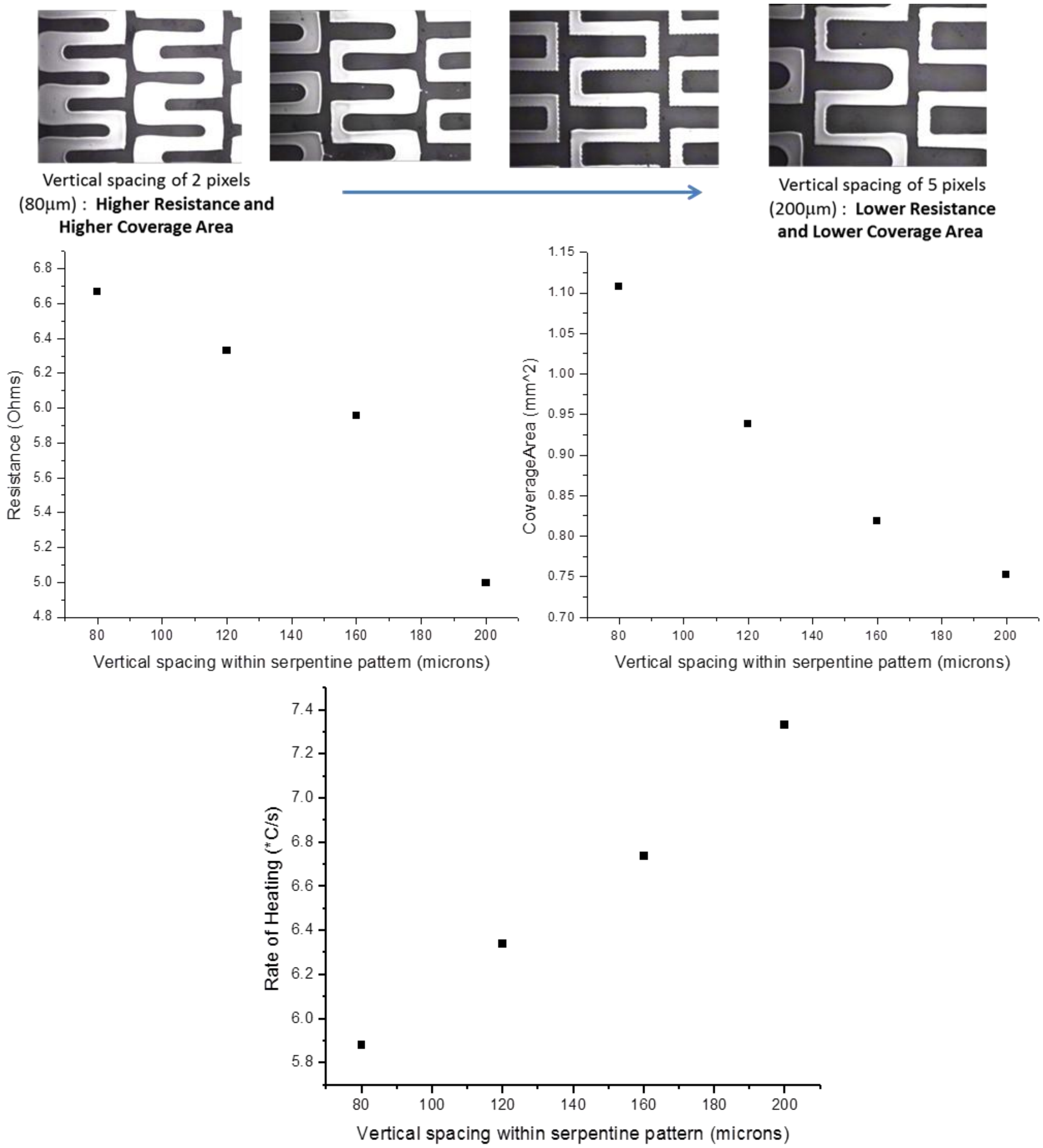

Figure 76. Resistance, Coverage Area, and Rate of Heating as a function of vertical spacing in the serpentine pattern ('b' in Figure 54).

Figure 77 completes this analysis by relating the three outputs to horizontal spacing between the serpentine lines. In a fixed heater pattern width, as the horizontal spacing increases, fewer serpentine lines are printed in the heater pattern. Fewer serpentine lines in parallel lead to higher resistance. This is illustrated in the first graph in Figure 77. As the horizontal spacing increases, the coverage area or the amount of gold in a given section of the heater decreases, resulting in the second graph in Figure 77. With increased horizontal spacing, the decreasing coverage area dominates in contributing towards the lower rate of heating, as seen in the third graph in Figure 77.

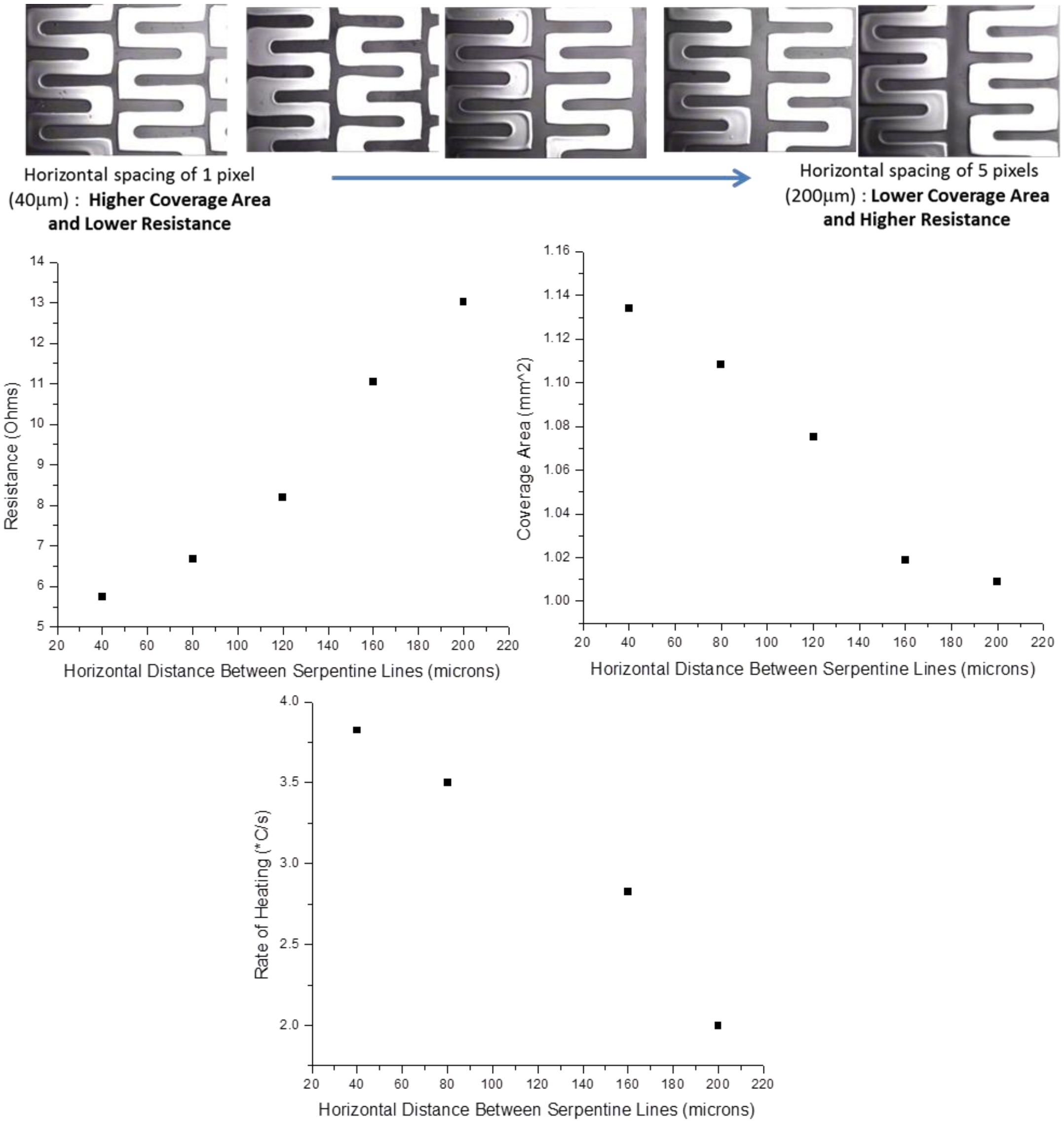

Figure 77. Resistance, Coverage Area, and Rate of Heating as a function of horizontal spacing between serpentine lines.

In the above experiment, varying the heater patterns by changing line width, and horizontal and vertical spacing within pattern, has allowed for the control of resistance, coverage area, and heating rate of heaters. The control of heating rate is especially useful for PCR because the required heating rate for a PCR mixture is dependent on the primer, which is one of the components in the mixture. Depending on the type of primer that a particular PCR application requires, the heating rate needs to be tuned. The results shown in Figure 75, Figure 76, and Figure 77 are therefore useful for this purpose and for other PCR related applications which might require the control of the studied output parameters.

Having thus printed, optimized, and characterized the gold inkjet printed heaters and RTDs, the next step is to integrate the printed devices with the microchip bioprocessor system and demonstrate PCR. This integration is shared in the next chapter.

3.6 Conclusion and Future Work

This chapter has presented the numerous steps taken to achieve optimized, repeatable and uniform inkjet printed heaters and RTDs. To summarize, the best substrate treatment for the borofloat glass substrate was first finalized to be piranha clean with ~10mins of UVO as needed. Next the print parameters, namely, drop spacing, drop velocity, and print height, were optimized for the printing of gold nanoparticle ink (NPG-J) on the glass substrate. Drop spacing of 35μm, drop velocity of 8-9m/s, and print height of 0.95-1mm resulted in a smooth uniform printed line with lowest line edge roughness. COMSOL was then used to simulate and optimize heater patterns, temperature profile and temperature gradients. The desired result of a heater pattern with a simple design, low voltage requirement, high temperature differential, and low temperature gradient was achieved. This was then implemented with printing, and print inconsistencies were mitigated by use of multiple pixel-wide lines, appropriate spacing in the pattern and optimized line widths for both the RTD and heater patterns. The final optimized printed RTD and heater structures were then electrically and thermally characterized and are ready now to be integrated into the microfluidic chip. The integration will be discussed in Chapter 4.

The cause of the bulging behavior that initially occurred in both the heater and RTD patterns can be better understood. Although an experimental solution was found to mitigate the bulges, modeling it further with more pattern shapes (star shaped pattern, for example) and variation of different parameters (spacing within the pattern shape, for example) will help generalize the cause and effect of the bulging phenomena. Obtaining a more thorough understanding and a general trend for the bulging behavior and other print inconsistencies such as contact pad 'wicking', will continue to ensure 'error-free', uniform and repeatable printed devices.

3.7 Sources

[1] H.Y. Tseng and V. Subramanian, "All inkjet printed self-aligned transistors and circuits applications," in *Electron Devices Meeting (IEDM), 2009 IEEE International*, 2009, pp. 1-4.

[2] L. Yang and M. M. Tentzeris, "Design and Characterization of Novel Paper-based Inkjet-Printed RFID and Microwave Structures for Telecommunication and Sensing Applications," In *Microwave Symposium, 2007. IEEE/MTT-S International*, 2007, pp. 1633-1636.

[3] N. M. Toriello et al., "Integrated microfluidic bioprocessor for single-cell gene expression analysis," *Proceedings of the National Academy of Sciences*, vol. 105, no. 51, pp. 20173 – 20178, Dec. 2008.

[4] R. G. Blazej, P. Kumaresan, and R. A. Mathies, "Microfabricated bioprocessor for integrated nanoliter-scale Sanger DNA sequencing," *Proceedings of the National Academy of Sciences*, vol. 103, no. 19, pp. 7240 -7245, May 2006.

[5] J. A. Rogers, P. Kuo, A. Ahuja, B. J. Eggleton, and R. J. Jackman, "Characteristics of Heat Flow in Optical Fiber Devices That Use Integrated Thin-Film Heaters," *Applied Optics*, vol. 39, no. 28, pp. 5109-5116, Oct. 2000.

[6] H. Kipphan, *Handbook of print media: technologies and production methods*. Springer, 2001.

[7] Dimatix Materials Printer DMP-2800 Series User Manual. V. 1.5.0.1., *Fujifilm Dimatix, Inc.,* 2007.

[8] J. P. Rolland, R. M. Van Dam, D. A. Schorzman, S. R. Quake, and J. M. DeSimone, "Solvent-Resistant Photocurable 'Liquid Teflon' for Microfluidic Device Fabrication," *J. Am. Chem. Soc.*, vol. 126, no. 8, pp. 2322-2323, 2004.

[9]C. H. Ahn et al., "Disposable smart lab on a chip for point-of-care clinical diagnostics," *Proceedings of the IEEE*, vol. 92, no. 1, pp. 154- 173, Jan. 2004.

[10] G. S. Fiorini, R. M. Lorenz, J. S. Kuo, and D. T. Chiu, "Rapid Prototyping of Thermoset Polyester Microfluidic Devices," *Anal.Chem.*, vol. 76, no. 16, pp. 4697-4704, 2004.

[11] H. Kobayashi and M. J. Owen, "Surface properties of fluorosilicones," *Trends in polymer science*, vol. 3, no. 10, pp. 330-335.

[12] H. Schmid and B. Michel, "Siloxane Polymers for High-Resolution, High-Accuracy Soft Lithography," *Macromolecules*, vol. 33, no. 8, pp. 3042-3049, 2000.

[13] Y. S. Heo et al., "Characterization and Resolution of Evaporation-Mediated Osmolality Shifts That Constrain Microfluidic Cell Culture in Poly(dimethylsiloxane) Devices," *Anal. Chem.*, vol. 79, no. 3, pp. 1126-1134, 2006.

[14] "Borofloat 33 borosilicate glass, high temperature glass." [Online]. Available: http://www.pgo-online.com/intl/katalog/borofloat.html. [Accessed: 16-Jan-2012].

[15] P. Buffat and J.-P.Borel, "Size effect on the melting temperature of gold particles," *Physical Review A*, vol. 13, no. 6, pp. 2287-2298, Jun. 1976.

[16] K. O'Brien, " MarvellNanoLab Summer Internship 2011," *End of Internship presentation: Nanolab, UC Berkeley*, 2011.

[17] "UVO Cleaner ®- Utilizing ozone and UV for cleaning glass slides etc." [Online]. Available: http://www.jelight.com/uvo-ozone-cleaning.php. [Accessed: 18-Jan-2012].

[18] J. R. Vig, "UV/ozone cleaning of surfaces," *Journal of Vacuum Science & Technology A: Vacuum, Surfaces, and Films*, vol. 3, no. 3, pp. 1027-1034, May 1985.

[19]P. C. Duineveld, "The Stability of Ink-Jet Printed Lines of Liquid with Zero Receding Contact Angle on a Homogeneous Substrate," *Journal of Fluid Mechanics*, vol. 477, pp. 175-200, 2003.

[20] D. Soltman, "Understanding Inkjet Printed Pattern Generation," *PhD Dissertation Thesis,* University of California, Berkeley, May 2011.

[21] D. Soltman and V. Subramanian, “Inkjet-Printed Line Morphologies and Temperature Control of the Coffee Ring Effect,” *Langmuir*, vol. 24, no. 5, pp. 2224-2231, 2008.

[22]COMSOL Multiphysics 3.5a User Guide. [Online]. Available: http://math.nju.edu.cn/help/mathhpc/doc/comsol/guide.pdf .[Accessed: 18-Jan-2012].

[23]COMSOL Multiphysics 3.5a Modeling Guide. [Online]. Available: http://math.nju.edu.cn/help/mathhpc/doc/comsol/guide.pdf .[Accessed: 18-Jan-2012].

[24] V.N.Hoang, G.V. Kaigala, and C.J.Backhouse, “Optimization of Thin Film Heater/Sensor Design for Miniature Devices using Finite Element Analysis,” *COMSOL Multiphysics User’s Conference*, Boston, 2005.

[25] I. Wyzkiewicz et al., “Self-regulating heater for microfluidic reactors,” *Sensors and Actuators B: Chemical*, vol. 114, no. 2, pp. 893-896, Apr. 2006.

[26] W. Lee, W. Fon, B. W. Axelrod, and M. L. Roukes, “High-sensitivity microfluidic calorimeters for biological and chemical applications,” *Proceedings of the National Academy of Sciences*, vol. 106, no. 36, pp. 15225 -15230, 2009.

[27] “High Performance Probe Systems□ :: Cascade Microtech, Inc.:” [Online]. Available: http://www.cmicro.com/products/probe-systems/high-performance-probe-systems. [Accessed: 30-Jan-2012].

4. Integration of Inkjet Printed Heaters and RTDs with Biological Microfluidic System: Demonstration of Polymerase Chain Reaction (PCR)

4.1 Introduction and Motivation

Polymerase Chain Reaction (PCR) is a method in biology developed by Dr. Kary Mullis in the 1980s and is now a common and often indispensable technique used in medical and biological research labs for a variety of applications. These include cloning, identification of genetic fingerprints (forensic sciences), and the detection and diagnosis of infectious diseases. The PCR method relies on thermal cycling and results in the amplification of a single or a few copies of a piece of DNA across several orders of magnitude, generating thousands to millions of copies of the DNA sequence of interest.

The PCR mixture typically includes[1]:

- **DNA template** - sample DNA that contains the target sequence.
- **DNA polymerase** - a type of heat stable enzyme that synthesizes new strands of DNA complementary to the target sequence using a DNA template, primers, and nucleotides,
- **Primers** - short pieces of single-stranded DNA that are complementary to the target sequence. The polymerase begins synthesizing new DNA from the end of the primer. In a PCR experiment, two primers (reverse and forward primer) are designed to match the DNA template. Through complementary base pairing, one primer attaches to the top strand at one end of the spliced template DNA, and the other primer attaches to the bottom strand at the other end.
- **Nucleotides (dNTPs or deoxynucleotide triphosphates)** - single units of the bases A, T, G, and C, which are essentially "building blocks" for new DNA strands.

These components are diluted in buffer and DI water to maintain stability and appropriate concentration.

PCR is based on the thermal cycling of the PCR mixture. Thermal cycling consists of heating and cooling of the mixture as many times as needed (typically 30-35 cycles) to achieve the necessary amplification. The PCR process is described below:

Step1-Heat to 95 °C: In this step, the DNA template (double stranded DNA- dsDNA) in the mixture is denatured into 'single strand' DNA as shown in Figure 78.

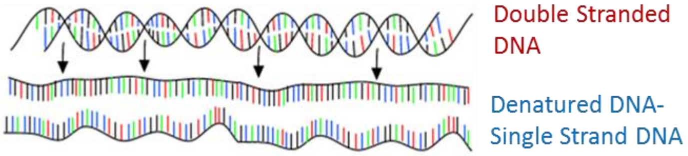

Figure 78. Step 1 of PCR: DNA template denatured into single stranded DNA.

Step 2-Cool down to 50-60 °C: This is the annealing step where the primers bind to the interested target sequence, as seen in Figure 79.

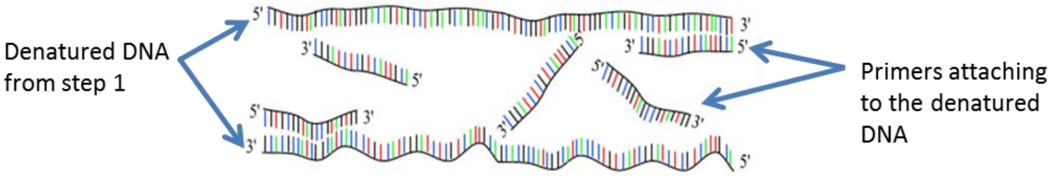

Figure 79. Step 2 of PCR: Forward and Reverse primers attach to the denatured DNA from step1.

Step 3- Heat to 72 °C: This is the extension step for the polymerase to complete the sequence by extending the primers using the individual nucleotides (A, T, C, and G) in the mixture, as illustrated in Figure 80. The end result of one cycle is that from 1 DNA template, 2 copies have been formed.

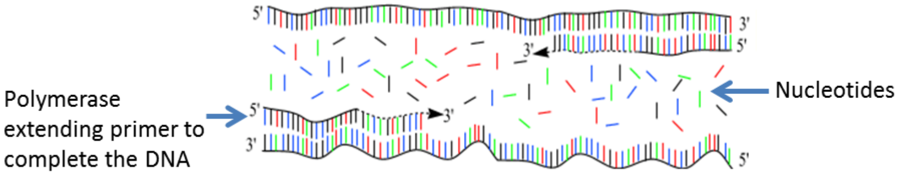

Figure 80. Step 3 of PCR: Polymerase extends the primer to form new DNA sequences.

Since a single template DNA is doubled after every cycle, the end result can be written as $2^{([\# \text{ of cycles}]+1)}$ = total amount of DNA. The doubling trend after each cycle is illustrated in Figure 81. At the end of the 35th cycle, 68 billion copies of the template DNA have been produced.

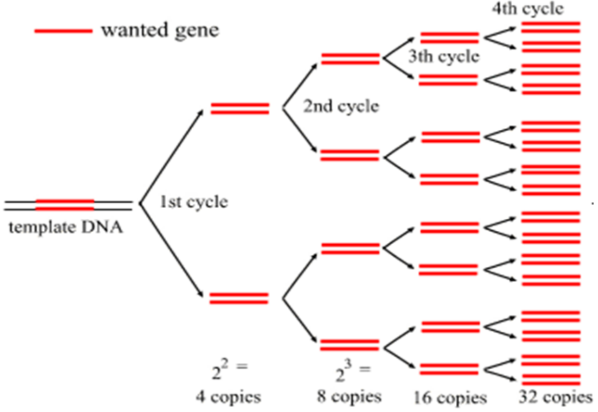

Figure 81. DNA amplification that occurs after every cycle [2].

The importance and effectiveness of PCR is clear from the discussion above. As mentioned in Chapter 3, heaters and RTDs were inkjet printed for use in the thermal cycling process of PCR. PCR is very sensitive to temperatures in each step. In other words, the heaters and RTDs have to work together well in outputting the exact temperature needed at each step. In this chapter, the effectiveness of inkjet printed gold heaters and RTDs will be demonstrated using PCR.

PCR is a fundamental technique in many biological applications including STR (short tandem repeat) typing. STR refers to a short section of an individual's DNA that is used to discriminate that individual from another, a process also known as DNA profiling. Although 99.9% of human DNA sequences are the same in every person, enough of the DNA is different to distinguish one individual from another, and these are categorized into STRs. Gender typing is an application of STR technology where a section of an individual's DNA reveals the gender of the individual. In this project, gender typing is used as a proof of concept for the demonstration of PCR using printed devices.

A process flow of a typical gender typing application in forensics is shown in Figure 82. A DNA sample is first collected from a crime scene. Using an integrated microfluidic system, PCR is performed with this sample, and the amplified product is analyzed using a fluorescent detector. Using results from the detector, the DNA sample is classified as that of a male or a female. This process also allows for DNA sequencing, identification of an individual, etc.

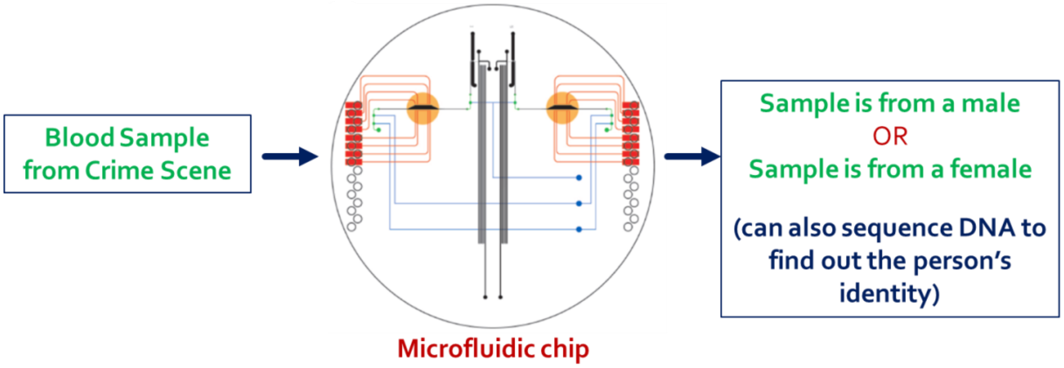

Figure 82. Process flow of a typical STR typing (gender identification) application in forensics.

STR typing applications[3] are in need of a faster, cheaper, and a better method to address the arising challenges in this field. Microfabrication technology can significantly advance STR analysis by transforming the entire process to a nanoliter scale in a miniaturized and integrated microfluidic format. Such an integrated system will decrease time and reagent consumption, making the process more automated, robust, and free of contamination from manual sample handling. Printed electronics takes this one step further and makes the process even more efficient and cost effective. This will be demonstrated in the following sections of this chapter.

Before PCR can be demonstrated using printed devices, the glass substrate with the heater and the PCR reactor has to be in contact with the RTD substrate. This was discussed in Chapter 3 and will be reviewed here again. The basic configuration of a bioprocessor chip contains at least 2 layers of substrates in order to form microfluidic channels and to facilitate the proper functioning of the RTDs and heaters for PCR. The microfluidic channels are important because the functioning and efficiency of a lab-on-a-chip (LOC) system relies on the channels (or trenches that are etched out in the substrate), in which all processes and reactions occur. In other words, a fast (through capillary electrophoresis) and efficient (low volume consumption and no evaporation during thermal cycling) microfluidic system is possible because of the narrow channels that are etched in the substrate.

To form the channels, one layer of the substrate has the etched trenches while the other substrate 'closes' the channels to form a leak-free bioprocessor chip capable of electrophoresis. In addition, the RTD will be placed in between to be in close contact with the PCR chamber. The two substrate layers (shown as glass wafers in Figure 83 and Figure 84) are therefore thermally bonded to form the channels in the chip before use in a biological microfluidic system. Figure 83 and Figure 84 illustrate the cross-sections of the 2 glass substrate layers. The fabrication of the channel layers and the rest of the devices on the chip will be discussed in the following section.

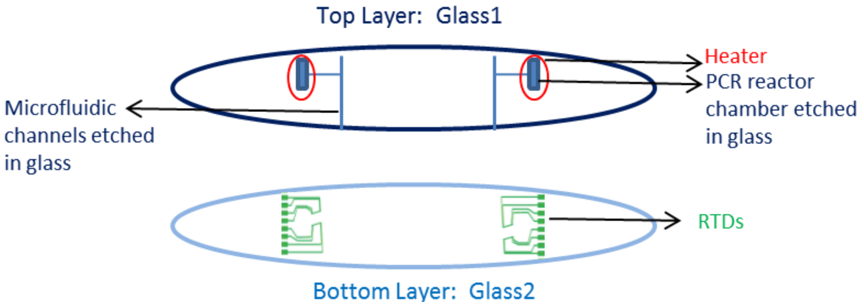

Figure 83. The cross section of the bioprocessor microfluidic chip.

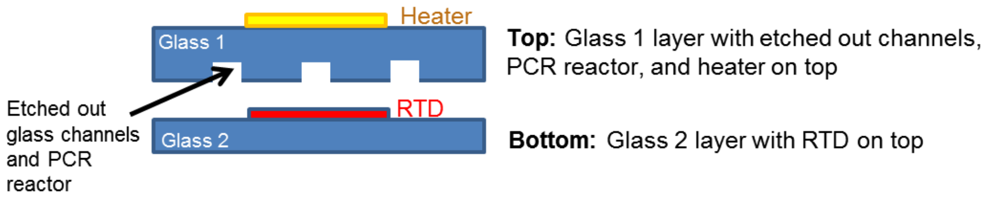

Figure 84. Another cross-section of the microfluidic chip.

When the substrates are bonded together, the RTD is in contact with the PCR chamber. The RTD sensor lines are <1mm away from the reactor. The heater is on the bottom of the glass with the etched PCR reactor. Although some dissipation of heat occurs between the heater and PCR reactor across the 0.5mm substrate, since the RTD is in contact with the PCR reactor, the input voltage to the heater can be adjusted accordingly to maintain the desired temperature at any given time. From experimental evidence, the measured temperature differential across the 0.5mm thick substrate did not exceed 5^{o}C.

The following section discusses challenges and solutions thereof of using two types of bonding techniques, thermal and anodic, to accommodate biocompatibility and the temperature threshold of printed devices. After successful bonding, the integration and demonstration of PCR is presented.

4.2 Integration with Biological Microfluidic System

4.2.1 Fabrication of Channel Wafers

The importance of microfluidic channels has already been discussed. To summarize, microfluidic channels are crucial in the functioning of the microfluidic system since they play an important role in facilitating a fast and efficient system. The advantages that an integrated microfluidic system provides, such as minimum time and reagent consumption, depend on the narrow etched microfluidic channels in the glass substrate. Therefore, to form the channels, two substrate layers are required. Moreover, the two layers need to be bonded together to ensure that PCR, electrophoresis and other processes can occur on this chip. Two types of bonding will be discussed, namely anodic and thermal bonding.

For both types of bonding, the fabrication process of the channel wafers (glass 1 layer in Figure 84) stays the same. The fabrication process for glass1 is described below:

1) Borofloat glass wafers (used in Chapter 3) are first cleaned with piranha solution.

2) The glass wafers are then coated with an amorphous silicon (A-Si) layer (used as a hard mask for etching). The glass wafers were sent for coating to *UHV Sputtering, Morgan Hill, CA.* 200nm of silicon was deposited on both sides of the glass wafers. Silicon deposition can also be done using a PECVD furnace.

3) The wafers are piranha cleaned again and baked at 120^{0}C for 10 minutes.

4) Next, the wafers are primed with HMDS, hexamethyldisilazane for 5 minutes.

5) The wafers are spin coated with Microposit S1818 positive photoresist at 2500rpm for 30 seconds. The photoresist needs to be evenly distributed on the wafer to yield good feature definition.

6) The wafers are then baked on a hotplate at 120^0C for 2 minutes and 30 seconds.

7) The wafers are exposed to UV light using an appropriate mask to define channels.

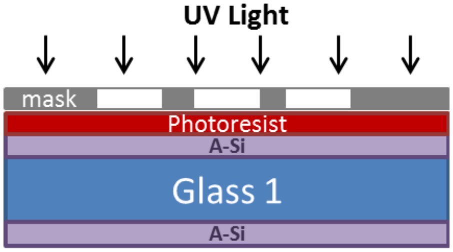

8) The wafers are developed in Microdev (S1818 developer), in a 1:1 ratio of water to developer.

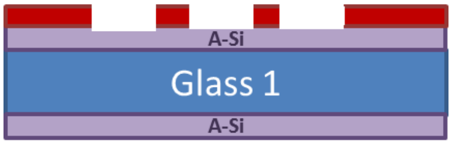

9) A-Si is etched in open channel areas using a plasma etching system. 1 minute of O_2 plasma followed by 1.5 minutes of SFO_6 plasma etch completely removes the 200nm of A-Si in channel areas.

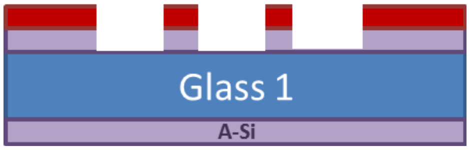

To avoid etching of silicon at the bottom of the glass wafer, the back side is covered with dicing tape *(Silicone-Free Adhesive Plastic Film,* Ultron Systems, Inc., Moorpark, CA*)*that is resistant to plasma and acids at short time exposures. The A-Si needs to be present on the back side of the wafer to prevent this side from etching in the following step.

10) The channels are etched by dipping the glass wafers in 49% HF for 4 minutes at an etch rate of ~8μm/minute. The final etched depth is ~35μm.

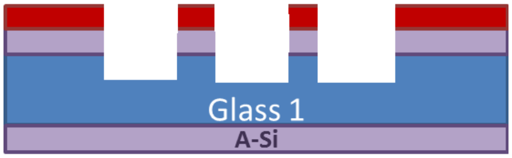

11) The dicing tape from step 9 is removed since it is not compatible with the resist stripper used in this step. The photoresist on the substrate is then stripped by soaking in heated Baker-PRS 3000 resist stripper for 20 minutes.

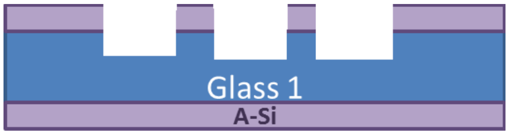

12) A-Si is etched from back side of wafer using the same process as step 9. The A-Si on the top side is kept on the wafer till the very end to avoid contamination. The back side of the wafer has to be cleared to facilitate the following drilling step.

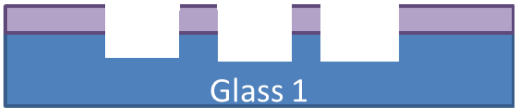

13) Input and output holes (for fluid transfer and electrophoresis)and holes to make contact to RTDs were drilled into the etched glass wafer with a 1.25-mm-diameterdiamond-tipped drill bit, a protective resin layer, and a backing wafer; the latter two are used to prevent residual cracking near the drilled holes. The holes are drilled using a drilling setup made by *Cameron Micro Drill Presses* [4].

14) Finally, A-Si is etched from top side of the wafer using the same process as step 9.

This fabrication procedure was sometimes altered by substituting an evaporated Chrome (20 Angstroms)/ Gold (1000 Angstroms) as a hard mask in place of the Amorphous Silicon layer in Step 2. As a result, in step 14, a gold etchant (Gold Etchant Type TFA, Transene Company, Inc.) followed by a chrome etchant (CR-7, Cyantek Corporation) was used to remove the gold and chrome layers [5].

The top view of the etched glass wafer is shown in Figure 85. It was placed on top of a bare silicon wafer to obtain a good image. The different parts of this microfluidic channel wafer, namely RTD contact holes, cathode, anode, waste, and PCR chamber, are labeled in Figure 85. The importance of each of these components will be explained in section 4.3.

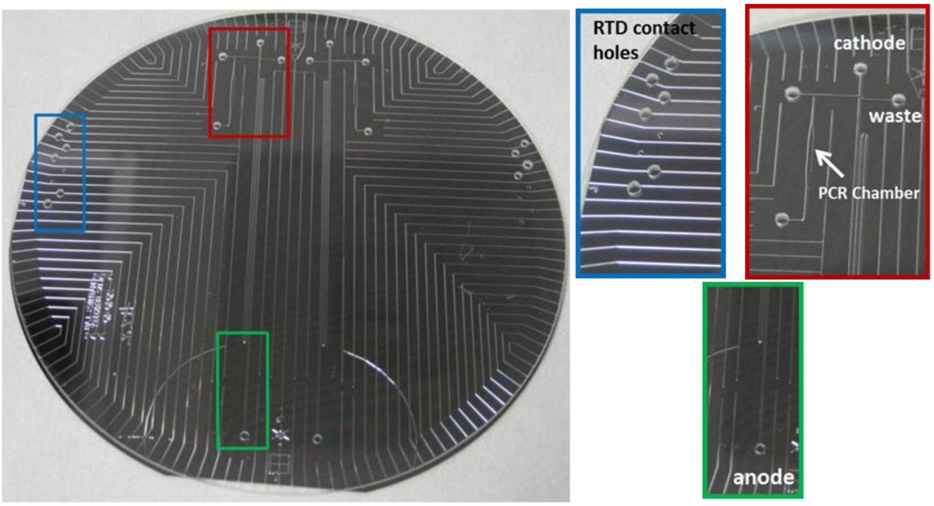

Figure 85.Top view of the etched glass wafer.

The following steps precede the demonstration of PCR using printed heaters and RTDs:
1) RTD is printed on Glass2 using optimized conditions from Chapter 3.
2) Glass1 (fabricated in this section) is bonded to Glass2 using desired bonding method.
3) Heater is printed on Glass 2 (on the outside of the bonded chip).

Each of these steps will be discussed in the next few sections for both thermal and anodic bonding.

4.2.2 Thermal Bonding

Thermal bonding of glass occurs above the glass transition temperature (T_g). Holding two glass wafers together at a relatively brittle and liquid state (i.e. at T_g) for a few hours facilitates the bonding of the wafers. The borofloat glass wafers used in this project had a T_g of 525^0C[6].

Glass1 has been fabricated in the previous section. Glass2 is first treated with piranha solution to arrive at an optimum surface for printing (discussed in Chapter 3). Gold RTDs are then printed (using optimized conditions from Chapter 3) and annealed (at 250^0C for 1 hour) on Glass2 such that they match the location and orientation of the PCR chamber in Figure 85.

The thermal bonding of the glass wafers in this project was conducted using a Centurion™ NeytechQex Vacuum Furnace pictured in Figure 86.

Figure 86. Centurion NeytechQex vacuum furnace used for thermal bonding of glass wafers.

The two glass layers are assembled in between two graphite blocks as shown in Figure 87. Graphite has high thermal conductivity compared to glass. The graphite blocks ensure that glass wafers reach the desired T_g to bond together. Additional graphite powder is sprinkled on the graphite blocks before placing the glass wafers to enhance this effect. The graphite-wafer assembly is then placed into the furnace. A stainless steel disk (1 kg) is then placed on top of the assembly. The steel disk prevents warping of glass (in the +/- Z direction) during high temperature bonding.

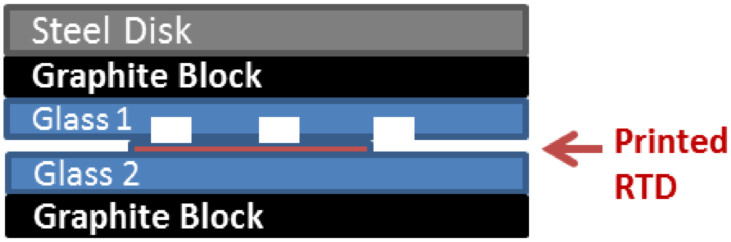

Figure 87. Wafers and graphite blocks set up for thermal bonding.

The first few steps of the thermal bonding recipe includes a few cycles of vacuum (30 mmHg or below) and nitrogen purge to keep the furnace free of contamination. The recipe then includes ramp and hold steps at desired temperatures for bonding. These steps had to be optimized in this project to minimize high temperature exposure to the printed gold RTDs. Optimization of the thermal bonding recipe and the corresponding clean treatments will be discussed next.

4.2.2.1 Initial Bonding Recipe and Results

The first thermal bonding test was conducted using a working (but not completely optimized) bonding recipe used by Professor Mathies' group at UC Berkeley. The experimental protocol for this test and the corresponding results are presented in this section.

a) Cleaning treatments before bonding

Glass1 layer was cleaned with piranha solution right before bonding. Glass2 was piranha cleaned before printing of RTDs but not right before bond because of the gold pattern on the surface. It was kept as clean as possible between initial piranha clean treatment before print and before bonding.

b) Thermal Bonding Recipe

The recipe steps entered into the furnace are listed below:
1) 3-4 cycles of vacuum and nitrogen purge
2) Ramp from room temperature to 500^0C at 20^0C/min
3) Hold at 500^0C for ~20 minutes
4) Ramp from 500^0C to 650^0C at 5^0C/min
5) Hold at 650^0C for 10 hours to bond
6) Cool down to room temperature
7) Release furnace pressure to atmosphere to unload

c) Results

The results from this bonding test were not very promising. To begin with, the glass did not bond around the microfluidic channel areas, as seen by the Newton's rings in Figure 88. The presence of Newton's rings indicates that an air gap or unbounded areas exist at these spots. Also, the initially conductive RTDs became non-conductive after bonding. The silver epoxy labeled in the figure below is applied after bonding and protects the gold contact pads of RTDs and heaters from being scratched during measurements. These results are discussed in detail in the following section.

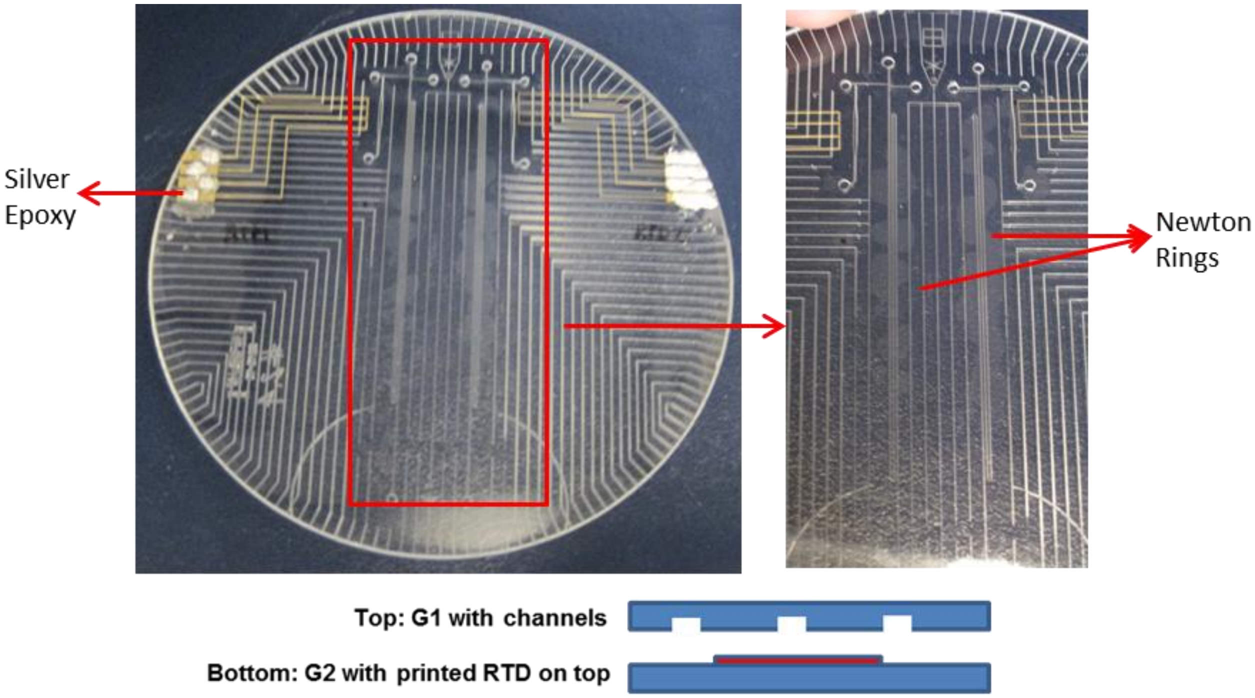

Figure 88. Initial thermal bonding results exhibit Newton's rings and non-conductive RTDs.

4.2.2.2 Discussion of Initial Bonding Results and New Optimized Solutions

a) Discussion of Results

The Newton's rings seen in Figure 88 were caused by the unclean surface of the RTD wafer (i.e. glass2 layer). Although glass1 was cleaned in piranha solution right before bond, glass2 could not be cleaned because of the gold pattern on the surface. UV-Ozone (UVO) treatment performed using *Jetlight UVO Cleaner 42* [7] resulted in a clean surface for glass2 without affecting the printed RTDs. Different UVO clean times were tested: 20 minutes, 1 hour, 1.5 hours, and 2 hours. While all four tests yielded good bonds, longer UVO cleaning times (> 1 hour) resulted in non-conductive RTDs.

Although the reasoning for this behavior needs to be studied further, the trend can be explained by understanding the annealing process of the printed gold RTDs. When gold is printed and annealed, 99% of the organic solvent in the ink evaporates during anneal. The remaining organic solvent is most likely helping the gold 'stick' to the glass. When the substrate with the RTD is exposed to long UVO treatments, the residual organic solvent may be getting removed, causing the RTDs to delaminate and become nonconductive. Therefore, the UVO treatment time had to be minimized.

Looking more closely at the non-conductive RTDs that resulted after bonding, the behavior shown in Figure 89 is observed. After high temperature thermal bonding, the gold patterns becomes extremely porous. When the porosity is too high, a conductive path ceases to exist and results in non-conductive RTDs.

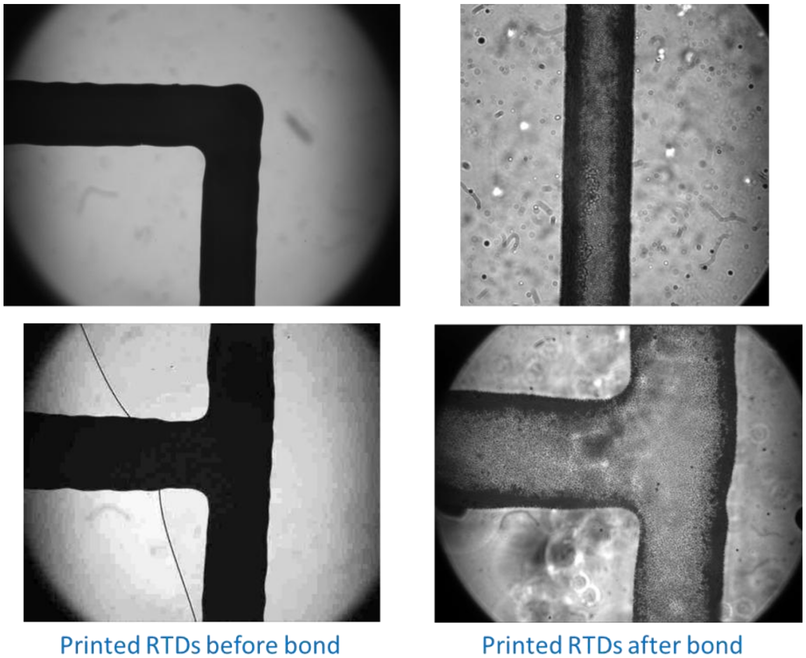

Figure 89. The printed gold patterns become porous after thermal bonding, leading to non-conductive RTDs.

The porosity and discontinuity that occurs with gold nanoparticle films at high temperatures have been studied previously[8]. A summary of results from Vakarelski et al [8]explaining this behavior is shown in Figure 90.

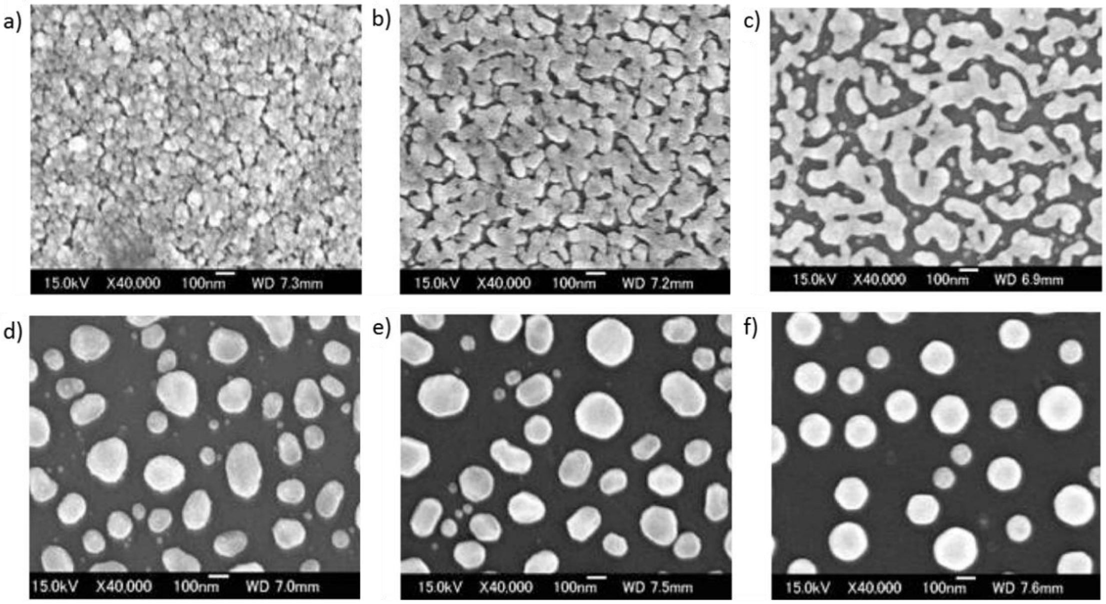

Figure 90. SEM of gold nanoparticle films as a function of increasing temperature: (a) 25^{0}C, (b) 150^{0}C, (c) 250^{0}C, (d) 450^{0}C, (e) 900^{0}C and (f) 1100^{0}C**[8]**.

The absolute temperatures shown in Figure 90 are specific to the type of gold nanoparticle films studied in the referenced paper. In that studied system, 150^{0}C was the ideal temperature for the gold nanoparticle films to result in highest conductivity; as the temperature increased above150^{0}C, fragmentation started to occur as nanoparticles started migrating within the film, causing conductivity of the film to drop. As temperature increased further, the nanoparticle films started migrating and coalescing even more to form individual disconnected agglomerates, thus resulting in a nonconductive film. The same behavior is being observed with the printed RTD films as they experience high thermal bonding temperatures for 10+ hours.

b) New Optimized Solutions

Two parameters were varied to arrive at conductive RTDs after thermal bonding. First, different iterations of the bonding recipe were tested to minimize the time and high temperature exposure to printed RTDs. The initial bonding recipe was altered. First, the ramping rate from room temperature to ~650^0C was increased. This reduced the time of high temperature exposure. The printed RTDs were tested to withstand temperatures up to 350^0C without displaying any appearance or conductivity changes. So, the recipe was adjusted keeping this temperature in mind. Next, the time required for bonding at 650^0C was not originally optimized since evaporated platinum RTDs (previously used in place of printed gold RTDs) did not exhibit any porosity or conductivity problems after bonding. Since this was a concern for printed gold RTDs, after a few iterations and bonding tests, the time required for the bonding was optimized and reduced from 10 hours to 1 hour (minimum amount of time needed), reducing the overall high temperature exposure time significantly. Finally, since the T_g of the borofloat glass wafers was 525^0C, temperatures between 525^0C and 650(initial bonding temperature) were tested to minimize the temperature necessary to get a good bond. The temperatures tested included 550^0C, 575^0C, 590^0C, 600^0C, 620^0C, 625^0C, and 650^0C. 625^0C was necessary to get a good repeatable bond. These results are also summarized in Table 6.

The final optimized recipe is presented below:
1) 3-4 cycles of vacuum and nitrogen purge
2) Ramp from room temperature to 350^0C at 20^0C/min
3) Hold at 350^0C for ~20 minutes
4) Ramp from 350^0C to 600^0C at 20^0C/min
5) Ramp from 600^0C to 625^0C at 5^0C/min
5) Hold at 625^0C for 1 hour to bond
6) Cool down to room temperature
7) Release furnace pressure to atmosphere to unload

This new recipe has reduced the overall time of exposure to temperatures above 350^0C (i.e. temperatures that affect printed gold RTD conductivity) from 10 hours 74 minutes (old recipe) to 1 hour 55 minutes (new recipe), and still resulted in a great bond. The repeatability of a good bond result with the new recipe was tested and verified multiple times, confirming a new optimized working recipe.

The new recipe had to be combined with the optimization of another parameter to arrive at conductive RTDs after thermal bond. The dimensions of the lines that form the RTD were varied to test the dimensions that survived the optimized new recipe. The two structures in Figure 91 were printed with the specified dimensions. The structure in Figure 91a varied the width of the lines alone while Figure 91b varied the thickness (height) and width of the lines that form the RTD. These structures were printed multiple times on different substrates and bonded to test for conductivity.

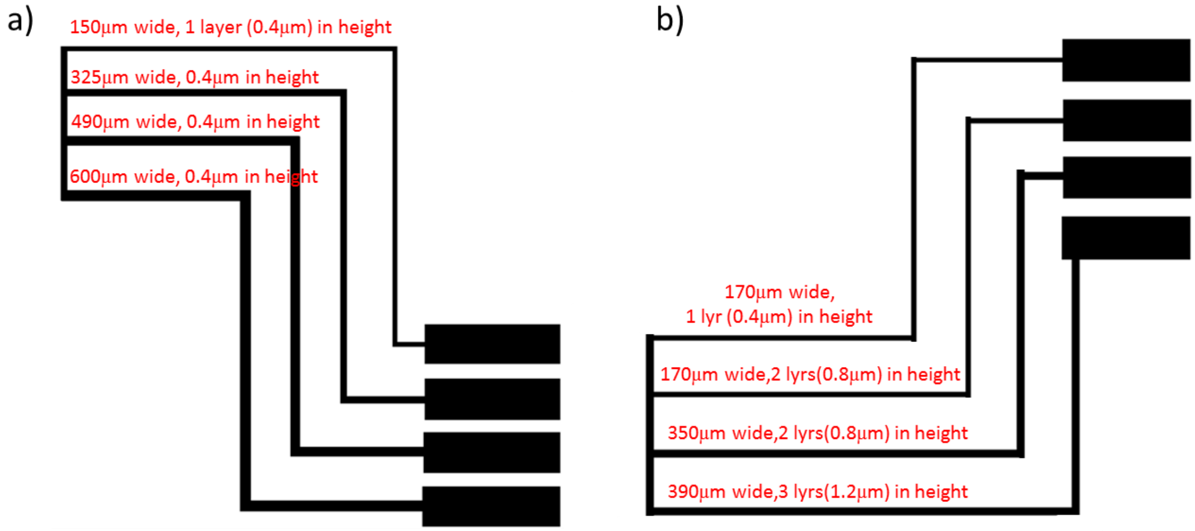

Figure 91. The RTD line dimensions were varied to confirm the ideal width and height for conductive RTDs: a) Varying width of lines, b) Varying width and height of lines.

Although the wider lines in Figure 91a were conductive at times after bonding with the new optimized recipe, the results were not consistent. The last three lines in Figure 91b resulted in conductive RTDs in all of the bonding tests. In other words, regardless of the width, the thicker (in height) lines (2 layers or higher) always resulted in conductive RTDs after thermal bond. Therefore, for the new bonding recipe to yield conductive RTDs, RTD lines of 0.8µm (1 layer= 0.4µm) or higher is required. The parameters optimized in this section are summarized in Table 6.

	UVO Clean of Glass2 Wafer				Dimensions of RTD lines			Bonding Temperature (^{0}C)			
	20mins	1 hour	1.5 hrs	2 hrs	1 layer height - ~0.4µm (any width)	2 layer height - ~0.8µm (any width)	3 layer height - ~1.2µm (any width)	550	600	625	650
Good Thermal Bond?	Yes	Yes	Yes	Yes	N/A	N/A	N/A	No	No	Yes	Yes
Conductive RTDs?	Yes	No	No	No	No	Yes	Yes	Yes	Yes	Yes	Yes

Table 6. Summary of results for good thermal bond and conductive RTDs as discussed in this section.

The green columns in Table 6 result in the desired thermal bond characteristics and conductive RTDs. Having thus optimized for good bond and conductive RTDs, the next step is to print the heaters on the bonded sample. Before describing this process, initial results from anodic bonding will be discussed.

4.2.3 Anodic Bonding

Anodic bonding is a low temperature bonding process that assists in bonding of glass to glass wafers. The printed gold layers can easily endure the lower temperatures. Therefore, anodic bonding was simultaneously studied as a good alternative for thermal bonding.

The theory behind anodic bonding is delineated in Figure 92.

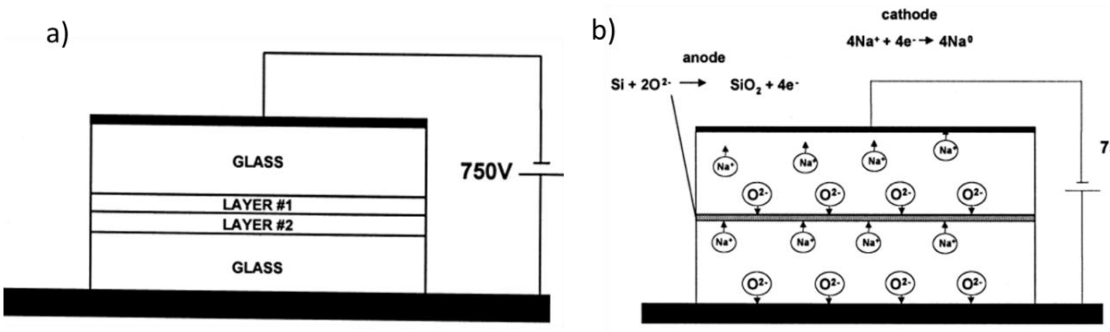

Figure 92. Anodic bonding setup and mechanism: a) schematic of the setup inside the anodic bonder, b) working mechanism of anodic bonding **[9]** .

Layer # 1 and #2 in Figure 92a will be explained shortly. As seen in Figure 92b, when a voltage is applied to the glass layers and heated to 350-400^{0}C as required by anodic bonding, the sodium oxide in the glass layers splits up into sodium and oxide ions. The glass layer with the negative polarity (glass1) pulls the positive sodium ions from both glass layers towards the top edge of glass1, where the sodium ions get neutralized. The glass layer with the positive polarity (glass2) pulls the negative oxygen ions towards the bottom edge of glass2. Due to the high electric field, the glass wafers are attracted to each other and the oxygen ions moving towards the anode react at the glass-glass interface with silicon, forming an irreversible silicon-oxygen-silicon bond between wafers. *In order to keep the sodium ions from diffusing and interrupting this chemical bond at the glass-glass interface, a sodium diffusion barrier needs to exist.* The choices for these intermediate layers (between glass1 and 2) have been studied previously and are shown in Table 7.

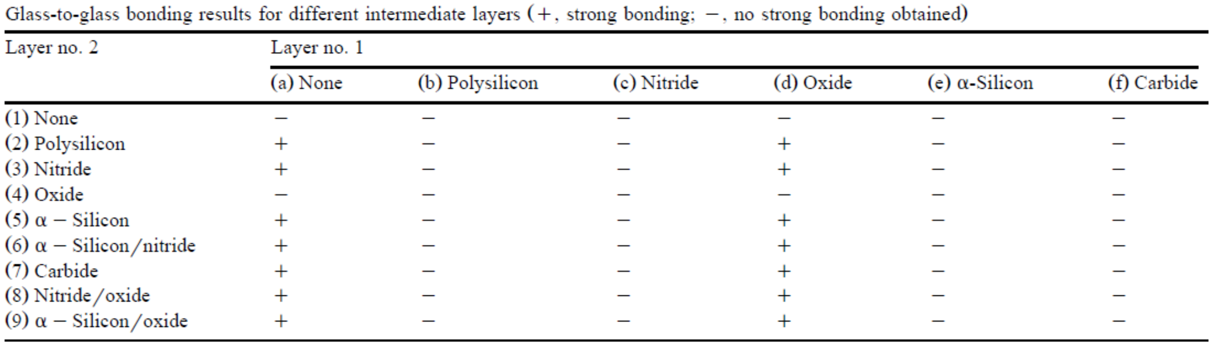

Glass-to-glass bonding results for different intermediate layers (+, strong bonding; −, no strong bonding obtained)

Layer no. 2	Layer no. 1					
	(a) None	(b) Polysilicon	(c) Nitride	(d) Oxide	(e) α-Silicon	(f) Carbide
(1) None	−	−	−	−	−	−
(2) Polysilicon	+	−	−	+	−	−
(3) Nitride	+	−	−	+	−	−
(4) Oxide	−	−	−	−	−	−
(5) α − Silicon	+	−	−	+	−	−
(6) α − Silicon/nitride	+	−	−	+	−	−
(7) Carbide	+	−	−	+	−	−
(8) Nitride/oxide	+	−	−	+	−	−
(9) α − Silicon/oxide	+	−	−	+	−	−

Table 7. Intermediate layers between glass wafers that function as a sodium diffusion barrier layer and contribute towards the bonding of the two glass wafers. The chart above indicates combination of the interfacial layers that result in good bonding of the two glass wafers **[9]**.

Layer 1 and Layer 2 in Table 7correspond to the same labels in Figure 92a. As seen in Table 7, many choices for layer 1 and 2 lead to a good bond.

To be used for biological applications, the background fluorescence of the layers used needs to be minimal. As discussed in Chapter 1, the final step in any detection or sequencing application today is use of a laser detector. The laser detector senses the fluorescently tagged DNA in the microfluidic channel. To keep this process as effective as possible, the inherent fluorescence from the substrate needs to be very low.

Thus, minimizing the number of intermediate layers was desirable. None of the choices in the layer 2 column, except oxide, require an additional layer 1 to form a good bond. Particularly, polysilicon, (Si)-nitride, α-Si, and (Si)-carbide do not require an additional oxide layer within layer 2 to form a good bond. The choices were further narrowed down to (Si)-nitride and α-Si based on available glass-compatible low temperature deposition tools.

The thickness of the layers had to be minimized to reduce background fluorescence, but a certain thickness is also required to form a good bond. The nitride and amorphous silicon layers were deposited using *Oxford2*, a PECVD system[10]. The glass wafers were piranha cleaned right before deposition of the nitride and α-Si layers.

The background fluorescence of the (Si)-nitride and α-Si layers were tested using a laser-induced fluorescence with the Berkeley rotary confocal scanner [11]. The scanner detects 4 different wavelengths, namely red, yellow, green and blue. The results from nitride and α-Si layers of relatively low thicknesses are shown in Figure 93. The random spikes seen in all three graphs in Figure 93 are as a result of the detector hitting a corner of the sample, one of the microfluidic channels or a dust particle.

The graphs in Figure 93 show that the typical glass substrate used for biological applications emits almost no background fluorescence. The blue wavelength detected in both the nitride and amorphous silicon layer result in a wave-like pattern because of a focusing issue with the detector. The other three wavelengths (red, yellow, and green) can be compared to the reference glass substrate. The 50nm nitride layer exhibits higher background fluorescence than the 20nm amorphous silicon layer on glass. The red wavelength detected in the nitride layer is especially high. The intensity the 3 focused wavelengths (red, green, and yellow) in the amorphous silicon layer is comparable to the reference glass substrate, and the glass substrate was later focused to exhibit a low background fluorescent intensity on the blue wavelength as well. Therefore, amorphous silicon was used as layer 2 for the anodic bonding experiments.

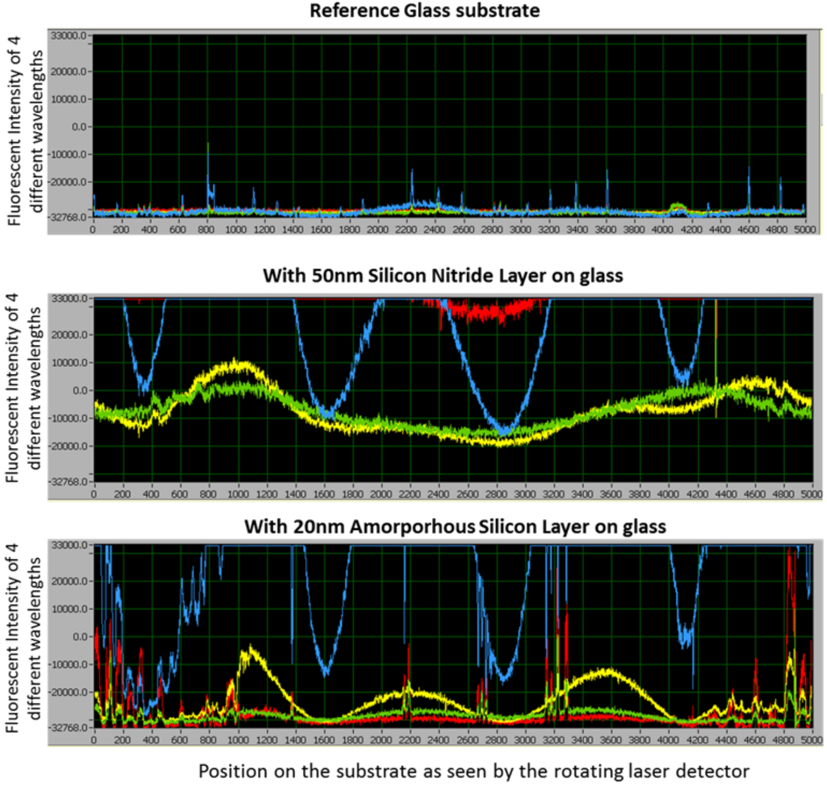

Figure 93. Background fluorescence results of reference glass substrate, 50nm silicon nitride on glass, and 20nm amorphous silicon on glass.

Anodic bonding of the glass wafers was performed using a Karl Suss SB6 Thermocompression & Anodic Bonder[10]. The glass-Si-glass substrate setup used for anodic bonding is shown in Figure 94.

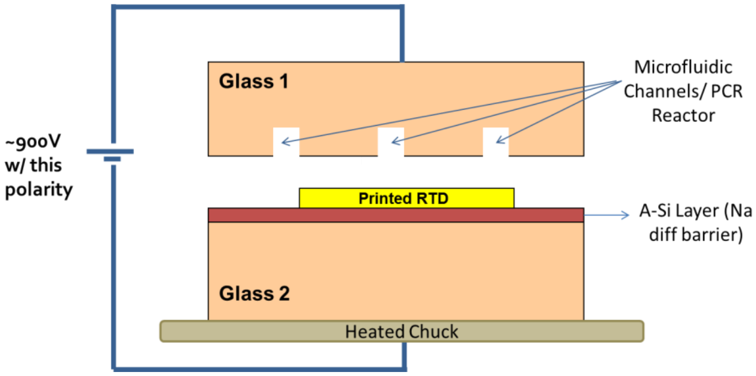

Figure 94. Substrate and RTD pattern setup for anodic bonding.

The channels (and PCR reactor) in the Glass1 layer was defined using the protocol described in section 4.2.1. *The fabrication process for the glass2 layer for anodic bonding is described below:*

1) Glass2 layer was cleaned with piranha solution.

2) PECVD system was used to deposit the desired thickness of amorphous silicon layer.

3) Glass2 layer was cleaned with piranha solution (after the deposited barrier layer).

4) Gold RTDs were inkjet printed with the optimized print parameters from Chapter 3.

5) Right before bond, glass1 layer was piranha cleaned and glass2 layer with the printed RTD was cleaned with 1 hour of UVO treatment.

The contact angle formed by the gold ink on piranha cleaned α-Si in step 4 above is lower than that formed on piranha cleaned glass layer. Therefore, the print pattern had to be made thinner to accommodate for the spreading.

The heatable chuck inside the bonder holds the setup in Figure 94. The electrodes come down to apply the set voltage after the substrate is heated to the desired temperature.

The anodic bonding process used by the bonder is described below:

1) The setup in Figure 94 is entered into the chamber.

2) The desired recipe is entered into the bonder software system.

3) The chuck heats the glass-Si-glass setup to the set temperature.

4) The electrode system comes into contact with the substrate setup and applies the set voltage.

5) The bonder holds the voltage and temperature till the wait condition is satisfied. Many parameters can be used for the hold condition, including time, current level, etc. The most effective hold condition for anodic bonding is when the final current level is below 10% of the maximum current level detected when the wafers are being bonded. This concept is further depicted in Figure 95, a screenshot of a tracking tool available within the bonder that tracks the current level as a function of time.

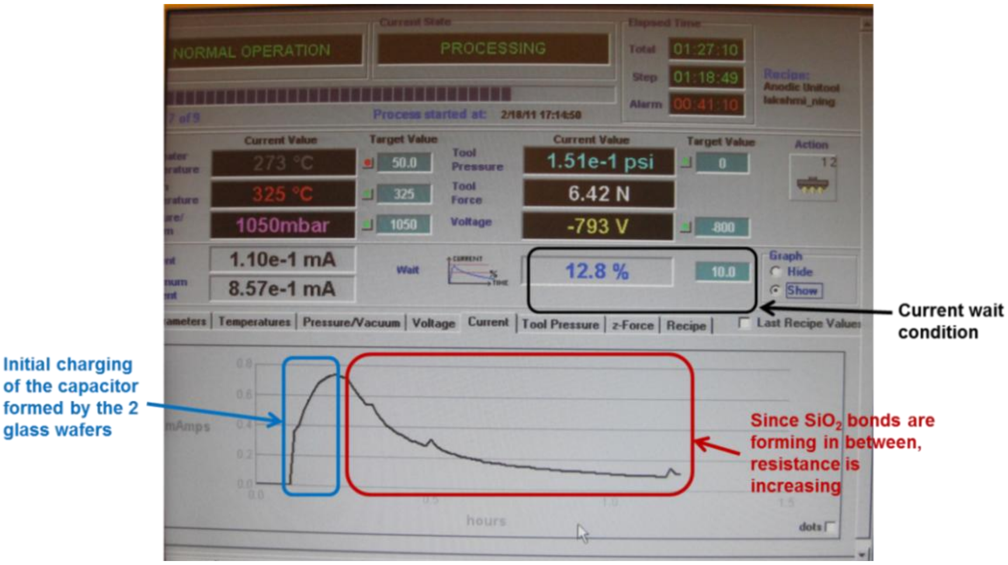
Current State

NORMAL OPERATION

PROCESSING

Elapsed Time

Total 01:27:10

Step 01:18:49

Alarm 00:41:10

Recipe:
Anodic Unitool
lakshmi_ning

7 of 9

Process started at: 2/18/11 17:14:50

	Current Value	Target Value		Current Value	Target Value
ater erature	273 °C	50.0	Tool Pressure	1.51e-1 psi	0
rature	325 °C	325	Tool Force	6.42 N	
re/ n	1050mbar	1050	Voltage	-793 V	-800

nt 1.10e-1 mA

mum nt 8.57e-1 mA

Wait 12.8 % 10.0

Graph ○ Hide ● Show

ameters | Temperatures | Pressure/Vacuum | Voltage | Current | Tool Pressure | z-Force | Recipe |

☐ Last Recipe Values

Current wait condition

Initial charging of the capacitor formed by the 2 glass wafers

Since SiO_2 bonds are forming in between, resistance is increasing

Figure 95. Screenshot of the anodic bonder control software. The graph shows the current (mAmps) measured from the glass wafer setup inside the bonder as a function of time (hours) during the bonding process.

The time vs. current graph in Figure 95 illustrates the principle behind anodic bonding. Since the glass-glass assembly inside the bonder is essentially a capacitor, the initial increase in current seen in this graph is due to the initial charging of the capacitive plates (glass wafers). Once the bonding process starts and SiO_2 bonds start forming in between the glass wafers, the current drops because the overall resistance in the system in increasing.

Although an intermediate 20nm α–Si diffusion barrier layer resulted in the lowest background fluorescence, a 100nm α–Si barrier layer was needed to get a good anodic bond. Also, the temperature and voltage needed for the glass-αSi-glass system in Figure 94 had to be optimized to achieve good bonding. Anodic bonding experiments were conducted using 700-1000V at 300-400^{0}C. *The optimum combination for the borofloat glass wafer anodic bonding was 900V at 325^{0}C.* 5-7 hours of bonding were required to reach <10% of the maximum current and a good bond. The final anodically bonded sample is shown in Figure 96. The heater was printed after glass1 and glass2 wafers were anodically bonded and is also shown in Figure 96. The substrate treatment needed to print good heaters (after anodic and thermal bonding of the wafers) will be discussed in the next section.

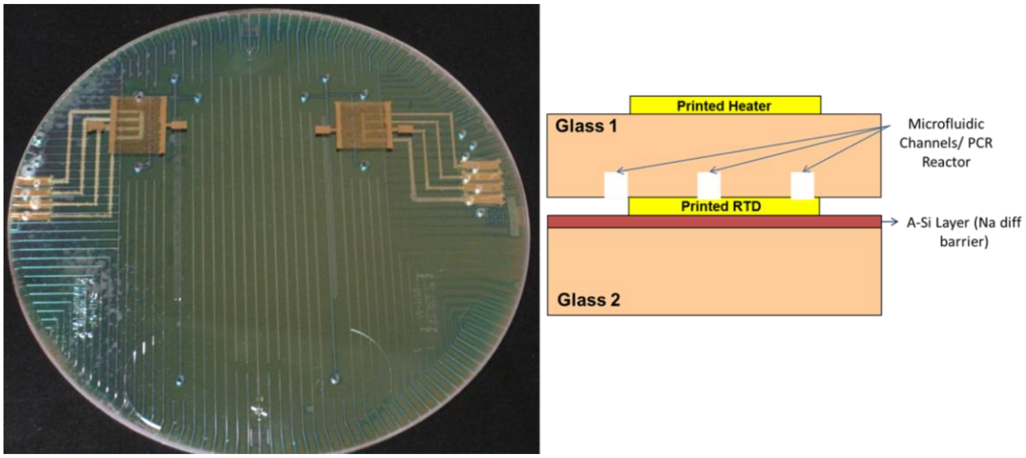

Figure 96. Image and schematic of the final anodically bonded sample using optimized bond and clean parameters.

The thicker 100nm α–Si barrier layer required for good anodic bonding makes the bonded structure unusable for biological applications because of the relatively higher background fluorescence. But, silicon can be removed by Pottasium Hydroxide (KOH). The background fluorescence is a concern only in microfluidic channels because the DNA detection only happens in these channels. Silicon was therefore selectively removed in these etched out channels in the bonded structure.

Because the glass wafers have been in the bonder for a few hours at 325^0C and especially since the anodic bonder was *not* under vaccuum during bonding, the α–Si layer in the channel has a thin layer of oxide on it. Before using KOH to revome silicon, HF was used to etch the thin layer of oxide on the exposed silicon surface in the channel areas. HF and other fluids move in the microfluidic channels through capillaryforces[12,13]. *The process used to etch α–Si from the channels is described below:*

a) 5:1 HF solution is left in the channel for 1 minute to etch the thin layer of oxide on the α–Si.

*b)*The etch rate of silicon at different temperatures using 10% KOH is shown in Figure 97. Using this data, the substrate is placed on a hot plate set to the desired tempreature and KOH is kept in the channels for the appropriate time.

c) KOH is then removed from the channels with water.

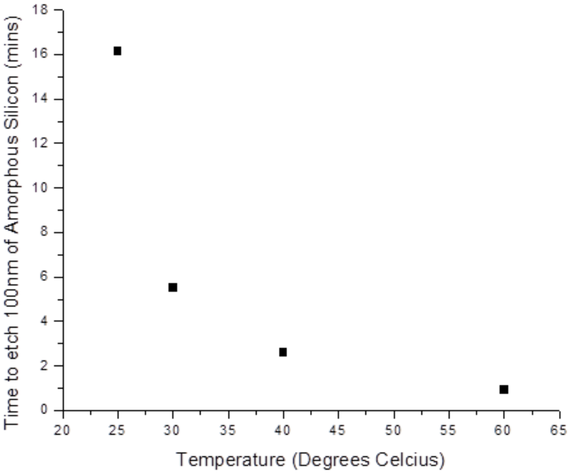

Figure 97. Etch rate of 100nm of amorphous silicon in 10% KOH at different temperatures.

In this experiment, the substrate was heated to 30^0C and 10% KOH was left in the channel for about 16 minutes. As expected, the silicon was etched out of the channels. Figure 98 shows zoomed in images of different parts of the bonded channels after the α–Si was etched out.

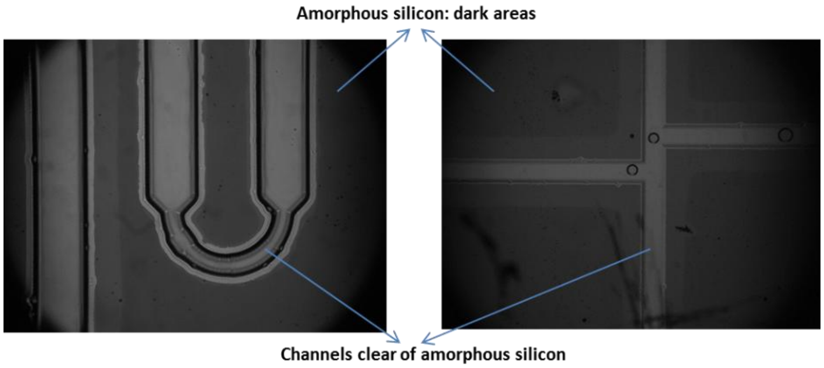

Figure 98. Micrographs of different parts of the bonded channels after etching of silicon.

The fluorescent tests of these clear channels showed the same results as those from the reference glass substrates and therefore proved to be biocompatible. With this anodic bonding experiment, 10% KOH proved to be too high of a concentration since overnight, the silicon etched laterally more than expected, causing inaccuracy in the reactor dimensions. Using ~1% KOH should result in a controllable etch of silicon in the channels making the anodic bonding a potentially feasible, print-compatible and biocompatible process for microfluidic applications.

4.2.4 Printing Heater after bonding

To demonstrate PCR in this project, thermal bonding (discussed in section 4.2.2) was used. Before PCR can be demonstrated, heaters need to be printed on the bonded samples.

When glass has been exposed to high temperatures (such as in thermal bonding or anodic bonding), the glass surface becomes very hydrophilic after bonding [14, 15]. Since the glass surface has a very low contact angle after bond, the heater print spreads more than desired and becomes uncontrollable. Different surface treatments were attempted to get an ideal surface energy for uniform and controllable heater printing.

Since the surface is very hydrophilic, HMDS would be a viable option to increase the contact angle. Unfortunately, the adhesion between printed gold and HMDS was very poor. When HDMS was used, the printed gold delaminated during anneal, measurement and consequent processes. Other options such as plasma clean, organic solvent clean, and UVO clean were also attempted to ‘revive’ the glass surface, but they either made the surface more wetting for the gold ink and/or did not lead to the uniform surface needed for printing of heaters.

Referring back to the optimized surface treatments in Chapter 3, the bonded system could not be dipped in piranha solution because the solution would attack the RTDs that are in between the bonded wafers through the open contact pad holes (shown in Figure 85). Therefore, the area right above the PCR chamber was selectively cleaned with piranha solution to facilitate uniform heater printing. This process worked for thermally and anodically bonded substrates. Two different setups were used for the local piranha clean, and they are shown in Figure 99 and Figure 100. The first set up (Figure 99) uses acid resistant tape to cover the RTD contact holes and any other areas or openings that would allow piranha solution to enter the bonded wafers.

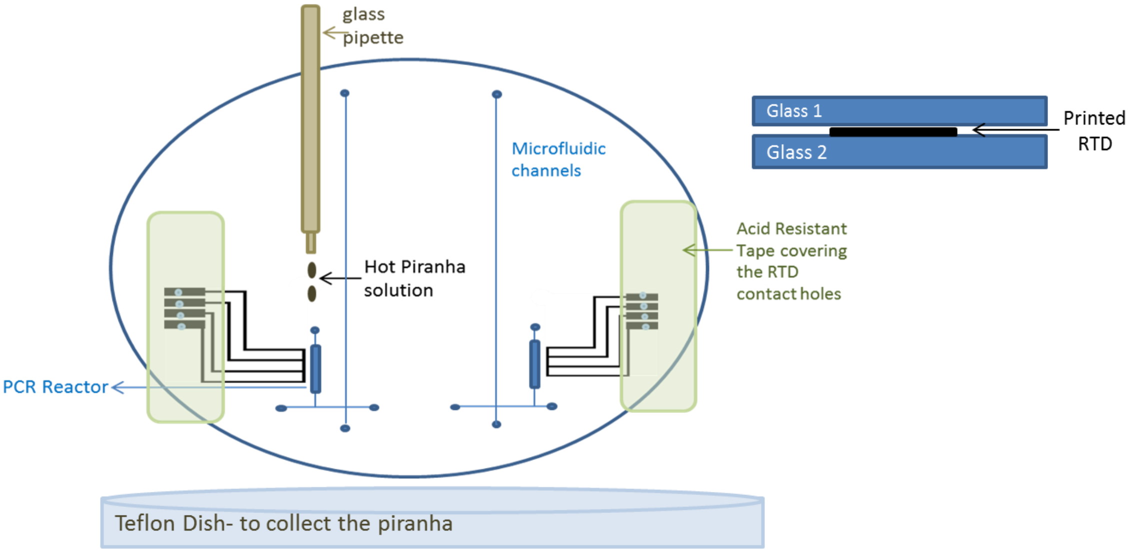

Figure 99. Top view (left) and cross section (right) of cleaning setup1 on a bonded chip to get clean surface for heater printing.

Using a glass pipette, hot piranha solution was carefully pipetted multiple times to cover the area where the heater was to be printed. The wafer was held at an angle in a Teflon dish during pipetting such that the piranha solution would empty into the dish and not spread to other areas of the bonded substrates. The areas that were piranha cleaned were then pipetted with water to clean the residual piranha solution, as per usual protocol with piranha cleaning treatments. The second setup is demonstrated in Figure 100.

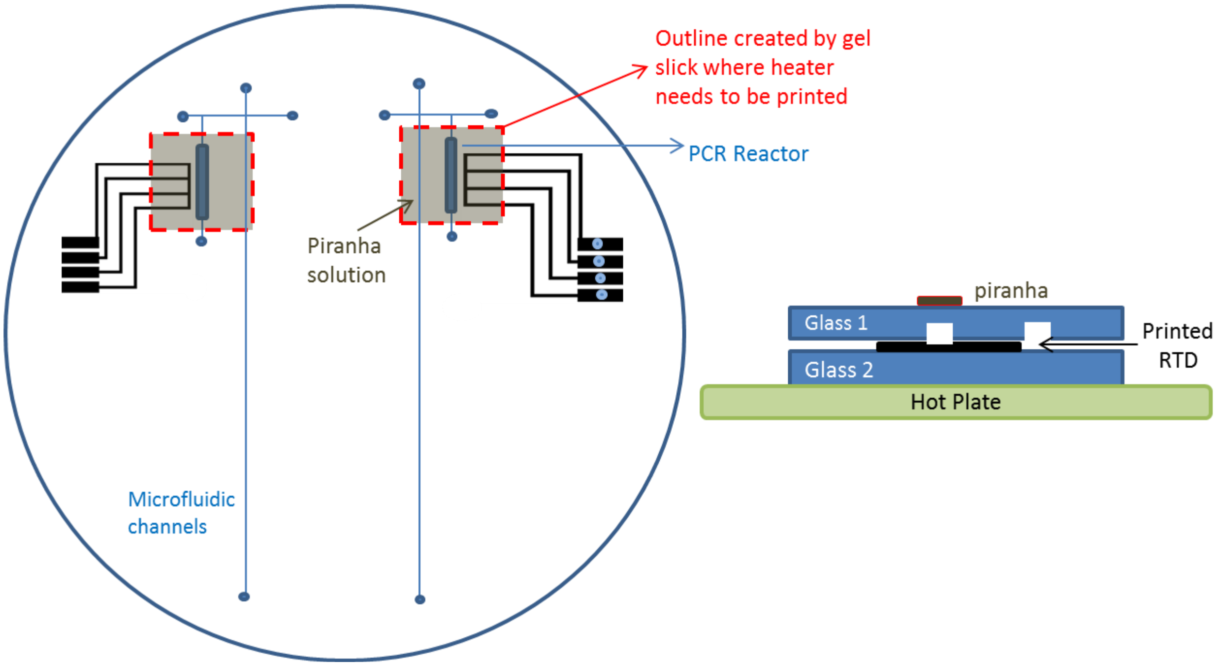

Figure 100. Top view and cross section of cleaning setup2 on a bonded chip to get clean surface for heater printing.

This setup (Figure 100) used a highly hydrophobic coating called gel slick. Gel slick glass plate coating is used in many biological environments for changing the surface energies of the glass surfaces. In this case, gel slick was used to contain the area holding the piranha solution. A gel slick coating was applied using a q-tip applicator and outlined the rectangular area where the heater would be printed. The substrate was then placed on a hot plate set to 90^0C and piranha solution was pipetted into that outlined area. The gel slick prevented the piranha solution from spreading to other open parts of the wafers including the RTD contact holes. The substrate was held on the hot plate for 10 minutes. The piranha solution was then carefully evacuated and the cleaned area was rinsed with water. Both setups (Figure 99 and Figure 100) proved to be successful in providing a surface with appropriate surface energy for uniform printing of gold heaters.

The final step in making the bonded substrates viable for PCR demonstration is to make contact to the printed RTDs and heaters. To prevent scratching of the exposed contact pads of the printed devices, silver epoxy *(Thorlabs - Electrodag 5810 Conductive Silver Epoxy*)[16]was applied to these pads. Silver paste and epoxy are mixed together and are initially applied in a paste form. The silver epoxy is then hardened and becomes conductive when annealed at 90^0C for an hour or at room temperature for 24 hours.

The final thermally bonded microfluidic chip with printed RTDs and heaters is shown below in Figure 101. This bonded chip is used next to demonstrate PCR.

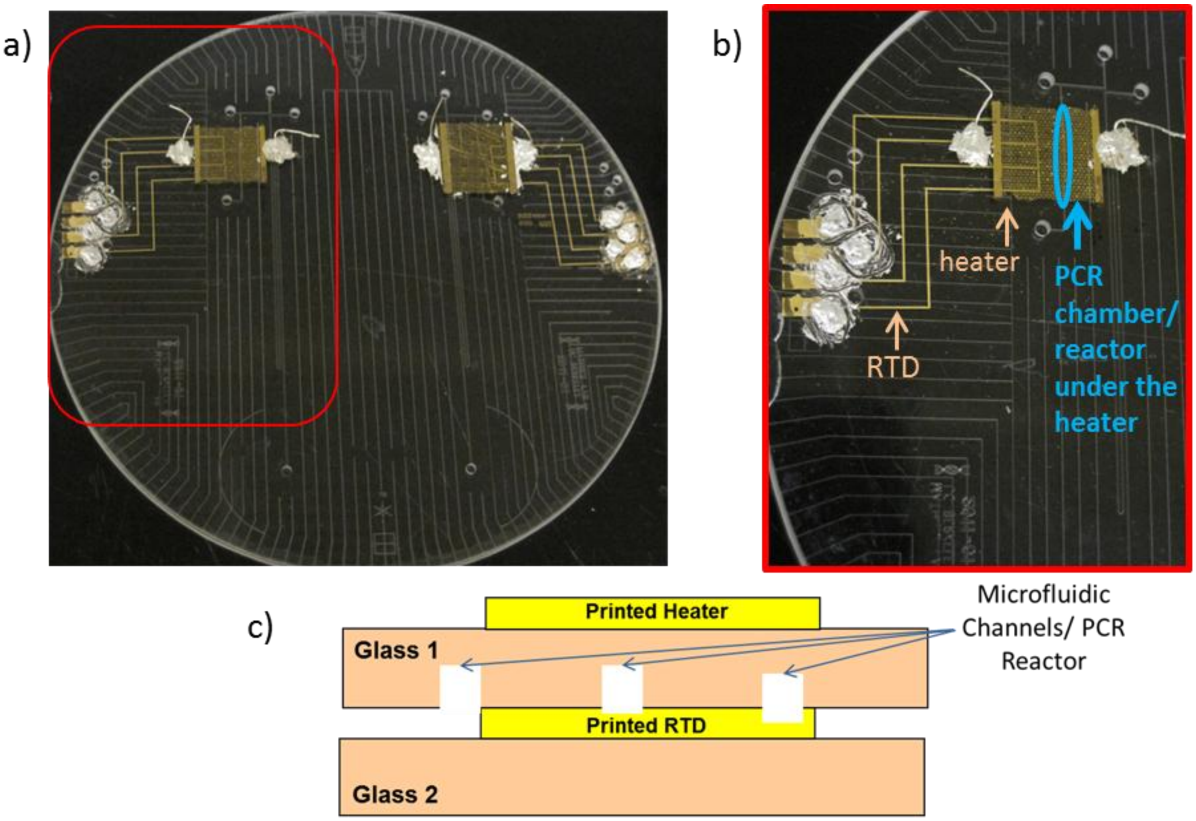

Figure 101. Final thermally bonded chip used to demonstrate PCR: a) An image of the entire chip with two microfluidic channels and reactors (left and right sides of the chip); b) A zoomed-in version of the section of chip (left side) which is used to demonstrate PCR in this project; c) Cross section of the thermally bonded chip.

4.3 PCR Demonstration using Printed RTDs and Heaters

PCR, an important and fundamental biological technique, was chosen to demonstrate the effectiveness and usability of inkjet printed gold heaters and RTDs in biological microfluidic applications. In particular, gender typing (described in section 4.1), an application of STR technology, was used as a proof of concept for this demonstration. PCR on male and female DNA was conducted using printed heaters and RTDs, and fluorescent detection of the amplified product was performed. The results from these experiments are presented below.

As discussed earlier in this chapter, PCR requires thermal cycling (~32 cycles) of a cocktail of DNA templates, primers, nucleotides and polymerase between denaturing (95^0C), annealing (50-60^0C depending on primer) and extending (72^0C) conditions. Important steps required for the demonstration of PCR precede and follow the PCR thermal cycling process. Each of these steps will now be discussed.

1) **Initial cleaning:** To begin with, the microfluidic channels (PCR reactor included) are cleaned with piranha solution (3:1 ratio of H_2SO_4: H_2O_2). The chip is placed on a hot plate at 90^0C for 10 minutes with piranha solution in its channels.

Capillary flow facilitates the flow of piranha solution in the narrow microfluidic channels. In addition, vacuum is applied as needed to assist the flow of solutions in the channels.

The purpose of piranha clean in this step is to remove atmospheric and organic contaminants from the channels before DNA and other sensitive materials are introduced. After 10 minutes of piranha clean, the channels are washed with Millipore filtered de-ionized water to remove the residual piranha solution.

2) **Neutralizing charge in channels:** The water clean in the previous step leaves the microfluidic channel walls positively charged. This affects the DNA and the following electrophoresis steps. Therefore, to suppress electroosmotic flow, the channel is coated with DEH100[17], a dynamic capillary array coating to neutralize the charge in the channels. DEH100 is diluted with methanol (1:1) and allowed to coat the channels for 5 minutes. It is then evacuated from of the channels.

3) **Preparation of linear polyacrylamide gel (LPA):** 3-5% LPA gel is used in channels (at inlet and outlet holes) to control the flow of fluids. For example, when a drop of gel is placed at an outlet hole of a microfluidic channel, the flow of fluid in the channel is blocked because capillary forces in the channel are constricted by the gel blocking the outlet. Therefore, the fluid in the channel is stationary after a certain amount of flow. During polymerization of the capture gel (next step), PCR, and other steps that require the fluid to be held in a particular section of the chip, blocking gel is used.

10mL of 5% LPA gel was made in-house using the following components and protocol[18]*:*
Components:

1. 40% acrylamide solution (from *Bio-Rad* [19]) - polymerizing component
2. 10X TTE Buffer-Tris TAPS EDTA (TTE) buffer- the 10× TTE buffer contains500 mMTris-base, 500 mM TAPS acid, and 10 mM Na_2EDTA
3. Nuclease Free Water
4. TEMED (Tetra Methyl Ethylene Diamene)*- 20% v/v in H_2O
5. APS (Ammonium Per Sulfate)*- 10% w/v in H_2O

*TEMED and APS are used to catalyze the polymerization of acrylamide to form the LPA gels.

Protocol:

1. To calculate the amount of 40% acrylamide solution needed, 5% w/v of LPA (i.e.0.5 g in 10mL of total solution) is adjusted to the 40% acrylamide solution to get to the final concentration. Therefore, 1.25mL (0.5g/40%) of the 40% acrylamide solution is needed to arrive at the 5% LPA concentration. This amount is changed depending on the required total concentration and total volume of the solution. The amount of 10X TTE buffer stays constant at 1mL and the amount of nuclease free water is calculated to add up to a total volume of 10mL.
2. 1.25mL of 40% acrylamide solution, 1mL of 10X TTE buffer, and 7.75mL of nuclease free water is therefore mixed in a 20mL glass vial. The vial is then tightly sealed with a septum and paraffin sealing films (‘parafilm’). Two syringe needles are inserted through the septum, making sure both are long enough to touch the solution inside. One needle is inserted into the solution for bubbling argon; the other is above the solution and serves as a vent. The solution is sparged with argon for 2-3 hours.
3. 5µL of TEMED and 5µL of APS are then added to the vial through the septum using a Hamilton syringe and mixed well. The vial is sealed again using parafilm and argon is allowed to flow on top of the solution for 30 minutes -1hour.

4. The vial is then left in the refrigerator (at ~4^0C) overnight with tightly parafilmed septum. Any exposure to oxygen or moisture inhibits the formation of the LPA gel.

4) **Preparation of photopolymer solution to form capture gel:** The capture gel serves to capture the sample of interest after PCR. The capture gel contains streptavidin, a protein that is used extensively in molecular biology and bionanotechnology because of its affinity to biotin, also known as Vitamin B7. The streptavidin-biotin bond is one of the strongest non-covalent interactions known in nature[20]. Streptavidin is in the capture gel, and biotin is tagged to one of the primers in the PCR mixture. This will be explained further in the following steps. A solution containing the necessary components for capture will be photopolymerized to form the capture gel.

The streptavidin capture gel consists of the following components:

1. 30% Bis-acrylamide solution (19:1)- polymerizing component
2. 10X TTE Buffer
3. Streptavidin acrylamide (Invitrogen, Carlsbad, CA, USA):1 mg of powder
4. Nuclease Free Water
5. VA-086[21]- A non-nitrile nonionic halogen free azo compound initiator that triggers the polymerization of the above solution.

To prepare a 500μL of photopolymerization solution, the following protocol was followed:

1. In the 1mg bottle of streptavidin acrylamide, 316.7μL of nuclease free water, 50μL of 10X TTE buffer, and 83.33 μL of 19:1 Bis: acrylamide 30% acrylamide solution are all added. This solution is vortexed to make sure it is completely mixed.
2. This solution is then transferred to an opaque 2-mL scintillation vial with Teflon closure (such as product C4013-17A from National Scientific).
3. The vial is tightly closed and sealed with parafilm. Two syringe needles are inserted through the Teflon enclosure. One needle is inserted into the solution for bubbling nitrogen; the other is above the solution and serves as a vent. The solution is sparged in nitrogen for 10-20 minutes.
4. After sparging for 10-20 minutes, in a dark room, 50 μL of VA-086(2% in DI water) is inserted into the sparged solution through the Teflon enclosure using a Hamilton syringe. The solution is then gently mixed (vortexed) and covered with parafilm. It is then stored at 2-3^0C.

5) **UV Exposure for photopolymerization and formation of capture gel:** Before introducing reagents and solutions into the sample wells (drilled input/output holes) and channels, Gel Slick (discussed earlier in this chapter) is transferred onto a dry techwipe, and spread evenly over the entire external surface of the chip. The coating is allowed to dry completely and any residual gel slick is wiped off. The purpose of the Gel Slick coating is to make the chip surface, especially that around the sample wells, hydrophobic in order to keep each sample drop within its respective sample well.

Going forward, the wells on the microchip (drilled input/output holes) will be addressed using the labels in Figure 102. Each of the sample wells serves different purposes in the following steps.

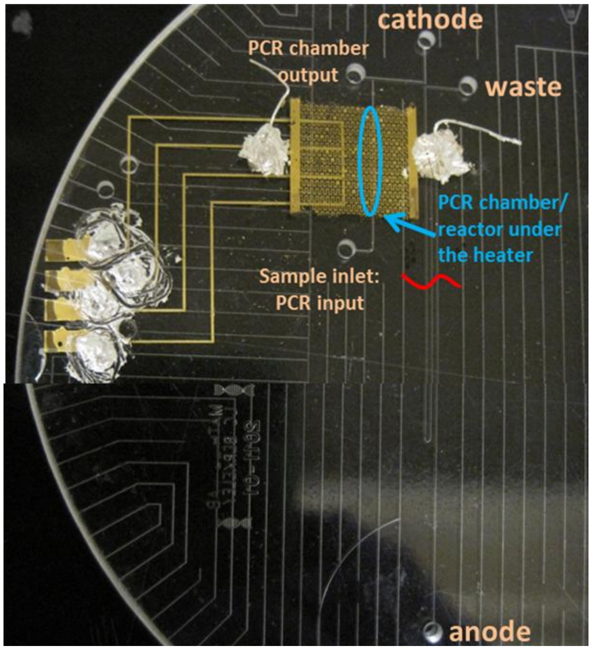

Figure 102. The different nodes of the microfluidic chip are labeled.

To prevent the photopolymer solution from moving during UV exposure, 5% LPA gel is loaded at the anode and at the PCR input (Figure 102) such that it fills ~1cm of the channel starting with the respective wells. The following steps are then followed to form the capture gel:

1. The photomask and the microchip are held together by vacuum on an inverted microscope stage. The chip is then aligned to the photomask using alignment windows. The size of the exposure window used for this alignment was ~250μm by 250μm square area. 4X magnification was used on the microscope to allow appropriate amount of UV light for the desired capture gel size. Since the capture gel will be used to purify the species of interest right after PCR, it needs to be formed between the PCR chamber output and waste nodes. The photopolymerization setup is illustrated in Figure 103.

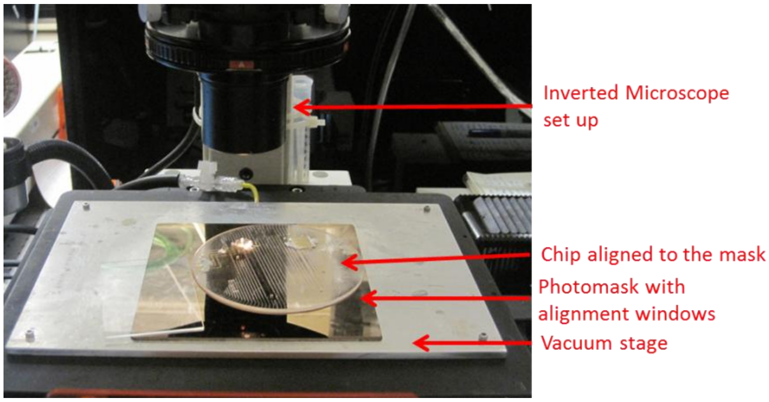

Figure 103. Microscope, mask and microchip setup for photopolymerization of capture gel.

2. *The photopolymerization process is done in a dark room with minimal exposure of light to the solution.* The cathode and PCR chamber output wells are filled with solution and allowed to flow through the channels by capillary action. Bubbles in the channels and solution are cleared by evacuating at the waste node.

3. Excess solution is then evacuated from the waste, cathode, and PCR chamber output wells and replaced with a drop of 5% LPA gel. The sample is left on the microscope to stabilize for 5 minutes. Once the solution inside the channels has stabilized and is free of bubbles, the mask is aligned again if needed to the microchip, as shown in Figure 104. UV light is then used to initiate the gel photopolymerization in this exposed area for 8 minutes.

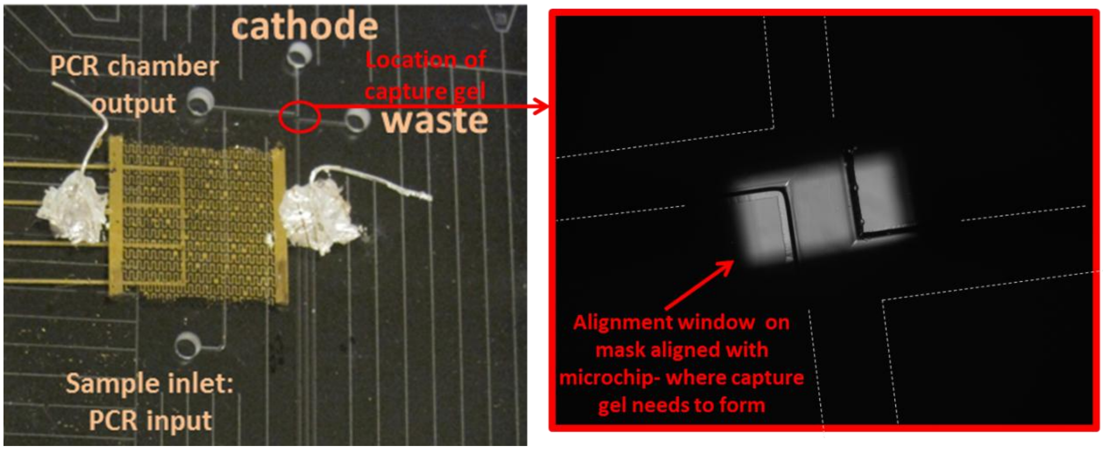

Figure 104. Capture gel location and the corresponding alignment window aligning the mask and microchip.

4. Once the exposure is finished, the blocking gel in the PCR input and anode are evacuated. The formation of the capture gel from one of the experiments in this project is shown in Figure 105.

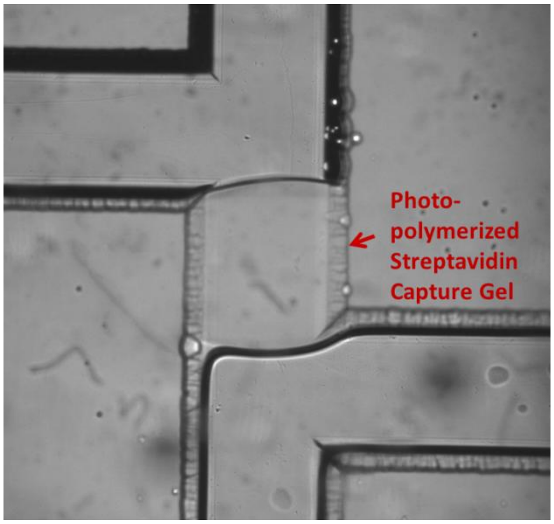

Figure 105. Streptavidin capture gel formed as a result of UV photopolymerization.

5. Finally the 5% LPA gel is also evacuated from the cathode, waste, and PCR output wells and replaced with 1X TTE buffer. The capture gel will dry unless it is surrounded by some form of moisture.
6. Evacuation and/or pushing of water/buffer to release the backing gels in different parts of the channels needs to be done carefully such that the capture gel is not accidentally vacuumed or pushed out. Evacuating or pushing at the waste, cathode and PCR output nodes is especially risky since the resistance (length of channel) between these nodes and the capture gel is very small.

6) **Making the PCR Mixture:** The PCR mixture recipe used in this project is from Professor Mathies' group at UC Berkeley [22, 23, 24].

Gender identification (sex-typing) is commonly performed in conjunction with STR typing using PCR products generated from the amelogenin gene that occurs on both the X- and Y-chromosome. Amelogenin is a protein found in developing human tooth enamel and can be used in gender determination of samples from unknown human origin through PCR [25].

In this project, as a proof of concept, primers and template DNA (of known gender origin) from the amelogenin gene are used, PCR is performed using printed devices, and the output is expected to confirm the female or male origin of the inputted template DNA.

In real life applications (forensic sciences for example), the template DNA would be from a human sample and the gender origin would not be known. PCR would be conducted using primers from the amelogenin gene and the template DNA of unknown origin, and the result would determine the gender. With a standard amelogenin test, if the DNA was of female origin, only a single fluorescent peak would be observed in a laser detector correlating with the XX chromosome configuration, while DNA of male origin would exhibit two peaks corresponding to the XY chromosome configuration. X and Y chromosomes are associated with 2 different sequences of DNA, with the Y chromosome having a slightly longer length (6 base pairs longer) of DNA.

The components for the amelogenin PCR mixture in this project are calculated to yield a total volume of 50μL. The components and the corresponding volumes are shown in Table 8.

	Components	Initial Concentration (as bought)	Final concentration used	Amount Used (μL) (for 50μL total volume)
1	Nuclease Free DI water			39.4
2	Gold ST*R buffer	10X	1X	5
3	FAM–tagged Amelogenin Forward Primer	10μM	300nM	1.5
4	Biotin-tagged Amelogenin Reverse Primer	10μM	300nM	1.5
5	Male DNA- 9948 *OR* Female DNA- 9947A	10ng/μL	0.2ng/μL	1
6	AmpliTaq Gold	5 units/μL	0.16 units/μL	1.6

Table 8. Components in the amelogenin PCR mixture.

The *Gold ST*R10X buffer* (from *Promega)* is used to maintain the stability of the DNA in solution. In addition, the Gold ST*R buffer also contains 2mM of each of the nucleotides (A, T, C, and G) necessary for the extension step in PCR. The *FAM-tagged forward primer* extracted from the amelogenin gene serves the additional purpose of tagging the final amplified outputs with fluorescein amidite (FAM) for laser detection. The *biotin-tagged reverse primer,* also extracted from the amelogenin gene, assists in binding of the amplified outputs to the streptavidin capture gel. *Male and Female DNA templates*, extracted from the amelogenin gene, was purchased from *Promega*. Both the female and male DNA were amplified and detected in two different experiments to demonstrate PCR using printed devices. Finally, the *AmpliTaq Gold* (from *Invitrogen)* is the Taq DNA polymerase that assists in the extension step in PCR.

The recipe used to obtain the PCR mixture is described below:

a. All of the components in Table 8are very sensitive to atmospheric and human contamination. Therefore, they are mixed together in a HEPA/UV Sterilizing PCR Workstation. Gloves are worn and cleaned often using ethanol to minimize contamination to the PCR mixture.
b. Components 1-5 are pipetted into a 1mL microcentrifuge tube in the order shown in Table 8 and mixed thoroughly in a vortexer.
c. The AmpliTaq Gold (Taq) is added last. The Taq is active in relatively warm temperatures. Therefore, as soon as the Taq is included in the mixture, it is stored in the refrigerator till the microchip is ready for PCR.

7) **Preparing the microchip and the PCR reactor:**

1. To begin with, backing gel is applied in *the area above the capture gel* to prevent the PCR material from moving during the thermal cycling process. 5% LPA backing gel is too viscous and might push out the capture gel. Therefore, 4% LPA gel is synthesized using the protocol discussed earlier (step 3).
   a. 4% LPA gel is pushed from the PCR output node such that the gel travels towards the cathode. A drop of 1X TTE buffer is placed in the cathode sample well to keep the LPA gel hydrated.
   b. To clear any gel that might have been pushed into the PCR chamber in the previous step, buffer is pushed from the PCR input node such that gel in the PCR chamber comes out of the PCR output well.
2. The area below the capture gel is filled with TTE buffer.
3. The TTE buffer, which was used to clean out the PCR chamber in the previous steps, contains EDTA (Ethylenediaminetetraacetic acid**)**, which is harmful to DNA and to the PCR process. The following step therefore clears the PCR chamber of any residual EDTA.
   a. The PCR chamber part of the chip is coated with 1% BSA (bovine serum albumin) solution (in water) for 5-10 minutes. The purpose of BSA is to clear the EDTA and to keep the polymerase and DNA from sticking to the channel surface during PCR.
   b. The BSA is then evacuated and the PCR chamber is rinsed with water.
4. The PCR mixture is then fed into the PCR chamber. The mixture is evacuated at the PCR output to clear bubbles in the chamber. After filling the PCR chamber, the PCR input and output wells are evacuated and loaded with 5% LPA gel.
5. *The microchip should now have the configuration in Figure 106 right before PCR (next step).* In addition, the cathode, waste, and anode wells should be filled with buffer and the PCR output and input wells should be filled with 5% LPA gel to prevent the flow of the PCR mixture during thermal cycling.

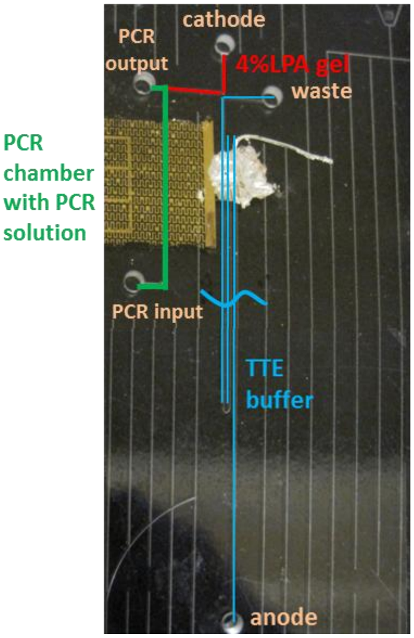

Figure 106. The configuration of the microchip right before PCR.

8) **<u>PCR</u>:** Thermal cycling of the PCR reactor is controlled by a LABVIEW graphical interface (*National Instruments*) with the printed heater underneath the PCR thermal cycling reactor. RTDs are contacted by using electrical pins, and 1 mA is passed through the outer leads. The voltage drop across the inner leads as a function of temperature is measured in real-time using a signal conditioner(*5B31-01; Analog Devices*) and a data acquisition board(*National Instruments*). The output drives a proportional integral derivative (PID) controller that regulates 0–8 V for heating and pressurized air for active cooling. The PCR setup in shown in Figure 107.

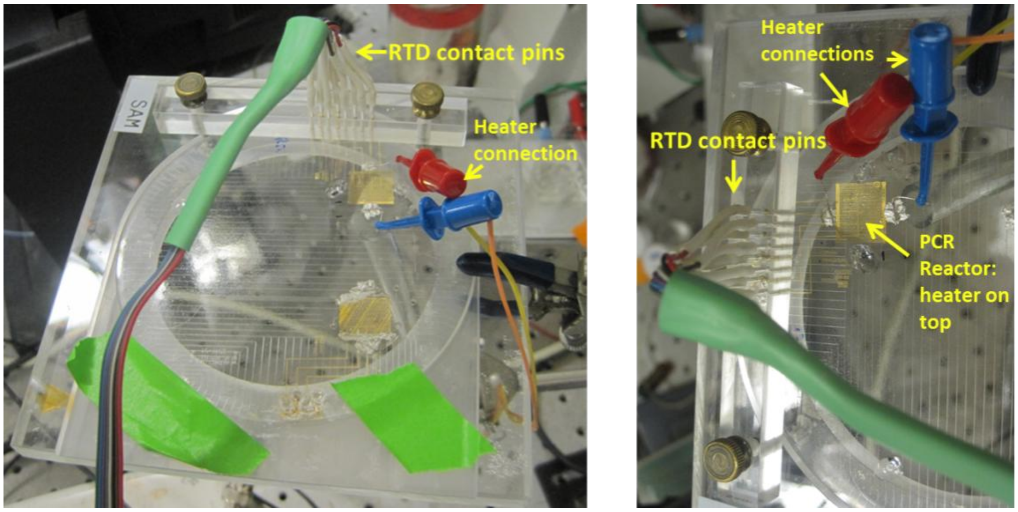

Figure 107.PCR thermal cycling setup with external connections to the heaters and RTDs.

1. First, the RTD is calibrated with a hot plate and a four point probe setup. The results from the RTD calibration in this chip are shown in Figure 108. The equation from this

calibration is entered into the thermal cycling software so that it can provide real-time information for the signal conditioner and the data acquisition board. In other words, the calibration helps control the heater temperature as detected by the RTD during thermal cycling.

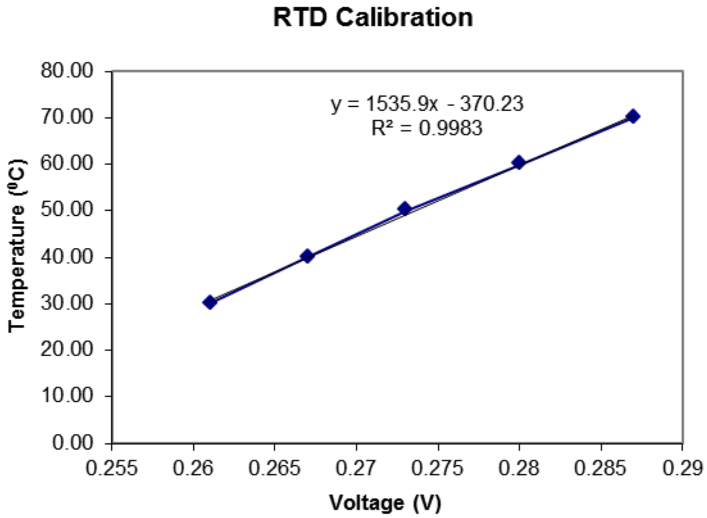

Figure 108. RTD calibration results from the microchip system used in this project.

2. The timing for the different steps in PCR is determined by the volume of PCR mixture and the tool used to conduct PCR. With Amelogenin PCR, a standard 25µL solution requires 1 minute each for denaturing and annealing while the extension step requires 1.5 minutes per cycle. The microchip chip contains a ~300nL PCR reactor, and therefore the timing for each step is reduced. The final recipe for PCR thermal cycling for this project is shown in Table 9:

Step #	Temperature (⁰C)	Time	Cycles	Reason for step
1	95	8 minutes	First cycle (1 cycle)	Activate the Taq polymerase at the beginning
2	95	20 seconds	32 cycles	Denaturing
3	58	30 seconds		Annealing
4	70	30 seconds		Extending
5	70	5 minutes	Last cycle (1 cycle)	Extra time at the end for Taq to finish extension of any incomplete sequences

Table 9. PCR thermal cycling recipe.

3. PCR is now performed on chip using printed RTDs and heaters.
4. The measured temperature profile of the 32 cycles of thermal cycling during PCR is shown in Figure 109. This graph demonstrates that the printed devices *precisely* follow the desired temperature profile during PCR. The required ramp and cool down times in the thermal cycling process is added to the total time such that the actual hold time at each temperature satisfies the recipe in Table 9.

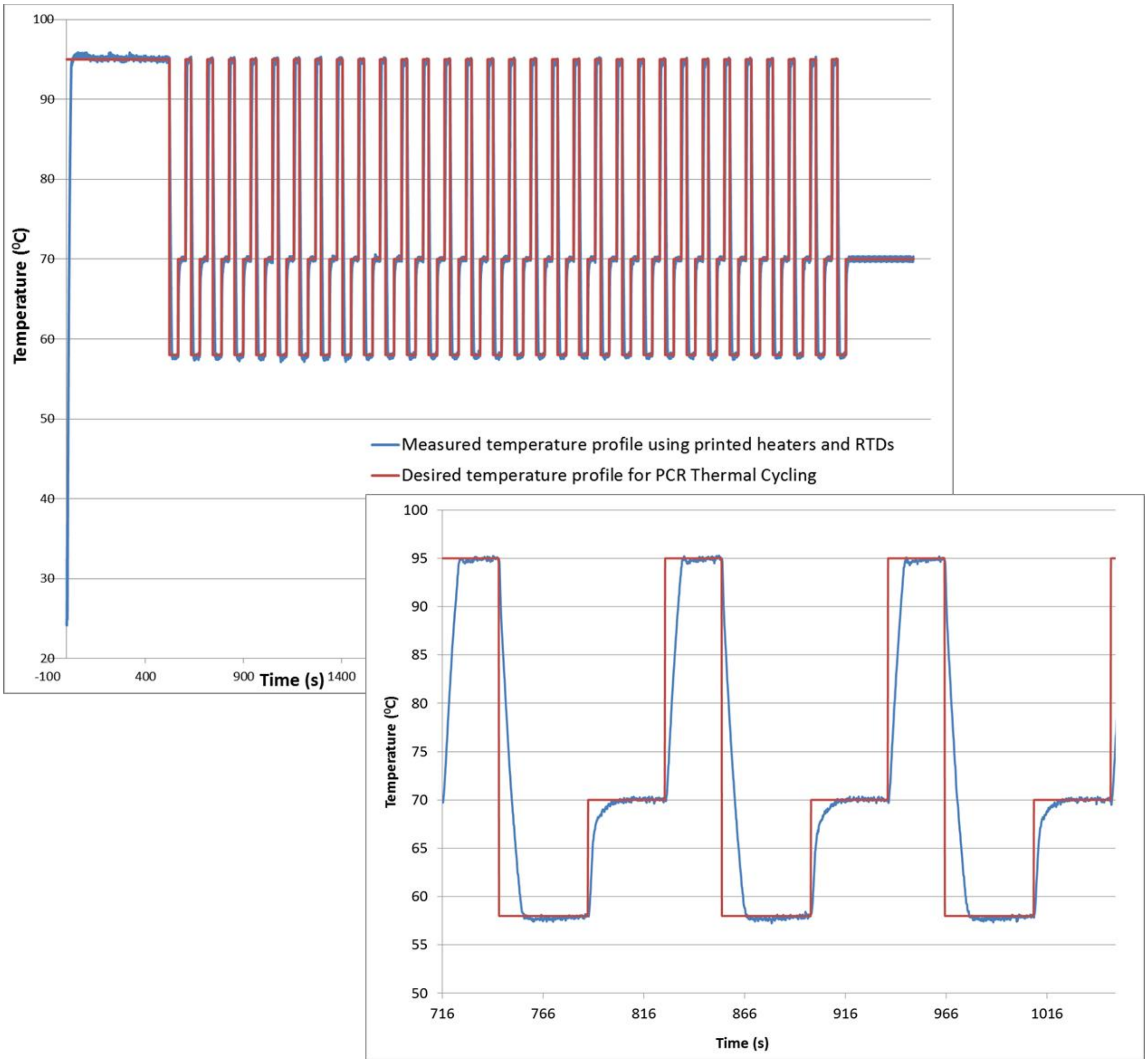

Figure 109. Thermal cycling temperature profile of PCR performed using printed heaters and RTDs.

Thus, PCR has been completed, and the following step discusses the capture of the species of interest from the PCR output.

9) **Capture:**

1. Still keeping the configuration in Figure 106, the capture step is now performed. The PCR reactor has the amplified sample of interest.
2. The chip is removed from the thermal cycling setup and placed under a fluorescent microscope with a heatable chuck. The temperature is set to 30^0C.
3. The amplified sample is electrophoretically driven from the PCR chamber to the waste node via the capture gel; the capture gel is therefore able to capture the species of interest during this process. This setup is demonstrated in Figure 110.

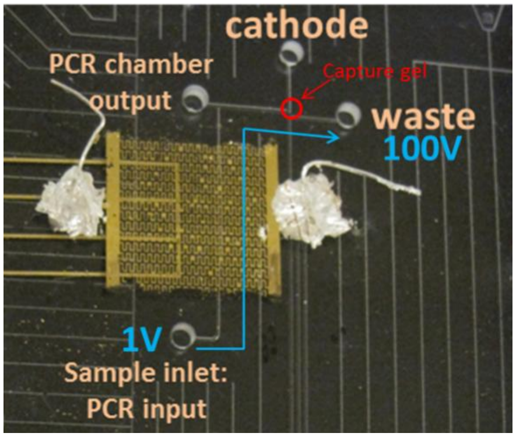

Figure 110. Capture setup to move the PCR product from the PCR chamber to the waste via the capture gel.

Since DNA is negatively charged, the sample will electrophoretically migrate towards the waste node as indicated in Figure 110. The electrophoresis setup in Figure 110 is held for ~5 minutes.

4. Once the PCR chamber is completely empty (verified using the fluorescent microscope), any residual PCR product from the previous step that has moved towards the cathode is electrophoretically driven from the cathode to the waste chamber as indicated in Figure 111. This setup is held for 100 seconds.

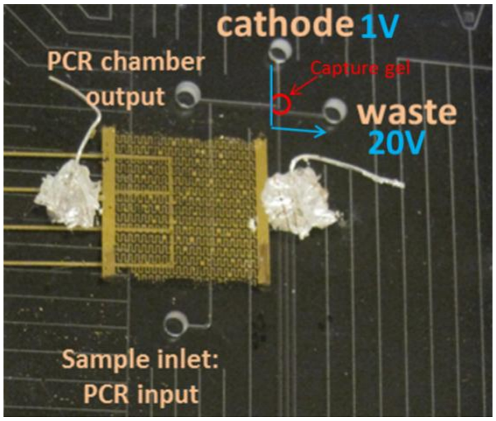

Figure 111. Capture setup to move residual PCR product from the cathode to the waste.

5. Analytes of interest usually capture in the capture gel through the biotin-streptavidin interaction *only* if PCR worked. The capture sequence and results from the PCR product of the female template DNA PCR reaction are shown in Figure 112 and Figure 113. The results from the male template DNA PCR reaction are shown in Figure 114 and Figure 115. The capture images were taken using a fluorescent microscope unless otherwise indicated.

In Figure 112 and Figure 114, the first image on top shows a micrograph of the zoomed in chip. In the capture sequence images that follow, Capture_0 refers to the fluorescent image of the channel when the PCR product is still in the reactor (i.e. the PCR chamber is fluorescing). Capture_final shows the image after capture of the PCR products on the capture gel (analytes of interest are on the capture gel). Figure 113 and Figure 115 show a zoomed in version of the capture gel with the captured species of interest. The fluorescent image confirms the capture.

CAPTURE SEQUENCE and RESULTS: PCR with Female DNA (9947a from Promega)

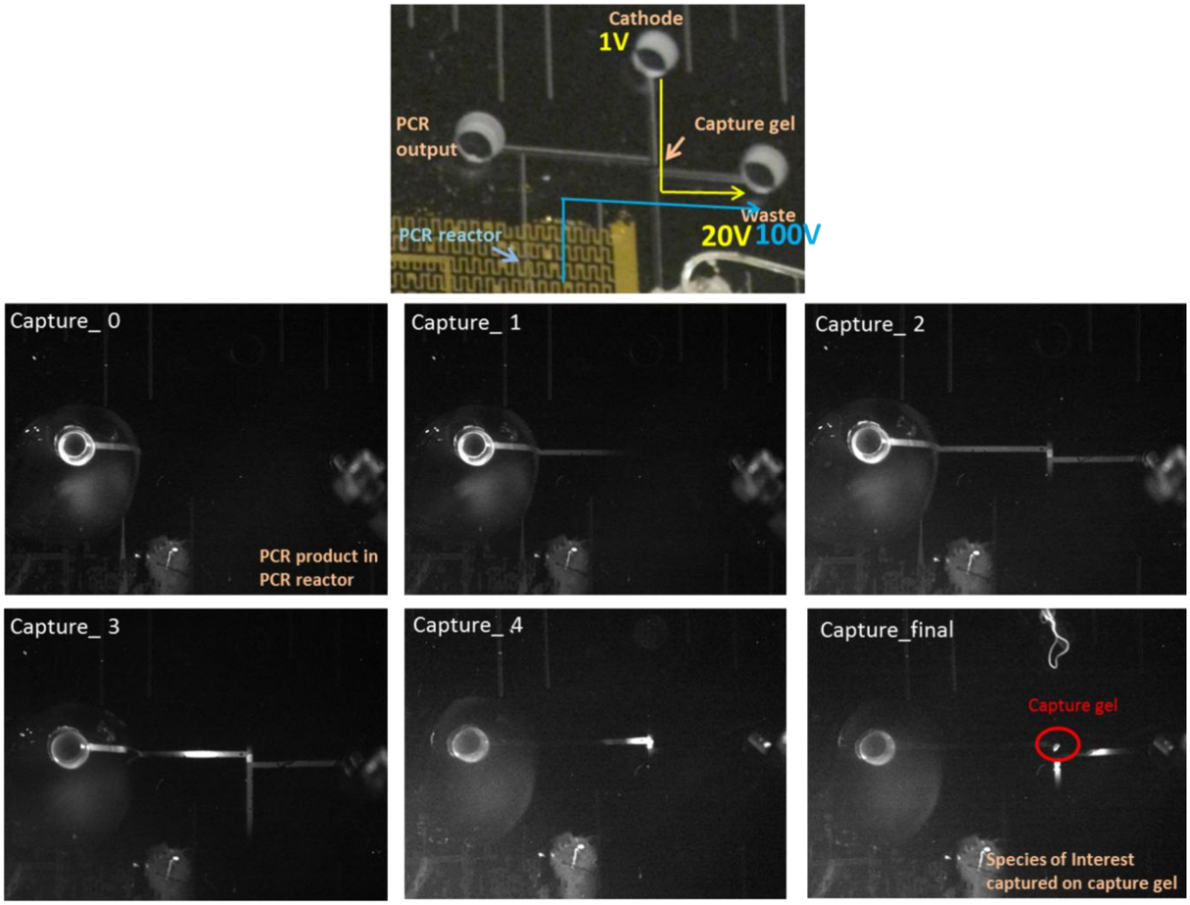

Figure 112. Female DNA PCR: Sequence of fluorescent images taken at different time indices during capture. At Capture_0, the PCR product is still in the reactor. By Capture_final, the PCR product has been moved electrophoretically from the PCR chamber to the waste; the species of interest has been captured on the capture gel.

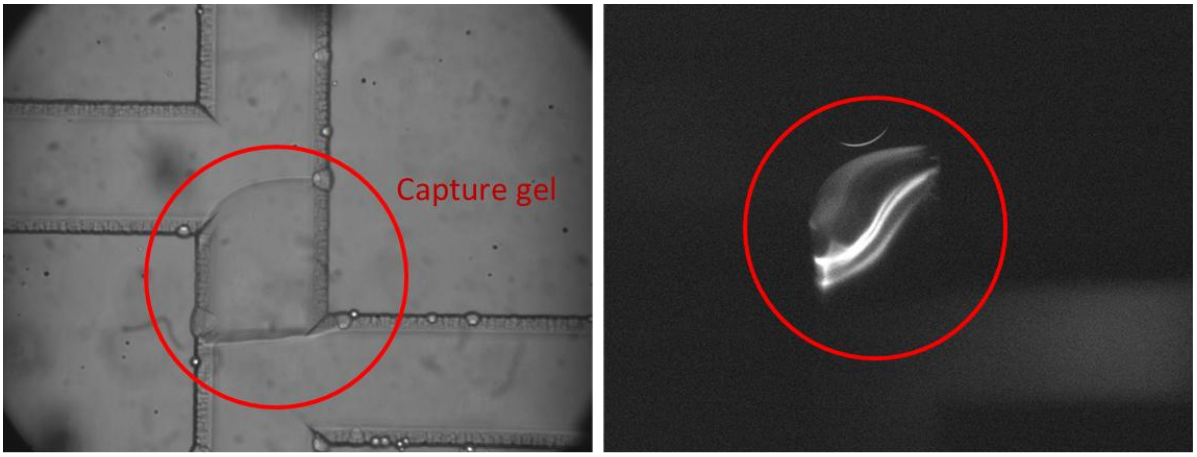

Bright Field Image

Fluorescent image of the capture gel after species of interest was captured

Figure 113. Female DNA PCR: Image after capture step shows that the species of interest has been captured on the capture gel. The fluorescent image on the right confirms the capture.

CAPTURE SEQUENCE and RESULTS: PCR with Male DNA (9948 from Promega)

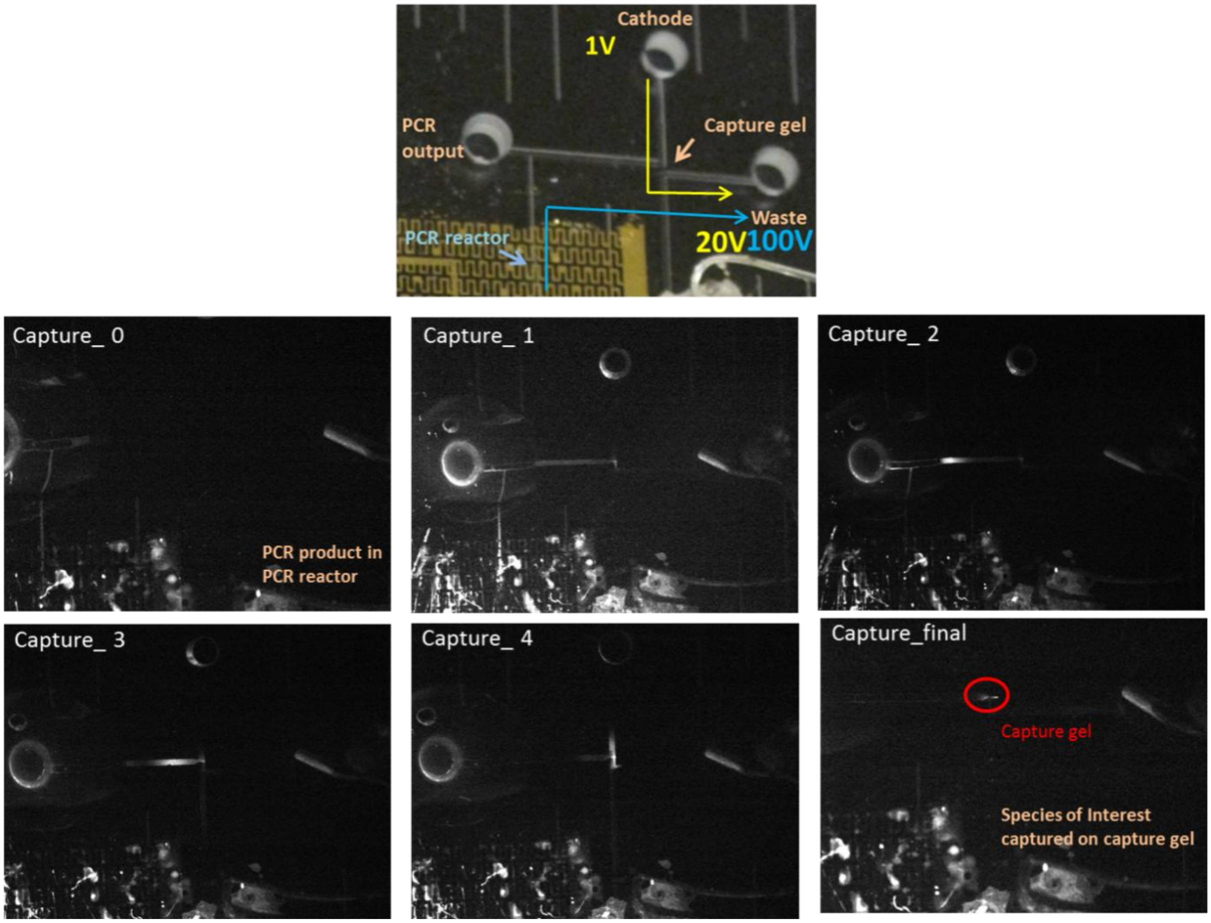

Figure 114. Male DNA PCR:Sequence of fluorescent images taken at different time indices during capture. At Capture_0, the PCR product is still in the reactor. By Capture_final, the PCR product has been moved electrophoretically from the PCR chamber to the waste; the species of interest has been captured on the capture gel.

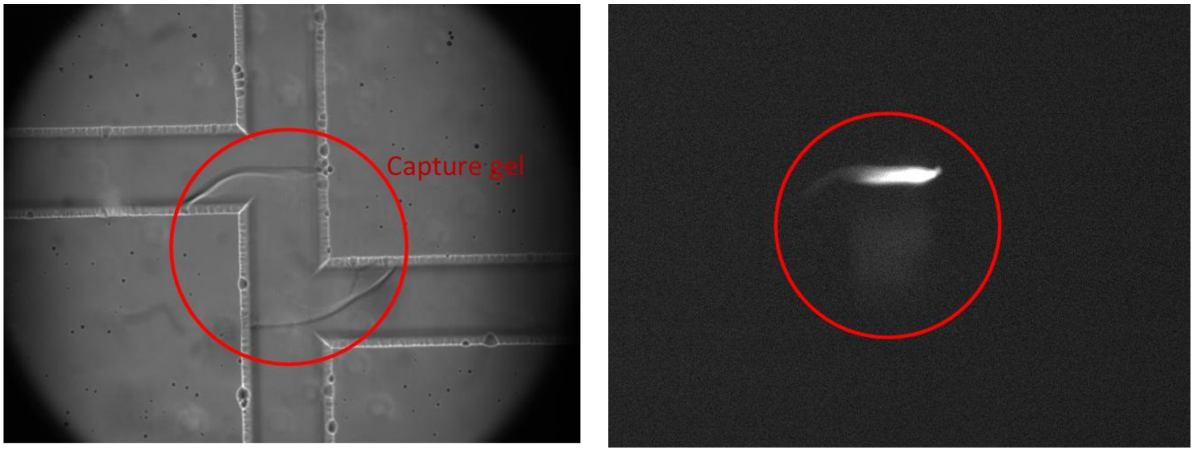

Bright Field Image

Fluorescent image of the capture gel after species of interest was captured

Figure 115. Male DNA PCR: Image after capture step shows that the species of interest has been captured on the capture gel. The fluorescent image on the right confirms the capture.

10) **Loading Separation Gel for Capillary Electrophoresis:** Once the capture process is done, the captured species can now be detected using capillary gel electrophoresis[26, 27] and a fluorescent laser detector.

1. The buffer from the area below the capture gel is evacuated and replaced with separation gel needed for detection. 4% LPA gel with 6M urea is used as the separation gel. *The urea prevents the DNA from sticking to itself, each other, and the gel during electrophoresis.* 4% LPA gel is synthesized using the same protocol as that described in step 3 with the addition of 6M of urea.
2. Before loading the gel into the channel, the gel is spun down in a spinner at 3000rpm for 5 minutes to remove bubbles. The gel is then loaded at the anode using an automatic pressure loader that applies 200psi of pressure to push the gel through the channel. The chip should now have the following configuration:

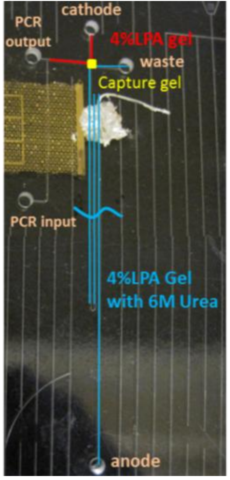

Figure 116. Configuration of the microchip right before laser detection of the captured species.

11) **Laser (Fluorescent) Detection: FINAL RESULTS**

1. The chip is now placed on the laser detector chuck. The electrophoresis and laser detector setup used for this step is shown in Figure 117. A voltage is applied from the cathode to anode such that the PCR products migrate towards the laser detector and eventually to the anode.2000V is applied from the cathode to the anode resulting in an electric field of ~135V/cm.
2. *The DNA electrophoretically travels through the gel at different times based on its molecular weight or length (# of base pairs)* and therefore fluorescent peaks are observed at different times based on the lengths of the DNA. The loaded gel is sensitive enough to detect single base pair differences.
3. The electrophoretically separated FAM-labeled products from the channel were detected using laser-induced fluorescence with the Berkeley rotary confocal scanner, described in detail in a previous work [11].
4. Once the electrophoresis setup is ready, the substrate is heated to 67^0C in order to release the captured DNA from the streptavidin capture gel.
5. Once the DNA is released, it starts migrating towards the anode. The laser detector scans right before the sample reaches the anode as indicated in Figure 117. The blue light laser in the detector excites the FAM products and all 4 wavelengths (red, blue, green, and yellow) are detected by the scanner.

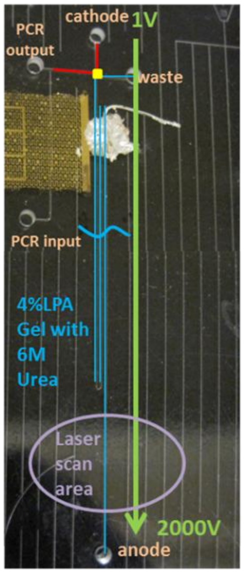

Figure 117. Electrophoresis and laser scanner setup of microchip on the fluorescent detector.

6. *The FINAL results from the fluorescent detection (FD) are shown in Figure 118, Figure 119, Figure 120, and Figure 121.*
7. Figure 118 shows FD results from a ladder DNA experiment done on this microchip. Ladder DNA experiments are conducted to calibrate the chip, the gel, and the electrophoresis setup to confirm the accuracy of the male and female PCR performed on the chip. Ladder DNA ET400 [28] contains a series of DNA with different lengths (base pairs)and emits at a red wavelength. A capture gel is not used in this case since the ladder DNA is not biotin-tagged.
    a. <u>Experiment Setup of Ladder DNA experiment:</u> The ladder DNA is inputted at the PCR output node and electrophoretically moved *towards* the waste such that the channel area between the PCR output and waste is filled with the ladder DNA.
    b. Then the electrophoresis setup shown in Figure 117 is followed to get the FD results in Figure 118.
8. Figure 119 and Figure 120 show the fluorescent detection results from PCR conducted using male and female DNA, respectively. The male DNA results show two peaks corresponding to the X and Y chromosomes while the female DNA results shown only peak. In both cases, the primer peaks represent the primers that were not used in PCR but were still immobilized on the streptavidin capture gel.
9. Figure 121 shows the final comparison of the 3 experiments without the primer peaks. The X chromosome correlates with a DNA of 106 base pairs, while a Y chromosome contains a DNA sequence of 112 base pairs. This figure compares ladder DNA migration time to female and male DNA peaks, confirming the accuracy of the PCR results.
10. The X chromosome peaks at a migration time of about ~556 seconds and the Y chromosome peaks at a time of ~569 seconds. As seen from the ladder DNA results, each additional base pair leads to about 2-2.5 second delay in migration time. This correlates well with the results seen with the male and female DNA PCR. The primers peak at ~381 seconds in both cases.
11. **These results have therefore confirmed the successful and accurate demonstration of PCR using printed RTDs and heaters!**

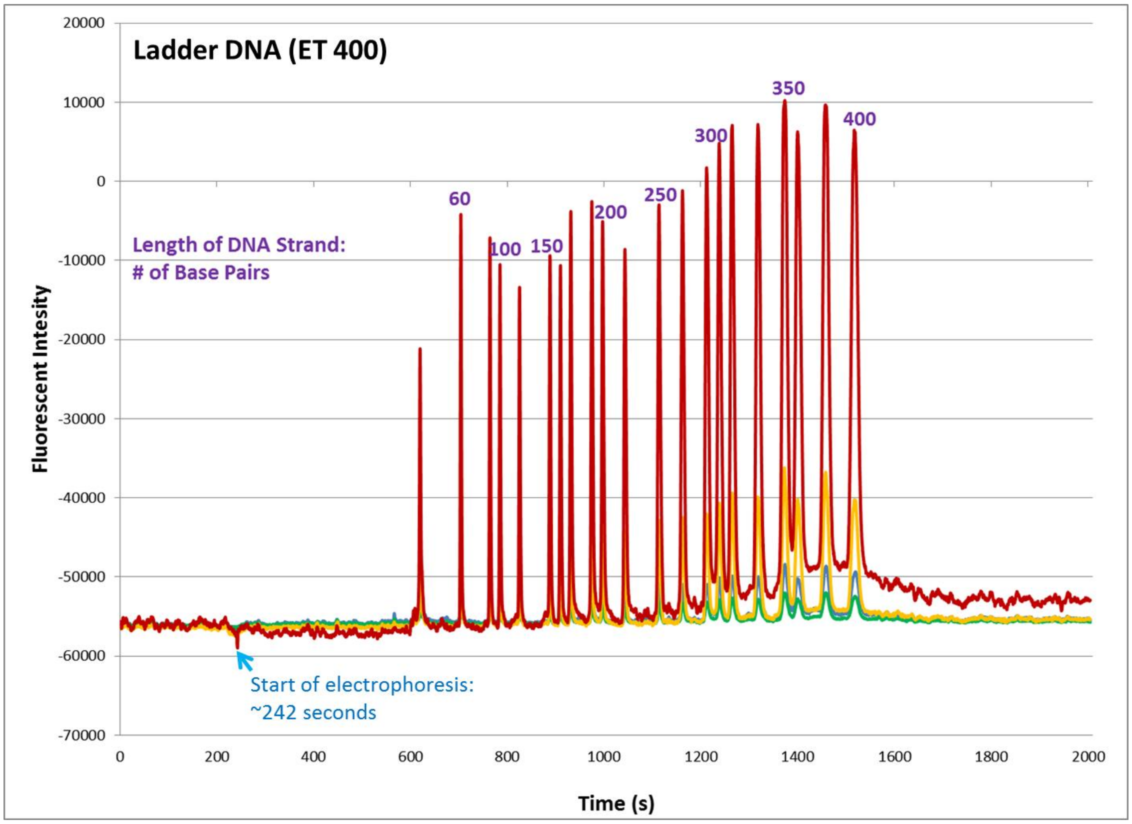

Figure 118. Fluorescent Detection results of ladder DNA used for calibration of microchip, gel, and electrophoresis.

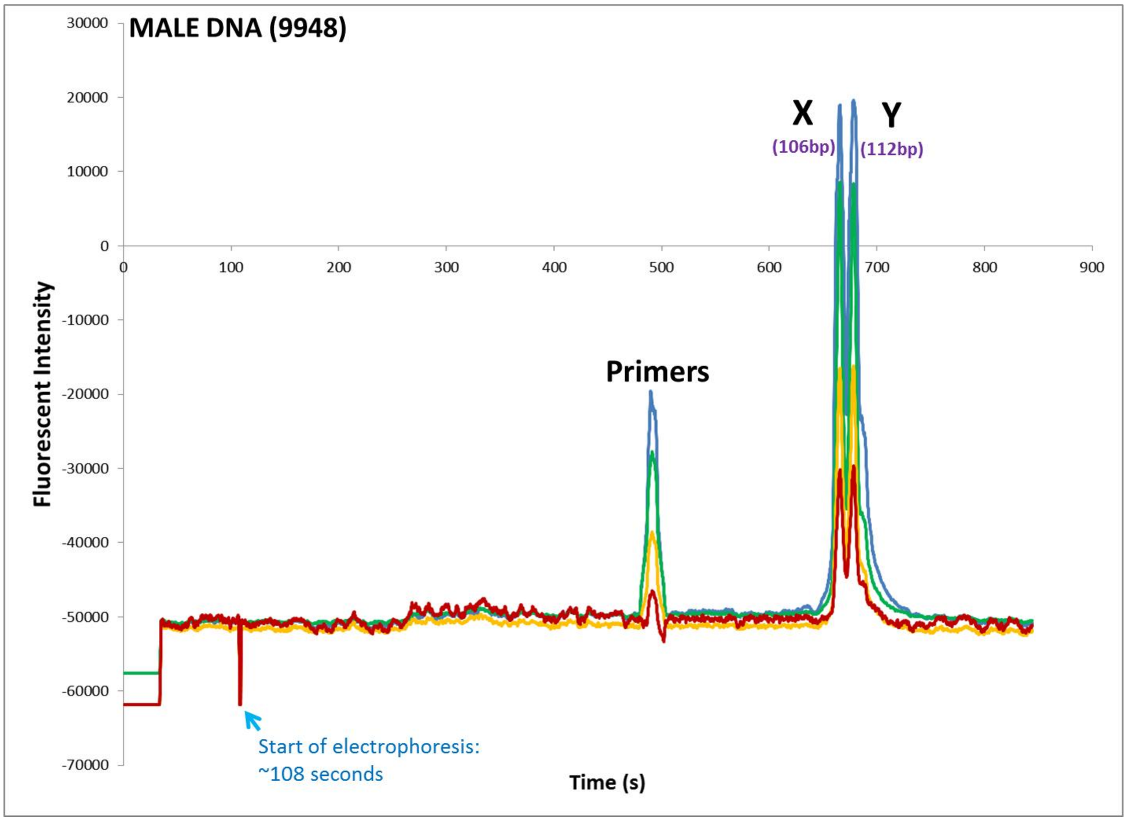

Figure 119. Fluorescent detection results of PCR product from male DNA.

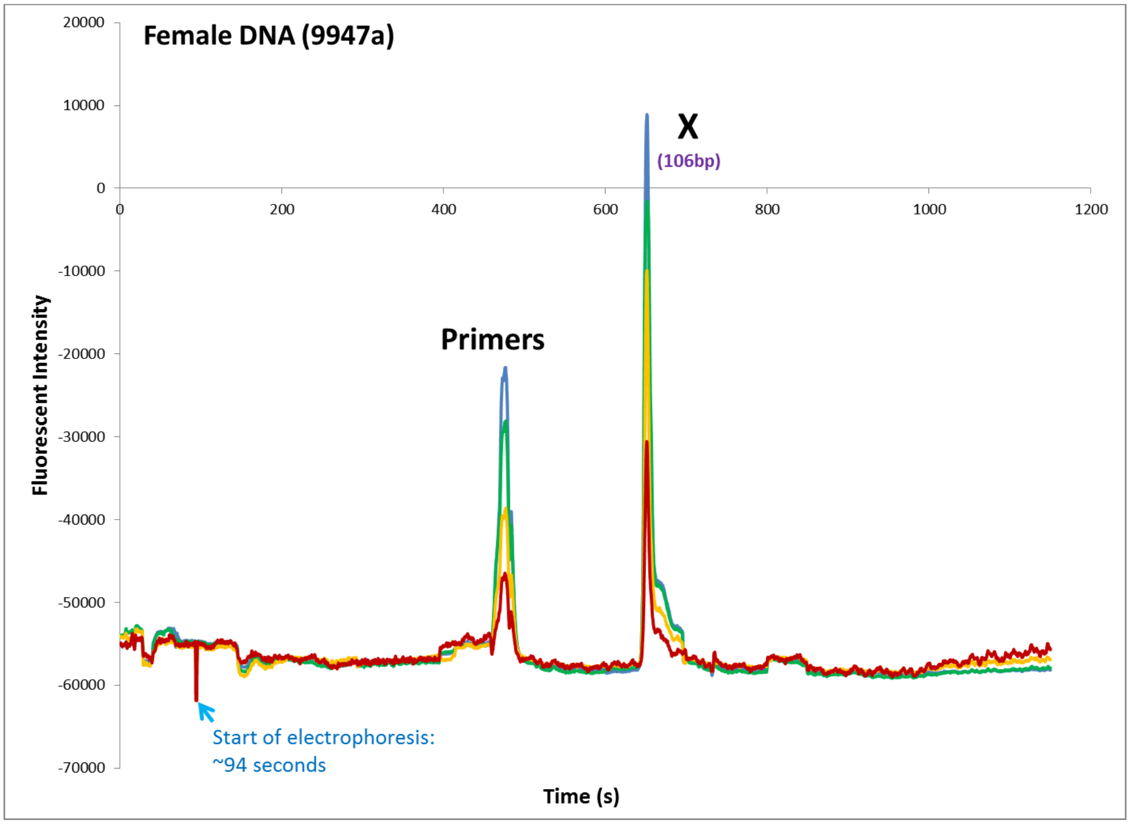

Figure 120. Fluorescent detection results of PCR product from female DNA.

.

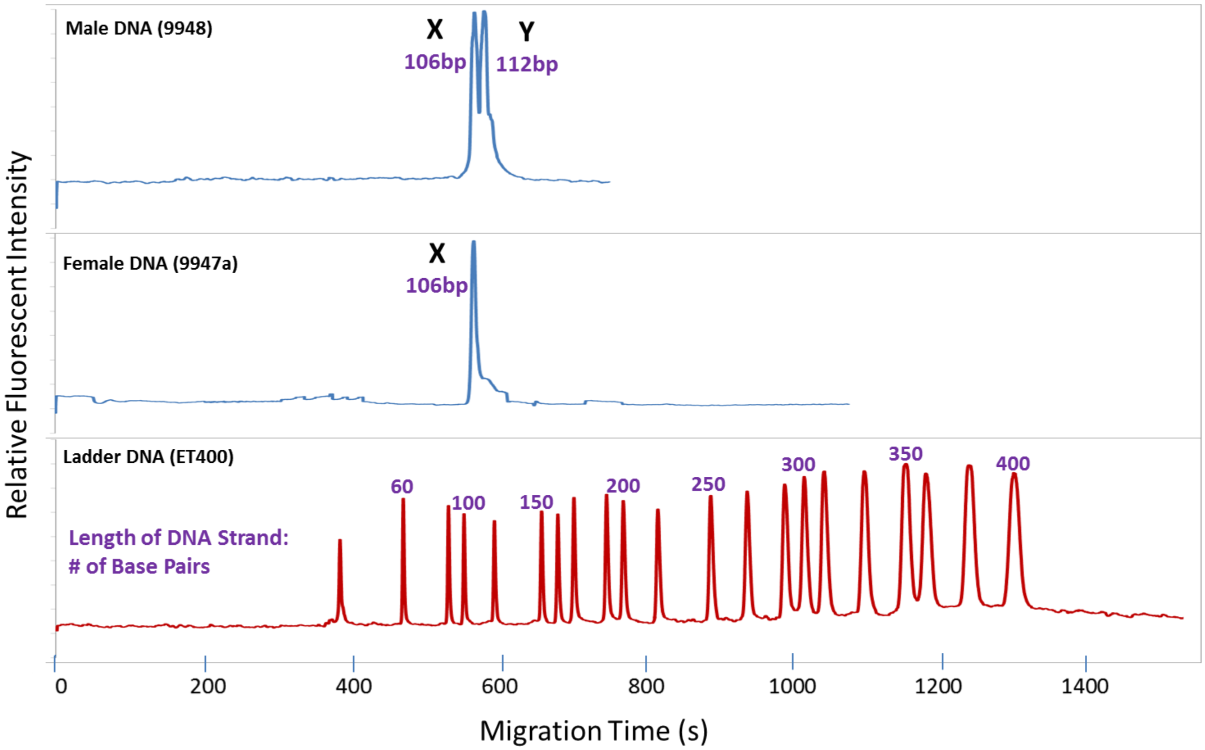

Figure 121. Normalized data shows that the X and Y peaks in both the male and female DNA PCR experiment occur at the correct migration times as calibrated by the ladder DNA, proving the effectiveness of printed devices.

4.4 Conclusion and Future Work

The major steps discussed in this chapter are schematically summarized in Figure 122 below.

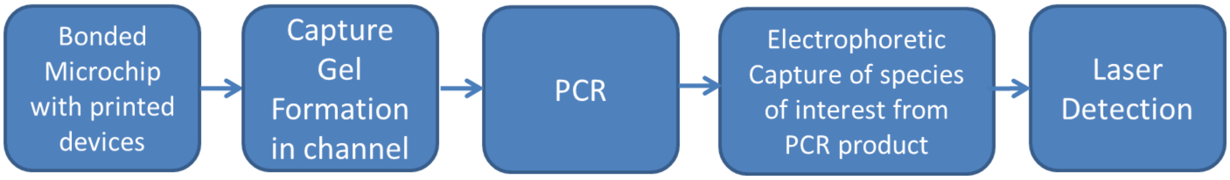

Figure 122. Major steps in the biological demonstration of printed devices.

The microchip was first thermally bonded to form microfludic channels and to enable the functioning of printed devices (RTDs and heaters) that are important for PCR. Thermal bonding required optimization in this project since printed devices had to survive the temperatures used for bonding. Nanoparticle based thin films have a relatively lower threshold for temperature stability compared to films that have been evaporated or sputtered. This obstacle was successfully overcome and a working thermal bonding recipe was finalized.

PCR was next demonstrated using these printed devices. Gender typing (discriminating between male and female DNA) was used as a proof of concept for this demonstration. The first major step in demonstrating PCR was to form the capture gel inside the channel. The capture gel selectively immobilizes the species of interest after PCR. Thermal cycling was then performed to amplify the DNA in the given sample. The sample was then purified and the species of interest was captured on the capture gel. The final step involved electrophoretically moving these species through the laser detector for fluorescent detection of the amplified DNA.

The successful functioning of printed devices for PCR was demonstrated as the results correctly exhibited the fluorescent peaks of male (XY peaks) and female (X peak) DNA for the corresponding samples. Moreover, the accuracy of the printed devices was confirmed when the migration times of the male and female DNA precisely matched the expected times for these DNA sequences. PCR was thus successfully demonstrated using inkjet printed heaters and RTDs.

State of the art fabrication of RTDs and heaters involves numerous processing steps and layers [22, 23, 24]. The tedious process involves masks, photolithography, and deposition and removal of layers. As shown in Chapters 3 and 4, the steps required to define the devices using printed electronics are far fewer. More importantly, since the integrated microfluidic chip is constantly evolving to achieve higher efficiency and to serve new biological applications, the location, structure and dimensions of the devices on the chip are also evolving. The flexibility provided by printed electronics for this purpose is unmatched. It eliminates the need for newer masks and processing steps to define the new structures. Therefore, printed electronics has many advantages over the state of the art fabrication of biological microfluidic systems and has the potential of making the process more efficient and effective.

Since this chapter has involved the integration of printed electronics and biology, many steps have required optimization to satisfy the requirements of both areas. More work is left to be done to better understand some of these optimization steps. Experiments can be done in the future to systematically study the effect of high temperature thermal bonding typically used in biological applications on printed devices. Some ideas include different metals for printing, a wider range of dimensions (thicknesses, widths and lengths, for example) for heaters and RTDs than that studied in this chapter, and other aspects that might help the printed structures withstand the high temperatures. Alternatively, anodic bonding can be studied further for use in biological applications.

To further the use of printed devices in biology, other applications that might require the use of printed RTDs, heaters, and other printed structures can be explored and tested. With the successful PCR demonstration in this chapter, printed RTDs and heaters have been shown to be effective, accurate, efficient, and useful for biological microfluidic applications.

4.5 Sources

[1]"Polymerase Chain Reaction (PCR)." [Online]. Available: http://www.ncbi.nlm.nih.gov/projects/genome/probe/doc/TechPCR.shtml. [Accessed: 06-Feb-2012].

[2] "Home Page of Dr. Andy Vierstraete." [Online]. Available: http://users.ugent.be/~avierstr/. [Accessed: 06-Feb-2012].

[3]J. M. Butler, *Forensic DNA typing: biology, technology, and genetics of STR markers*. Academic Press, 2005.

[4]"Cameron Micro Drill Press." [Online]. Available: http://www.cameronmicrodrillpress.com/cnc.html. [Accessed: 20-Feb-2012].

[5]Z. H. Fan and D. J. Harrison, "Micromachining of capillary electrophoresis injectors and separators on glass chips and evaluation of flow at capillary intersections," *Anal. Chem.*, vol. 66, no. 1, pp. 177-184, 1994.

[6]"Borofloat 33 borosilicate glass, high temperature glass." [Online]. Available: http://www.pgo-online.com/intl/katalog/borofloat.html. [Accessed: 08-Feb-2012].

[7]"UVO Cleaner ®- Utilizing ozone and UV for cleaning glass slides etc." [Online]. Available: http://www.jelight.com/uvo-ozone-cleaning.php. [Accessed: 14-Feb-2012].

[8] I. U. Vakarelski, R. Maenosono, J. W. Kwek, and K. Higashitani, "Thermal modification of layer-by-layer assembled gold nanoparticle films," *Colloids and Surfaces A: Physicochemical and Engineering Aspects*, vol. 340, no. 1–3, pp. 193-198, May 2009.

[9] A. Berthold, L. Nicola, P. Sarro, and M. Vellekoop, "Glass-to-glass anodic bonding with standard IC technology thin films as intermediate layers," *Sensors and Actuators A: Physical*, vol. 82, no. 1–3, pp. 224-228, May 2000.

[10]"UC Berkeley Marvell Nanofabrication Laboratory Lab Manual." [Online]. Available: http://nanolab.berkeley.edu/labmanual/labmantoc.html. [Accessed: 15-Feb-2012].

[11]Y. Shi, P. C. Simpson, J. R. Scherer, D. Wexler, C. Skibola, M. T. Smith, and R. A. Mathies, "Radial Capillary Array Electrophoresis Microplate and Scanner for High-Performance Nucleic Acid Analysis," *Anal.Chem.*, vol. 71, no. 23, pp. 5354–5361, 1999.

[12]E. E. Miller and R. D. Miller, "Physical Theory for Capillary Flow Phenomena," *Journal of*

Applied Physics, vol. 27, no. 4, pp. 324–332, Apr. 1956.

[13] E. W. Washburn, "The Dynamics of Capillary Flow," *Phys. Rev.*, vol. 17, no. 3, pp. 273–283, Mar. 1921.

[14]G. E.V., "Dynamic contact angles: Temperature dependence and the influence of the state of the adsorption film," *Advances in Colloid and Interface Science*, vol. 39, pp. 235–255, Apr. 1992.

[15] J. A. Pask and R. M. Fulrath, "Fundamentals of Glass-to-Metal Bonding: VIII, Nature of Wetting and Adherence," *Journal of the American Ceramic Society,* vol. 45, no. 12, pp. 592–596, Dec. 1962.

[16]"Thorlabs.com - EG58 Electrodag 5810 Silver Epoxy 4.4g." [Online]. Available: http://www.thorlabs.com/thorproduct.cfm?partnumber=EG58. [Accessed: 16-Feb-2012].

[17] "Dynamic capillary array coating for MegaBACE capillaries: DEH100", by *Gel Company.* [Online]. Available: http://www.gelcompany.com/products/applied-biosystems/3100-3130-3130xl/accessories/6299-dynamic-capillary-array-coating-for-megabace-capillaries-100-m?vmcchk=1. [Accessed: 19-Feb-2012].

[18] P. Liu, S. A. Greenspoon, S. H. Yeung, J. R. Scherer, and R. A. Mathies, "Integrated sample cleanup and microchip capillary array electrophoresis for high-performance forensic STR profiling," *Methods Mol. Biol.*, vol. 830, pp. 351–365, 2012.

[19] R. G. Blazej, P. Kumaresan, and R. A. Mathies, "Microfabricated bioprocessor for Integrated nanoliter-scale Sanger DNA sequencing," *Proceedings of the National Academy of Sciences*, vol. 103, no. 19, pp. 7240 –7245, May 2006.

[20] P. C. Weber, D. H. Ohlendorf, J. J. Wendoloski, and F. R. Salemme, "Structural origins of high-affinity biotin binding to streptavidin," *Science,* vol. 243, no. 4887, pp. 85–88, Jan. 1989.

[21] N. M. Toriello, E. S. Douglas, N. Thaitrong, S. C. Hsiao, M. B. Francis, C. R. Bertozzi, and R. A. Mathies, "Integrated microfluidic bioprocessor for single-cell gene expression analysis," *Proceedings of the National Academy of Sciences,* vol. 105, no. 51, pp. 20173 –20178, Dec. 2008.

[22] M. C. Ruiz-Martinez, J. Berka, A. Belenkii, F. Foret, A. W. Miller, and B. L. Karger, "DNA sequencing by capillary electrophoresis with replaceable linear polyacrylamide and laser-induced fluorescence detection," *Anal. Chem.*, vol. 65, no. 20, pp. 2851–2858, 1993.

[23] "40% Acrylamide Solution #161-0141: Life Science Research: Bio-Rad." [Online]. Available: http://www.bio-rad.com/prd/en/US/adirect/biorad?cmd=catProductDetail &vertical=LSR&country=US&lang=en&productID=161-0141. [Accessed: 20-Feb-2012].

[24] “Water soluble Azo initiators > VA-086.” [Online]. Available: http://www.wakochem.co.jp/specialty/waterazo/VA-086.htm. [Accessed: 19-Feb-2012].

[25]S. KM, M. A, K. CP, and G. P, “A rapid and quantitative DNA sex test: fluorescence-based PCR analysis of X-Y homologous gene amelogenin.,” *BioTechniques*, vol. 15, no. 4, p. 636, Oct. 1993.

[26]J. A. Luckey, H. Drossman, A. J. Kostichka, D. A. Mead, J. D’Cunha, T. B. Norris, and L. M. Smith, “High speed DNA sequencing by capillary electrophoresis,” *Nucl. Acids Res.*, vol. 18, no. 15, pp. 4417–4421, Aug. 1990.

[27]J. A. Luckey and L. M. Smith, “Optimization of electric field strength for DNA sequencing in capillary gel electrophoresis,” *Anal. Chem.*, vol. 65, no. 20, pp. 2841–2850, 1993.

[28] “GE Healthcare Life Sciences - Products - MegaBACE^{TM} ET Size Standards.” [Online]. Available:http://www.gelifesciences.com/aptrix/upp01077.nsf/Content/Products?OpenDocument&moduleid=164369. [Accessed: 22-Feb-2012].

5. All-Printed, Electrostatically Actuated, PDMS Microfluidic Valves

5.1 Introduction and Motivation

Microvalves are essential components of lab-on-a-chip (LOC) systems. Since the LOC device integrates all components of a lab onto a hand-held chip, multiple processes occur here. Holding and facilitating flow of fluids in this chip requires a microfluidic valve.

Microfluidic valves can be grouped into two categories, namely active and passive microvalves. Active microvalves can be categorized further into mechanical, non-mechanical, and external valves. Mechanical active microvalves typically couple a flexible membrane to magnetic [1,2], electric (electrostatic and electrokinetic) [3,4,5], piezoelectric [6,7], thermal [8,9]or other actuation methods. Non-mechanical active valves consist of a movable membrane which is actuated by functionalized smart materials such as those capable of phase change [10,11], and rheological materials [12,13]. Finally, external active valves are membranes that are actuated by the aid of external systems such as built-in modular [14,15] or pneumatic[16, 17] means.

Although less popular with microfluidic chips than active valves, passive valves have also been studied for biological LOC applications. Passive microvalves, sometimes referred to as check valves, only open to forward pressure, showing diode-like characteristics. They are typically incorporated in inlets and outlets of reciprocal displacement micropumps. Passive mechanical microvalves contain mechanical moving parts, such as flaps [18, 19] and spherical balls [20,21]. Passive valves without mechanical moving parts (i.e. non mechanical valves) use a diffuser element [22,23] or capillary forces [24,25] to obtain a working valve. A more comprehensive study of active and passive valves researched over the last two decades can be found elsewhere [26].

For the purposes of this project, electrostatic valves are of interest. Electrostatic valves have the advantage of fast response time, relatively easy fabrication, being able to provide contamination and leakage free valves (robustness), repeatability, and not needing auxiliary devices (such as external vacuum supply in pneumatic valves). Some disadvantages include high actuation voltage requirements, although this is not a big concern for biological microfluidic applications since electrophoresis requires very high voltages as well.

The basic structure required for electrostatic microvalves is illustrated in Figure 123. The open valve configuration occurs when the metal electrodes are held at the same potential. When there is a potential difference between the two metal electrodes, the valve membrane gets actuated due to electrostatic attraction between the two electrodes. The valve is thereby able to close the channel successfully, as illustrated in the cross sectional view of the actuated valve in Figure 123.

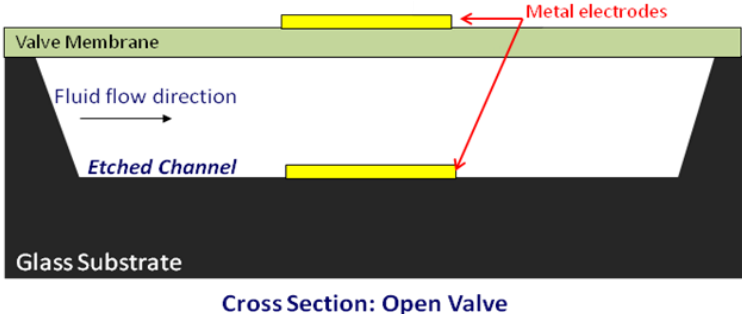

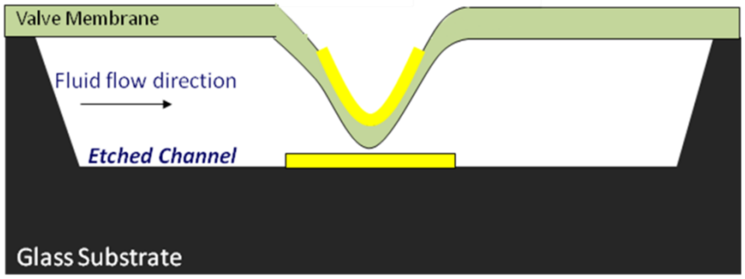

Cross Section: Actuated Valve

Figure 123. Basic functioning of an electrostatic microvalve; the open valve (top) is when both electrodes are grounded while the actuated valve (bottom) is triggered by a potential difference between the two electrodes.

Traditional fabrication of electrostatically actuated PDMS valves is difficult as it requires orthogonal compatibility between layers that is not easily achievable. In other words, integrating electrostatic valves in a microfluidic chip using standard subtractive processing techniques (lithography, etching, sputtering/evaporation) affects the entire chip during fabrication. High temperature processing needed for this type of fabrication requires the PDMS membrane to be formed last. Solvents required to etch photoresists affect and swell PDMS [27]. Many such obstacles deter researchers from simultaneously utilizing the advantages of PDMS and electrostatic actuation.

Printed electronics provides a solution to this barrier. Printing allows for selective deposition of materials where desired, making the fabrication of electrostatic PDMS valves more practical. The advantages of glass over PDMS as a substrate for microfluidic system have been discussed in chapter 3 of this thesis. Printing can potentially facilitate deposition of PDMS in just the areas of the chip that requires valves, thereby making use of the advantage of glass and PDMS in different parts of the chip.

Here, for the first time, we present all printed, electrostatically actuated PDMS microvalves designed for biological microfluidic applications. This chapter begins with COMSOL simulation of PDMS valves, followed by print, integration and characterization of the same.

5.2 Simulation-based Valve Design

Designing a valve involves the optimization of many parameters including dimensions of the valve membrane, distance between electrodes, and actuation voltage. In particular, the optimum valve structure would demonstrate low voltage requirements for a desired deflection. Before a valve can be printed, the different factors that define its structure need to be optimized. Since this optimization involves numerous parameters, simulation based design (SBD) becomes useful.

SBD provides a platform to vary and analyze these parameters efficiently. In other words, a matrix of design parameters can be tested simultaneously to arrive at a feasible design with reasonable voltage requirements. As mentioned in Chapter 3, since SBD uses first-principle-based simulations of the multiphysics interactions in the functioning of a valve, it is accurate and deterministic. In other words, once a simulated design is finalized and implemented, the experimental results can be expected to be very similar to the simulated results if not identical. In this project, this was verified when the valve actuation voltage suggested by the simulations matched very closely to the actual voltage requirements in experiments. Therefore, to make use of the advantages that SBD provide for optimization of a system with numerous parameters, the valves were designed using COMSOL.

The valves were simulated initially to verify the feasibility of the structure that was designed to be printed and to obtain expected values for voltage, deflection, dimensions and other important parameters. The simulations were continued throughout the experimental phase of the valves (discussed in the next section) as well and served as a feedback system to relate experimental values to COMSOL simulations.

COMSOL has already been introduced in chapter 3 of this thesis. A more detailed description of COMSOL, its features, and its in-built modules can be found in *COMSOL Multiphysics User's Guide* [28]and in the *COMSOL Multiphysics Modeling Guide* [29].

For the simulation of valves, the electrostatics, moving mesh, and plane strain application modes in COMSOL were used. These modes (sub-modules) will be discussed next:

1) **Electrostatics:** The electrostatics application mode falls under the electromagnetics module in COMSOL and assists in modeling static electric fields. By combining the definition of potential with Gauss' law, the equation of continuity, and Poisson's equation, this mode is able to model electric fields and potentials. With the simulation of valves, the electrostatics application mode is used to define the electric potential at the two electrodes above and below the valve membrane that provides the electrostatic force to actuate the valves. The electrostatics application mode is coupled with the two other modes described below to simulate the PDMS valve actuation.

2) **Moving Mesh (ALE):**Using the ALE(Arbitrary Lagrangian Eulerian) formulation, the moving mesh application mode is used to create models where the geometry (i.e. the mesh) changes shape due to some physics in the model. The moving mesh model allows study of both static and time-dependent deformations where the geometry of the problem of interest changes its shape due to the dynamics of the problem. In the case of valves, moving mesh module allows modeling of the deformation of PDMS relative to air, which is set as the surrounding 'material'.

3) **Plane Strain:** The plane strain mode falls under the structural mechanics module. The structural mechanics module provides predefined interfaces for elasto-plastic, hyperelastic, and viscoelastic material models like PDMS. Material models can be isotropic, orthotropic, or fully anisotropic, and local coordinate systems can be used to specify material properties. The plane strain application mode solves for global displacements in the x and y directions. The applied loads are assumed to be constant through the specified thickness in these directions. In the simulation of valves, the plane strain mode couples with the electrostatics and moving mesh modes to model the 2-D simulation of valves.

Using the discussed application modes, COMSOL simulates and optimizes the PDMS valve structure. PDMS was decided to be the material of choice for the valve membrane based on structural requirements that had to be met. This will be discussed further in the following section. The physical parameters and material properties of PDMS were extracted from literature sources [30, 31] and were entered into the plane strain mode. In this simulation, the thickness of the PDMS valve membrane was set to 20μm, and the length of the PDMS in the +/- X direction was set to 500μm. These values were based on printable dimensions for PDMS (discussed later in this chapter). Also, the distance between the two electrodes was set to 70μm, an initial estimate based on the etched glass substrates. The result from 2-D simulation of a PDMS valve using the aforementioned dimensions is shown in Figure 124.

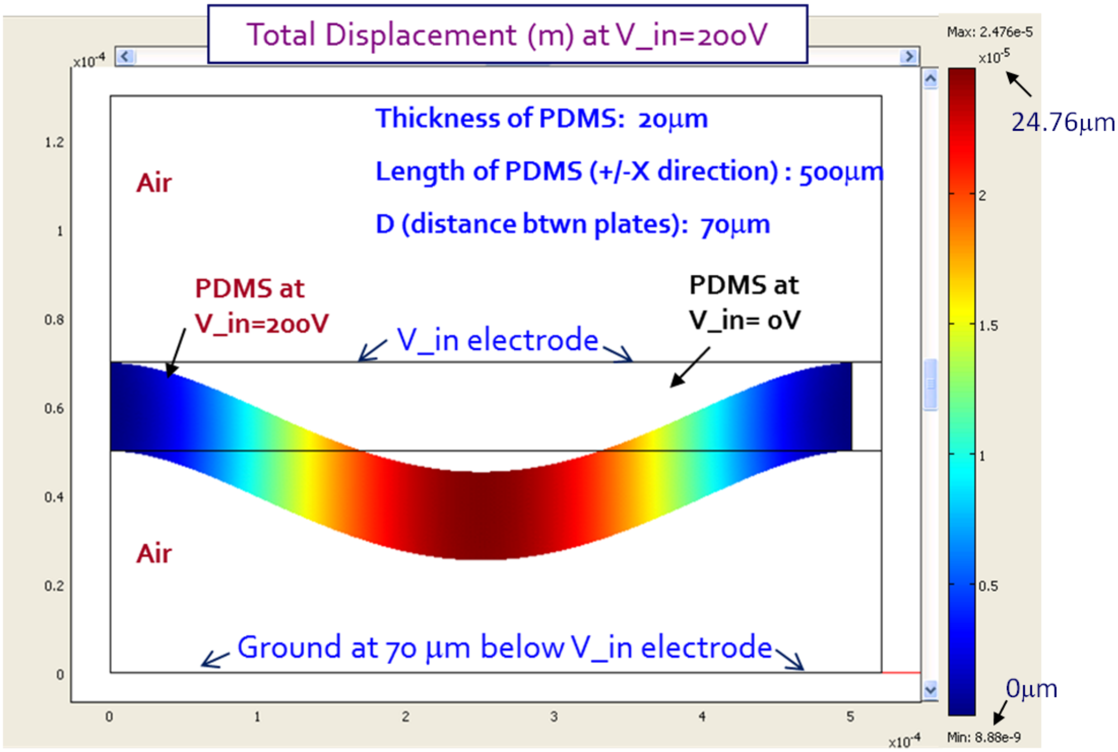

Figure 124. Results from 2-D COMSOL simulation of electrostatically actuated PDMS valve.

The results in Figure 124 show that with the specified dimensions, a deflection of ~25μm can be achieved with a PDMS valve membrane given an input voltages of 200V. The channel depth typically ranges anywhere from 15-35μm and therefore 25μm is a reasonable closed valve deflection for the given voltage. This initial result verified the feasibility of the valve structure that was to be printed. 3-D simulation of valves can provide more information and this will be done in the future work of this project. In addition, Figure 125 shows the relationship between deflection and voltage for the 2-D simulation presented in Figure 124.

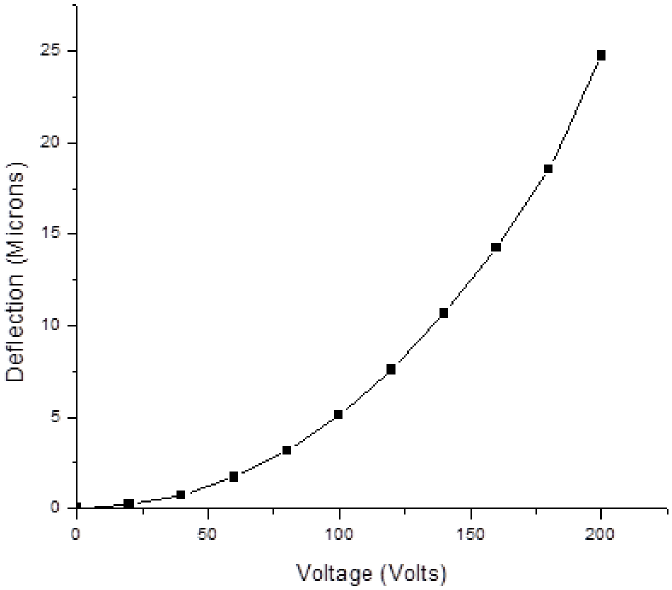

Figure 125. Deflection as a function of voltage for the 2-D simulation in Figure 124.

The relationship in Figure 125 is supported by equations that define the deflection of the PDMS valve. The PDMS valve is represented by a basic cantilever beam structure with two anchored points as shown in Figure 126.

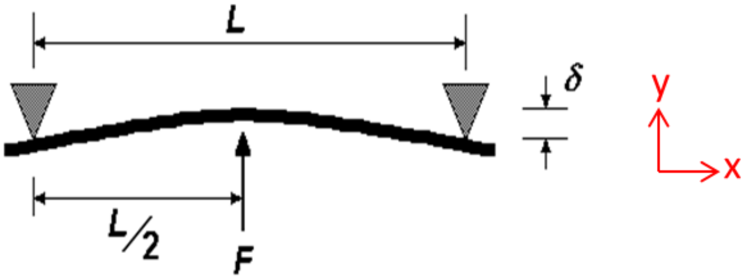

Figure 126. Cantilever beam structure with two anchored points representing the PDMS valve structure.

The equation for the deflection of the beam δ *is:*

$$\delta = FL^3 / (48E\ I)$$

where:

F= force applied (in the case of electrostatic force, F is in the form of voltage)
L= the width of PDMS in +/- X direction that covers the channel (can also be defined by the width of the channel)
E= Young's Modulus of PDMS (~500KPa)
I= moment of Inertia

To define these terms further,

I= $bh^3/12$
where:
b= the length of the PDMS in the direction perpendicular to the page (i.e. into the page)
h= thickness of the PDMS membrane (in the Y direction)

F= V q/d
where:
F= electrostatic force
V= applied voltage
q= unit charge
d= distance between the two metal electrodes

The equation for the deflection of the beam (or PDMS membrane in this case) reveals all the parameters that affect the deflection value. Figure 125 can be explained using the force parameter, **F,** which is directly related to deflection**.** Since **d** AND **V** in the force equation are changing as voltage changes (since at each V, the PDMS is deflecting bring the electrode closer together), F changes exponentially.

Other important information is also revealed by the deflection equation. The most significant parameter is the thickness of the membrane (**h** in the equation) since it changes the amount of deflection by a cubic factor. Also, although making the width of the PDMS over channel (or width of channel) as large as possible would make the deflection larger for a given voltage according to the equation, the width of the channel is limited by the processes performed in biological microfluidic applications. Specifically, the wider the channel, the higher the current generated during electrophoresis. When the current is too high, the biological solution in the channels heats up causing undesired bubbles in the channels and leading to erroneous results.

Limitations exist for the **h** parameter as well and this will be discussed in section 5.3.3. Optimization of these parameters for printability, biology, and valve operation had to be done to arrive at a working valve.

The printing of each of the layers of the PDMS valve and integration thereof will be discussed next.

5.3 Printing of Microfluidic valves

5.3.1 Fabrication of Printed Valves

To give context to the rest of this section, the basic fabrication steps of the valve will now be listed. The details and optimization of each of these steps will be discussed later in this section. The basic process steps are as follows:

1) Glass channels are first wet-etched using the process described in the previous chapter using an amorphous silicon or a gold mask.

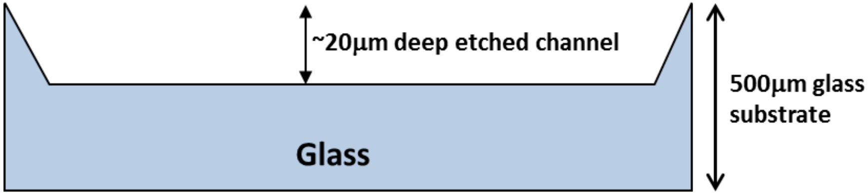

The mask used for this etch contains channel widths varied from 250-600µm to arrive at the optimum width for printing and valve operation.

2) Next, electrode 1 is printed inside the channel and annealed.

3) The sacrificial layer is printed inside the channel and baked to harden inside the channel.

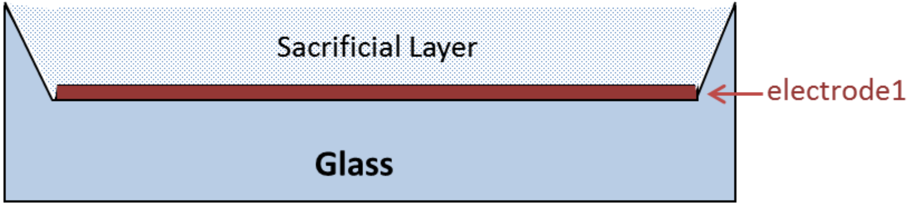

4) The valve membrane is printed and annealed to cure.

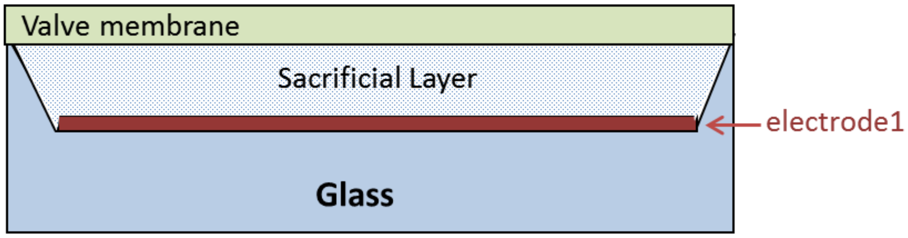

5) The sacrificial layer is then removed.

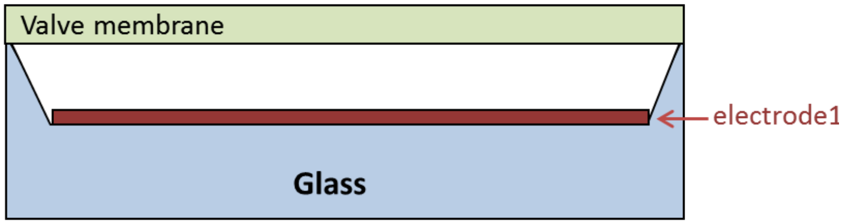

6) The electrode 2 layer is printed on top of the valve membrane and annealed.

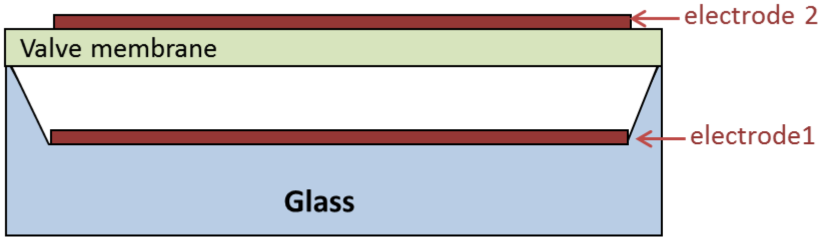

7) The valve is then tested and deflected by applying a potential difference between electrode2 and electrode1.

5.3.2 Printers Used for Valve Formation

A combination of pneumatic and inkjet printers were used for printing the different layers of the valve.

a) **Dimatix Fujifilm inkjet printer:** The features and operation of the Dimatix printer have already been discussed in Chapter 3 and can also be found in the Dimatix Manual [32]. *The Dimatix inkjet printer was used to print electrodes 1 and 2.* The details of printing these layers will be discussed in the next section.

b) **Pneumatic/Dispenser printer:** The pneumatic printer (also known as extrusion printer) uses 'direct write dispenser printing' technology for printing of materials. Direct write dispenser-printing technology is a versatile and scalable manufacturing technique for additive deposition of novel materials. The pneumatic printing system is composed of a syringe and needle connected to a pneumatic controller and mounted onto an *x–y–z* stage, as shown in Figure 127 and Figure 128. All functions are automated via custom java software. To pattern a material using the dispenser printer, an ink is loaded into a syringe, extruded through a hollow needle of predetermined dimensions and 'written' onto a substrate via a succession of drops or 'shots'. The drop size is determined by the needle's dimensions, ink rheology and applied pressure. The resulting printed film morphology depends on the dimensions of the extruded drops as well as the traversing distance, speed and time between shots [33]. *The substrate traverses in this printing system and not the needle/syringe system.* The operation of the printer is shown in Figure 128.

To summarize, ink is extruded from a syringe needle directly onto a substrate in an additive fashion by pneumatic control. The stage is temperature controlled and can be heated during printing if necessary. A large range of functional materials can be printed using this printer onto a variety of substrates including printed circuit boards (PCB), glass, and silicon wafers.

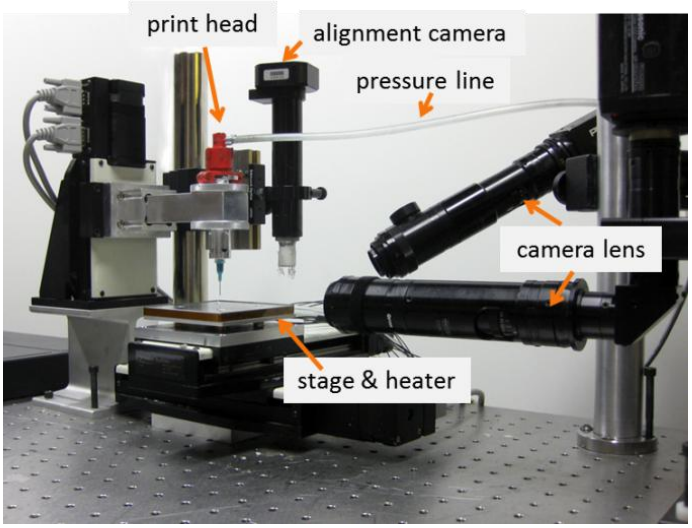

Figure 127. Dispenser printer with a heatable stage and air-pressure controlled dispending system [33].

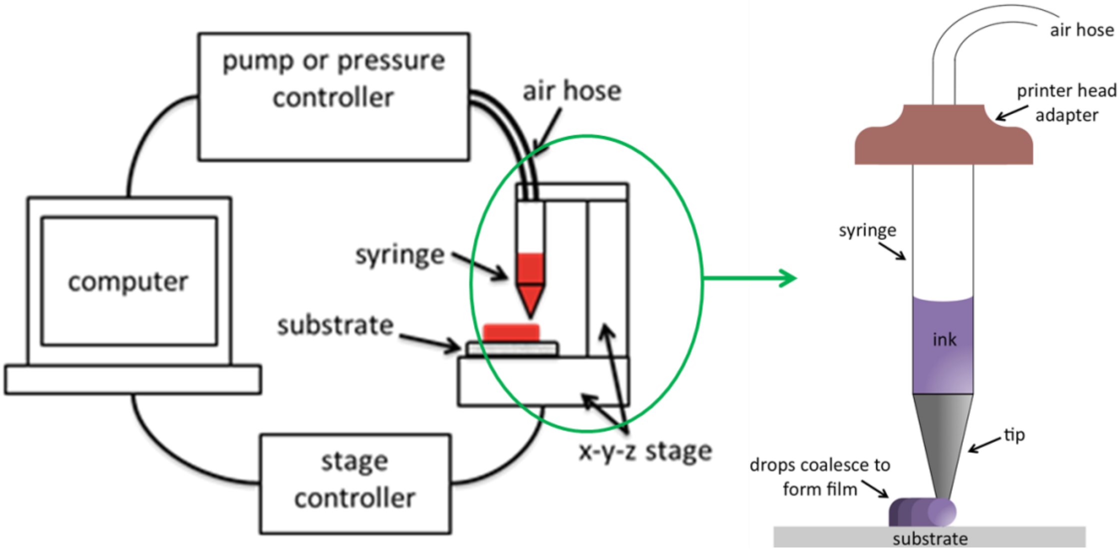

Figure 128. Schematic that describes the basic operation of the pneumatic printer [33].

As shown in Figure 128, the ink is pneumatically dispensed in a controlled way and the drops coalesce on the substrate to form a film. This printer can accommodate a wider range of materials as inks compared to inkjet printers such as the Dimatix. In particular, a wider range of viscosities of inks can be printed. A wide range of thicknesses and widths can also be printed because the printer tip (indicated in Figure 128) ranges from 150μm to 1μm, as shown in Figure 129. More details on the features and operation of this printer can also be found on the Berkeley Manufacturing Institute Lab site [34].

In the printing of valves, the pneumatic printer was used to print the sacrificial layer and the valve membrane. The sacrificial layer and the valve membrane both required tall features. The dimensions of the sacrificial layer were determined by the channels in the microfluidic chip. The dimensions of the valve membrane were determined by structural requirements needed to yield a functioning valve. In both cases, the required tall features could not be easily printed with inkjet printer since the inkjet printer is ideal for printing finer features. The pneumatic printer has an advantage in this regard and was therefore used for the printing of these layers.

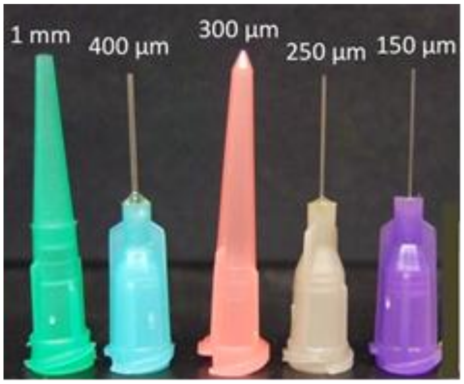

Figure 129. The size range of tips (*from McMaster-Carr)* available for use with the pneumatic printer [33] .

5.3.3 Valve Formation: Fabrication and Printing of the Different Layers of the Valves

The basic fabrication steps for the formation of valves were listed in section 5.3.1. Each of these steps will now be discussed in detail.

Step 1: Etching channel in Glass

The fabrication process used to etch channels in glass has already been discussed in Chapter 4, and the same protocol was followed here. The height and width profile of the wet-etched channel, measuring using Tensor Alpha Step 200 Profilometer (ASIQ), is shown in Figure 130. This particular sample had a mask channel width of 400µm and an isotropically etched width of about 440µm. The channels used for the valves had an etched depth of 17-20µm. Wet-etched channels have rounded corners in the bottom since the etch is isotropic, but ASIQ is not capable of detecting these rounded corners since the angular resolution is limited by the angle of the profilometer tip. Therefore, although the shape of the profile in Figure 130 is not completely representative of the actual channel, the values for the height and width of the etched channel are accurate.

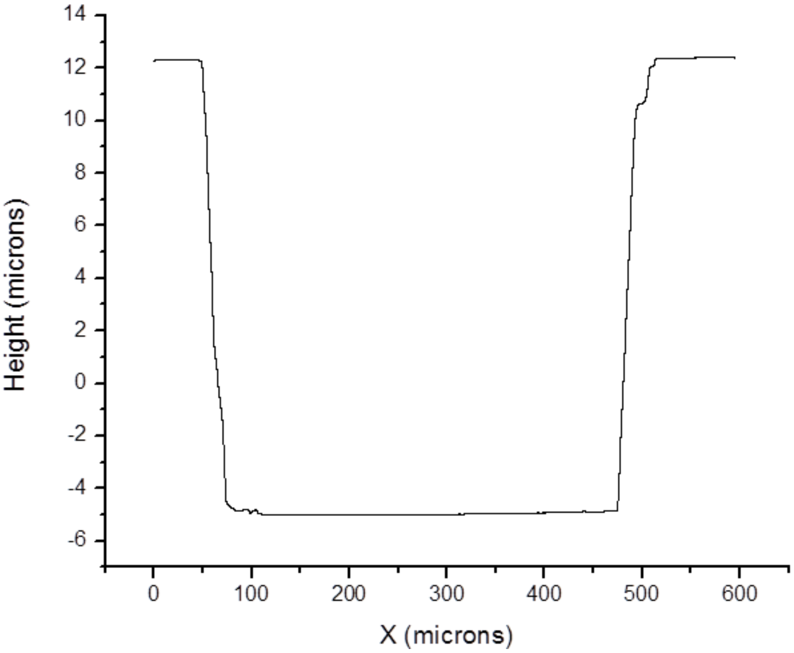

Figure 130. ASIQ height and width profile of etched channel with a depth of ~17µm.

Step 2: Printing of electrode 1 inside channel

The electrode inside the channel had to be printable and biocompatible since biological solvents will be in contact with this material. The electrode was printed inside the channel instead of the bottom of the etched glass substrate (can be printed last and made contact to easily) in order to reduce the distance between the two electrodes, thereby reducing the voltage needed for a reasonable deflection.

Substrate Treatment and Print Parameters: Gold nanoparticle ink (NPG-J from Chapter 3) was used to print electrode 1 inside the channel. The borofloat glass substrate referred to in Chapter 3 was used for the printing of valves as well. The substrate was first cleaned with piranha solution as optimized earlier. A layer of gold was then printed using Dimatix inkjet printer to cover the entire channel using the optimized print parameters from chapter 3, namely 35μm drop spacing, 8-9m/s drop velocity and 0.95-1mm print height. The substrate/ink was then annealed at 250^{0}C for 1 hour.

A top view image of gold printed and annealed inside the channel is shown in Figure 131.

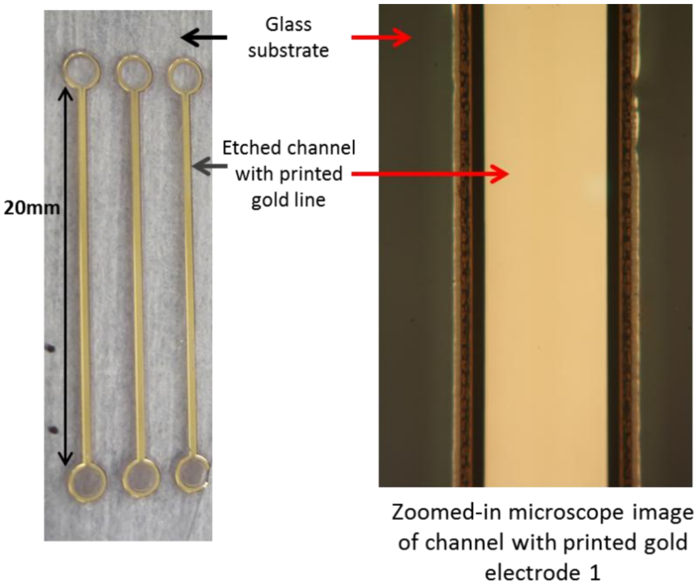

Figure 131. Top view images of gold electrode (electrode 1) inkjet printed inside the etched channel.

Step 3: Printing of sacrificial layer inside channel

The sacrificial layer had to be easily printable, removable and orthogonally compatible with the valve membrane. Since PDMS was narrowed down to be the choice of material for the valve membrane (detailed in the next step), the sacrificial layer had to be removed with a solvent or method than does not swell or chemically modify affect PDMS.

Studies on solvent compatibility of PDMS [27] reveals water as the only solvent with the least effect on PDMS formation and swelling. Although some alcohols also fall under this category, none of them are as inert as water for PDMS. Therefore, Poly methyl methacrylate (PMMA) and other common sacrificial layers that require organic solvents such as acetone for removal cannot be used.

The choices for sacrificial layer were narrowed down to gelatin and poly vinyl alcohol (PVA), both of which are removable with water. Both have been used as sacrificial layers previously with PDMS [35, 36]. In order to avoid the additional processing steps that gelatin requires and its inherent swelling [111], PVA was narrowed down to be the choice of material for the sacrificial layer. PVA is highly soluble in water. Also, since PVA does not chemically interact with PDMS in any way [112], it works well as a sacrificial layer. Specifically, 99+% hydrolyzed PVA with a molecular weight of 89000-98000 (*from Sigma Aldrich)* was used to form the sacrificial layer for the valve.

Printer: *The pneumatic printer was used instead of inkjet printers for printing PVA* because the dimensions (~400µm line width) and thicknesses (~20µm) needed for the sacrificial layer were more feasible with the pneumatic printer.

Substrate Treatment: The substrate with gold inside the channel cannot be cleaned in a piranha solution or any other method that might affect the printed gold electrodes. Therefore, no clean treatment was performed right before PVA printing.

When printing PVA, which is water-based, the solution tends to wet the hydrophilic surfaces (glass) better than the printed gold electrodes from Step 2 which are relatively hydrophobic. Thus, PVA printing initially posed some challenges. PVA needs to be printed inside the channel on top of the gold electrode and not on the outside (of the channel) hydrophilic glass surface. The selective hydrophobic treatment was therefore performed by applying small amounts of gel slick (discussed in previous chapters) carefully in the areas right outside the channel in order to make the glass surface relatively more hydrophobic than the gold electrode. This step prevents the PVA from spreading in the areas right outside the channel, which would make the formation of the valve membrane difficult.

Print Parameters and PVA Solution:
The pneumatic printer has the following variable print parameters:

1. *Shot Spacing (Drop Spacing)*- spacing between each drop
2. *Move Time*- the amount of time the system waits before moving the substrate for the subsequent drop (the distance moved at every move time is the drop spacing)
3. *Tip size*- range of sizes shown in Figure 129
4. *Air Pressure (Shot Pressure)*- amount of air pressure applied to deposit a drop
5. *Distance from tip to substrate*

Another variable solution parameter is the concentration of PVA. The optimization of these parameters will be discussed next.

To begin with, tip size had to be minimized to accommodate printing inside the smallest possible channel width(electrophoresis limitations). It is desirable to keep the channel width under 500µm to avoid overheating during electrophoresis. *The smallest tip, a 30 gauge 150µm inner diameter tip, was therefore chosen.* The air pressure also had to be minimized for reducing line width. The range available on the printer was 20kPa to 400kPa. *The minimum pressure required to print a smooth line with the optimized PVA concentration (discussed next) was 50-55kPa.* The tip had to be as close to the substrate as possible without dragging the substrate. *This distance was therefore optimized to be ~150µm.*

The optimization of PVA concentration will be discussed next. PVA is soluble in warm water. Therefore, using a heating mantle set-up, a range of concentrations (weight% in water) was solubilized in 80^0C water. The data shown in Figure 132 was measured using a rheometer (*Brookfield Digital Rheometer*) and shows the viscosity as a function of the PVA concentration.

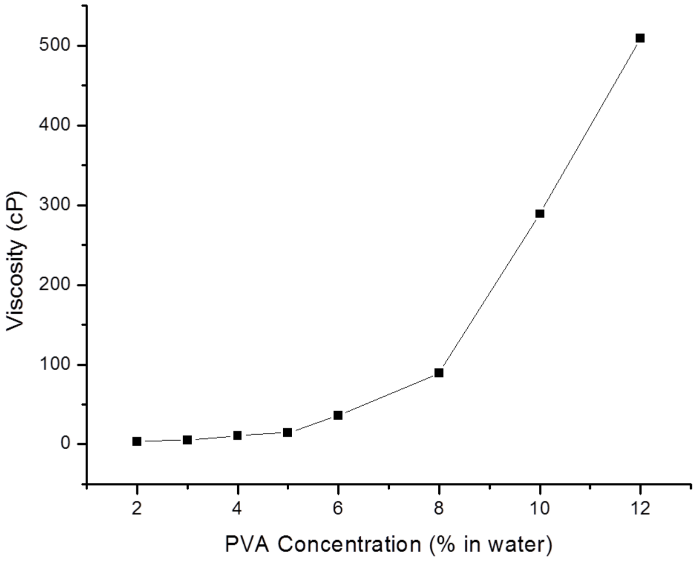

PVA Conc	Visc (cP)
2%	3.62
3	4.89
4	10.9
5	14.8
6	35.6
8	89.5
10	289
12	509

Figure 132. Viscosity of a range of PVA concentrations.

2% and 4% PVA had too low of a viscosity, and even with the lowest pressure and tip size, the print was still not controllable. 8% PVA did not allow smooth printing with the smallest tip (~150µm) since the solution was too viscous. Therefore, the 27 gauge or 200µm tip had to be used to print the 8% PVA, resulting in a line width of ~800µm, a slightly higher than desired width. Similar results were obtained from 10% and 12% solutions since the viscosity was relatively higher. *6% PVA was therefore chosen to print inside the channel leading to a line width of ~400µm using the smallest tip and the lowest possible pressure.*

The remaining two print parameters (drop spacing and move time) will now be optimized using 6% PVA prints. The results from PVA lines printed with varying drop spacing on a borofloat glass wafer and the corresponding line edge roughness (LER) measurements are shown in Figure 133. LER has been discussed in Chapter 3. *As seen in Figure 133, a drop spacing of 0.2mm gave the most stable line.*

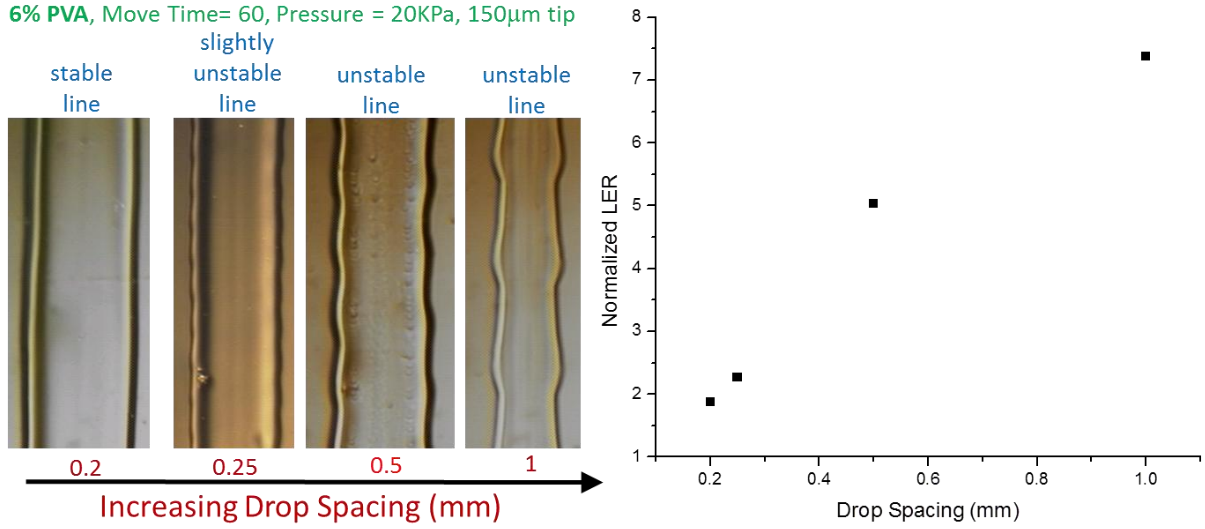

Figure 133. 6% PVA prints (left) and LER results (right) as a function of increasing drop spacing.

Move time was varied from 10-100ms, and the slowest print gave the most stable lines. This is demonstrated in Figure 134. *Therefore, 100ms was selected as the move time for the sacrificial layer prints.*

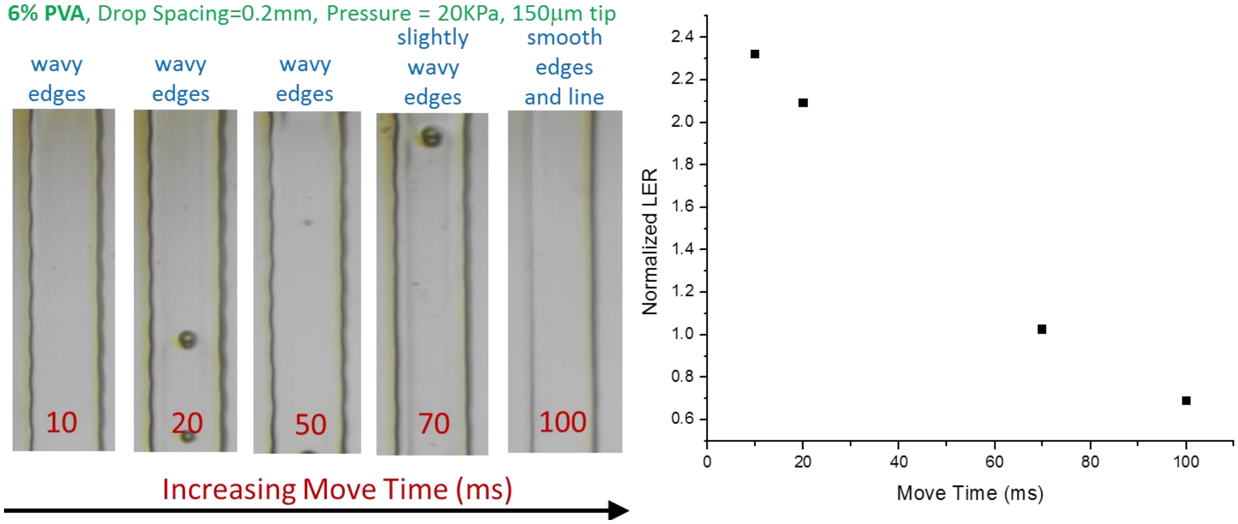

Figure 134. 6% PVA prints (left) and LER results (right) as a function of increasing move time.

Overcoming Coffee-Ring Effect:

The coffee ring effect has been previously studied in printed electronics [37]. It is a big concern in the printing of the sacrificial layer in this project because the water-based PVA film formation inside the channel determines the foundation of the PDMS valve membrane that follows. Therefore, if the PVA print inside the channel has high coffee ring edges, the PDMS membrane will have an uneven base, leading to printing and deflection concerns in the latter part of this process. Therefore achieving an even print for the PVA is crucial. Although printing PVA inside a trench has different dynamics than printing on a flat surface, the formation of coffee ring and the suppression thereof in both cases occur in the same way.

Two ways of suppressing the coffee ring effect include temperature control of substrate when printing [38,39] and a co-solvent system [40,41]. A combination of both of these techniques was used to print PVA in this project. Controlling substrate temperature during printing provides a solution to coffee ring formation as it helps increase the evaporation rate of the solvent upon droplet deposition on the surface, preventing the movement of fluid to the edges, thus eliminating the formation of the coffee-ring. *With PVA film printing, upon raising the substrate temperature to 70°C, the water solvent (in the PVA solution) almost instantaneously evaporated upon droplet deposition, eliminating more than 80% of the coffee-ring.*

Using co-solvent inks by including a solvent with a low evaporation rate locally varies the surface tension in the solution and reverses coffee ring effect. Ethylene glycol (EG) has been studied previously in a PVA/water solution [40]. In the aforementioned study, for 1% PVA solution(in water), 0.2 % EG (in water) was necessary to eliminate the coffee ring entirely. Anything above the 0.2% EG concentration caused the deposited drop to take a longer time to dry at all points making the coffee ring effect worse. Anything below this concentration was not enough to suppress the coffee ring. *Similarly, in this project, 0.9% EG was needed with 6% PVA (and 70°C substrate temperature) to minimize the coffee ring effect.*

Dyeing of PVA solution to track removal of sacrificial layer after PDMS formation: In order to track the removal of PVA after PDMS print and curing, a blue dye marker *(Brilliant Blue R-250 from Fisher Scientific)* was included in the mixed PVA solution. To minimize the effects of the blue dye powder on the solution, a 0.05 % (w/v) of Brilliant blue powder was mixed as part of the solution and this amount was enough to track the removal of PVA.

Summary of optimized parameters: The optimized parameters for PVA printing discussed thus far are listed below:

a) Optimized Print Parameters:
- *Drop Spacing:* **0.2mm**
- *Air Pressure:* **50-55 kPa**
- *Substrate Move Time:* **100ms**
- *Tip/Needle Size:* **30 gauge or 150µm**
- *Distance from tip to substrate:* **150µm**

b) Other Optimized Parameters: Based on the print parameters above, the smallest achievable channel width was ~400µm**.** The PVA printed line width (using optimized parameters above) fit well in the channel dimensions mentioned below.
- *Channel Width*: **400 µm mask width, 440 µm etched width**
- *Channel Depth:* **16-17 µm**
- *# of PVA layers needed to fill channel:* **1 layer**
- *Substrate temperature during print:* **70^0 C**

c) Components in PVA solution**:** The process to mix these components will be discussed next.
- *% PVA in water:* **6 % (w/w)**
- *% Ethylene Glycol:* **0.9 % (v/v)**
- *% Brilliant Blue Powder:* **0.05 % (w/w)**

Summary of Processing Steps for PVA:

The processing steps for making the PVA layer is as follows:

1) In a 20mL glass vial, 15mL of filtered DI water is heated to 80^0C (using a heating mantle setup).
2) 0.9574g of PVA (6% w/w in 15mL of water) is then solubilized in the warm water till a clear solution is obtained.
3) After the mixed solution is cooled down to 45^0C or less, 0.135mL (0.9% v/v in 15mL of water) of ethylene glycol (EG) is included in the vial and mixed (vortexed) thoroughly.
4) 0.0075g (0.05% w/w in 15mL of water) of brilliant blue R-250 powder is then mixed with the solution.
5) The PVA (with EG and blue dye) is now ready for print.
6) The pneumatic printer chuck is heated up to 70^0C.
7) Gel slick is applied right outside the etched channel areas to facilitate the wetting of PVA on the gold electrodes inside the channel.
8) The substrate is then aligned to the tip and chuck on the pneumatic printer. Using the optimized print parameters, the 6% PVA solution (with EG and blue dye) is printed inside the channel.
9) The PVA inside the channel is baked at 95^0C for 5 minutes to remove residual water [42].
10) The profile is then measured to verify uniform filling of the channel.

Final Results for PVA print inside channel:

A top view micrograph of a section of the PVA print inside the channel is shown in Figure 135.

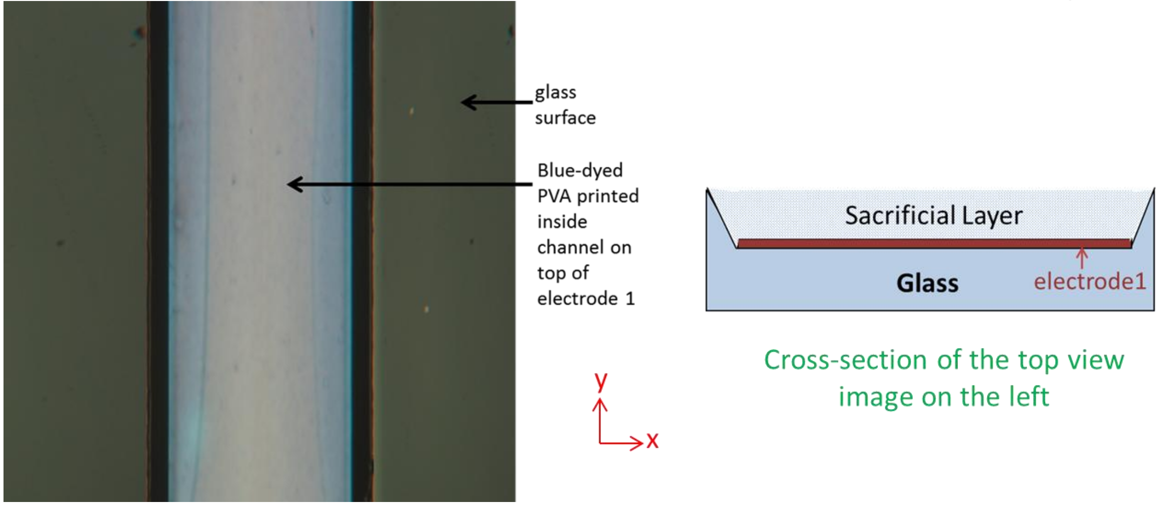

Figure 135. Top view image of the blue-dyed PVA printed (and baked) inside channel on top of electrode 1; the cross section of this top view image is on the right.

The ASIQ profile (scan in the X direction) of PVA inside channel after print and bake is shown in Figure 136. The small coffee ring seen on the sides of the channels (~2μm) does not pose a problem for the printing and functioning of the valve membrane, as seen in following sections.

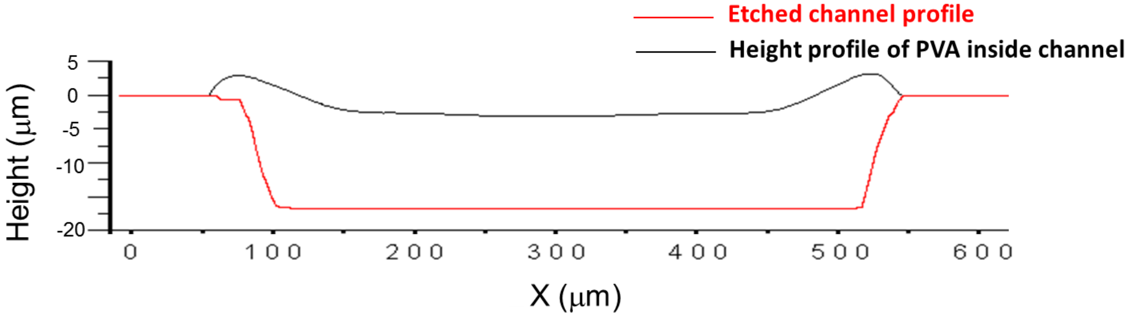

Figure 136. ASIQ height profile of PVA printed (and baked) inside channel.

The Wyko NT3300 Optical 3D Profiling System was used to obtain the non-contact interferometry image in Figure 137. This image shows the uniformity across PVA in the channel, confirming its use for the subsequent steps.

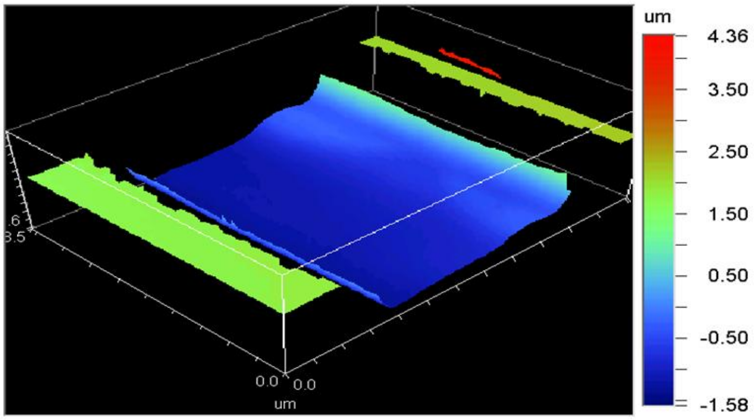

Figure 137. WYKO interferometry image (of PVA) verifies the uniform filling of PVA inside channel.

Step 4: Printing of valve membrane

Several biocompatible and potentially printable materials were considered as valve membranes, including PMMA [42], SU-8 [43, 7], Polyimide [44, 45], Parylene [46], and PDMS [47]. To increase the deflection for a given voltage and to have maximum elasticity, the young's modulus value (E) of the valve membrane needs to be low (see equation in section 5.2). Compared to PDMS with a low E value of 360 -870KPa, PMMA, Polyimide, Parylene and PMMA all have an E value of ~4GPa, almost 4 orders of magnitude higher than PDMS. Moreover, PDMS is a better choice also because of its ability to adapt and shape well into any cavity. It is hydrophobic, and unless a high pressure is applied, it prevents any fluid from passing through a closed valve even if there are inevitable openings in the corners of the channels. In addition, PDMS is a dielectric electroactive polymer (EAP) [48] and can bend easily under applied electric field. For all of the aforementioned reasons, and because it can be easily integrated into existing biological microfluidic applications, PDMS was chosen as the material for valve membrane.

In this project, a Sylgard 184 kit was used to mix the PDMS. A 10:1 ratio of Sylgard polymer base to curing agent was mixed thoroughly in a weighing boat and sonicated to remove any bubbles. Using the pneumatic printer, PDMS was printed within 2 hours of mixing since the curing process starts very soon after the curing agent is added.

One of the concerns of building/printing a valve membrane is its ability to stay above the channel after the sacrificial layer has been removed. In other words, when the sacrificial layer is removed after PDMS print and cure, the PDMS membrane should not collapse into the channel. One way to prevent the collapse is by having the correct dimensions and aspect ratios for the channel and the membrane. Aspect ratio of the channel **(A_C)** is defined as the width of the channel (indicated as 'C' in Figure 138a) over the depth of the channel (indicated as 'E' in Figure 138b). Aspect ratio of the PDMS membrane **(A_P)** is defined as width of the membrane over the channel (same as 'C' in Figure 138a) over the thickness of the PDMS membrane (indicated as 'D' in Figure 138b). The value for length of PDMS, 'A' in Figure 138a, should be minimized to aid in faster removal of PVA after PDMS print and cure (discussed in the next step). The value for 'B' is arbitrary and is determined by the print. Only the part of PDMS that stands over the channel (same as channel width 'C' in Figure 138a) is significant.

In this thesis, A_P was varied to arrive at a noncollapsable PDMS membrane. A_C will be studied in the future work of this project to optimize the valve structure further.

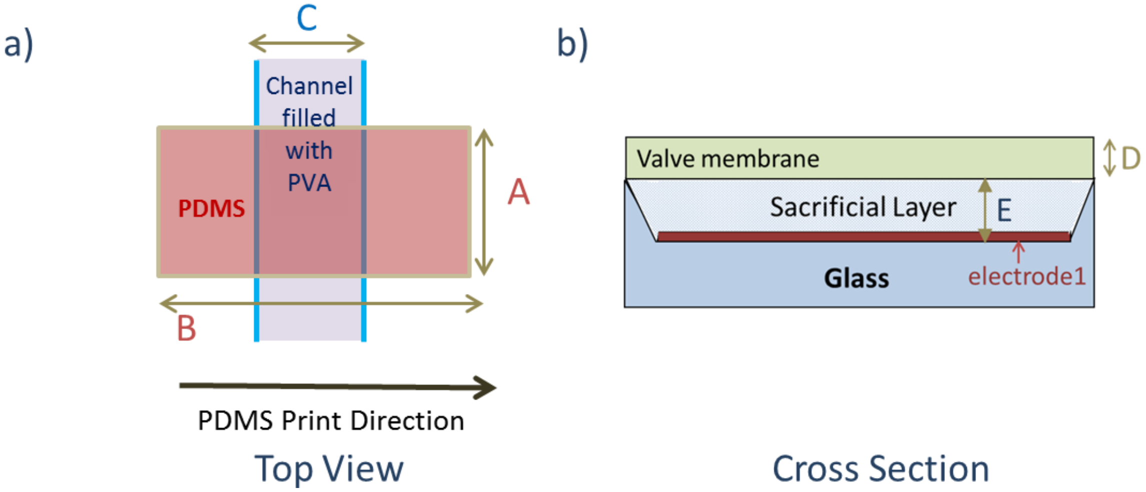

Figure 138. Schematic of the a) top view and b) cross section of PDMS print setup and dimensions.

Before experiments can be done to vary the dimensions and aspect ratios, the print parameters in the pneumatic printer (defined in step 3) had to be optimized for printing of PDMS. As with PVA, the distance from tip to substrate was kept at 150µm for PDMS as well. The optimization of the other four parameters, tip size, drop spacing, move time, and air pressure, will now be discussed. To begin with, the graphs in Figure 139 and Figure 140 relate move time to length of PDMS ('A' in Figure 138a) and thickness of PDMS membrane ('D' in Figure 138b). These values were measured using Tensor Alpha Step 200 Profilometer (ASIQ).

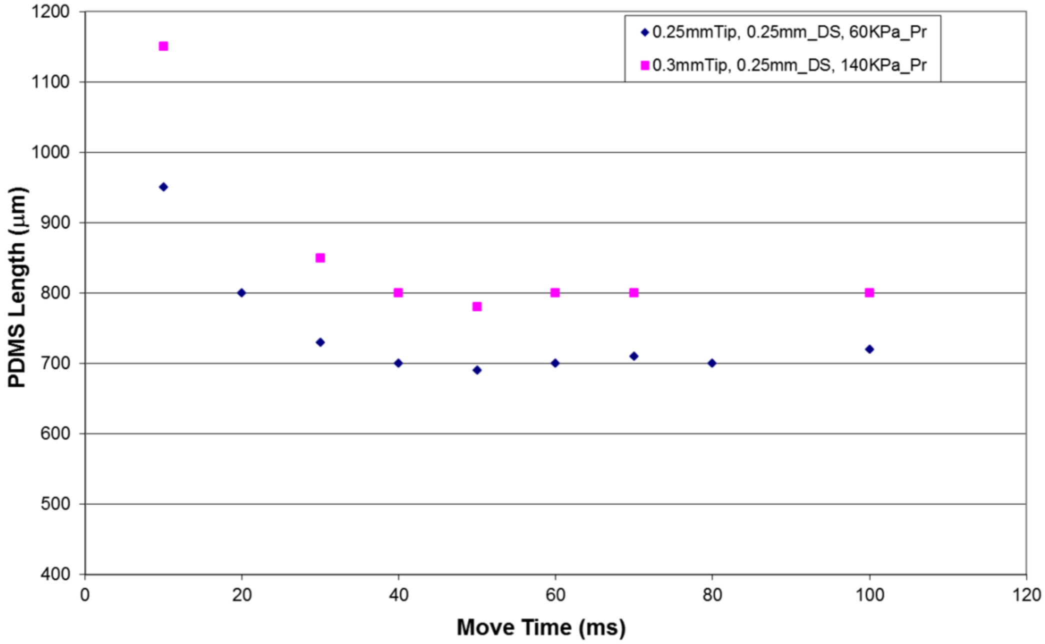

Figure 139. The length of PDMS ('A' in Figure 138a) as a function of varying move times in the pneumatic printer.

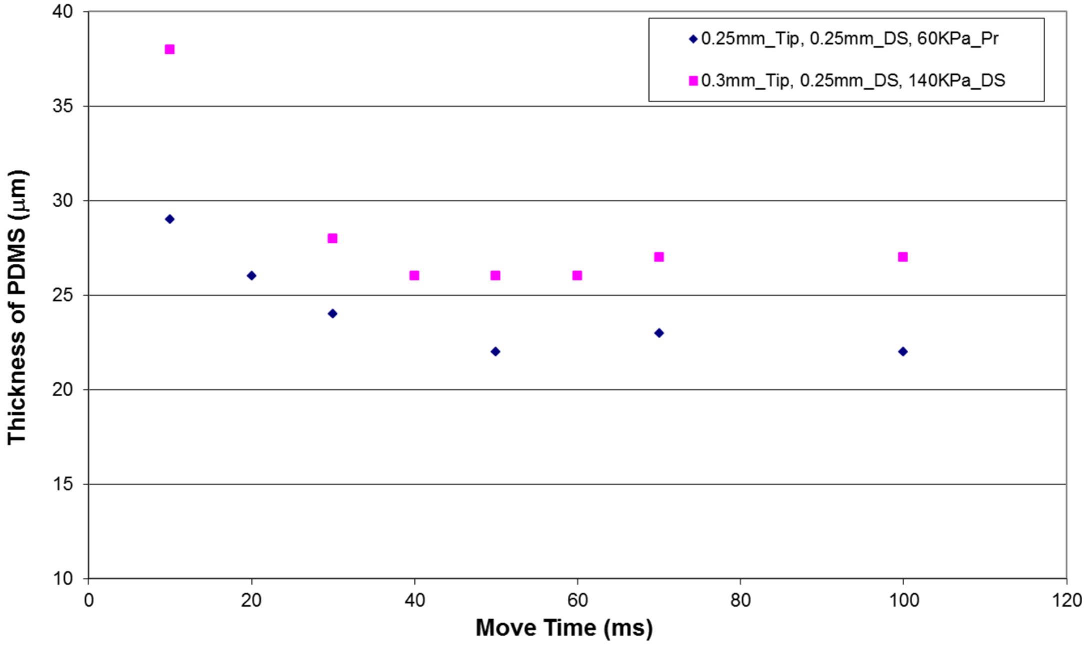

Figure 140. The thickness of PDMS('D' in Figure 138b) as a function of varying move times in the pneumatic printer.

The 26 gauge or 250µm tip was the smallest tip size that could be used to print PDMS since the viscosity of PDMS used here is ~3900cPs. In Figure 139 and Figure 140, while the move time (MT) was varied, the drop spacing (DS) was held constant at 0.25mm and tip size and air pressure (Pr) were varied between the two values indicated in the legend. *Since the PDMS length needs to be minimized, move times of 40ms or greater achieved this goal.* The required thickness for PDMS will be discussed shortly and the move times will be adjusted accordingly. The length and thickness results with varying drop spacing are presented next in Figure 141 and Figure 142.

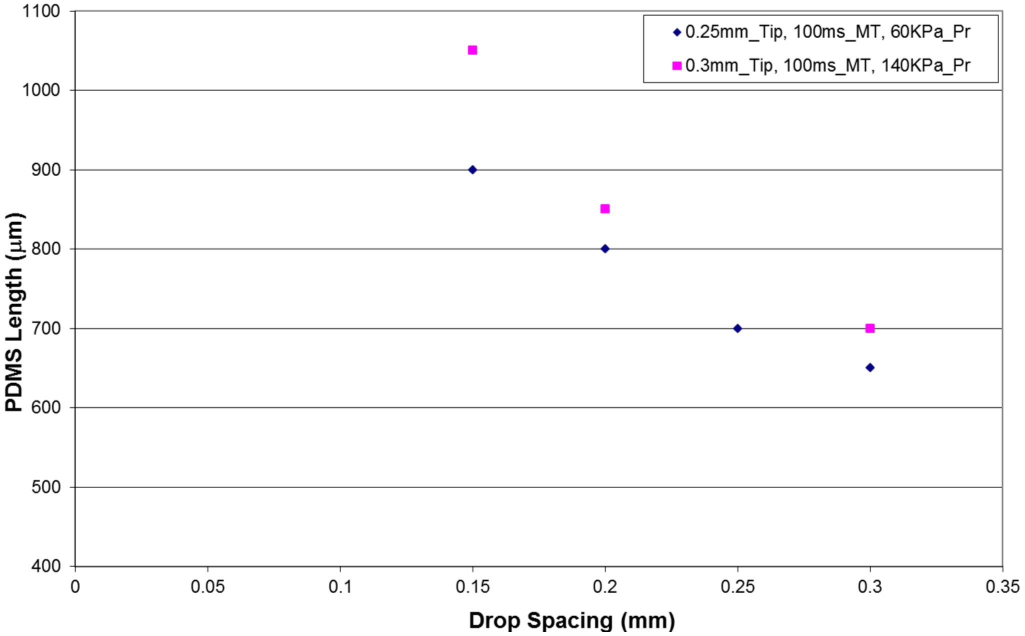

Figure 141. The length of PDMS ('A' in Figure 138a) as a function of varying drop spacing in the pneumatic printer.

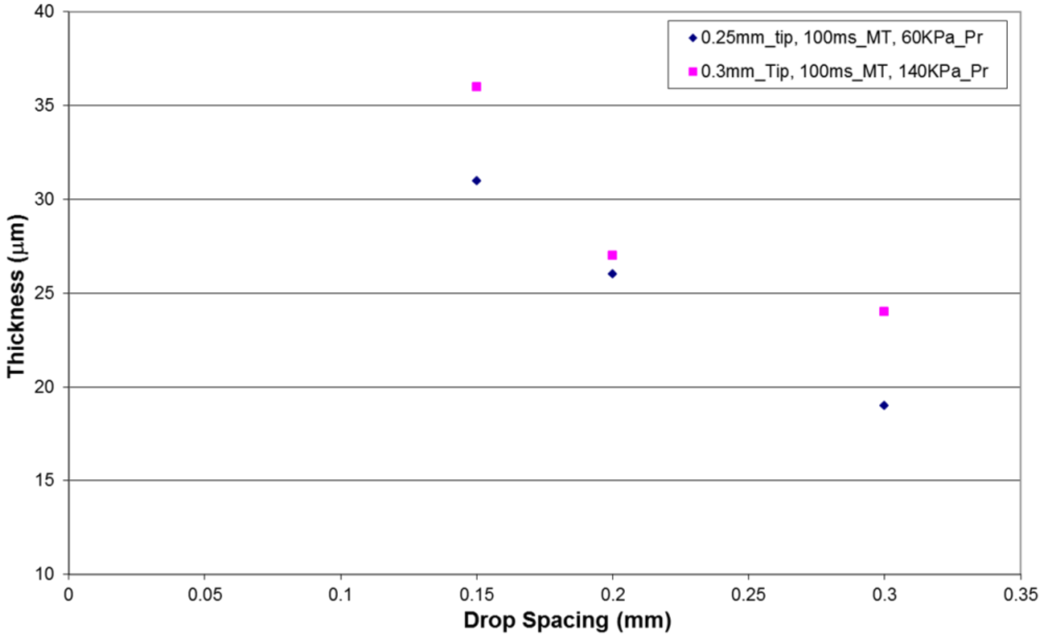

Figure 142. The thickness of PDMS('D' in Figure 138b) as a function of varying drop spacing in the pneumatic printer.

In Figure 141 and Figure 142, a drop spacing greater than 0.3mm resulted in non-uniform and broken lines. The appropriate drop spacing was obtained based on thickness requirements discussed next. Finally, the resulting length and thickness of PDMS as a function of air pressure (or shot pressure) is shown in Figure 143 and Figure 144.

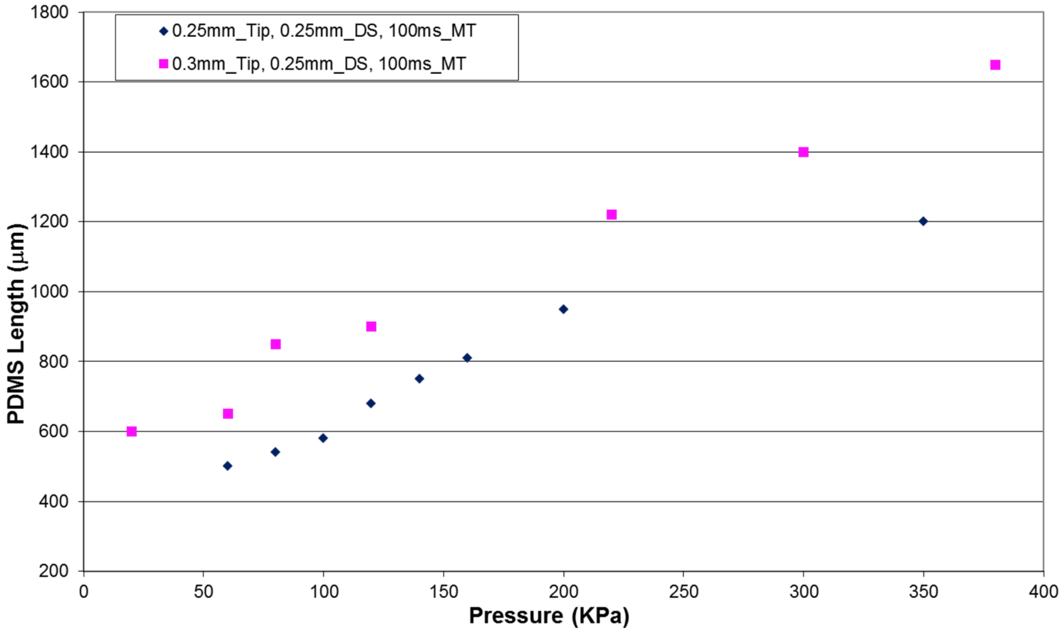

Figure 143. The length of PDMS ('A' in Figure 138a) as a function of varying air pressure in the pneumatic printer.

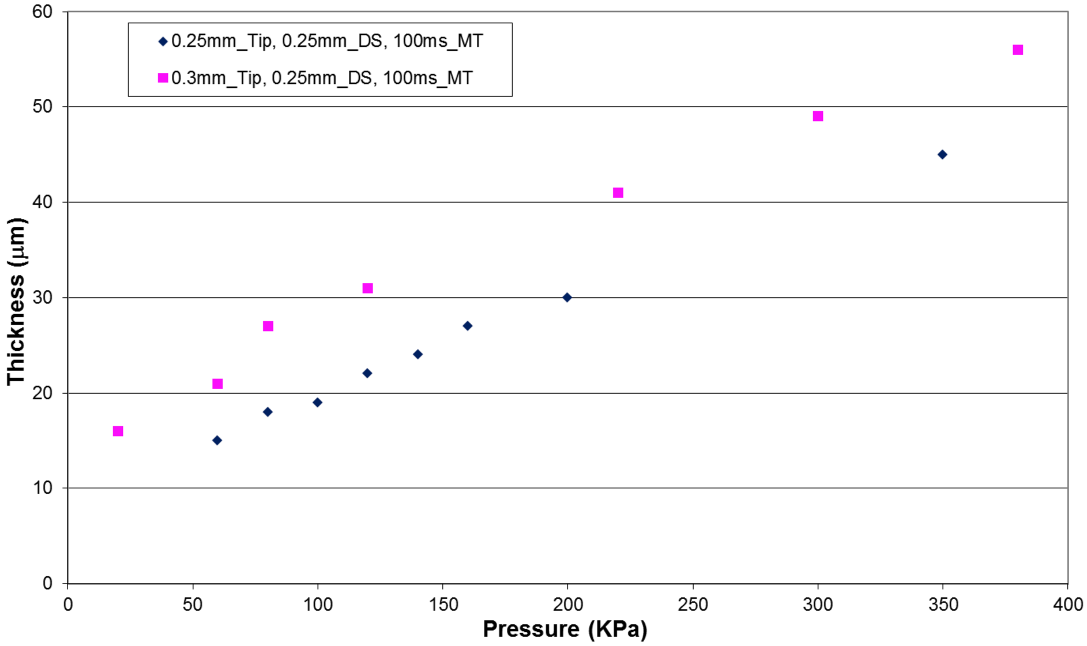

Figure 144. The thickness of PDMS('D' in Figure 138b) as a function of varying air pressure in the pneumatic printer.

In Figure 139-Figure 144, by varying the print parameters in the pneumatic printer, the relationship between these parameters and the dimensions of PDMS was systematically studied. Once the aspect ratios of working valves are finalized, the data from Figure 139-Figure 144 provide an efficient way of printing the desired dimensions by setting appropriate values for print parameters.

The optimization of the aspect ratio of the PDMS membrane will be discussed next. While the channel depth and the PDMS width over channel (same as channel width) were held constant at ~17µm and ~440µm respectively, the thickness of the PDMS membrane was varied to change the aspect ratio of the PDMS membrane, A_P. To review, A_P is the ratio of the width of the membrane over the channel ('C' in Figure 138a) over the thickness of the PDMS membrane (indicated as 'D' in Figure 138b).

PDMS thickness was varied from 9.5µm to 130µm in increments of 7-10 µm, resulting in A_P that varied from ~46:1 down to ~3:1. *Ratios above ~9:1 resulted in collapsed membranes after removal of PVA.* The collapse of the membrane was verified by attempting to pass fluid in the channel under the valve. A micrograph of one of the collapsed membranes with A_P of 20:1 is shown in Figure 145. These initial tests were conducted without electrode 1.

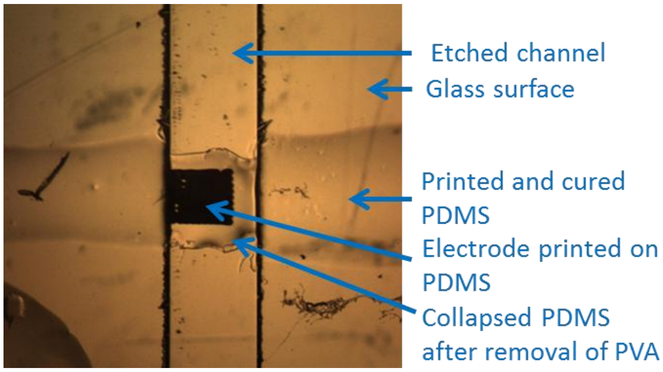

Figure 145. Collapsed PDMS membrane with an A_p of 20:1.

Going forward, all membranes had an A_P less than 9:1. The print parameters were adjusted to obtain PDMS thicknesses above ~50µm (A_P = ~8.8:1) and minimum PDMS length ('A' in Figure 138a) given a constant horizontal PDMS width (channel width) of 440µm. The electrical and mechanical characterization of three of these working membranes will be discussed shortly.

Although PDMS can be cured at a temperature as high as 195^0C thereby reducing curing time, PVA carbonizes at 150^0C, posing a limit on PDMS curing temperature. Carbonization of PVA leads to changes in PVA molecular structure, making it impossible to remove PVA from the channel. Therefore, after print, PDMS was cured at 65^0C for 4 hours. A micrograph of PDMS membrane printed (and cured) on PVA is shown in Figure 146.

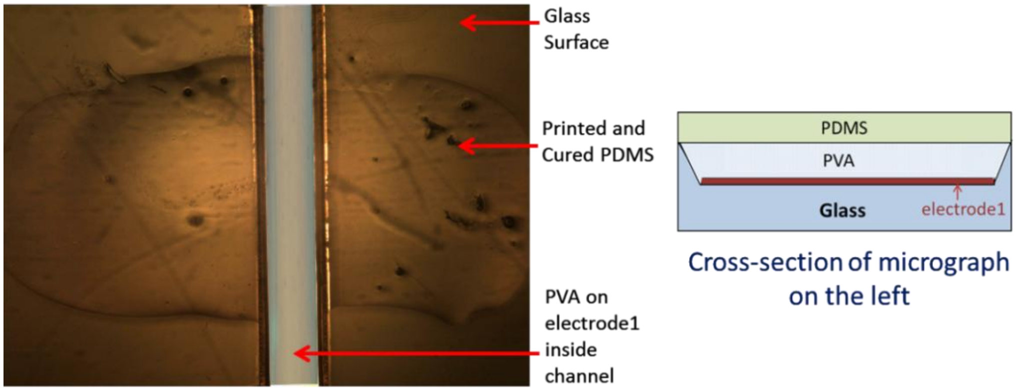

Figure 146. Micrograph (left) and schematic of cross-section (right) of PDMS valve membrane printed on PVA.

The ASIQ profile of the PDMS membrane *before* PVA removal is shown in Figure 147.

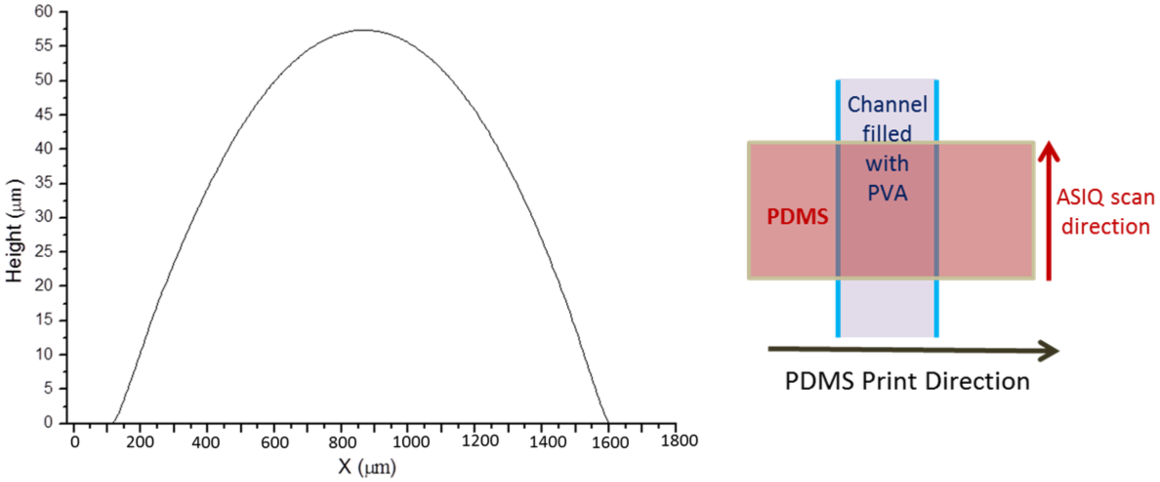

Figure 147. ASIQ height profile of PDMS printing over PVA.

Because of a high viscosity and a low evaporation rate, coffee ring affect is not a problem with PDMS. The removal of PVA after PDMS print and cure will be discussed next.

<u>Step 5: Removal of sacrificial layer</u>

PVA was removed by immersing the glass substrate in 70-80^{0}C water. Since water has to travel through a small cross section of 17mm deep times the length of PDMS ('A' in Figure 138a), this length parameter needs to be minimized. The relationship between length and the immersion time needed to completely remove PVA is shown in Figure 148.

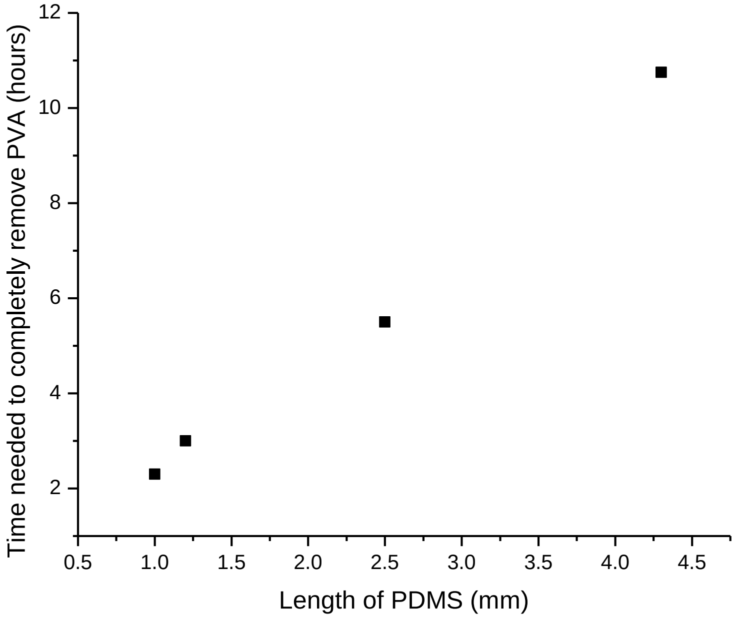

Figure 148. Immersion time required to completely remove PVA as a function of length of PDMS.

Although sonicating the substrate in hot water could have removed the PVA faster, sonication caused the PDMS layer to delaminate and therefore was not used. A micrograph of the PDMS valve on the channel after removal of PVA is shown in Figure 149. PVA, as seen from this figure, has been completely removed.

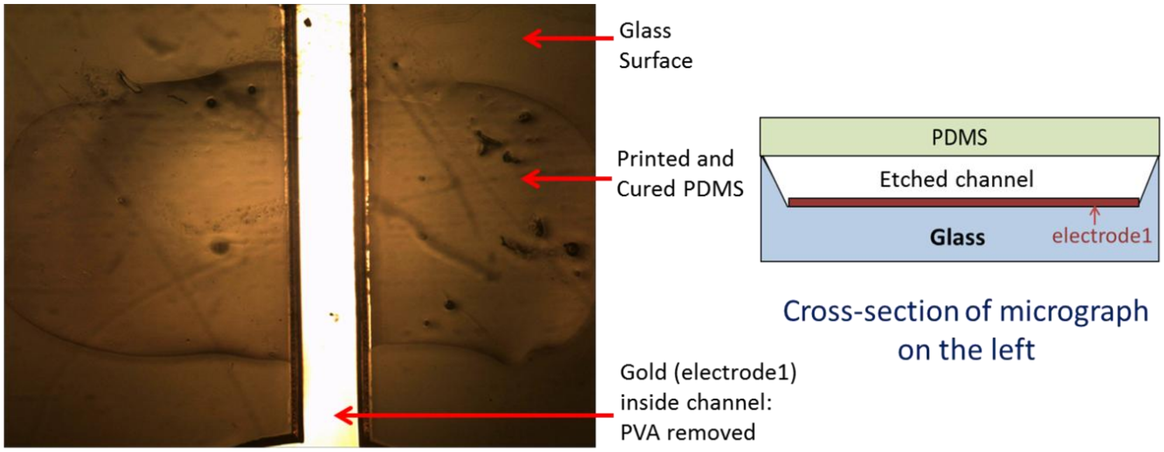

Figure 149. A micrograph of the PDMS membrane over the channel after removal of PVA.

Two initial tests were done to confirm the removal of PVA and the stability of the PDMS membrane. First, the ASIQ profile of PDMS over the channel matches the profile seen in Figure 147, showing that no changes have occurred to the PDMS membrane after PVA removal. Next, fluid was placed at one end of the open valve, and with capillary forces, it traveled to the other end of the valve through the channel. This test not only confirms that the PVA has been removed and that the PDMS has not collapsed, but it also shows that the PDMS seal is strong enough for use in these microfluidic systems subject to capillary forces.

Step 6: Printing of Electrode 2

One of the last steps before final testing of valves is printing of electrode 2 on the PDMS membrane. PDMS surface is very hydrophobic with a contact angle $>100^0$. Printing on this surface is difficult unless the surface is treated to yield lower contact angles. UV-Ozone (UVO), discussed in chapter 3, was used to treat the PDMS surface to make it more hydrophilic and printable. UVO modification of PDMS has been previously studied to understand the effects of the treatment on the chemical structure of PDMS and on its Young's modulus [49, 50]. Because printing on PDMS only requires ~30 minutes of UVO on PDMS surface, the chemical modification caused by the treatment is not a concern and does not change the Young's modulus of PDMS significantly.

Electrode2 was printed using the Dimatix inkjet printer (discussed in Chapter 3). The print parameters were optimized using a similar study as that shared in Chapter 3. Initially, both gold and silver nanoparticle inks were optimized for print on PDMS. The silver ink used was Cabot's CCI-300 material, and the gold ink, NPG-J, was the same as that used for print of heaters and RTDs. The printed gold and silver films have to be annealed at 250^0C (for 1 hour) and 150^0C (for 30 minutes), respectively, after print in order for them to be conductive. PDMS cannot withstand temperatures higher than 200^0C, and therefore, gold electrodes made using NPG-J ink prints could not be used for electrode2. Even though silver is not an inert metal like gold, since electrode 2 is on the external part of the valve and not in contact with any biological fluids, silver works as a good material for electrode2.

Results from silver CCI-300 prints on UVO treated PDMS substrates are shown in Figure 150. A drop spacing of 25µm, print speed of 8.5m/s, and a print height of 1mm was optimized to obtain stable silver prints on PDMS. As seen in Figure 150, without any treatment, the silver ink remains as individual drops on PDMS because the solvent in the silver ink is alcohol-based and requires a hydrophilic surface. 31 minutes of UVO was required to obtain a uniform silver print pattern on PDMS.

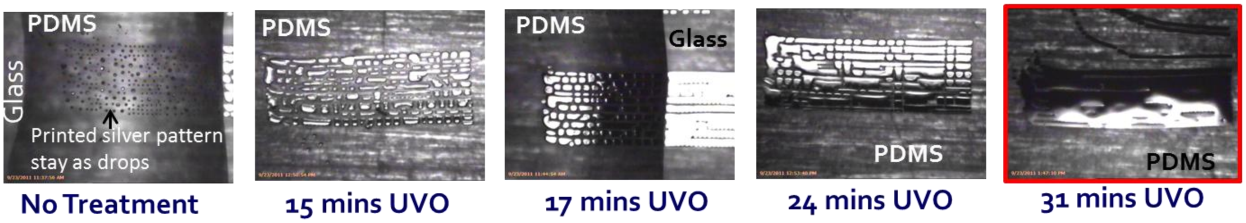

Figure 150. Micrographs of inkjet printed silver (CCI-330) pattern on UVO treated PDMS surfaces; 31 minutes of UVO was needed to obtain good prints.

Studies have been conducted previously on the reversible stretchability of thin metal films on PDMS substrates [51]. A metal film bonded to a plastic substrate can sustain plastic deformation by tens of percent but fatigues easily if subjected to cyclic loading. However, a metal film on an elastomeric substrate such as PDMS can be stretched repeatedly over hundreds of cycles without fatigue and remain conductive. Metal thin films deposited on PDMS usually form with built-in microcracks with lengths of microns or less. The ligaments in the microcracked metal film form a percolating network that helps maintain electrical conductivity. When the elastomeric substrate goes through large elongation or bend, the metal network twists and deflects out of the plane but remains bonded to the elastomeric substrate. Therefore, the metal film experiences only small strains and deforms elastically without suffering fatigue. Gold metal films were studied in the referenced work. All printed thin films exhibit similar mechanical characteristics and are usually more flexible than sputtered or evaporated metal thin films. Therefore, the reversible stretchability behavior was expected to be the same for the silver thin films printed on PDMS substrates as well. More work can be done in the future to understand printed thin metal film deformation on PDMS substrates.

Integrating all the layers and printing leads for contact

Integrating all of the layers and processes from steps 1-6 in this section, the final valve structure was formed. To make contacts to the valves, leads were printed from electrodes 1 and 2 and connected to a voltage supply. The image of the final structure (after step 6) of one of the printed valves is shown in Figure 151. A schematic of the cross-section of the final valve structure is also shown in this figure.

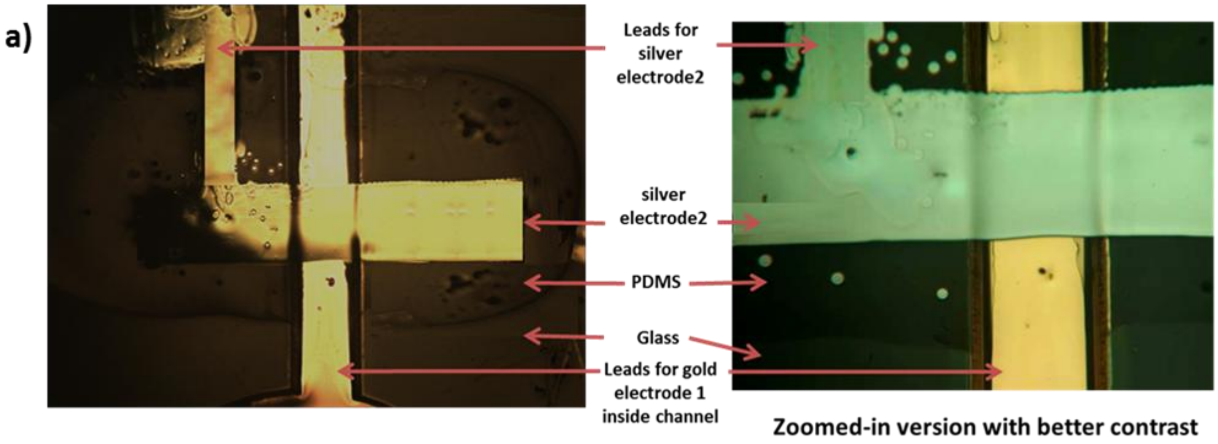

Figure 151. a) Micrograph and b) cross-section of final all-printed PDMS valve structure.

These valves will now be electrically and mechanically characterized to demonstrate valve deflection and operation.

5.4 Characterization of All-Printed PDMS Valves

The four common ways of characterizing deflection include capacitance measurements, interferometry images (using WYKO), focal length measurement using microscope, and flow rate measurements. Since the PDMS valve deflection required high voltages, capacitance measurement was not possible because of voltage limitations with the measurement tool. Interferometry and focal length measurements were difficult with this particular valve structure because of multiple layers on top of each other, leading to focus problems. Therefore, flow rate measurements were conducted to measure deflection. The WYKO Interferometer will be used for the real time analysis of the valve, and this will be explained shortly. The setup shown in Figure 152 was used to measure the flow rate and deflection of the valve.

The water was dyed in order to have better visibility when calculating flow rate. A constant vacuum pressure of 12.6psi or 85KPa was applied at one end of the valve, while a measured drop was placed on the other end. A potential difference was applied between electrode 1 and 2 using an external power supply. For each voltage, flow rate was calculated by keeping the initial drop amount constant (1μL) and recording the time it took for the drop to completely empty by flowing through the channel. The flow was facilitated by a vacuum setup. The measurements conducted for three printed valves with PDMS thickness ('D' in Figure 138a) of 55μm, 90μm, and 100μm, are shown in Figure 153.

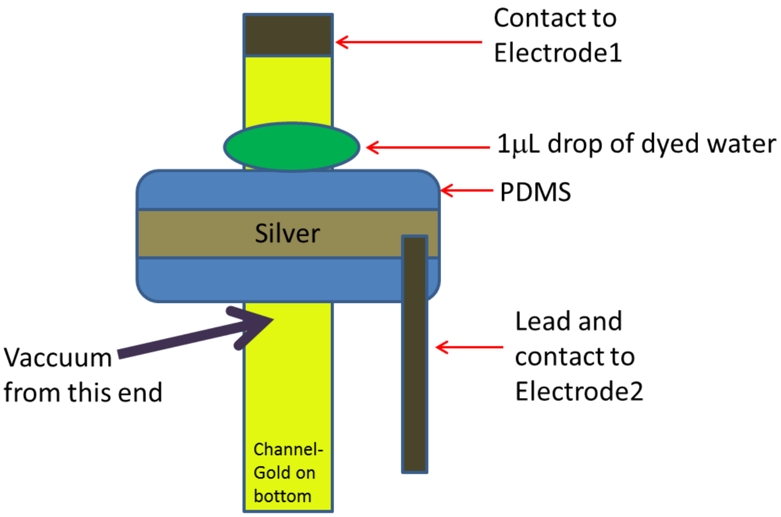

Figure 152. Schematic of setup used to measure flow rate as a function of voltage.

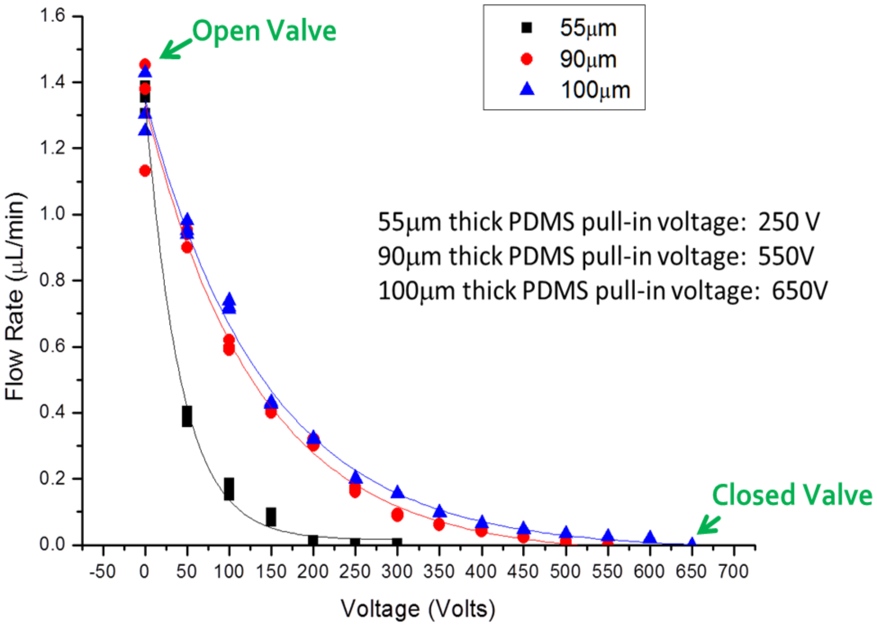

Figure 153. Flow rate measurements as a function of voltage for printed valves with 3 different PDMS thicknesses.

As indicated in Figure 153, the measured pull-in voltages for 55μm, 90μm, and 100μm are 250V, 550V, and 650V respectively. At these voltages, no flow of fluid occurred. The increasing voltage with thicker membranes is expected as verified by the equations shared in section 5.2. Since deflection is inversely proportional to the thickness of the PDMS membrane, the thicker membranes require a higher voltage for the same deflection. The deflection value in this case is approximately the depth of the etched channel.

The exponential decay seen in Figure 153 can be attributed partly to the exponential increase seen in the voltage vs. deflection graph in Figure 125. Moreover, although 3-D simulation of valves has not been conducted and the exact 3-D configuration of the deflected membrane at the each voltage has not been studied yet, the exponential decay seen in the flow rate graph likely relates to the way the PDMS is deflecting and conforming into the channel at each subsequent voltage. In other words, although the absolute deflection in the z direction is slower at initial voltages (seen in Figure 125), since PDMS is a viscoelastic material, it can be inferred that the membrane is deflecting and fitting into the channel cavity in ways that initially causes the exponential decrease in flow rate. Simulations and experiments can be done in the future to understand the deflection of the valve in 3-D.

The dynamic characteristics of the printed valves were also measured. The setup in Figure 152 was used again for the flow rate measurements. To record the time, the deflection and relaxation of the valve at each voltage was recorded as a video using the WYKO interferometry tool. By mapping the deflection and relaxation times from the video to the flow rate recorded using setup in Figure 152, the graph in Figure 154 was obtained. Real-time results from valves with the three different PDMS thicknesses are shown in Figure 154. Multiple cycles of closed and open configurations were recorded, some of which are shown in this graph. In addition, to see the dynamic characteristics a little clearer, results from one of the three valves is isolated and shown in Figure 155. A zoomed in version of one cycle (open and close) is also shown in Figure 156.

The deflection and relaxation times increased as the PDMS thicknesses increased. Specifically, for the 55μm thick PDMS membrane, the deflection to completely close the valve took an average of ~1.55 seconds and the relaxation to completely open the valve took an average of ~5.5 seconds. Similarly, the deflection times and relaxation times for the 90μm thick PDMS membrane was ~2.2-2.5 seconds and ~6.5 seconds, respectively. Finally, the 100μm thick PDMS membrane required a deflection time of ~3 seconds and ~7 seconds to open.

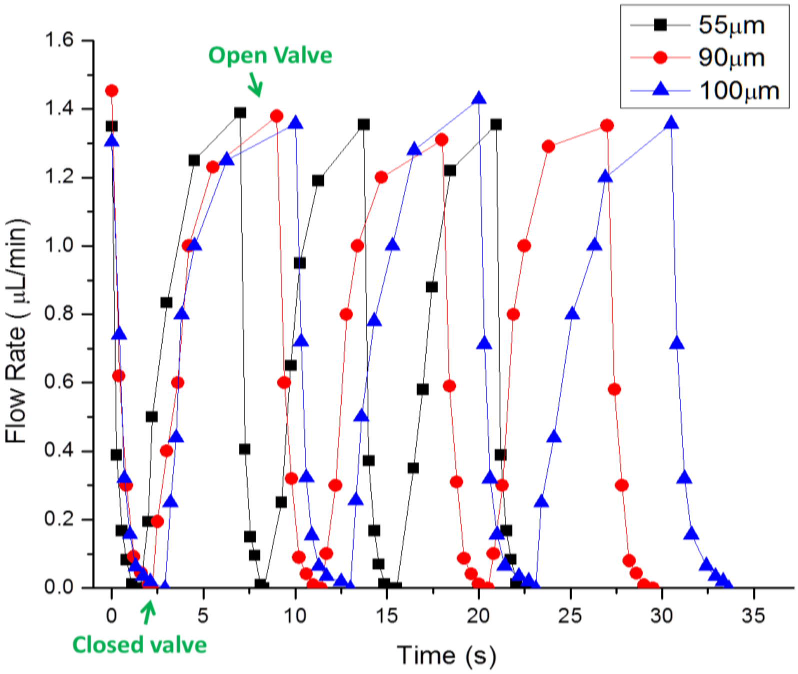

Figure 154. Dynamic characteristics of printed PDMS valve deflection for 3 different PDMS thicknesses.

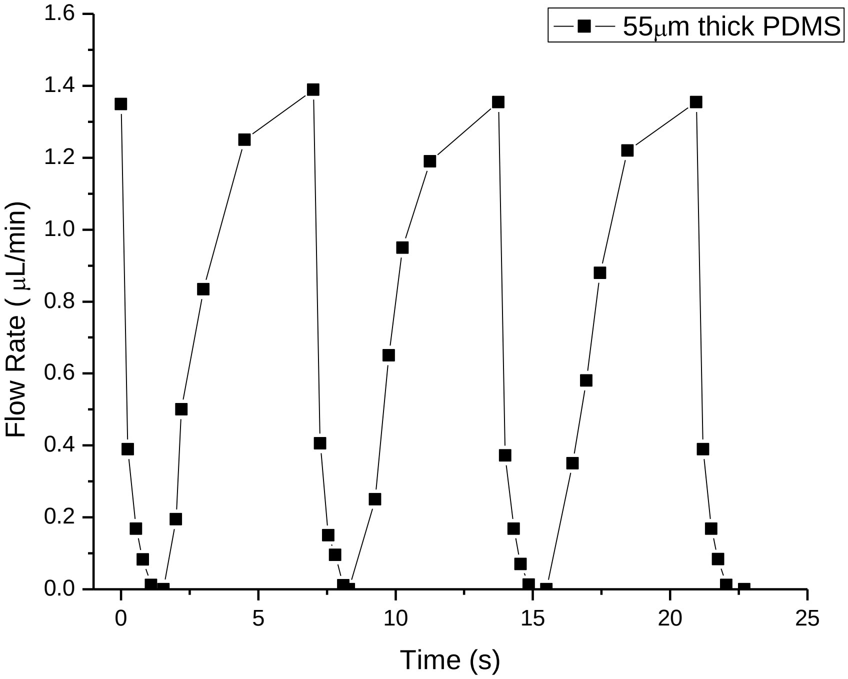

Figure 155. Dynamic characteristics of the PDMS valve with a PDMS thickness of 55μm; the local minima represents a closed valve configuration while the local maxima represents an open valve configuration.

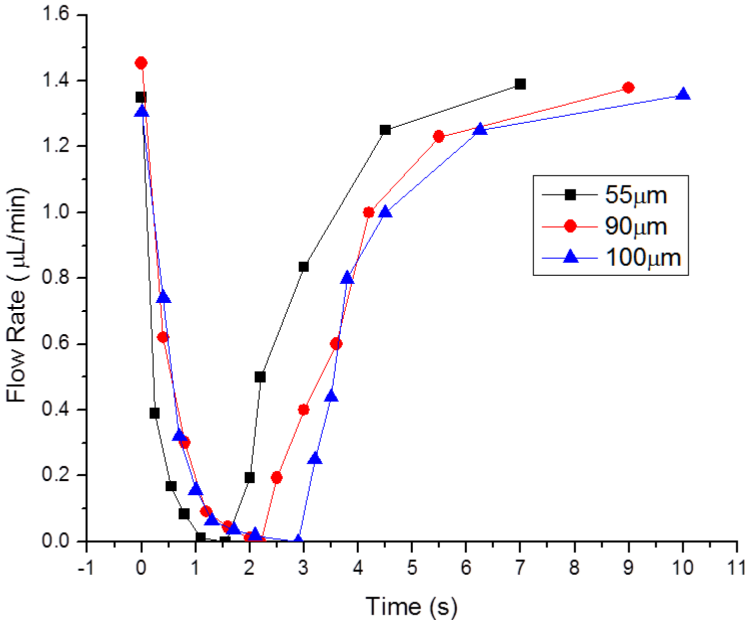

Figure 156. Zoomed-in version of one cycle of the dynamic characteristics of printed PDMS valve deflection; the local minima represents a closed valve configuration while the local maxima represents an open valve configuration.

Deflection and relaxation of the PDMS valves require different times (as seen in Figure 156) because when deflecting, an actuation force is being applied, facilitating the deflection of the valve thereby making this process faster. Relaxation occurs naturally without any applied force and is dependent on the mechanical properties of PDMS. Since there is no external force assisting the relaxation of the valve, the time required for this is longer than that needed for deflection.

The difference in the required times (for deformation and relaxation) among the three different PDMS thicknesses seen in Figure 154 is explained using the Kelvin–Voigt Model [52]. This model can be represented by a purely viscous damper and purely elastic spring connected in parallel as shown in Figure 157.

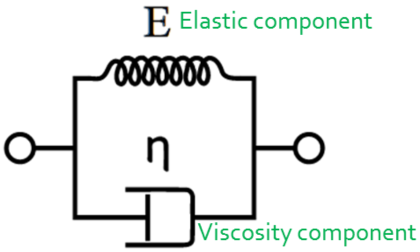

Figure 157. Schematic that represents the Kelvin-Voigt model.

The deformation in this model (represented by ε or strain) is described by the following equations:

Deflection: $\varepsilon(t) = \frac{\sigma_0}{E}(1 - e^{-\lambda t}),$

Relaxation: $\varepsilon(t > t_1) = \varepsilon(t_1)e^{-\lambda(t-t_1)}.$

whereλ is the rate of deformation and relaxation and $\lambda = \frac{E}{\eta}$, where E is the Young's Modulus and η is the viscosity.

Studies have been conducted previously where E, Young's Modulus, is known to change as a function of thickness, as shown in Figure 158, because of the way polymer chains form and arrange in PDMS [53].

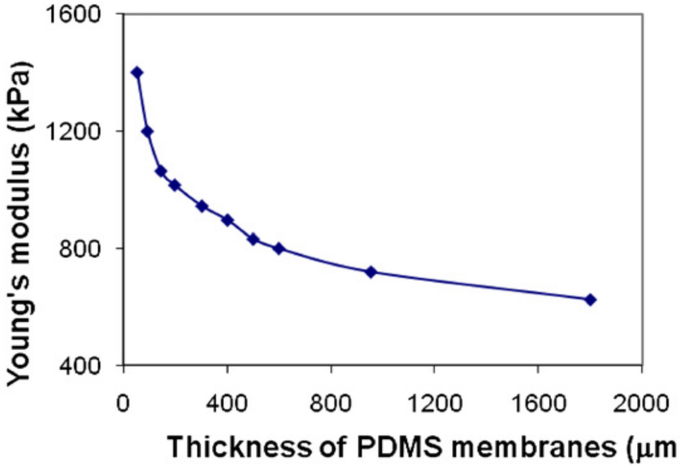

Figure 158. Young's Modulus as a function of thickness of PDMS membrane [53].

Since the Young's Modulus is decreasing as thickness of PDMS increases, the rate of deformation and relaxation is smaller for thicker PDMS membranes, leading to longer open and close cycles for valves.

Thus, the characterization of valves in this section has presented the successful functioning of printed PDMS valve structures.

5.5 Conclusion and Future Work

The successful demonstration of all-printed electrostatically actuated PDMS valves has been presented in this chapter. The valve structure was first designed using COMSOL. Each layer of the valve was then printed using pneumatic (dispenser) or inkjet printer. A gold electrode was first inkjet printed inside the etched glass channel. The channel was then filled with PVA (using pneumatic printer), which served as a sacrificial layer for the formation of the valve. Next, PDMS was printed using the pneumatic printer and then cured to harden. PVA was then removed by immersion in hot water. Finally, a silver electrode was printed on PDMS and served as the 2nd electrode to facilitate the functioning of the electrostatic valve. Optimizing the aspect ratio of the PDMS membrane yielded a noncollapsable valve structure. Flow rate measurements and dynamic characteristics were measured to characterize the valve. The thinnest PDMS membrane (55μm) closed the channel completely (i.e. flow rate = 0) at a pull in voltage of 250V. This PDMS membrane took ~1.5 seconds to close and ~5.5 seconds to open. While the closing time was accelerated by the external actuation force, the opening time was determined by the mechanical characteristics of the PDMS. Importantly, each layer of the valve, flow rates and time scales in the dynamic characteristics are all compatible with biological micofluidic applications.

The valve structure and the functioning of the device can be enhanced even further. To begin with, when printing a sacrificial layer (such as PVA) inside a channel, better understanding of the wetting behavior of this layer inside a trench, especially side-wall interaction, can provide for an even more uniform sacrificial layer, potentially enhancing the subsequent formation of the PDMS membrane. Also, since the time required to remove the sacrificial layer currently poses a bottleneck, research on making this process faster would be beneficial.

PDMS as a valve material can be better understood using 3-D simulations and experiments that reveal the 3-D configuration of the deflecting valve at subsequent voltages. The stretchability of printed metal films on PDMS can be researched further to obtain lifetime values for the valves. Also, since the location of valve deflection is essentially determined by the location of electrode2, printing different configurations for electrode 2 has the potential of facilitating faster, more effective, and lower power consuming valves by concentrating the electric field where desired. Some examples of print configurations for electrode2 on PDMS is shown in Figure 159.

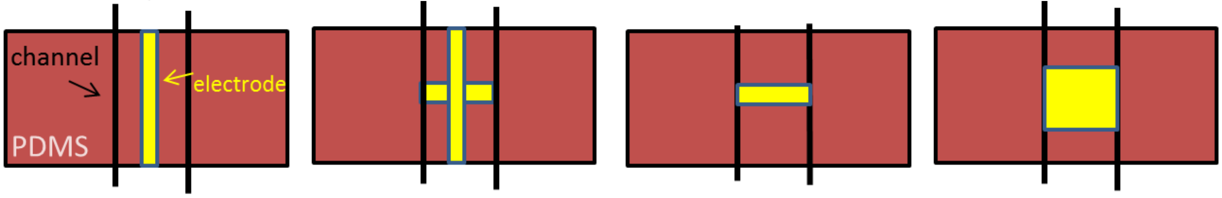

Figure 159. Different print configurations for electrode2 that can potentially enhance the functioning of valves.

Valve seats can also be varied to enhance the functioning of valves. A valve seat represents the size and shape of the area where the valve will be placed. Having a different shape and size for the valve seat than the rest of the channel has been shown to faciliate good mechanical characteristics for the valve [6, 9]. The design in this chapter used the channel size and shape as a valve seat. Valve seats of different shapes and sizes, as those shown in Figure 160, can be integrated into the mask used for etching glass channels.

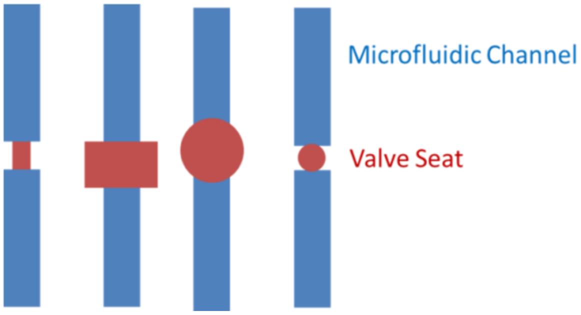

Figure 160. Examples of shapes and sizes for valve seats that could potentially enhance functioning of valves.

Finally, pressure tests should also be conducted in the future to test the robustness and leakage of closed valves.

Integrating the printed valves with biological microfluidics in the future and demonstrating its effectiveness along with the heaters, RTDs, and sensors presented thus far, represents the long-term vision for the printed valve presented in this chapter.

5.6 Sources

[1] M. Khoo and C. Liu, “A novel micromachined magnetic membrane microfluid pump,” in *Proceedings of the 22nd Annual International Conference of the IEEE Engineering in Medicine and Biology Society, 2000*, 2000, vol. 3, pp. 2394–2397 vol.3.

[2] C. Fu, Z. Rummler, and W. Schomburg, “Magnetically driven micro ball valves fabricated by multilayer adhesive film bonding,” *Journal of Micromechanics and Microengineering*, vol. 13, no. 4, p. S96–S102, Jul. 2003.

[3] B. S. Driggs, M. M. Enzelberger, and S. R. Quake, “Electrostatic valves for microfluidic devices,” U.S. Patent 723210919-Jun-2007.

[4] J. K. Robertson and K. D. Wise, “A nested electrostatically-actuated microvalve for an integrated microflow controller,” in *IEEE Workshop on Micro Electro Mechanical Systems, 1994, MEMS ’94, Proceedings*, 1994, pp. 7–12.

[5] B. J. Kirby, T. J. Shepodd, and E. F. Hasselbrink Jr., “Voltage-addressable on/off microvalves for high-pressure microchip separations,” Journal of Chromatography A, vol. 979, no. 1–2, pp. 147–154, Dec. 2002.

[6] P. Shao, Z. Rummler, and W. K. Schomburg, “Polymer micro piezo valve with a small dead volume,” *Journal of Micromechanics and Microengineering*, vol. 14, no. 2, pp. 305–309, Feb. 2004.

[7] N.-T. Nguyen and T.-Q. Truong, “A fully polymeric micropump with piezoelectric actuator,” *Sensors and Actuators B: Chemical*, vol. 97, no. 1, pp. 137–143, Jan. 2004.

[8] P. W. Barth, “Silicon Microvalves For Gas Flow Control,” in *The 8th International Conference on Solid-State Sensors and Actuators, 1995 and Eurosensors IX.. Transducers ’95*, 1995, vol. 2, pp. 276–279.

[9] J.-H. Kim, K.-H.Na, C. J. Kang, D. Jeon, and Y.-S. Kim, “A disposable thermopneumatic-actuated microvalve stacked with PDMS layers and ITO-coated glass,” *Microelectronic Engineering*, vol. 73–74, no. 0, pp. 864–869, Jun. 2004.

[10] D. J. Beebe, J. S. Moore, J. M. Bauer, Q. Yu, R. H. Liu, C. Devadoss, and B.-H. Jo, “Functional hydrogel structures for autonomous flow control inside microfluidic channels,” *Nature*, vol. 404, no. 6778, pp. 588–590, Apr. 2000.

[11] L. Klintberg, M. Karlsson, L. Stenmark, and G. Thornell, “A thermally activated paraffin-based actuator for gas-flow control in a satellite electrical propulsion system,” *Sensors and Actuators A: Physical*, vol. 105, no. 3, pp. 237–246, Aug. 2003.

[12] K. Yoshida, M. Kikuchi, J.-H. Park, and S. Yokota, “Fabrication of micro electro-rheological valves (ER valves) by micromachining and experiments,” *Sensors and Actuators A: Physical*, vol. 95, no. 2–3, pp. 227–233, Jan. 2002.

[13] A. Hatch, A. E. Kamholz, G. Holman, P. Yager, and K. F. Bohringer, “A ferrofluidic magnetic micropump,” *Journal of Microelectromechanical Systems*, vol. 10, no. 2, pp. 215–221, Jun. 2001.

[14] Z. Yang and R. Maeda, “Socket with built-in valves for the interconnection of microfluidic chips to macro constituents,” *Journal of Chromatography A*, vol. 1013, no. 1–2, pp. 29–33, Sep. 2003.

[15] K. W. Oh, C. Park, K. Namkoong, J. Kim, K.-S. Ock, S. Kim, Y.A. Kim, Y.K. Cho, and C. Ko, “World-to-chip microfluidic interface with built-in valves for multichamber chip-based PCR assays,” *Lab Chip*, vol. 5, no. 8, pp. 845–850, Jul. 2005.

[16] W. H. Grover, A. M. Skelley, C. N. Liu, E. T. Lagally, and R. A. Mathies, “Monolithic Membrane Valves and Diaphragm Pumps for Practical Large-Scale Integration into Microfluidic Devices,” *Sensors and Actuators B-Chemical*, vol. 89, pp. 315–323, 2003.

[17] A. Luque, J. M. Quero, C. Hibert, P. Flückiger, and A. M. Gañán-Calvo, “Integrable silicon microfluidic valve with pneumatic actuation,” *Sensors and Actuators A: Physical*, vol. 118, no. 1, pp. 144–151, Jan. 2005.

[18] W. Y. Sim, H. J. Yoon, O. C. Jeong, and S. S. Yang, “A phase-change type micropump with aluminum flap valves,” *Journal of Micromechanics and Microengineering*, vol. 13, no. 2, pp. 286–294, Mar. 2003.

[19] P. Voigt, G. Schrag, and G. Wachutka, “Electrofluidic full-system modeling of a flap valve micropump based on Kirchhoffian network theory,” *Sensors and Actuators A: Physical*, vol. 66, no. 1–3, pp. 9–14, Apr. 1998.

[20] D. Accoto, M. C. Carrozza, and P. Dario, “Modeling of micropumps using unimorph piezoelectric actuator and ball valves,” *Journal of Micromechanics and Microengineering*, vol. 10, no. 2, pp. 277–281, Jun. 2000.

[21] C. Fu, Z. Rummler, and W. Schomburg, “Magnetically driven micro ball valves fabricated by multilayer adhesive film bonding,” *Journal of Micromechanics and Microengineering*, vol. 13, no. 4, p. S96–S102, Jul. 2003.

[22] H. Andersson, W. van der Wijngaart, P. Nilsson, P. Enoksson, and G. Stemme, “A valve-less diffuser micropump for microfluidic analytical systems,” *Sensors and Actuators B: Chemical*, vol. 72, no. 3, pp. 259–265, Feb. 2001.

[23] C. J. Morris and F. K. Forster, “Low-order modeling of resonance for fixed-valve micropumps based on first principles,” *Journal of Microelectromechanical Systems*, vol. 12, no. 3, pp. 325– 334, Jun. 2003.

[24] Andersson H., van der Wijngaart W., Griss P., Niklaus F., and Stemme G., “Hydrophobic valves of plasma deposited octafluorocyclobutane in DRIE channels,” *Sensors and Actuators B: Chemical,* vol. 75, no. 1, pp. 136–141, 2001.

[25] T.-S. Leu and P.-Y. Chang, “Pressure barrier of capillary stop valves in micro sample separators,” *Sensors and Actuators A: Physical*, vol. 115, no. 2–3, pp. 508–515, Sep. 2004.

[26] K. W. Oh and C. H. Ahn, “A review of microvalves,” *Journal of Micromechanics and Microengineering*, vol. 16, no. 5, p. R13–R39, May 2006.

[27] J. N. Lee, C. Park, and G. M. Whitesides, “Solvent Compatibility of Poly(dimethylsiloxane)-Based Microfluidic Devices,” *Anal. Chem.*, vol. 75, no. 23, pp. 6544–6554, 2003.

[28] COMSOL Multiphysics 3.5a User Guide. [Online]. Available: http://math.nju.edu.cn/help/mathhpc/doc/comsol/guide.pdf. [Accessed: 18-Jan-2012].

[29] COMSOL Multiphysics 3.5a Modeling Guide. [Online]. Available: http://math.nju.edu.cn/help/mathhpc/doc/comsol/guide.pdf .[Accessed: 18-Jan-2012].

[30] G. A. A. Rodríguez, C. Rossi, and K. Zhang, “Multi-physics system modeling of a pneumatic micro actuator,” *Sensors and Actuators A: Physical*, vol. 141, no. 2, pp. 489–498, Feb. 2008.

[31] H. Prentice-Mott, D. Irimia, A. Russom, and M. Toner, “Modeling a Microscale Proportional Flow Controller,” *Proceedings of the COMSOL Conference*, Boston, 2007.

[32] Dimatix Materials Printer DMP-2800 Series User Manual. V. 1.5.0.1., *Fujifilm Dimatix, Inc.,* 2007.

[33] C. C. Ho, J. W. Evans, and P. K. Wright, “Direct write dispenser printing of a zinc microbattery with an ionic liquid gel electrolyte,” *Journal of Micromechanics and Microengineering*, vol. 20, no. 10, p. 104009, Oct. 2010.

[34] “Welcome to Berkeley Manufacturing Institute | BMI.” [Online]. Available: http://bmi.berkeley.edu/. [Accessed: 29-Feb-2012].

[35] A. P. Golden and J. Tien, “Fabrication of microfluidic hydrogels using molded gelatin as a sacrificial element,” *Lab Chip*, vol. 7, no. 6, pp. 720–725, May 2007.

[36] J. Guan, A. Chakrapani, and D. J. Hansford, “Polymer Microparticles Fabricated by Soft Lithography,” *Chem. Mater.*, vol. 17, no. 25, pp. 6227–6229, 2005.

[37] S. B. Fuller, E. J. Wilhelm, and J. M. Jacobson, “Ink-jet printed nanoparticle microelectromechanical systems,” *Journal of Microelectromechanical Systems*, vol. 11, no. 1, pp. 54–60, Feb. 2002.

[38] S. Molesa, D. R. Redinger, D. C. Huang, and V. Subramanian, “High-quality inkjet-printed multilevel interconnects and inductive components on plastic for ultra-low-cost RFID applications,” *PROC. 769, H8.3.1*, vol. 769, p. 2003.

[39] D. Soltman and V. Subramanian, “Inkjet-Printed Line Morphologies and Temperature

Control of the Coffee Ring Effect," *Langmuir*, vol. 24, no. 5, pp. 2224–2231, 2008.

[40] E. Tekin, P. J. Smith, S. Hoeppener, A. M. J. van den Berg, A. S. Susha, A. L. Rogach, J. Feldmann, and U. S. Schubert, "Inkjet Printing of Luminescent CdTe Nanocrystal–Polymer Composites," *Advanced Functional Materials*, vol. 17, no. 1, pp. 23–28, Jan. 2007.

[41] D. Kim, S. Jeong, B. K. Park, and J. Moon, "Direct writing of silver conductive patterns: Improvement of film morphology and conductance by controlling solvent compositions," *Applied Physics Letters*, vol. 89, no. 26, p. 264101–264101–3, Dec. 2006.

[42] N. Ferrell, J. Woodard, and D. Hansford, "Fabrication of polymer microstructures for MEMS: sacrificial layer micromolding and patterned substrate micromolding," *Biomed Microdevices*, vol. 9, no. 6, pp. 815–821, Dec. 2007.

[43] F. Walther, M. Hennemeyer, M. Kaiser, H. Herberg, and R.W. Stark, "Investigation of the surface properties of SU-8 for biological applications," *European Cells and Materials,* Vol. 10, Suppl.5, page BS22, 2005.

[44] Wego A. and Pagel L., "A self-filling micropump based on PCB technology," *Sensors and Actuators A: Physical*, vol. 88, no. 3, pp. 220–226, 2001.

[45] C. Goll, W. Bacher, B. Büstgens, D. Maas, W. Menz, and W. K. Schomburg, "Microvalves with bistable buckled polymer diaphragms," *Journal of Micromechanics and Microengineering*, vol. 6, no. 1, pp. 77–79, Mar. 1996.

[46] G.-H. Feng and E. S. Kim, "Micropump based on PZT unimorph and one-way parylene valves," *Journal of Micromechanics and Microengineering*, vol. 14, no. 4, pp. 429–435, Apr. 2004.

[47] S. K. Sia and G. M. Whitesides, "Microfluidic devices fabricated in poly(dimethylsiloxane) for biological studies," *Electrophoresis*, vol. 24, no. 21, pp. 3563–3576, Nov. 2003.

[48] S. Niamlang and A. Sirivat, "Electromechanical Responses of a Crosslinked Polydimethylsiloxane," *Macromolecular Symposia*, vol. 264, no. 1, pp. 176–183, Mar. 2008.

[49]Y. Berdichevsky, J. Khandurina, A. Guttman, and Y.-H. Lo, "UV/ozone modification of poly(dimethylsiloxane) microfluidic channels," *Sensors and Actuators B: Chemical*, vol. 97, no. 2–3, pp. 402–408, Feb. 2004.

[50] J. Song, D. Tranchida, and G. J. Vancso, "Contact Mechanics of UV/Ozone-Treated PDMS by AFM and JKR Testing: Mechanical Performance from Nano- to Micrometer Length Scales," *Macromolecules*, vol. 41, no. 18, pp. 6757–6762, 2008.

[51] S. Lacour, D. Chan, S. Wagner, T. Li, and Z. Suo, "Mechanisms of reversible stretchability of thin metal films on elastomeric substrates," *Applied Physics Letters,* vol. 88, no. 20, 2006.

[52] “Mathematical Models of Viscoelastic Behavior.” [Online]. Available: http://www.see.ed.ac.uk/~johnc/teaching/fluidmechanics4/2003-04/visco/index.html. [Accessed: 19-Mar-2012].

[53] M. Liu, J. Sun, Y. Sun, C. Bock, and Q. Chen, “Thickness-dependent mechanical properties of polydimethylsiloxane membranes,” *Journal of Micromechanics and Microengineering*, vol. 19, no. 3, p. 035028, Mar. 2009.

6. Conclusions and Future work

The goal of this dissertation was to demonstrate the capability of printed electronics in major modules of biological microfluidic systems. To review, the major modules of the microfluidic chip are: 1) initial biological processes (such as polymerase chain reaction or PCR), 2) electrophoretic separation and capture, and 3) detection. The contributions of this thesis in each of these modules are summarized in Figure 161. These contributions will be detailed below.

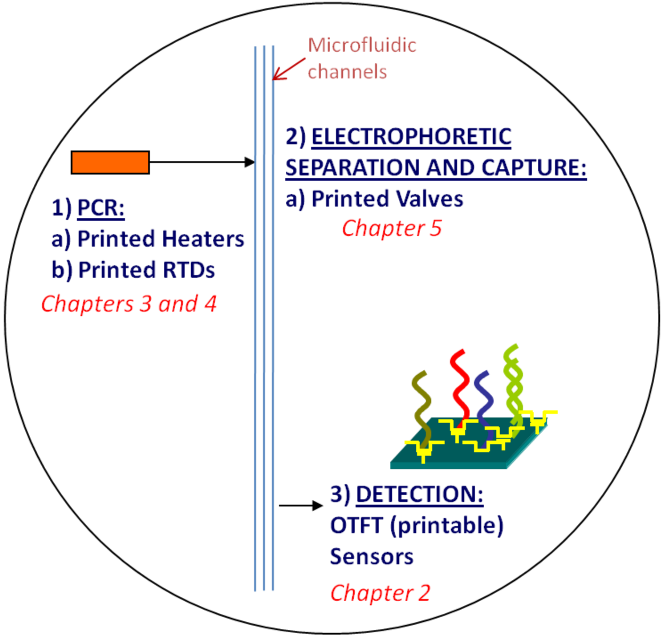

Figure 161. Schematic of the contributions of this thesis as relevant to the biological microfluidic chip.

6.1 Contributions of this Work

Previous work by Zhang et al [1] has shown the potential of organic (pentacene) thin film transistors (OTFT) for DNA detection by showing different electrical performance shifts in response to single and double stranded DNA. To achieve the ultimate goal of detecting genetic diseases using OTFTs, the sensor needs to be able to detect at the level of single nucleotide polymorphisms (SNP) [15]. In order to achieve this level of detection, Chapter 2 of this thesis delved into two aspects of using OTFTs for genetic disease detection, namely the investigation of physical origins of the observed electrical shifts, and the characterization of the pentacene surface to allow optimization of the same for DNA immobilization and sensor sensitivity.

To begin with, results from TOF-SIMS analysis along with corresponding electrical results confirmed the immobilization of DNA on pentacene surface. TOF-SIMS results showed that the sample with the immobilized DNA resulted in the highest amount of phosphate groups, a signature of the compounds on the backbone of DNA. This sample also resulted in the highest electrical performance shifts, thereby correlating the electrical results with the TOF-SIMS analysis. The TOF-SIMS results thus revealed the high selectivity of the sensor to detect DNA and confirmed the physical origin of the observed electrical transduction behavior.

The morphological and electrical characteristics of pentacene transistors were then carefully studied as a function of pentacene evaporation conditions, namely thickness of pentacene, substrate temperature, and input current. The goal was to be able to arrive at an ideal morphology for highest DNA sensitivity. Once the pentacene surface was characterized, the

DNA was immobilized on the surface, and the electrical shifts (quantified by I_{dsat} ratios) were analyzed as a function of the input parameters. A combination of both of these experiments allowed for the optimization of the pentacene surface (in terms of morphology) for highest DNA sensitivity and effective DNA immobilization. To summarize the results, thinner films, higher substrate temperature, and higher input current provided for highest sensitivity of pentacene film to DNA. These evaporation conditions ensured that DNA was immobilized in the channel part of the transistor, where it contributed most towards the shift of transistor characteristics. The surface with the highest sensitivity shifted the electrical characteristics of the transistor by a factor of 6, thereby highlighting the potential of pentacene OTFTs to function as effective DNA sensors. This proposed sensor system is valuable because of the advantages it provides over the state of the art optical detection technology, namely higher sensitivity, label-free detection, portability, ultra-low cost, and an overall faster method.

Chapter 3 presented another major contribution of this work, which is the optimization, print, and characterization of important components in PCR. Specifically, inkjet printed heaters and RTDs were designed and optimized for use in biological microfluidic applications. In order to arrive at an appropriate surface and surface energy for print, substrate treatments and print parameters were optimized. COMSOL was then used to simulate and optimize heater patterns, temperature profile and temperature gradients. The desired result of a heater pattern with a simple design, low voltage requirement, high temperature differential, and low temperature gradient was achieved. This was then implemented with printing, and print inconsistencies were mitigated by use of multiple pixel-wide lines, appropriate spacing in the pattern and optimized line widths for both the RTD and heater patterns. The final optimized printed RTD and heater structures were then electrically and thermally characterized to be integrated into the microfluidic chip.

The dimensions of the realized heaters (with leads) were ~13.5 X 19mm. With an applied voltage of 12V, temperatures of >100°C were achieved with the heaters, thus covering the full temperature range necessary for PCR. Although biological applications do not typically require temperatures higher than 100°C, the heaters have successfully reached temperatures of 250-270^0C at 25V showing potential for use in other applications as well. The printed gold RTDs (2-RTD structure) measured ~2.45 X 2.65cm and demonstrated a sheet resistivity of $3.9\text{x}10^{-5}$ Ohms-cm.

The experiments in Chapter 4 were conducted in collaboration with Professor Richard Mathies' group at University of California, Berkeley. Specifically, using printed heaters and RTDs, PCR was demonstrated in an integrated microfluidic chip. This chip was first thermally bonded to form microfluidic channels and to enable the functioning of printed devices (RTDs and heaters) that are important for PCR. PCR thermal cycling was then performed on a sample using the printed heaters and RTDs. The species of interest (amplified DNA) from the sample was selectively captured and electrophoretically driven through the laser detector.

Gender typing (discriminating between male and female DNA) was used as a proof of concept for this demonstration. Therefore, the successful functioning of printed devices for PCR was confirmed when the results from the laser detector correctly exhibited the fluorescent peaks of male (XY peaks) and female (X peak) DNA for the corresponding samples. Moreover, the accuracy of the printed devices was confirmed when the migration times of the male and female DNA precisely matched the expected times for these DNA sequences. PCR was thus successfully demonstrated using inkjet printed heaters and RTDs.

State of the art fabrication of RTDs and heaters involves a tedious process of using masks, photolithography and subtractive processing steps. Chapters 3 and 4 revealed the advantages of using printed electronics to fabricate these devices. Since the integrated microfluidic chip is constantly evolving to achieve higher efficiency and to serve new biological applications, the flexibility that printed electronics can provide in defining new devices and structures is unmatched.

Finally, in Chapter 5, the successful demonstration of all-printed electrostatically actuated PDMS valves was presented. Simulation based design was first used to finalize the valve structure. Each layer of the PDMS valve, namely the electrodes and the valve membrane, was then printed using pneumatic and inkjet printers. Optimizing the aspect ratio of the PDMS membrane yielded a noncollapsable valve structure. Flow rate measurements and dynamic characteristics were then measured to characterize the valve. With the 440μm wide and 16μm deep microfluidic channels used in this project, flow rates of 1.5μL/minute were observed in open valves. Moreover, the thinnest PDMS membrane (55μm) closed the channel completely (i.e. flow rate = 0) at a pull-in voltage of 250V. This PDMS membrane took ~1.5 seconds to close and ~5.5 seconds to open. While the closing time was accelerated by the external actuation force, the opening time was determined by the mechanical characteristics of the PDMS. More importantly, each layer of the valve, flow rates and time scales in the dynamic characteristics were all compatible with biological micofluidic applications.

The contributions of this thesis have thus been summarized in this chapter. The advantages that each of the printed or printable devices provides over its respective state of the art structures highlight the valuable contribution that printed electronics can make to biological applications. This work has also provided some interesting future directions to further the use of printed electronics in biology.

6.2 Future Work

Integration of the printed valves, PCR components (printed heaters and RTDs) and OTFT sensors into a biological microfluidic chip and demonstration of all three components together represent the long-term vision for this work. In acheiving this goal, many research topics are yet to be explored and studied.

The first steps in integration have been demonstrated using printed RTDs and heaters. The valves and sensors are yet to be integrated and tested with the microfluidic chip. Since the goal is to be able to ultimately use the OTFT DNA sensor in the microfluidic chip, the sensor needs to showcase sensitivity at the level of a single point mutation (or a single DNA base pair mismatch). This level of sensitivity is required for microfluidic applications such as genetic disease detection, and DNA sequencing, to name a few. For this purpose, more work on hybridization detection and particularly on single point mutation (‘single nucleotide polymorphism’) needs to be performed. One way to facilitate this research is to make the DNA immobilization on pentacene surface more stable and predictable. Although DNA immobilization is dependent on the pentacene morphology, the exact location of the immobilization is difficult to predict. Future work can focus on chemically modifying the pentacene surface to covalently bind to the DNA. This way, the orientation of the DNA is clear, and future experiments with hybridization will be more controllable.

The functioning of the printed PDMS valves can also be better understood in order to optimize the valve structure further. 3-D simulations of valves and their deflection will help highlight the parameters that can improve the valve structure and the required actuation voltages. In addition, studying factors such as the valve seat (size and shape of the area where the valve will be placed), and size and shape of electrodes (determines the shape and size of valve) can also enhance the functioning of the valve. The stretchability of printed metal films on PDMS can be researched further to obtain lifetime values for the valves. Finally, pressure and leakage tests will complete the analysis required to obtain a valve that can be integrated into a microfluidic chip.

Printed electronics can also facilitate the formation of channels in the microfluidic system when applicable. For example, PDMS can be printed on a glass substrate to form microfluidic channels, eliminating the need for conventional fabrication of etched glass channels. The printing of PDMS channels also eliminates the need for bonding of multiple substrate layers. Although PDMS has some disadvantages (porosity, lack of transparency, etc.) in biological applications, the printing of PDMS channels can optimize the use of glass and PDMS on the microfluidic chip as required.

Finally, ideas for integrating all the printed components on a microfluidic chip will now be shared. The integration of PCR components has already been shown. When glass channels are used, the microfluidic chip can be designed such that valves are needed on one side of the chip that can be left open for printing of these devices. This is illustrated in Figure 162, where glass layer 2 covers glass layer 1 entirely except for the channel areas that require valves. Moreover, the sensor can be printed on a flexible substrate such that it can be attached to the microfluidic chip by adhesive or other means. The sensor can be disposed and replaced as necessary since printing allows for a cost-effective system. A vision of the whole integrated system is illustrated in Figure 162.

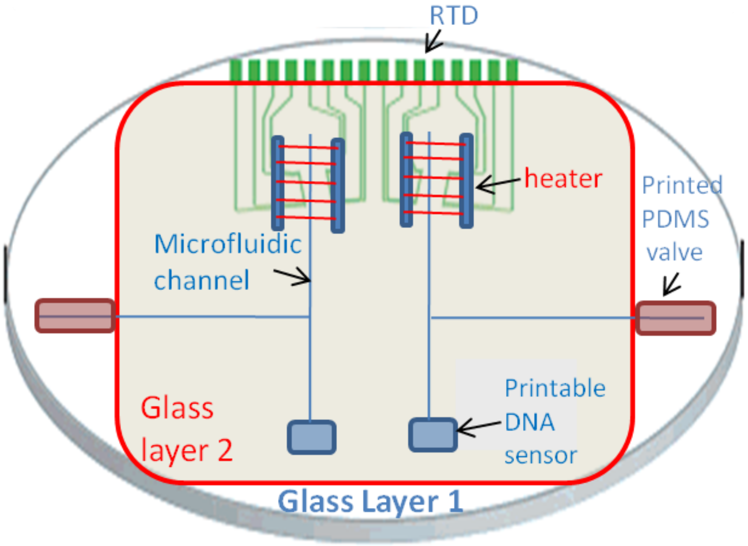

Figure 162. Vision of the microfluidic chip with all printed devices integrated together.

This thesis has thus revealed a relatively unexplored and exciting research area for printed electronics. Printed electronics has shown promising results in making biological applications more effective and efficient. Specifically, in this thesis, we have successfully demonstrated all-printed gold heaters, gold resistive temperature detectors, and electrostatically actuated PDMS microfluidic valves designed for biological microfluidic applications. In addition, work on DNA sensors using printable organic (pentacene) thin film transistors has shown promising results, bringing us a step closer in achieving printable DNA sensors capable of reaching the sensitivity necessary for genetic mutation detection and sequencing analyses. This work has also paved the way for exciting future research areas for printed electronics, facilitating more applications of this technology in the future for biological applications.

6.3 Sources

[1] Q. Zhang, "OTFT-Based DNA Detection System," Ph.D. dissertation, University of California-Berkeley, 2007.

[2] "What are single nucleotide polymorphisms (SNPs)?" *Genetics Home Reference.* [Online]. Available: http://ghr.nlm.nih.gov/handbook/genomicresearch/snp. [Accessed: 07-Jan-2012].